

Technische Universität München
TUM School of Engineering and Design

Smoothed particle hydrodynamics for multi-physics coupling problems

Xiaojing Tang

Vollständiger Abdruck der von der TUM School of Engineering and Design der Technischen Universität München zur Erlangung einer

Doktorin der Ingenieurwissenschaften (Dr.-Ing.)

genehmigten Dissertation.

Vorsitz: Prof. Dr.-Ing. Gisela Detrell Domingo

Prüfende der Dissertation:

1. Prof. Dr.-Ing. Oskar J. Haidn
2. Prof. Dr.-Ing. Dianlei Feng

Die Dissertation wurde am 08.11.2024 bei der Technischen Universität München eingereicht und durch die TUM School of Engineering and Design am 24.02.2025 angenommen.

Acknowledgement

I would like to express my sincere gratitude to those who have supported me throughout my research journey and the completion of this thesis.

First and foremost, I extend my heartfelt appreciation to my supervisor, Professor Oskar Haidn, for his invaluable suggestions, encouragement, and insightful feedback. His expertise and dedication have greatly influenced my work and fostered my growth as a researcher. I would also like to thank my mentor, Xiangyu Hu, for his unwavering support and mentorship. His patience, encouragement and insightful discussions have been instrumental in shaping my research and understanding of complex concepts.

Additionally, I extend my gratitude to my colleagues, Dong Wu, Zhentong Wang, Chi Zhang, Chenxi Zhao, Feng Wang, Tiziano Santese, Shuaihao Zhang, Bo Zhang, Mai Ye for their collaboration, camaraderie, and valuable insights. Working alongside you has enriched my experience and made this journey enjoyable.

To my parents, Lifeng Tang and Guie Tang, I am profoundly grateful for your love, support, and sacrifices. Your unwavering belief in me has been a constant source of motivation, and I owe much of my success to your encouragement. I would like to acknowledge my sister, Xiaochen Tang, for her love and support throughout my academic journey. Your presence in my life has been a source of strength.

Lastly, I would like to thank everyone who contributed in one way or another to my research and academic development. Your support has made this endeavor possible.

Munich, October 07, 2024

Xiaoqing Tang

Abstract

In many scientific and engineering disciplines, physical systems are characterized by the intricate interplay of multiple physical processes. Simulations for this complex scenarios are used to validate theoretical models and hypotheses, allowing for better alignment between theoretical predictions and real-world observations. This work addresses the complexities and challenges inherent in simulating multi-physics phenomena, including thermal-fluid interactions, structural dynamics, and multi-time scale processes, using the smoothed particle hydrodynamics (SPH) method.

The first part of this thesis introduces a robust SPH framework designed to effectively simulate thermal-fluid-structure interaction (TFSI) problems. This framework incorporates strong coupling at material interfaces and utilizes techniques such as kernel modifications and multi-time stepping to enhance computational accuracy and efficiency. This newly integrated method is applied to study the thermal augmentation owing to the existence of vortices induced by different immersed structure configurations. The detailed heat and vortex information obtained by the present SPH TFSI solver indicates that the FSI reinforces the heat transfer via vortexes interaction with fluid within the boundary layer. Through simulations, this study demonstrates the versatility and potential of the mesh-free SPH approach for complex industrial heat transfer applications.

The second part of the thesis addresses the challenges associated with modeling plate and shell structures with large aspect ratios, particularly when thickness variations are present.

A new adaptive smoothed particle hydrodynamics (ASPH) approach is proposed, integrating a fully dimensional model with a framework for anisotropic particle resolution. Several numerical experiments, including an example focused on the deformation of a porous film caused by uneven internal fluid pressure along its thickness, are performed to evaluate the method's computational precision and efficiency. The comparison of the results with benchmark data and conventional isotropic SPH models shows strong alignment, supporting the effectiveness of the ASPH method across diverse applications.

In the third part, the thesis explores the intricacies of multi-time scale coupling, which is crucial for accurately simulating processes that evolve at different time scales. An explicit multi-time step algorithm is proposed within the SPH framework, combined with a solid dynamic relaxation scheme to address the challenges of achieving equilibrium in fast solid response processes. This innovative approach allows for efficient simulations by decoupling processes with distinct time scales, significantly reducing computational time while ensuring the reliability of results.

Collectively, this thesis presents significant advancements in SPH methodologies for simulating complex fluid and solid dynamics, contributing valuable insights and tools for a wide range of industrial and scientific applications. The findings highlight the versatility of SPH in addressing diverse challenges in multi-physics simulations and establish a foundation for future research in this evolving field.

Zusammenfassung

In vielen wissenschaftlichen und ingenieurtechnischen Disziplinen sind physikalische Systeme durch das komplexe Zusammenspiel mehrerer physikalischer Prozesse gekennzeichnet. Simulationen für diese komplexen Szenarien werden verwendet, um theoretische Modelle und Hypothesen zu validieren, was eine bessere Abstimmung zwischen theoretischen Vorhersagen und realen Beobachtungen ermöglicht. Diese Arbeit befasst sich mit den Komplexitäten und Herausforderungen, die mit der Simulation von Mehrphysikphänomenen verbunden sind, einschließlich thermischer-fluiddynamischer Wechselwirkungen, Strukturmechanik und Multi-Zeit-Skalen-Prozessen, unter Verwendung der Methode der geglätteten Partikelhydrodynamik (SPH).

Der erste Teil dieser Dissertation stellt ein robustes SPH-Rahmenwerk vor, das entwickelt wurde, um Probleme der thermischen-fluid-strukturellen Wechselwirkung (TFSI) effektiv zu simulieren. Dieses Rahmenwerk integriert eine starke Kopplung an Materialgrenzen und nutzt Techniken wie Kernmodifikationen und Multi-Zeit-Schritte, um die Rechenleistung und Effizienz zu steigern. Diese neu integrierte Methode wird angewendet, um die thermische Verstärkung aufgrund der Existenz von durch verschiedene eingetauchte Strukturkonfigurationen induzierten Wirbeln zu untersuchen. Die detaillierten Wärme- und Wirbelinformationen, die von dem präsentierten SPH-TFSI-Löser gewonnen wurden, zeigen, dass die Fluidstrukturwechselwirkung (FSI) den Wärmeübergang durch die Wechselwirkung von Wirbeln mit Fluid innerhalb der Grenzschicht verstärkt. Durch Simulationen demonstriert diese Studie die Vielseitigkeit und das Potenzial des maschinenfreien SPH-Ansatzes für komplexe industrielle Wärmeübertragungsanwendungen.

Der zweite Teil der Dissertation befasst sich mit den Herausforderungen, die mit der Modellierung von Platten- und Schalenstrukturen mit großen Seitenverhältnissen verbunden sind, insbesondere wenn Dickenvariationen vorhanden sind. Eine adaptive Methode der geglätteten Partikelhydrodynamik (ASPH) wird entwickelt, die ein anisotropes volldimensionales Modell mit einem anisotropen Partikelauflösungsrahmen integriert. Eine Reihe von numerischen Beispielen, zusammen mit einer spezifischen Anwendung, die die Deformation eines porösen Films aufgrund nichtuniformen inneren Fluiddrucks in Dickenrichtung betrifft, werden durchgeführt, um die rechnerische Genauigkeit und Effizienz der vorgeschlagenen ASPH-Methode zu bewerten. Vergleichende Analysen unserer Ergebnisse mit Referenzdaten und traditionellen isotropen SPH-Lösungen zeigen enge Übereinstimmungen und bestätigen die Eignung der vorliegenden ASPH-Methode in verschiedenen Szenarien.

Im dritten Teil untersucht die Dissertation die Komplexität der Mehrzeit Skalierungskopplung, die entscheidend ist für die genaue Simulation von Prozessen, die sich in unterschiedlichen Zeitrahmen entwickeln. Ein expliziter Mehrzeit-Schritt-Algorithmus wird innerhalb des SPH-Rahmenwerks vorgeschlagen, kombiniert mit einem dynamischen Entspannungsschema für feste Stoffe, um die Herausforderungen der Erreichung des Gleichgewichts in schnellen Reaktionsprozessen von festen Stoffen zu bewältigen. Dieser innovative Ansatz ermöglicht effiziente Simulationen, indem Prozesse mit unterschiedlichen Zeitrahmen entkoppelt werden, was die Rechenzeit erheblich verkürzt und gleichzeitig die Zuverlässigkeit der Ergebnisse gewährleistet.

Insgesamt stellt diese Dissertation bedeutende Fortschritte in den SPH-Methodologien zur Simulation komplexer Fluid- und Festkörperdynamik vor und bietet wertvolle Erkenntnisse sowie Werkzeuge für ein breites Spektrum industrieller und wissenschaftlicher Anwendungen. Die Ergebnisse heben die Vielseitigkeit von SPH bei der Bewältigung vielfältiger Herausforderungen in Mehrphysik-Simulationen hervor und legen eine Grundlage für zukünftige Forschungen in diesem sich entwickelnden Bereich.

Contents

List of Figures	ix
1 Introduction	1
1.1 Numerical simulation and methods	1
1.1.1 Multi-physics problems	1
1.2 SPH application and modification	3
1.2.1 TFSI simulation	3
1.2.2 multi-time scale coupling	4
1.2.3 Thin plate and shell structure	5
1.3 Outline	7
2 Physical models and governing equations	9
2.1 Solid equations	9
2.1.1 Motion and deformation	9
2.2 Fluid and diffusion equations	10
2.3 Fluid transportation coupling porous media deformation	11
2.3.1 Mass and momentum equations	11
2.3.2 Fick's law	12
2.3.3 Effective stress on solid	12
3 Methodology	15
3.1 Theory and basics of SPH	15
3.2 SPH discretization for fluids and solids	16
3.3 Discretization of fluid-structure and thermal coupling	16
3.4 SPH discretization for fluid-structure interaction	17
3.5 ASPH theory	18
3.5.1 ASPH principles	18
3.5.2 Kernel functions in ASPH	20
3.5.3 Correction of the derivatives	20
3.6 Multi-time step algorithm	21
4 Summaries of publications	23
4.1 An integrative SPH method for heat transfer problems involving fluid-structure interaction	23
4.1.1 Summary of the publication	23
4.1.2 Individual contributions of the candidate	24
4.2 Simulating plate and shell structures with anisotropic resolution using adaptive smoothed particle hydrodynamics	25
4.2.1 Summary of the publication	25
4.2.2 Individual contributions of the candidate	26

4.3	An explicit multi-time stepping algorithm for multi-time scale coupling problems in SPH	27
4.3.1	Summary of the publication	27
4.3.2	Individual contributions of the candidate	27
5	Conclusions	29
A	Original journal papers	31
A.1	Paper I	32
A.2	Paper II	48
A.3	Paper III	68
	Bibliography	111

List of Figures

1.1	Multi-physics problems: (a) surface temperature distribution of a cylindrical Li-Ion Battery [77], (b) multiscale simulation of crack propagation in silicon [34], (c) TFSI simulation [30], (d) schematic of multiscale blood clot modeling [80].	2
1.2	Particle interaction and the kernel function.	2
1.3	Schematic diagram of a heat transfer channel with a probe R in the middle of the channel located downstream.	4
1.4	Multi-time scale coupling simulation using implicit scheme, from Ref. [12]. . .	5
1.5	Schematic view of a thin structure.	6
2.1	Finite deformation process on a body \mathcal{B}	9
2.2	Partially saturated porous medium.	11
3.1	(a)Schematic view of a thin structure, (b) SPH isotropic resolution, (c) elliptical smoothing kernel.	19
3.2	Flowchart of the iterative scheme in multi-time step algorithm.	22
4.1	Stable temperature contours in four different cases.	24
4.2	2D thin plate: the deformation at the final time instant colored by von Mises strain from SPH and ASPH with different anisotropic ratios.	25
4.3	2D thin plate: the nondimensionalized y position of the very center point of the beam, from SPH and ASPH with different anisotropic ratios.	26
4.4	3D fluid-structure interaction: the deformation colored by water saturation at different time instants.	27
4.5	3D fluid-structure interaction: bending amplitude of the center point compared with experimental data and results from other numerical models.	28

Introduction

1.1 Numerical simulation and methods

1.1.1 Multi-physics problems

In many scientific and engineering disciplines, physical systems are characterized by the intricate interplay of multiple physical processes, such as fluid flow, thermal dynamics, electromagnetic fields, and structural mechanics. The challenge of capturing multi-physics interactions stems from the fact that each physical domain often obeys its own governing equations and has distinct time and spatial scales. For example, in aerospace engineering, the aerodynamics of an aircraft is influenced not only by fluid dynamics but also by structural deformation and heat transfer due to varying thermal loads. In biomedical engineering, the movement of blood through arteries depends on fluid dynamics as well as the elastic properties of vessel walls. Accurately modeling such systems is crucial for designing robust solutions and predicting the behavior of complex devices and natural systems [30, 34, 77, 80]. Having emerged as an essential tool in this context, Numerical multi-physics simulations are used to validate theoretical models and hypotheses, allowing for better alignment between theoretical predictions and real-world observations.

However, even has had a profound impact on fundamental science and engineering research, numerical simulation of multi-physics problems, for example, thermal-fluid-structure interaction (TFSI), still presents significant challenges due to the simultaneous involvement of fluid dynamics, solid deformation, and heat transfer. Specifically, in these systems, fluid pressure induces solid vibrations, which then affect the flow field and alter the temperature distribution within the fluid. The motion of the solid, driven by the fluid, influences both flow and temperature dynamics. The complex, nonlinear, and time-dependent interactions, particularly with large deformations and moving fluid-solid interfaces, create significant challenges for numerical simulations [49]. To date, two primary methods have been applied to address TFSI problems: (i) grid-based approaches, where the domain is divided into grids and the governing equations are solved over these discrete elements, and (ii) mesh-free methods, which are gaining increasing attention, where particles carry physical properties and the equations are solved within a Lagrangian framework [30].

In mesh-based methods, two main approaches are commonly discussed in the literature. The first is the monolithic approach, such as the arbitrary Lagrangian-Eulerian (ALE) method, where the fluid and solid equations are solved simultaneously within a unified solver. Despite its widespread use in TFSI simulations [1, 22, 65], ALE requires a remeshing process as the material interface evolves over time, which adds to the computational complexity and cost [47]. The second approach is the partitioned method, where a computational solid dynamics (CSD) solver is paired with a computational fluid dynamics (CFD) solver to independently resolve the solid and fluid equations, with a fluid-structure interaction (FSI) coupling solver managing the interface. One example is the immersed boundary method (IBM), where the

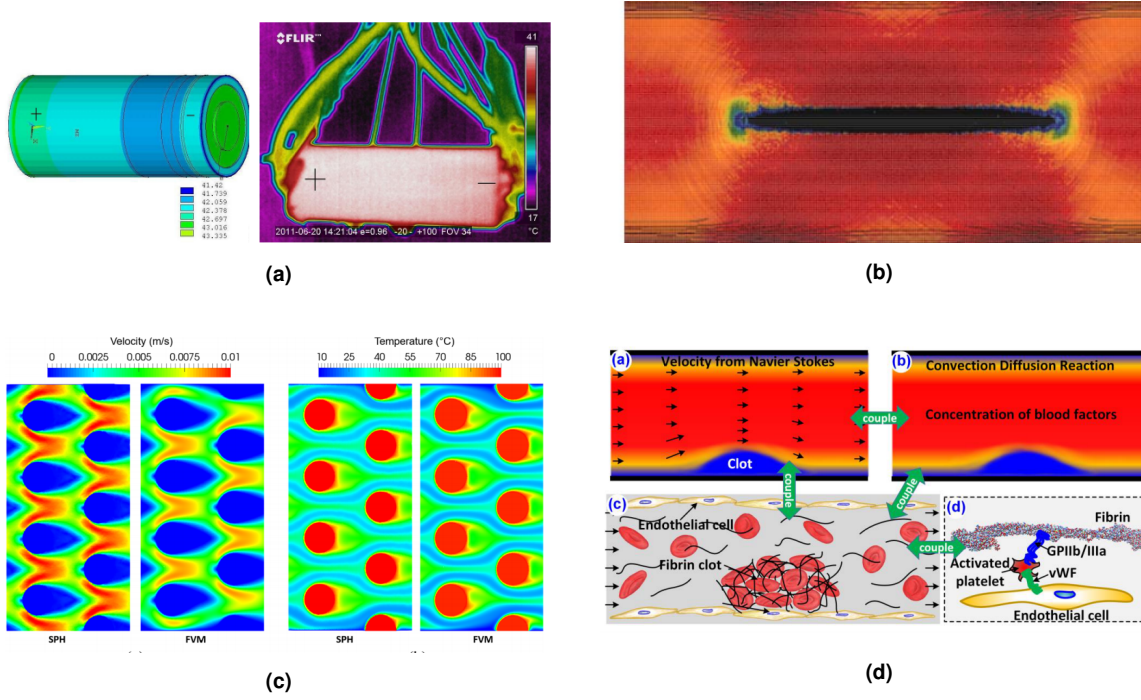


Figure 1.1: Multi-physics problems: (a) surface temperature distribution of a cylindrical Li-Ion Battery [77], (b) multiscale simulation of crack propagation in silicon [34], (c) TFSI simulation [30], (d) schematic of multiscale blood clot modeling [80].

structure is embedded in the fluid, reducing remeshing costs during simulations [73]. However, IBM requires adjustments to the motion equations to ensure displacement continuity and force equilibrium at the fluid-solid interface.

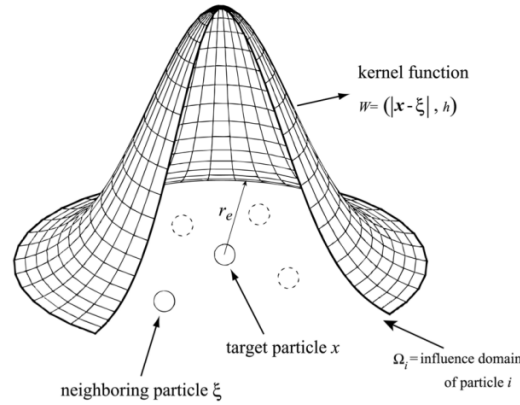


Figure 1.2: Particle interaction and the kernel function.

Mesh-free methods offer a highly attractive alternative for simulating not only TFSI problems but also other complex multi-physics systems, due to their inherent ability to handle moving interfaces. One such method, Smoothed Particle Hydrodynamics (SPH), was initially developed by Lucy [51], along with Gingold and Monaghan [25], for astrophysical simulations. In SPH, the continuum is represented by a set of particles, each carrying properties like mass, velocity, pressure, and density. These particles interact using kernel-based interpolation, where a smoothing kernel is employed to approximate field quantities and their derivatives. The meshless nature of SPH allows it to effectively tackle complex geometries

and large deformations, which are often difficult to manage with traditional grid-based approaches. Different with Eulerian methods that depend on fixed spatial grids, SPH uses a Lagrangian framework that follows particle motion, providing natural advantages for capturing advection and accurately modeling free-surface dynamics.

In more recent decades, SPH method has proven particularly useful for problems involving multiphase flows [55, 70, 72, 82], solid mechanics [43, 56, 86], fluid-structure interactions [28, 35, 36, 53], and scenarios involving highly dynamic or fragmented geometries [23, 41]. Applications such as modeling wave breaking, dam breaks, and multiphase mixing benefit from the ability of SPH to represent free surfaces and interfaces without the need for explicit tracking. Furthermore, SPH has been successfully employed in areas such as expansion, impact analysis, and biofluid simulations, where the interaction of complex physical processes plays a critical role. In recent years, advancements in computational power and algorithmic efficiency have expanded the applicability of SPH to increasingly complex and realistic scenarios. These developments have enhanced its predictive capability, making SPH a powerful tool for both academic research and industrial applications. As multi-physics problems continue to demand more sophisticated modeling approaches, SPH's ability to seamlessly handle complex couplings and large deformations makes it a method of considerable interest for modern numerical simulations. Comprehensive reviews are available in Refs. [27, 45, 52, 85].

1.2 SPH application and modification

1.2.1 TFSI simulation

In terms of thermal and mass diffusion, SPH has been effectively applied to simulate heat conduction [11, 71], convection [59, 79], and phase-change heat transfer problems [14]. For instance, Yang et al. [79] employed SPH to model natural convection, exploring how variations in Prandtl and Rayleigh numbers affect flow behavior. Vishwakarma et al. [76] used SPH to simulate heat conduction in irregular geometries, demonstrating that the method produces temperature profiles consistent with those obtained from commercial software such as Fluent, where grid-based approaches can encounter difficulties. Farrokhpanah [14] introduced an SPH-based model that considers transient heat conduction, specifically incorporating latent heat during the solidification process. These studies highlight SPH's capability to accurately model temperature distributions in both fluids and solids. Hosain et al. [30] further applied SPH to several heat transfer scenarios, such as heat conduction in water, heat transfer in laminar flow between plates, and heat exchanger tubes. Their SPH results were within the range of data obtained using the Finite Volume Method (FVM) and were validated against analytical models. However, their study did not address FSI coupling effects. Long [49] extended SPH's application by coupling it with the edge-based smoothed finite element method (ES-FEM) to handle TFSI problems, where ES-FEM was used for solid structures and SPH for fluid dynamics. To manage fluid-structure interaction, a ghost particle algorithm was employed, facilitating the resolution of fluid-structure conjugate heat transfer. While SPH shows strong potential in heat transfer applications, its use in TFSI problems remains somewhat under-explored in the literature. Moreover, many existing studies incorporate SPH alongside other methods to simulate fluid-structure interactions and heat transfer, which can add complexity and increase computational demands.

Therefore, we developed a strongly coupled SPH solver within a unified SPH framework to explore heat transfer enhancement using vortex generators. Several algorithms were employed to ensure numerical accuracy and stability, including a Riemann-based solver for fluid

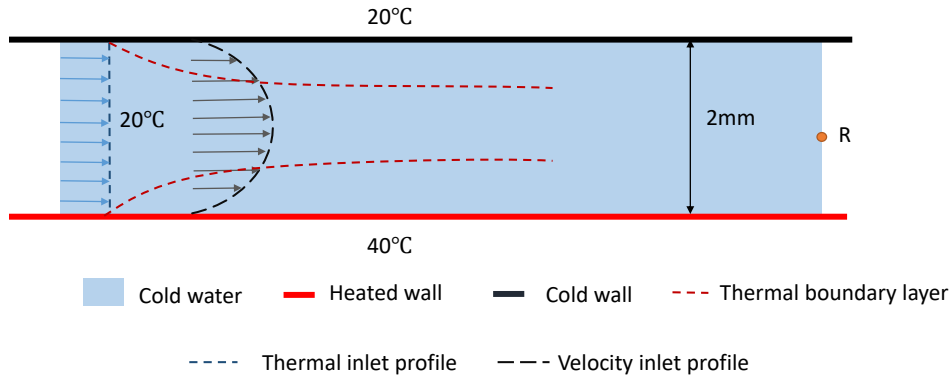


Figure 1.3: Schematic diagram of a heat transfer channel with a probe R in the middle of the channel located downstream.

dynamics, correction of derivatives in the total Lagrangian formulation for structural deformation, a multi-time stepping approach, the position-based Verlet scheme, and a second-order Runge-Kutta integrator for thermal simulations. To validate the SPH thermal and FSI solver, we first simulated heat transfer in a micro-channel and a fluid-structure interaction (FSI) case. Following this, we combined the thermal and FSI solvers to simulate a heat transfer channel featuring different vortex generators, analyzing the simultaneous interaction of heat transfer, fluid vortices, and solid deformation. The results demonstrated that the developed SPH TFSI solver excels at capturing thermal-fluid dynamics in TFSI scenarios, revealing the intricate relationship between vortex behavior and cooling efficiency. This study not only extends the application of the SPH method to TFSI problems but also introduces a versatile multi-physics solver capable of addressing a variety of industrial heat transfer challenges. The analysis further assesses SPH's effectiveness in modeling heat transfer in complex geometries, offering a foundation for optimizing heat transfer processes in numerous engineering contexts.

1.2.2 multi-time scale coupling

Despite its broad applicability, SPH exhibits limitations when addressing multi-scale coupling problems prevalent in diverse engineering domains, especially in scenarios involving rapid solid dynamics [8]. A major issue is the significant difference in time scales between fast and slow processes, which continues to pose difficulties for numerical simulations [37]. To handle multi-time scale problems, implicit, explicit, or hybrid coupling schemes can be used [5, 48]. The implicit scheme is particularly advantageous as it allows for the use of larger time steps during time integration [5, 19, 63], enabling a monolithic approach to address both fast and slow processes simultaneously. For example, Zhao [88] utilized an implicit Newmark scheme to simulate fluid flow through porous elastic solids, where the dynamics of the solid and the diffusion of the fluid happen on different time scales. Similarly, Gaston [17] used an implicit scheme to study the interactions between fluid dynamics, chemical reactions, and structural mechanics in a reactor. However, the implicit approach requires solving equations by inverting the stiffness matrix at every time step [18, 74], which significantly increases computational costs and memory requirements [69].

For enhancing computational efficiency, techniques involving explicit scheme are often preferred for addressing multi-time scale coupling problems due to their direct time integration and straightforward numerical formulation [6, 29, 64, 78]. By partitioning the mesh into subdomains and the governing equations into subsystems, explicit-implicit and explicit-

explicit partitions have been used to solve coupled-field dynamic problems, allowing multi-time step integrating with staggered solution procedures [3, 4, 32]. However, in systems displaying widely different characteristic response times, this methodology demands a large amount of staggered steps and frequent data exchanges per time step, making it economically challenging to apply to complex three-dimensional problems [15]. Explicit schemes have also been employed to simulate processes like material stretching and necking, where the load is applied over a long period, but the material's dynamic response occurs rapidly [13, 67]. Since the real-world load occurs over a long time scale, the simulation time must match this duration. However, the small stable time step sizes required for fast dynamic processes in explicit schemes mean that millions of time steps are often needed to simulate the full process, posing practical difficulties. To shorten the simulation time, the loading rate is typically increased artificially [9]. However, using an unrealistically high loading rate can introduce limitations and inaccuracies in the results [81], highlighting the importance of carefully balancing loading rates to maintain the accuracy of simulations. We implemented a multi-time



Figure 1.4: Multi-time scale coupling simulation using implicit scheme, from Ref. [12].

stepping algorithm in SPH, specifically designed to handle slow and fast processes by assigning large and small time steps, respectively. The method organizes time integration into two loops: an outer loop for slow processes using a larger time step, and an inner loop for fast solid dynamics with a smaller time step. However, the small time steps required for the fast processes can lead to numerous iterations of solid stress relaxation within a single outer loop cycle, which reduces computational efficiency. To mitigate this issue, a dynamic relaxation method based on an implicit operator splitting scheme [89] was introduced to speed up the convergence of the fast dynamic process toward equilibrium. To test the performance and efficiency of the algorithm, we first conducted simulations on a manuscript torsional case and tensile tests, covering both two-dimensional and three-dimensional examples. Following this, the algorithm was applied to simulate fluid diffusion in porous media coupled with elastic deformation, which is relevant to processes in chemical reactors such as the fuel cells of batteries. In these systems, fluid mixtures diffuse through a Nafion membrane, a slow process that affects battery performance by altering fluid concentration and membrane deformation. The results indicate that the developed algorithm offers significant improvements in both accuracy and computational efficiency compared to existing numerical methods.

1.2.3 Thin plate and shell structure

In spite of the aforementioned developments, SPH method faces challenges in simulating thin plate and shell structures. Plate and shell structures, characterized by one dimension

being much smaller than the other two, have been studied using meshless methods such as the element-free Galerkin approach [33, 39, 40] and the reproducing kernel particle method [10, 42, 61, 62, 68]. In the SPH framework, reduced-dimensional models are often employed for simulating thin structures [24, 50, 54, 87], where these structures are typically discretized using a single layer of particles to optimize computational efficiency. However, reduced-dimensional models are not suitable for cases that require consideration of variations in the reduced thickness direction. For example, when dealing with a thin porous membrane partially filled with fluid, which is common in the fuel cells of batteries [26, 58], nonuniform fluid concentrations necessitate finer resolution in the thickness direction to accurately capture the variations in fluid pressure. Although traditional full-dimensional SPH models with isotropic resolutions can handle such scenarios, the application of SPH to thin structures involving parameter variation in the thickness direction remains limited. This is primarily due to the significant computational cost involved, driving the need for the use of anisotropic resolutions.

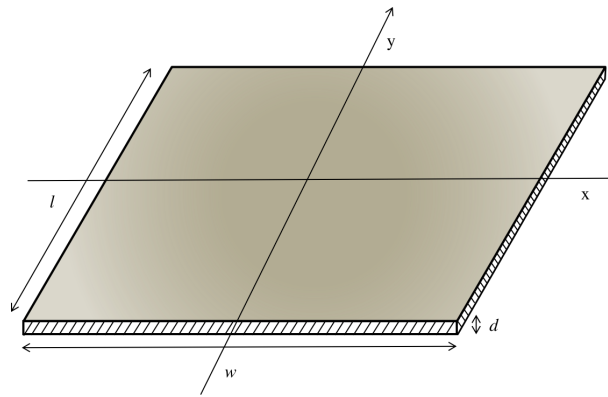


Figure 1.5: Schematic view of a thin structure.

Considering anisotropic particle resolution in SPH, particle spacing in the larger dimension of thin structures is significantly greater than in the thickness direction. With this type of anisotropic discretization, the use of an isotropic smoothing kernel, which defines a spherical domain of influence in SPH, becomes inadequate. To address this, the adaptive smoothed particle hydrodynamics (ASPH) method, a variant of SPH that incorporates anisotropic smoothing kernels, is introduced as a more suitable approach. The idea of using anisotropic smoothing kernels in SPH was first proposed by Gingold and Bicknell [7] for the study of cosmological dynamics. Later, Owen et al. [60] enhanced the ASPH method by introducing a mathematical formulation that replaced the scalar smoothing length—responsible for defining spherical kernels—with a smoothing tensor, allowing for the creation of ellipsoidal kernels through localized linear coordinate transformations. M. Liu and G. Liu [44] applied the ASPH approach to simulate micro-channel flows characterized by a high length-to-width ratio, where the adaptive kernel aligned with the geometry, reducing computational time. ASPH, with its more generalized elliptical influence domain, has also been used to simulate high-strain Lagrangian solid dynamics, particularly where anisotropic volume changes are observed [46]. In addition, Fu et al. [16] introduced the use of ellipsoidal kernels in ASPH, which enabled the particle distribution to adapt to anisotropic target functions. However, to the best of my knowledge, the application of ASPH for modeling thin structures has yet to be explored in the literature.

We expanded the application of the ASPH method to simulate thin structures by incorporating anisotropic resolutions. In this approach, the smoothing kernel is defined in conjunction with a linear transformation tensor, resulting in the particle's support domain forming an ellipsoidal region instead of a spherical one. Additionally, the correction matrix used

for ensuring first-order consistency in the kernel gradient was adjusted to account for the anisotropic kernel within the total Lagrangian framework of ASPH.

1.3 Outline

The remainder of this thesis is structured as follows. Chapter 2 summaries the theories and governing equations for fluid dynamics, diffusion dynamics, solid mechanics including the elastic and nonlinear hardening plastic solid characteristics and fluid structure interaction in porous media. The corresponding SPH discretization of these governing equations and ASPH theory for thin plate and shell are described in Chapter 3. Chapter 4 presents a detailed exposition of the proposed multi-time stepping algorithm, incorporating dynamic relaxation. Finally, Chapter 5 presents concluding remarks and recommendations for future work are given.

Physical models and governing equations

2.1 Solid equations

2.1.1 Motion and deformation

In this section, we briefly outline the essential physical principles of solid deformation, as well as the relevant notations and symbols used in the total Lagrangian framework. The analysis focuses on a solid body, denoted as \mathcal{B} , which occupies two regions: \mathcal{R}_0 and \mathcal{R} , corresponding to the body's configuration at initial time t_0 (where $t = 0$) and at time t , respectively. In the initial configuration \mathcal{R}_0 , the position of a material point is expressed as $\mathbf{X} \in \mathcal{R}_0$, while in the current configuration, it is denoted as $\mathbf{x} \in \mathcal{R}$. The motion of the solid body is described by an invertible mapping, ϕ , which transforms the material point \mathbf{X} to its position in the current configuration, $\mathbf{x} = \phi(\mathbf{X}, t)$, as illustrated in Figure 2.1. The Lagrangian velocity of a material point is thus defined by $\mathbf{v}(\mathbf{X}, t) = \frac{d\phi(\mathbf{X}, t)}{dt}$. The deformation gradient, denoted as \mathbf{F} , measures the extent of deformation from the reference configuration to the deformed configuration and is derived from the displacement vector $\mathbf{u} = \mathbf{x} - \mathbf{X}$ according to the equation:

$$\mathbf{F} = \frac{d\mathbf{x}}{d\mathbf{X}} = \nabla^0 \mathbf{u} + \mathbf{I}, \quad (2.1)$$

where ∇^0 represents the gradient operator in the reference configuration, and \mathbf{I} is the identity matrix.

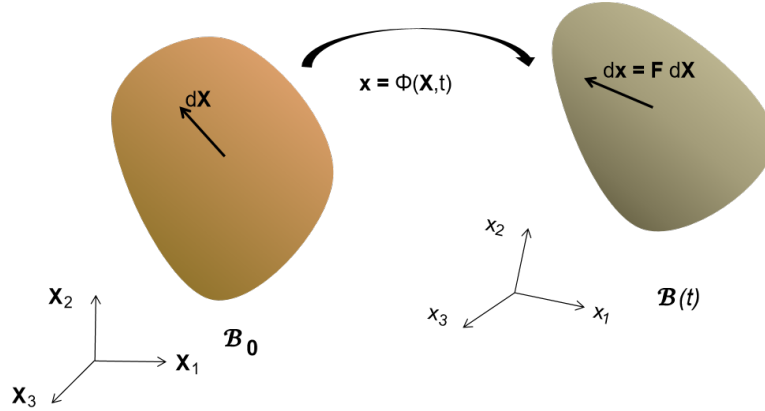


Figure 2.1: Finite deformation process on a body \mathcal{B}

Derived from the fundamental conservation laws of mass and momentum, within the Lagrangian framework, the governing equations for solid are expressed as follows

$$\begin{cases} \rho = \rho_0 \frac{1}{J} \\ \rho_0 \frac{dv}{dt} = \nabla^0 \cdot \mathbf{P}^T. \end{cases} \quad (2.2)$$

where ρ represents the density in the current configuration \mathcal{R} , and ρ_0 is the density in the initial configuration \mathcal{R}_0 . The Jacobian determinant $J = \det(\mathbf{F})$ denotes the local volume change, where $J > 1$ reflects expansion and $J < 1$ represents contraction. The term \mathbf{v} indicates velocity, while T represents the matrix transposition. The first Piola-Kirchhoff stress tensor, \mathbf{P} , which relates to the stress in the reference configuration, can be calculated as:

$$\mathbf{P} = \mathbf{F}\mathbf{S}, \quad (2.3)$$

where \mathbf{S} is the second Piola-Kirchhoff stress tensor. For isotropic, linear elastic materials, the second Piola-Kirchhoff stress tensor \mathbf{S} can be given by

$$\mathbf{S} = \lambda \operatorname{tr}(\mathbf{E})\mathbf{I} + 2\mu\mathbf{E}, \quad (2.4)$$

where \mathbf{E} is the Green-Lagrangian strain, determined by

$$\mathbf{E} = \frac{1}{2}(\mathbf{F}\mathbf{F}^T - \mathbf{I}). \quad (2.5)$$

Here, λ and μ are the Lamé parameters. The key material properties include Young's modulus E , Poisson's ratio ν , shear modulus $G = \mu$, and bulk modulus $K = \lambda + \frac{2\mu}{3}$, which are interrelated through the following equations

$$E = 2G(1 + \nu) = 3K(1 - 2\nu), \quad (2.6)$$

2.2 Fluid and diffusion equations

In thermal fluid-structure interaction (TFSI) problems, the thermal fluid is considered as incompressible and viscous. The governing equations consist of the mass conservation and momentum balance equations

$$\begin{cases} \frac{d\rho}{dt} = -\rho \nabla \cdot \mathbf{v} \\ \frac{d\mathbf{v}}{dt} = \frac{1}{\rho} (-\nabla p + \eta \nabla^2 \mathbf{v}) + \mathbf{F}^{S:p} + \mathbf{F}^{S:\nu} \end{cases}, \quad (2.7)$$

where ρ , \mathbf{v} , p , and η represent the fluid density, velocity, pressure, and dynamic viscosity, respectively. The terms \mathbf{F}^S and \mathbf{F}^S denote the forces exerted by the solid on the fluid due to pressure and viscosity. Under the weakly-compressible assumption, a linear equation of state is employed to approximate the pressure based on density variations, allowing us to simulate incompressible flow, as shown below [57]:

$$p = c^2(\rho - \rho^0), \quad (2.8)$$

where c is the artificial speed of sound, determined by the specific case, and ρ^0 is the reference density [57]. For the solid part of the TFSI problem, an isotropic and linearly elastic material model is adopted for the vortex generator. Therefore, the solid equations discussed earlier are applicable here as well. In terms of heat transfer, the governing equation follows Fourier's law, describing the rate of temperature change. To simplify the analysis and maintain focus on the core aspects, we neglect any external heat sources. Consequently, the heat transfer equations are formulated as follows

$$\frac{dT}{dt} = \nabla \cdot \left(\frac{k}{\rho c_p} \nabla T \right), \quad (2.9)$$

where T is the temperature, k the thermal conductivity coefficient and c_p the specific heat capacity.

2.3 Fluid transportation coupling porous media deformation

To capture the coupled behavior of fluid transport within porous media alongside the elastic deformation of the porous membrane, a fluid-structure interaction (FSI) model is proposed. This model considers the concurrent fluid flow through the porous solid material, leading to increased fluid pressure and the corresponding deformation of the solid structure. In this

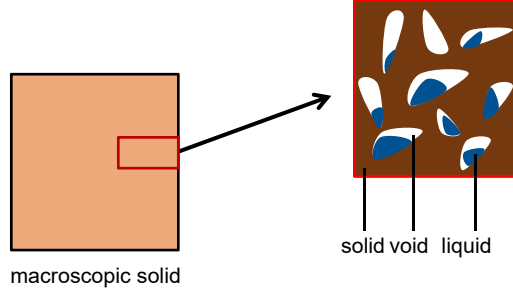


Figure 2.2: Partially saturated porous medium.

model, the heterogeneous material is treated as a continuous solid medium that contains uniformly distributed small voids, characterized by a homogeneous porosity denoted as c . When a fluid interacts with this medium, it infiltrates these small pores, leading to the formation of a mixture comprising both solid and fluid components, as depicted in Figure 2.2. To streamline this model, we employ the approach suggested by Zhao [88] to establish a momentum equation for the mixture. In this mixture model, state variables such as solid density ρ^s , locally fluid density ρ^l , solid velocity \mathbf{v}^s , and fluid saturation \tilde{c} are defined, allowing the fluid velocity to be computed in relation to the solid velocity.

2.3.1 Mass and momentum equations

In the context of a representative volume element dV , the macroscopic porosity c is defined as the ratio of the total pore volume dV^p to dV , represented mathematically as $c = \frac{dV^p}{dV}$. Note that the condition $0 < c < 1$ is applicable in all instances. When a porous solid contains a partial saturation of fluid, the level of fluid saturation \tilde{c} can be expressed as

$$\tilde{c} = \frac{dV^l}{dV}, \quad (2.10)$$

where dV^l signifies the volume of fluid present in the representative element dV . It follows that \tilde{c} will always be less than or equal to the maximum possible saturation c , i.e., $\tilde{c} \leq c$. The locally effective fluid density ρ^l , defined as the mass of the fluid per unit volume, varies with the degree of fluid saturation and can be expressed as

$$\rho^l = \frac{dm^l}{dV} = \frac{dm^l}{dV^l} \frac{dV^l}{dV} = \rho^L \tilde{c}, \quad (2.11)$$

where dm^l denotes the mass of the fluid contained within dV , ρ^L the fluid density, which is assumed to remain constant for incompressible fluids. For a porous solid that is partially saturated with fluid, the total linear momentum \mathbf{M} in the region \mathcal{R} can be expressed as the sum of the momentum from the fluid and the solid, represented by the equation:

$$\mathbf{M} = \rho \mathbf{v} = \rho^l \mathbf{v}^l + \rho^s \mathbf{v}^s, \quad (2.12)$$

where ρ and \mathbf{v} refer to the total density and velocity respectively, \mathbf{v}^l the velocity of fluid, ρ^s and \mathbf{v}^s the density and velocity of dry porous solid. Given the disparity between \mathbf{v}^l and \mathbf{v}^s , the fluid flux \mathbf{q} across the boundary ∂V of the element can then be described as

$$\mathbf{q} = \rho^l (\mathbf{v}^l - \mathbf{v}^s). \quad (2.13)$$

It is clear that when there is no fluid movement through the boundary, the fluid flux satisfies $\mathbf{q} = \mathbf{0}$, ensuring that the fluid mass within a given element remains constant. Fluid mass and momentum transfer between the microscopic solid components occur as fluid moves from areas with higher saturation levels to those with lower saturation. Consequently, within a mixture element dV , the linear momentum balance indicates that the change in momentum \mathbf{M} is influenced by two main factors: the stress applied to the element and the fluid flux of linear momentum represented by $\mathbf{v}^l \otimes \mathbf{q}$ across the boundary ∂V . Here, the symbol \otimes denotes the outer product of two vectors or tensors. Thus, the conservation of the total linear momentum for the mixture can be formulated as follows:

$$\frac{d\mathbf{M}}{dt} = \nabla \cdot \boldsymbol{\sigma} - \nabla \cdot (\mathbf{v}^l \otimes \mathbf{q}), \quad (2.14)$$

where $\boldsymbol{\sigma}$ denotes the Cauchy stress acting on the solid within the mixture. The stress $\boldsymbol{\sigma}$ is composed of the Cauchy stress $\boldsymbol{\sigma}^s$ due to the deformation of the solid and the pressure stress $\boldsymbol{\sigma}^l$ attributed to the fluid phase, as discussed in the following section 2.3.3.

2.3.2 Fick's law

In a partially saturated solid, the variations in fluid saturation drive the movement of fluid from regions with higher fractions to those with lower fractions. The resulting fluid flux conforms to Fick's law, expressed as:

$$\mathbf{q} = -D\rho^l \nabla \tilde{c}, \quad (2.15)$$

which indicates that the fluid flux is proportional to the diffusivity D , the effective fluid density ρ^l , and the gradient of fluid saturation \tilde{c} . Consequently, the time derivative of the fluid mass within the volume element dV can be related to the fluid flux \mathbf{q} across the boundary ∂V , represented as:

$$\frac{d\rho^l}{dt} = -\nabla \cdot \mathbf{q}. \quad (2.16)$$

2.3.3 Effective stress on solid

Building on the work of [2, 20, 21, 38], the total stress acting on the solid is the combination of the Cauchy stress $\boldsymbol{\sigma}^s$ due to deformation and the pressure stress $\boldsymbol{\sigma}^l$ arising from the fluid phase, expressed as:

$$\boldsymbol{\sigma} = \boldsymbol{\sigma}^s + \boldsymbol{\sigma}^l = \boldsymbol{\sigma}^s - p^l \mathbf{I}. \quad (2.17)$$

Here, p^l represents the fluid pressure. For hyper-elastic materials, the constitutive equation for the solid component is given by:

$$\boldsymbol{\sigma}^s = 2\mu \mathbf{e} + \lambda \text{tr}(\mathbf{e}) \mathbf{I}, \quad (2.18)$$

where the Eulerian-Almansi finite strain tensor \mathbf{e} can be computed as:

$$\mathbf{e} = \frac{1}{2}(\mathbf{I} - \mathbf{F}^T \mathbf{F}). \quad (2.19)$$

The Lamé parameter λ can be derived from the shear modulus μ and the bulk modulus K as follows:

$$\lambda = K - \frac{2\mu}{3}. \quad (2.20)$$

The fluid pressure is determined solely by the level of fluid saturation within the porous solid, represented as a function $p^l = p^l(\tilde{c})$, which can be expressed as:

$$p^l = C(\tilde{c} - \tilde{c}_0), \quad (2.21)$$

where C is a material constant and \tilde{c}_0 is the initial saturation. Further details can be found in [2].

Methodology

3.1 Theory and basics of SPH

As a Lagrangian, SPH tracks the motion of individual particles, meaning it represents computation domain as a collection of particles that carry properties such as mass, velocity, density, and internal energy. Each particle interacts with its neighbors to perform simulations. The fundamental concept of SPH involves the use of a smoothing kernel, which is a continuous function that defines the influence of neighboring particles. The kernel function W , which typically has the following properties: compact Support, normalization and symmetry, integrates the contributions of neighboring particles to compute physical properties. A continuum property function $f(\mathbf{r})$ at particle i can be approximated by averaging over the neighboring particles using the kernel function, presented as

$$f(\mathbf{r}) = \sum_j V_j f_j W(\mathbf{r}_{ij}, h) = \sum_j \frac{m_j}{\rho_j} f_j W(\mathbf{r}_{ij}, h), \quad (3.1)$$

where V_j is the particle volume of particle j , $\mathbf{r}_{ij} = \mathbf{r}_i - \mathbf{r}_j$ the distance between particles i, j , and m_j and ρ_j are the particle mass and density respectively. Correspondingly, the particle approximation for the derivative of the function $f(\mathbf{r})$ at particle i is expressed as

$$\begin{aligned} \nabla f(\mathbf{r}) &\approx \int_{\Omega} \nabla f(\mathbf{r}) W(\mathbf{r}_i - \mathbf{r}, h) dV \\ &= - \int_{\Omega} f(\mathbf{r}) \nabla W(\mathbf{r}_i - \mathbf{r}, h) dV \approx - \sum_j V_j f_j \nabla_i W_{ij}. \end{aligned} \quad (3.2)$$

Here, $\nabla_i W_{ij} = \nabla_i W(\mathbf{r}_{ij}, h) = \mathbf{e}_{ij} \frac{\partial W_{ij}}{\partial r_{ij}}$ represents the gradient of the SPH kernel function with respect to the direction of the distance vector $\mathbf{e}_{ij} = \frac{\mathbf{r}_{ij}}{r_{ij}}$. Referring to [84], the strong form of Eq. (3.2) is applied when defining the local structure of a field. In the strong form, the gradient ∇f is computed by taking the difference between the values of f at particles i and j , multiplied by the kernel gradient. Involving the explicit evaluation of the gradient of f based on the particle positions, it can be calculated as

$$\nabla f_i = f_i \nabla 1 + \nabla f_i \approx \sum_j V_j \nabla_i W_{ij} f_{ij}, \quad (3.3)$$

Furthermore, to provide a smoother approximation of the gradient, which can be beneficial in simulations with irregular particle distributions or large variations in particle properties, the weak form approximation of Eq. (3.2) is applied as

$$\nabla f_i = \nabla f_i - f_i \nabla 1 \approx -2 \sum_j V_j \tilde{f}_{ij} \nabla_i W_{ij}, \quad (3.4)$$

where $\tilde{f}_{ij} = \frac{f_i + f_j}{2}$. This form is based on the weighted averaging of the field gradient over the particle's neighbors using the kernel function. In practice, it is often derived from the principle of minimizing errors in the approximation of the field's derivatives.

3.2 SPH discretization for fluids and solids

By utilizing Eqs. (3.3) and (3.4), the governing equations for the fluid can be discretized following the approach described in [31]:

$$\begin{cases} \frac{d\rho_i}{dt} = 2\rho_i \sum_j \frac{m_j}{\rho_j} (\mathbf{v}_i - \tilde{\mathbf{v}}_{ij}) \nabla_i W_{ij} \\ \frac{d\mathbf{v}_i}{dt} = - \sum_j m_j \frac{p_i + p_j}{\rho_i \rho_j} \nabla_i W_{ij} + 2 \sum_j m_j \frac{\eta}{\rho_i \rho_j} \frac{\mathbf{v}_{ij}}{r_{ij}} \frac{\partial W_{ij}}{\partial r_{ij}} + \mathbf{F}_i^{S:p} + \mathbf{F}_i^{S:v} \end{cases}, \quad (3.5)$$

where $\tilde{\mathbf{v}}_{ij} = \frac{\mathbf{v}_i + \mathbf{v}_j}{2}$ is the average velocity.

To discretize solid mechanics, the undeformed initial configuration is treated as the reference state. Firstly, one has the gradient of the kernel function $\nabla_a^0 W_{ab}$ as

$$\nabla_a^0 W_{ab} = \frac{\partial W(|\mathbf{r}_{ab}^0|, h)}{\partial |\mathbf{r}_{ab}^0|} \mathbf{e}_{ab}^0. \quad (3.6)$$

To ensure first-order consistency, a correction matrix \mathbb{B}^0 is employed, as proposed in [66, 75]:

$$\mathbb{B}_a^0 = \left(\sum_b V_b (\mathbf{r}_b^0 - \mathbf{r}_a^0) \otimes \nabla_a^0 W_{ab} \right)^{-1}, \quad (3.7)$$

where indices a, b denotes solid particles. As previously stated, using the superscript $(\bullet)^0$, the correction matrix \mathbb{B}_a^0 is computed once in the initial reference configuration. The momentum conservation equation, as expressed in Eq. (2.2), can then be approximated in its strong form as follows:

$$\frac{d\mathbf{v}_a}{dt} = \frac{2}{m_a} \sum_b V_a^0 V_b^0 \tilde{\mathbb{P}}_{ab} \nabla_a^0 W_{ab} + \mathbf{F}_a^{F:p} + \mathbf{F}_a^{F:v}, \quad (3.8)$$

where $\tilde{\mathbb{P}}_{ab}$ is the averaged first Piola-Kirchhoff stress of the particle pair (a, b) defined as

$$\tilde{\mathbb{P}}_{ab} = \frac{1}{2} (\mathbb{P}_a \mathbb{B}_a^0 + \mathbb{P}_b \mathbb{B}_b^0). \quad (3.9)$$

The first Piola-Kirchhoff stress tensor is influenced by the deformation gradient tensor \mathbb{F} , which is derived from the displacement field as follows:

$$\mathbb{F}_a = \left(\sum_b V_b (\mathbf{u}_b - \mathbf{u}_a) \otimes \nabla_a^0 W_{ab} \right) \mathbb{B}_a^0 + \mathbb{I}. \quad (3.10)$$

3.3 Discretization of fluid-structure and thermal coupling

To handle the fluid-structure interaction, the flexible structure is treated as a moving boundary for the fluid, with a no-slip boundary condition applied. In this scenario, the forces

exchanged between the fluid and the solid are resolved using a strong two-way coupling approach. At the fluid-structure interface, the displacement, velocity, and forces are assumed to be consistent. To ensure this, the density-weighted inter-particle averaged pressure is used

$$p_{ia} = \frac{p_i \rho_a^d + p_a^d \rho_i}{\rho_i + \rho_a^d} \quad (3.11)$$

when computing the pressure force between a fluid-solid particle pair (i, a) . Following the method of Zhang et al. [83], the pressure and viscous forces exerted on a fluid particle i are computed as:

$$\mathbf{F}_i^{S:p} = -2 \sum_a V_i V_a p_{ia} \nabla_i W(\mathbf{r}_{ia}) \quad (3.12)$$

and

$$\mathbf{F}_i^{S:v} = 2 \sum_a \eta V_i V_a \frac{\mathbf{v}_i - \mathbf{v}_a^d}{r_{ia}} \frac{\partial W(\mathbf{r}_{ia})}{\partial r_{ia}}, \quad (3.13)$$

respectively. The imaginary pressure p_a^d and velocity \mathbf{v}_a^d are determined using the structure's surface normal vector \mathbf{n}_a as follows:

$$\begin{cases} p_a^d = p_i + \rho_i \max(0, (\mathbf{g} - \frac{d\mathbf{v}_a}{dt}) \cdot \mathbf{n}_a)(\mathbf{r}_{ia} \cdot \mathbf{n}_a) \\ \mathbf{v}_a^d = 2\mathbf{v}_i - \mathbf{v}_a \end{cases} \quad (3.14)$$

Momentum conservation between fluid particles i and solid particle a is achieved along the centerline of the interacting particle pair (i, a) , due to the anti-symmetric nature $\nabla_i W(\mathbf{r}_{ia}) = -\nabla_a W(\mathbf{r}_{ai})$ and the symmetric formulation of the inter-particle averaged pressure. The pressure and viscous forces in Eq. (3.8) are obtained by applying the relationships $\mathbf{F}_a^{F:p} = -\mathbf{F}_i^{S:p}$ and $\mathbf{F}_a^{F:v} = -\mathbf{F}_i^{S:v}$.

The heat diffusion in the SPH discretized form of Eq. (2.9) is expressed as:

$$\frac{dT_i}{dt} = \frac{1}{\rho c_p} \left(\sum_j \frac{m_j}{\rho_j} \frac{4k_i k_j}{k_i + k_j} \frac{T_{ij}}{r_{ij}} \frac{\partial W_{ij}}{\partial r_{ij}} + \sum_a \frac{m_a}{\rho_a} \frac{4k_i k_a}{k_i + k_a} \frac{T_{ia}}{r_{ia}} \frac{\partial W_{ia}}{\partial r_{ia}} \right), \quad (3.15)$$

where T_i only refers to fluid particles. The subscript j and a refer to contributions from neighboring fluid and solid particles within the support domain of particle i . The temperature differences are defined as $T_{ij} = T_i - T_j$ and $T_{ia} = T_i - T_a$.

3.4 SPH discretization for fluid-structure interaction

In the discretization process of the fluid-structure interaction model, each particle is associated with its position $\mathbf{x}_n = \phi(\mathbf{X}, t_n)$ at time t_n , along with an initial representative volume V^0 that divides the initial domain of the macroscopic solid. The deformation gradient \mathbf{F}_n for the solid phase is recorded to facilitate the update of the solid's current volume V_n and its density ρ_n^s . Furthermore, the fluid properties such as mass m_n^l , saturation level \tilde{a}_n , and density-weighted fluid velocity relative to the solid \mathbf{q}_n are also tracked. The fluid mass equation of particle i , expressed in Eq. (2.16), is discretized as

$$\frac{dm_i^l}{dt} = 2V_i \sum_j \frac{m_j}{\rho_j} (\mathbf{q}_i - \mathbf{q}_j) \tilde{\nabla}_i W_{ij}. \quad (3.16)$$

With the updated fluid mass, ρ^l is obtained subsequently through (2.11). Accordingly, based on Eq. (2.11) and Eq. (2.15), the fluid saturation \tilde{a} and the fluid flux \mathbf{q} is updated in the particle form as

$$\mathbf{q}_i = -K\rho^l V_i \sum_j \frac{m_j}{\rho_j} (\tilde{c}_i - \tilde{c}_j) \tilde{\nabla}_i W_{ij}. \quad (3.17)$$

With the fluid flux and stress calculated, we can derive discrete formulations for the momentum balance equation, as represented in Eq. (2.14), which can be expressed as follows:

$$\frac{d\mathbf{M}_i}{dt} = 2 \sum_j V_j (\boldsymbol{\sigma}_i + \boldsymbol{\sigma}_j) \tilde{\nabla}_i W_{ij} - 2 \sum_j V_j (\mathbf{v}_i^l \otimes \mathbf{q}_i + \mathbf{v}_j^l \otimes \mathbf{q}_j) \tilde{\nabla}_i W_{ij}, \quad (3.18)$$

where $\boldsymbol{\sigma}_i$ and $\boldsymbol{\sigma}_j$ are the stress tensors of particles i and j . We then determine the updated solid velocity \mathbf{v}^s by employing the definition of total momentum provided in Eq. (2.12). In this formulation, the total density of the mixture is given by the sum of the solid and fluid densities $\rho = \rho^s + \rho^l$, expressed as

$$\mathbf{v}^s = \frac{\mathbf{M} - \mathbf{q}}{\rho} = \frac{\mathbf{M} - \mathbf{q}}{\rho^s + \rho^l}. \quad (3.19)$$

Subsequently, the fluid velocity \mathbf{v}^l is obtained by applying Eq. (2.13) as

$$\mathbf{v}^l = \mathbf{v}^s - \frac{\mathbf{q}}{\rho^l}. \quad (3.20)$$

3.5 ASPH theory

As an extension of the standard SPH, adaptive Smoothed Particle Hydrodynamics (ASPH) introduced spatial adaptivity in the smoothing length, h , used to define the size of a particle's interaction region. In the standard SPH method, the smoothing length remains constant for each particle, which can lead to inaccuracies when dealing with problems that involve large variations in density, pressure, or velocity fields. ASPH addresses these limitations by adjusting the smoothing length and kernel functions to simulate the problems with anisotropic particle volume changes.

3.5.1 ASPH principles

In reference to [60], the position vector \mathbf{r} used in standard isotropic SPH is extended to a normalized form $\boldsymbol{\eta}$ in ASPH by applying a linear transformation tensor \mathbf{G} . This transformation is defined as $\boldsymbol{\eta} = \mathbf{G}\mathbf{r}$, which alters the kernel function representation to $W(\boldsymbol{\eta}) = W(\mathbf{G}\mathbf{r})$. Under this framework, the ASPH kernel value is computed as $W'(\mathbf{G}\mathbf{r})$ while the kernel maintains the normalization condition:

$$1 = \int W(\boldsymbol{\eta}) d\boldsymbol{\eta} = \int W'(\mathbf{G}\mathbf{r}) d\mathbf{r} = \int \|\mathbf{G}\| W(\boldsymbol{\eta}) d\mathbf{r}. \quad (3.21)$$

A discrete approximation of the continuous field f based on the contributions from neighboring particles can be written as

$$f_i = \sum_j \|\mathbf{G}\| V_j f_j W(\boldsymbol{\eta}_i - \boldsymbol{\eta}_j) = \sum_j \|\mathbf{G}\| \frac{m_j}{\rho_j} f_j W(\boldsymbol{\eta}_i - \boldsymbol{\eta}_j), \quad (3.22)$$

where $\boldsymbol{\eta}_{ij} = \boldsymbol{\eta}_i - \boldsymbol{\eta}_j$ is the normalized particle distance vector pointing from particle j to i . Furthermore, the gradient of the kernel function $\nabla W(\boldsymbol{\eta})$ can be represented as

$$\nabla W(\boldsymbol{\eta}) = \nabla W'(\mathbf{Gr}) = \frac{\partial W(\mathbf{Gr})}{\partial \mathbf{r}} = \frac{\partial \boldsymbol{\eta}}{\partial \mathbf{r}} \frac{\partial W}{\partial \boldsymbol{\eta}} = \mathbf{G} \frac{\boldsymbol{\eta}}{\eta} \frac{\partial W}{\partial \eta}. \quad (3.23)$$

This formulation takes into account the anisotropic scaling applied to the kernel, where the transformation matrix \mathbf{G} relates the particle positions to the normalized vector within the ASPH framework. Consequently, a weak form of the derivative of a variable field f at particle i can be written as

$$\nabla f_i = \nabla f_i - f_i \nabla 1 \approx -2 \sum_j \|\mathbf{G}\| V_j \tilde{f}_{ij} \nabla_i W_{ij}, \quad (3.24)$$

where $\tilde{f}_{ij} = (f_i + f_j)/2$ is the inter-particle average value.

Defined as a linear transformation that converts from real spatial coordinates \mathbf{r} to normalized coordinates $\boldsymbol{\eta}$, the matrix \mathbf{G} is influenced by both geometric scaling and rotational transformations. This includes smoothing lengths h in different directions and the rotation angle θ between the axes and the actual reference frame. Further details can be found in the work of Owen et al. [60]. In the case of two dimensions, \mathbf{G} is given by

$$\mathbf{G} = \begin{bmatrix} h_1^{-1} \cos^2 \theta + h_2^{-1} \sin^2 \theta & (h_1^{-1} - h_2^{-1}) \cos \theta \sin \theta \\ (h_1^{-1} - h_2^{-1}) \cos \theta \sin \theta & h_1^{-1} \sin^2 \theta + h_2^{-1} \cos^2 \theta \end{bmatrix}. \quad (3.25)$$

where h_1 represents the smoothing length along the semimajor axis and h_2 along the semiminor axis of an ellipse, and θ is the angle of rotation of the semimajor axis relative to the real reference frame. Detailed information can be found in the reference paper [60].

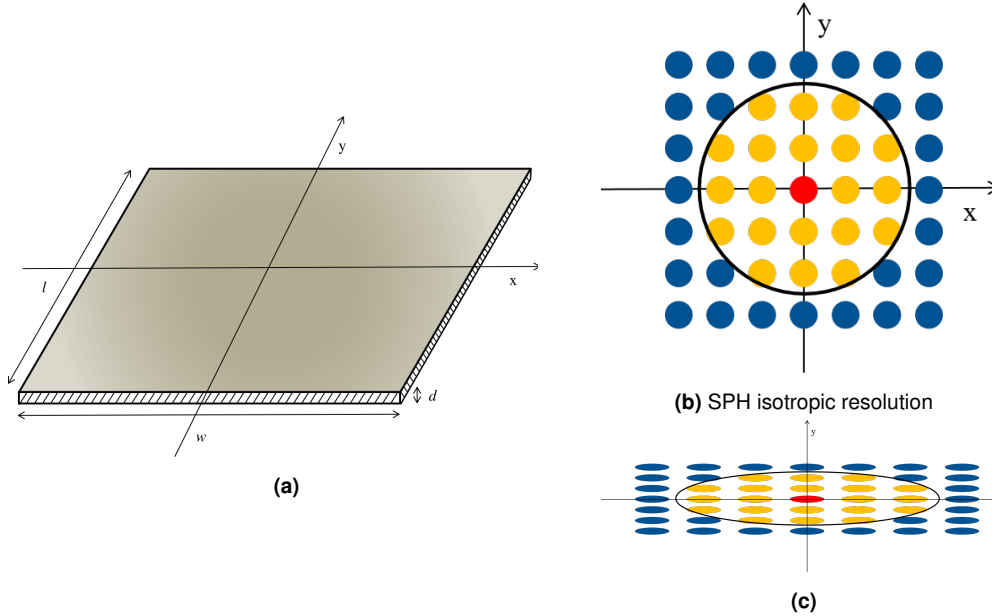


Figure 3.1: (a) Schematic view of a thin structure, (b) SPH isotropic resolution, (c) elliptical smoothing kernel.

For a thin structure with a large aspect ratio between its length and thickness, $R = l/d$, as shown in Figure 3.1a, normally an isotropic SPH discretization with a scalar smoothing length h is applied, as illustrated in Figure 3.1b, the yellow particles represent the support particles of the red particle. In order to ensure numerical accuracy and computational stability, a minimum number of neighboring particles is required in each direction. As the aspect ratio

R increases, this leads to a higher number of particles, which in turn raises computational costs. However, when using the ASPH method with anisotropic resolution, the traditional spherical support domain is replaced with an elliptical one in two-dimensional simulations. This adjustment allows for different smoothing lengths to be applied along each axis, as shown in Figure 3.1c, which reduces the number of particles and significantly decreases computational demands.

3.5.2 Kernel functions in ASPH

In this thesis, the Wenland kernel function is utilized, along with its first derivative. These kernel formations can be reformulated to align with the anisotropic ellipsoidal smoothing kernel as follows:

$$W^{v-D}(\eta) = A^{v-D} \begin{cases} (1 - \frac{\eta}{2})^4(1 + 2\eta), & 0 \leq \eta \leq 2 \\ 0, & \eta > 2 \end{cases} \quad (3.26)$$

$$\nabla W^{v-D}(\eta) = A^{v-D} \mathbf{G} \frac{\boldsymbol{\eta}}{\eta} \begin{cases} -5\eta(1 - \frac{\eta}{2})^3, & 0 \leq \eta \leq 2 \\ 0, & \eta > 2 \end{cases} \quad (3.27)$$

$$\frac{\partial W^{v-D}(\eta)}{\partial \eta} = A^{v-D} \|\mathbf{G} \frac{\boldsymbol{\eta}}{\eta}\| \begin{cases} -5\eta(1 - \frac{\eta}{2})^3, & 0 \leq \eta \leq 2 \\ 0, & \eta > 2 \end{cases} \quad (3.28)$$

where v means the dimension and

$$A^{1-D} = \frac{3}{4} \|\mathbf{G}\|, \quad A^{2-D} = \frac{7}{4\pi} \|\mathbf{G}\|, \quad A^{3-D} = \frac{21}{16\pi} \|\mathbf{G}\|. \quad (3.29)$$

Benefiting from the tensor \mathbf{G} , the displacement between two particles is mapped to the generalized position vector $\boldsymbol{\eta}$, the norm of which is compared with the cutoff radius to calculate the kernel function and kernel gradient value. Using normalized position vector $\boldsymbol{\eta}$ rather than \mathbf{r}/h in the discretization of quantities, the expression of dynamic equations in SPH and ASPH are identical.

3.5.3 Correction of the derivatives

For simulating solid mechanics, the first-order consistency is needed to be satisfied. Therefore, a correction tensor \mathbf{B} is introduced to the initial undeformed configuration within the total Lagrangian framework, as described in [66, 75]. This is expressed as:

$$\mathbf{F}_i^0 = \left(\sum_j V_j (\mathbf{r}_j^0 - \mathbf{r}_i^0) \otimes \nabla_i^0 W_{ij} \right) \mathbf{B}_i^0 = \mathbf{I}, \quad (3.30)$$

Equivalently, we have:

$$\mathbf{I} = \sum_j V_j (\mathbf{r}_j^0 - \mathbf{r}_i^0) \otimes (\nabla_i^{0T} W_{ij} \mathbf{B}_i^0) = \sum_j V_j (\mathbf{r}_j^0 - \mathbf{r}_i^0) \otimes (\mathbf{B}_i^{0T} \nabla_i^0 W_{ij})^T. \quad (3.31)$$

Since the correction with respect to the initial material coordinates is realized by applying \mathbf{B} to the gradient symbol as

$$\tilde{\nabla}^0 = \mathbf{B}_i^{0T} \nabla^0, \quad (3.32)$$

Using Eq. (3.30) and the tensor \mathbf{G} , the correction matrix \mathbf{B}^0 for particle i in ASPH is computed as:

$$\mathbf{B}_i^0 = \left(\sum_j V_j (\mathbf{r}_j^0 - \mathbf{r}_i^0) \otimes \nabla_i^0 W_{ij} \right)^{-1} = \left(\sum_j V_j (\mathbf{r}_j^0 - \mathbf{r}_i^0) \otimes (\mathbf{G}_i \frac{\eta_{ij}}{\eta_{ij}} \frac{\partial W}{\partial \eta_{ij}}) \right)^{-1}. \quad (3.33)$$

In the total Lagrangian formulation, the neighborhood of particle i is defined based on the initial configuration, and this set of neighbors remains fixed throughout the simulation. Clearly, \mathbf{B} is computed once under the initial reference configuration.

3.6 Multi-time step algorithm

In multi-time scale coupling involving solid dynamic problems, different time scales coexist. A multi-time step algorithm using an explicit scheme to accommodate various time scale processes is developed. Considering the fluid transportation coupling with porous solid deformation, the slow processes, fluid transport, are integrated with larger time step sizes, while the fast solid dynamics with smaller ones. With small time step size, the solid dynamics coupling with a damping scheme evolves to a quasi-equilibrium state. As the explicit integration operator is conditionally stable, a time step criterion Δt_s is required in solid simulation, given by

$$\Delta t_s = 0.6 \min \left(\frac{h}{c_s + |\mathbf{v}_s|_{\max}}, \sqrt{\frac{h}{|\frac{d\mathbf{v}_s}{dt}|_{\max}}} \right), \quad (3.34)$$

where the artificial sound speed of a solid structure is denoted as $c_s = \sqrt{K/\rho_s}$. The time step for internal fluid transport evolution is allowed to be much larger. According to the Fick's law, the maximum time step allowed for explicit time stepping of diffusion is characterized as [11]

$$\Delta t_d = 0.5 \frac{h^2}{D}, \quad (3.35)$$

stating that the time step is mainly limited by the parameter D and the kernel smoothing length h .

The multi-time step algorithm consists of two loops, an outer loop governing the overall dynamic progression through incremental execution of transportation relaxation denoted by g , and an inner loop describing the evolution of solid dynamics with k representing each stress relaxation step, as shown in fig. 3.2. Within one transport time step Δt_d , the time integration of structure should be computed as $k_0 = \lceil \frac{\Delta t_d}{\Delta t_s} \rceil + 1$ times. To optimize computation time, the inner loop is executed with a damping term to dissipate the kinetic energy and accelerate the relaxation of the solid transient response. Referring to Zhu's work [89], a viscous damping term \mathbf{f}^v is added to the solid momentum equation as

$$\frac{d\mathbf{v}}{dt} = \mathbf{f} + \mathbf{g} + \mathbf{f}^v, \quad (3.36)$$

where the added damping term \mathbf{f}^v can be discretized as

$$\mathbf{f}_a^v = \frac{\eta}{\rho_a} \nabla_a^2 \mathbf{v} = \frac{2\eta}{m_a} \sum_a V_a^0 V_b^0 (\mathbf{v}_a - \mathbf{v}_b) \nabla_a^0 W_{ab}, \quad (3.37)$$

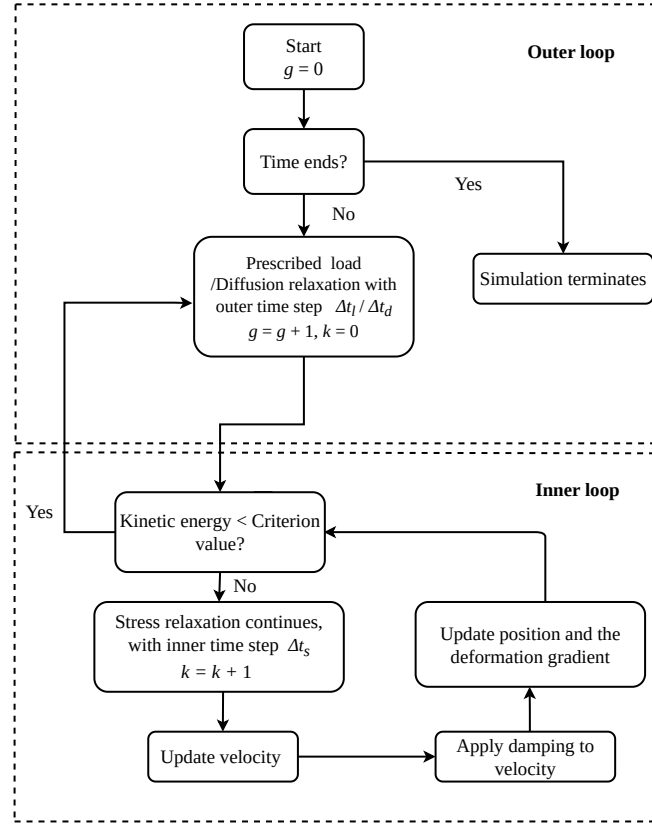


Figure 3.2: Flowchart of the iterative scheme in multi-time step algorithm.

where η is the dynamic viscosity, and for structures η is determined by the material properties and the physical shape of the solid body. Solid governing equations with additional damping are solved a small number of times k until the kinetic energy is reduced to a sufficiently small value E_k , marking the achievement of the equilibrium state of the system. After the equilibrium state of the solid deformation is achieved in the inner steps, a new outer step initiates and this iterative process is repeated until the conclusion of the designated physical computation time.

Chapter 4

Summaries of publications

In this chapter, the relevant publications of this thesis are briefly summarized

4.1 An integrative SPH method for heat transfer problems involving fluid-structure interaction

Xiaojing Tang, Chi Zhang , Oskar Haidn, and Xiangyu Hu

4.1.1 Summary of the publication

Thermal-fluid-structure interaction (TFSI) problems usually pose numerical complications in grid-based methods, which require remeshing scheme as the material interface changes. In this paper, an integrated smoothed particle hydrodynamics (SPH) solver with strong coupling scheme at the material interface is introduced to investigate the TFSI problem. Some algorithms including the Riemann-based solver for fluid equations, correction of the derivatives for structure deformation and multi-time stepping algorithm, position-based Verlet scheme, and the second-order Runge-Kutta integrator scheme for thermal simulation are adopted to guarantee numerical accuracy and stability.

In the present work, heat transfer process occurs between the solid wall and fluid. The SPH discretized form of the heat diffusion of Eq. (2.9) can be represented as

$$\frac{dT_i}{dt} = \frac{1}{\rho c_p} \left(\sum_j \frac{m_j}{\rho_j} \frac{4k_i k_j}{k_i + k_j} \frac{T_{ij}}{r_{ij}} \frac{\partial W_{ij}}{\partial r_{ij}} + \sum_a \frac{m_a}{\rho_a} \frac{4k_i k_a}{k_i + k_a} \frac{T_{ia}}{r_{ia}} \frac{\partial W_{ia}}{\partial r_{ia}} \right), \quad (4.1)$$

where T_i only refers to fluid particles. The subscript j and a respectively indicates contribution from neighboring fluid and solid particles within the compact support of particle i . Also $T_{ij} = T_i - T_j$ and $T_{ia} = T_i - T_a$ are the temperature difference.

In the simulation, we coupled heat transfer and FSI solvers together to simulate a heat transfer channel with different vortex generators and observe how heat transfer, fluid vortex, and solid deformation occur simultaneously. The stable temperature contours in four different cases are shown in fig. 4.1. The results show that the present SPH TFSI solver has a unique advantage in capturing the thermal fluid dynamics in TFSI problems, and can clearly explain the inner relation between vortex regime and cooling performance. The aim of this work is not only to extend the usage of the SPH method to TFSI applications, but also to provide a more flexible multi-physics solver which exhibits the possibility to address a wide range of industrial heat transfer problems.

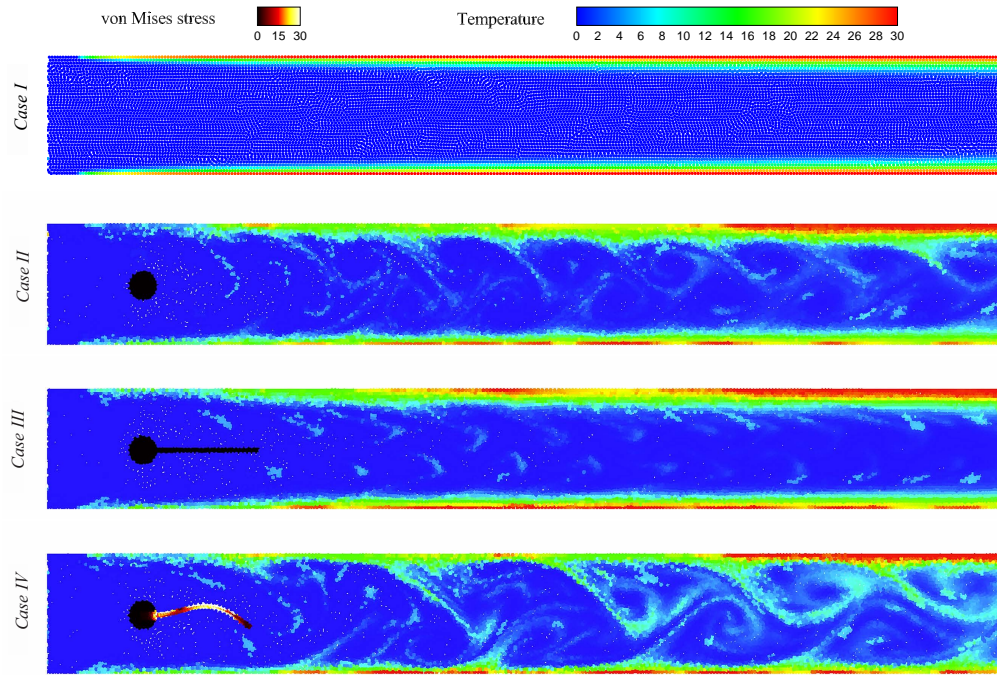


Figure 4.1: Stable temperature contours in four different cases.

4.1.2 Individual contributions of the candidate

This article was published in the international peer-reviewed journal *Acta Mechanica Sinica*. I contributed to this work by developing the method and writing the corresponding computer code for its implementation. I performed the simulations, analyzed the results, and authored the manuscript for publication.

4.2 Simulating plate and shell structures with anisotropic resolution using adaptive smoothed particle hydrodynamics

Xiaojing Tang, Dong Wu, Zhentong Wang, Oskar Haidn, Xiangyu Hu

4.2.1 Summary of the publication

To capture variations in the thickness direction of thin plate and shell structures, which the reduced-dimensional models fail to do, while simultaneously mitigating computational costs, an anisotropic full-dimensional model, integrated with an adaptive smoothed particle hydrodynamics method (ASPH), is developed.

The smoothing kernel is defined coupled with a linear transformation tensor, and thus the support domain of one particle turns out to be an ellipsoid area, rather than a spherical domain. Following Ref. [60], the position vector \mathbf{r} in the traditional isotropic SPH, is generalized to a normalized form $\boldsymbol{\eta}$ in ASPH through a linear coordinate transformation tensor \mathbf{G} . This transformation is expressed as $\boldsymbol{\eta} = \mathbf{G}\mathbf{r}$, resulting in the representation of the kernel function $W(\boldsymbol{\eta}) = W(\mathbf{G}\mathbf{r})$. The normalization undergoes a change: SPH: $\boldsymbol{\eta} = \mathbf{r}/h \rightarrow$ ASPH: $\boldsymbol{\eta} = \mathbf{G}\mathbf{r}$. With the gradient of the kernel function $\nabla W(\boldsymbol{\eta})$ being expressed as

$$\nabla W(\boldsymbol{\eta}) = \nabla W'(\mathbf{G}\mathbf{r}) = \frac{\partial W(\mathbf{G}\mathbf{r})}{\partial \mathbf{r}} = \frac{\partial \boldsymbol{\eta}}{\partial \mathbf{r}} \frac{\partial W}{\partial \boldsymbol{\eta}} = \mathbf{G} \frac{\boldsymbol{\eta}}{\eta} \frac{\partial W}{\partial \boldsymbol{\eta}}, \quad (4.2)$$

Furthermore, the correction matrix applied to the kernel gradient for first-order consistency is modified accordingly by integrating the nonisotropic kernel within the total Lagrangian framework in ASPH.

Numerical examples, including both two and three-dimensional cases are presented to comprehensively examine the ASPH method. Considering a thin flat plate with different anisotropic ratios, the simulated deformation evolution is illustrated in fig. 4.2. The nondimensionalized deflection variation of the central point of the plate against time for all simulation condition is depicted in fig. 4.3. It is observed that the position of the center point remains consistent across all anisotropic ratios, converging to the SPH solution, but saving a great amount of time demonstrating both accuracy and high efficiency.

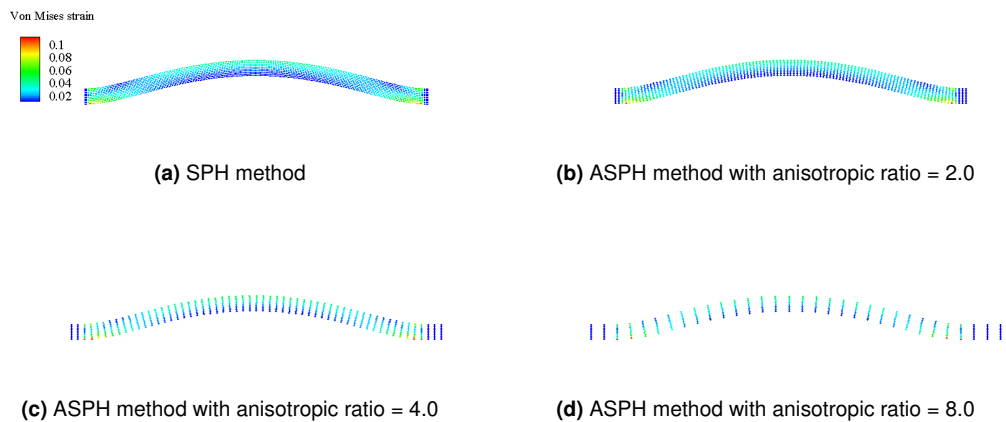


Figure 4.2: 2D thin plate: the deformation at the final time instant colored by von Mises strain from SPH and ASPH with different anisotropic ratios.

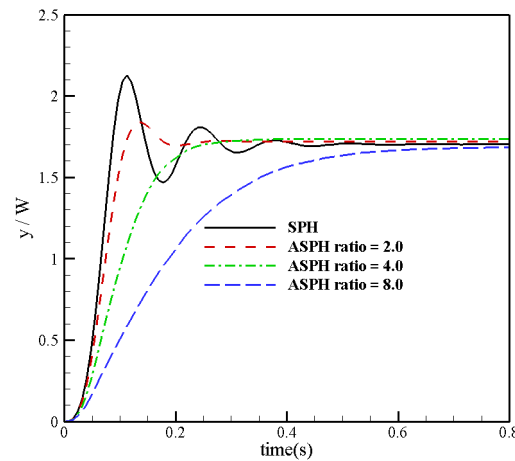


Figure 4.3: 2D thin plate: the nondimensionalized y position of the very center point of the beam, from SPH and ASPH with different anisotropic ratios.

4.2.2 Individual contributions of the candidate

This article was published in the international peer-reviewed journal *Engineering Analysis with Boundary Elements*. My contribution to this work involved conceptualization, developing the methodology writing the corresponding computer code for its implementation, and performing the investigation. I handled data curation, conducted simulations, analyzed the results, and was responsible for the original manuscript for publication.

4.3 An explicit multi-time stepping algorithm for multi-time scale coupling problems in SPH

Xiaojing Tang , Dong Wu, Zhentong Wang, Oskar Haidn, Xiangyu Hu

4.3.1 Summary of the publication

Simulating physical problems with multi-time scale coupling presents a considerable challenge due to the concurrent solution of processes with different time scales. To address this inherent conflict in the multi-time scale coupling problems, we propose an explicit multi-time step algorithm within the framework of smoothed particle hydrodynamics (SPH), coupled with a solid dynamic relaxation scheme, to quickly achieve equilibrium state in the comparatively fast solid response process. Two loops, specifically an outer and an inner loop, are organized to accommodate these respective time steps for effective time integration. Specifically, the slow process is integrated with a large time step in the outer loop, while the fast solid dynamic process coupling with a dynamic relaxation with a considerably smaller time step in the inner loop.

Without compromising the momentum conservation of the system, a viscous damping term \mathbf{f}^v is added to the solid momentum equation as

$$\frac{d\mathbf{v}}{dt} = \mathbf{f} + \mathbf{g} + \mathbf{f}^v, \quad (4.3)$$

where \mathbf{f} and \mathbf{g} represents the acceleration due to the surface and body forces.

This algorithm is applied to simulate the evolution of fluid diffusion in porous media coupled with elastic deformation. The deformation colored by water saturation at different time instants is shown in fig. 4.4. The obtained results, as plotted in fig. 4.5, demonstrate that the proposed algorithm outperforms previous numerical methods and experiments in terms of both accuracy and efficiency.

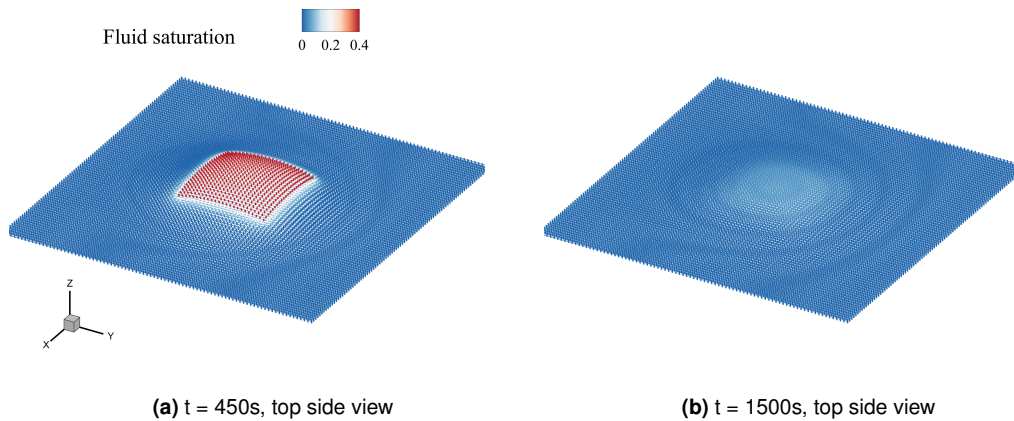


Figure 4.4: 3D fluid-structure interaction: the deformation colored by water saturation at different time instants.

4.3.2 Individual contributions of the candidate

This article was accepted in the international peer-reviewed journal *Communications in Computational Physics*. My contribution to this work included conceptualization, developing the

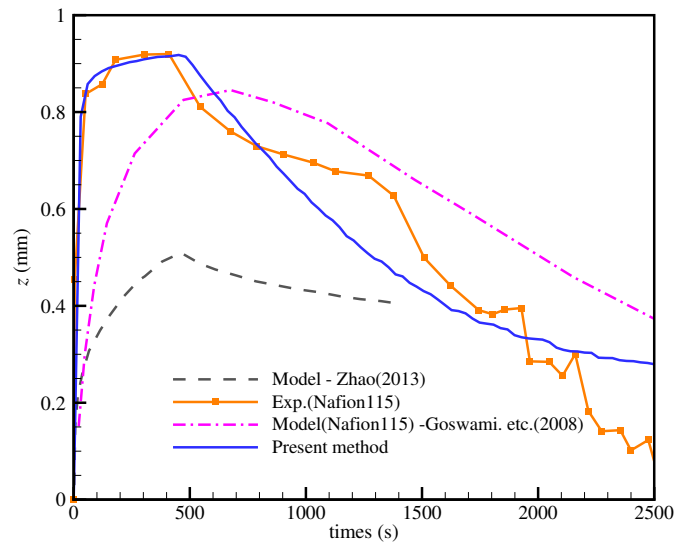


Figure 4.5: 3D fluid-structure interaction: bending amplitude of the center point compared with experimental data and results from other numerical models.

methodology development, coding for implementation, and conducting the investigation. I also managed data curation, performed simulations, analyzed the results, and prepared the original manuscript for publication.

Conclusions

This thesis explores the broader application potential of Smoothed Particle Hydrodynamics (SPH) in addressing multi-physics problems, solid mechanics, and multi-time scale coupling processes. By refining the SPH method, developing robust frameworks and innovative algorithms, this work demonstrates the versatility and effectiveness of SPH in simulating coupled thermal-fluid-structure interaction (TFSI), multi-scale processes, and the behavior of anisotropic materials like plates and shells.

The first part of the thesis introduced a new SPH-based methodology to simulate TFSI problems effectively, incorporating strong coupling at material interfaces and advanced techniques like kernel modification and multi time stepping. The solver is initially validated using two benchmark tests: one for heat transfer in a micro-channel and another for a fluid-structure interaction (FSI) case. Once validated, the study investigates the enhancement of heat transfer caused by vortices generated by various immersed structures. Leveraging the distinct capability of capturing the moving interface in thermal-fluid-structure interactions (TFSI), the solver effectively demonstrates the connection between vortex behavior and thermal dynamics. The findings indicate that heat transfer enhancement is significantly influenced by the interaction between vortices and the thermal boundary layer. This method's success in analyzing heat transfer and vortex interactions underscores its applicability to complex industrial scenarios.

To simulate plate and shell structures with variations in thickness, we utilized an Adaptive Smoothed Particle Hydrodynamics (ASPH) method that incorporates an anisotropic ellipsoidal smoothing kernel along with an anisotropic resolution scheme. This approach has allowed us to effectively model thin structures with large aspect ratios, especially those that necessitate adequate resolution in the thickness direction to capture variations that reduced-dimensional models cannot address. By leveraging fewer particles while achieving first-order consistency, the proposed ASPH method demonstrates both efficiency and comparable accuracy to conventional full-dimensional SPH methods in various static and dynamic contexts.

Lastly, the thesis tackled the intricacies of multi-time scale coupling by proposing an explicit multi-time step algorithm within the SPH framework. This algorithm, combined with a dynamic relaxation scheme, enabled efficient simulations of processes that evolve at different time scales, significantly reducing computational time without compromising accuracy. This approach enables the early termination of the solid stress relaxation inner loop, preventing unnecessary calculations. The performance of the algorithm is evaluated through three types of multi-time coupling problems: a manufactured torsional case, nonlinear hardening bar stretching, and fluid diffusion within porous media interacting with solid deformation. The results indicate both high accuracy and a considerable decrease in computational time.

The findings indicate that this integrative SPH approach effectively models intricate industrial scenarios where conventional mesh-based techniques become less applicable. Future work will focus on further exploration and enhancement of both SPH and ASPH methods for a wider range of applications.

Appendix A

Original journal papers

Here, the peer-reviewed journal publications of the present work are attached.

A.1 Paper I

Xiaojing Tang, Chi Zhang, Oskar Haidn, and Xiangyu Hu

An integrative SPH method for heat transfer problems involving fluid-structure interaction

In *Acta Mechanica Sinica*, Volume 39, Pages 722248, 2023

DOI:<https://doi.org/10.1007/s10409-022-22248-x>

Copyright ©2022, The Chinese Society of Theoretical and Applied Mechanics and Springer-Verlag GmbH Germany, part of Springer Nature. Reprinted with permission

An integrative SPH method for heat transfer problems involving fluid-structure interaction

Xiaojing Tang, Chi Zhang*, Oskar Haidn, and Xiangyu Hu

TUM School of Engineering and Design, Technical University of Munich, Garching 85748, Germany

Received August 19, 2022; accepted August 30, 2022; published online September 30, 2022

Thermal-fluid-structure interaction (TFSI) problems usually pose numerical complications in grid-based methods because of the coexistence of fluid dynamics, solid kinematics and heat transfer. In this paper, an integrated smoothed particle hydrodynamics (SPH) solver with strong coupling scheme at the material interface is introduced to investigate the TFSI problem. Some efficient techniques inclusive of kernel modification in the total Lagrangian formulation for solid dynamics and multi-time stepping for fluid structure interaction (FSI) are integrated to increase the computational accuracy and efficiency. Also the position-based Verlet scheme is applied to achieve the strict conservation of momentum. A two-stage Runge-Kutta integrator scheme is used to solve the heat diffusion equation. Two simulation cases are performed to test the present method including the numerical examples of heat transfer in a micro-channel and a FSI case. The heat transfer performance is investigated and quantified with different vortex generators in a heated channel flow. The detailed heat and vortex information obtained by the present SPH TFSI solver indicates that the FSI reinforces the heat transfer via vortexes interaction with fluid within the boundary layer. This study demonstrates the versatility and potential of the mesh-free SPH approach for industrial heat transfer applications involving vortex generators with large structure deformation.

Smoothed particle hydrodynamics, Heat transfer analysis, Thermal-fluid-structure interaction, Vortex generator

Citation: X. Tang, C. Zhang, O. Haidn, and X. Hu, An integrative SPH method for heat transfer problems involving fluid-structure interaction, *Acta Mech. Sin.* **39**, 722248 (2023), <https://doi.org/10.1007/s10409-022-22248-x>

1. Introduction

Heat transfer phenomena widely exist in various fields including aerospace, automobile industry, and electronic engineering [1–3]. As low heat transfer rates may decrease the working efficiency and reduce the lifetime of heat exchanger devices, tremendous attempts have been performed to increase the heat transfer efficiency, for example introducing passive or active vortex generators [4–6], which enhance mixing and heat transfer.

The study of heat transfer strengthening is usually difficult when coming to the thermal-fluid-structure interaction (TFSI) problem, where the fluid dynamics, solid deformation and heat transfer are involved together. Fluid induced

solid movements influence the flow and temperature fields. The intrinsic non-linearity and time-dependent nature involving large structure deformations and moving solid-fluid interface pose a great challenge to numerical simulation [7]. Up to date, two main methods have been employed to simulate the TFSI problem: (1) the mainstream grid-based methods, where the continuum domain is discretized into grids and over which the conservative equations are solved; (2) the newly developing mesh-free based methods, where particles with physical quantities are introduced to solve the corresponding equations within the Lagrangian framework, is seeing the growing interests [8].

For mesh-based methods, two approaches are introduced in literature. The first one is the so-called monolithic method such as the arbitrary Lagrangian Eulerian (ALE) method in which the fluid and solid equations are resolved simultane-

*Corresponding author. E-mail address: c.zhang@tum.de (Chi Zhang)
Executive Editor: Fei Xu

ously within a single solver. Although ALE has been widely used in the study of TFSI problems [9–11], a remeshing scheme is necessary as the material interface changes with time, increasing the algorithmic complexity and the computational cost [12]. The second one is the partitioned approach where usually a computational solid dynamics (CSD) solver is combined with a computational fluid dynamics (CFD) solver to solve flow and solid equations respectively and a FSI coupling solver is applied accordingly. One of this approach is the immersed boundary method (IBM) where the structure is surrounded by fluid and reduce the costs of remeshing in the simulation process [13]. However, in IBM, modification of the motion equations is required to satisfy the displacement consistency and force matching at the fluid-solid interface.

As an alternative, the meshless methods are very attractive in simulating TFSI problems owing to its natural convenience in handling the moving interface. As one of such methods, the smoothed particle hydrodynamics (SPH) is initially developed by Lucy [14] and Gingold et al. [15] for studying astrophysical problems. In more recent decades, the SPH method has been widely applied to simulate industrial applications such as single- and multi-phase flows [16–18], large strain analysis [19–21] and FSI [22–25]. Comprehensive reviews are available in Refs. [26–29]. Regarding the thermal and mass diffusion, SPH has been used successfully in modeling heat conduction [30, 31], convection [32, 33] and phase-change heat transfer problems [34]. Specifically, Yang et al. [32] modeled the natural convection to see how Prandtl and Rayleigh numbers influence the flow states via the SPH method. Vishwakarma et al. [35] applied SPH to predict the heat conduction in irregular geometries where problems may occur if using grid-based methods. They conclude that the temperature profiles prove the method have a good agreement with those obtained through commercial software, i.e., Fluent. Farrokhpanah et al. [34] introduced and evaluated a new SPH scheme to simulate model transient heat conduction, taking latent heat into account during solidification. These studies show that the SPH method is able to model and analyze temperature fields accurately within fluid or solid. Also, Hosain et al. [8] studied different heat transfer examples, involving heat conduction in water, heat transfer in laminar flowing fluid between plates and heat exchanger tubes. Compared with the results obtained from finite volume method (FVM), the SPH solutions are within the data range and the SPH is also validated by analytical solutions. However, they did not consider the FSI coupling effects. Long et al. [7] coupled the SPH method with the edge based smoothed finite element method (ES-FEM) to tackle TFSI problems where the ES-FEM is adopted to simulate solid and SPH to fluid. To handle FSI coupling, a ghost particle algorithm is adopted

and fluid-structure conjugate heat transfer is resolved accordingly. Although the SPH method shows great potential in the heat transfer studies, its application in TFSI is relatively limited in the literature to the best knowledge of the authors. Moreover, most of this literature are dependent on coupling SPH with other methods to simulate the fluid-structure and heat transfer, which increases the numerical complexity and computational efforts.

In this article, a strongly coupled SPH solver is presented to investigate the heat transfer enhancement with vortex generators. The solver of thermal diffusion equation is implemented in the open-source code SPHinXsys <https://www.sphinxsys.org> [36]. Some algorithms including the Riemann-based solver for fluid equations, correction of the derivatives in the total Lagrangian formulation for structure deformation and multi-time stepping algorithm, position-based Verlet scheme, and the second-order Runge-Kutta integrator scheme for thermal simulation are also adopted to guarantee numerical accuracy and stability. In the simulation, first, we simulated a micro-channel heat transfer and a FSI case to validate the present SPH thermal and FSI solver. Then, we coupled these two solvers together to simulate a heat transfer channel with different vortex generators and observe how heat transfer, fluid vortex, and solid deformation occur simultaneously. These numerical examples show that the present SPH TFSI solver has a unique advantage in capturing the thermal fluid dynamics in TFSI problems, and can clearly explain the inner relation between vortex regime and cooling performance. The aim of this work is not only to extend the usage of the SPH method to TFSI applications, but also to provide a more flexible multi-physics solver which exhibits the possibility to address a wide range of industrial heat transfer problems. The analysis and results also evaluate the capabilities of SPH in simulating heat transfer with complex geometries in a detailed way, providing a basis for the heat transfer optimization in many engineering applications process.

2. Governing equations

In the TFSI problem, the thermal fluid is considered as incompressible and viscous, and the governing equations are the mass conservation and momentum balance equation expressed as

$$\begin{cases} \frac{d\rho}{dt} = -\rho \nabla \cdot \mathbf{v}, \\ \frac{d\mathbf{v}}{dt} = \frac{1}{\rho} (-\nabla p + \eta \nabla^2 \mathbf{v}) + \mathbf{F}^{S:p} + \mathbf{F}^{S:v}, \end{cases} \quad (1)$$

where ρ , \mathbf{v} , p , η are the density, the velocity, the pressure, the dynamics viscosity and $\mathbf{F}^{S:p}$ and $\mathbf{F}^{S:v}$ the forces generated

from solid working on the flowing fluid due to the pressure and viscosity. Under the weakly-compressible assumption, we introduce a linear equation of state (EoS) to characterize the pressure via the variation of density to approximately simulate the incompressible flow as shown below [37]:

$$p = c^2(\rho - \rho^0), \quad (2)$$

where the artificial speed of sound c is defined dependent on the cases and ρ^0 is the initial density [37].

The deforming structure is considered to be elastic and the corresponding governing equations derived from the balance laws are mass and momentum conservation. Based on the continuum mechanics, the displacement \mathbf{u} of a material point is defined as $\mathbf{u} = \mathbf{r} - \mathbf{r}^0$. Here, \mathbf{r} and \mathbf{r}^0 denote the position of a material point in deformed and initial reference configuration, respectively. To characterize the structure kinematics, the deformation tensor \mathbf{F} is applied. According to the definition, \mathbf{F} is calculated with the unit matrix \mathbf{I} from

$$\mathbf{F} = \nabla^0 \mathbf{u} + \mathbf{I}. \quad (3)$$

We mark that all operators and quantities carrying superscript $(\cdot)^0$ are corresponding to the undeformed initial configuration. With the Lagrangian framework assumption, the governing equations of elastic structure read

$$\begin{cases} \rho = \rho^0 \frac{1}{J}, \\ \rho^0 \frac{d\mathbf{v}}{dt} = \nabla^0 \cdot \mathbf{P}^T + \mathbf{F}^{F:p} + \mathbf{F}^{F:v}. \end{cases} \quad (4)$$

In the above, Jacobian $J = \det(\mathbf{F})$. In contrast to the Cauchy stress which points the force measured in the deformed configuration, named as the first Piola-Kirchhoff stress tensor, \mathbf{P} relates stress within the initial configuration and T is the matrix transposition. Also, pressure force $\mathbf{F}^{F:p}$ and viscous force $\mathbf{F}^{F:v}$ correspond to those in fluid equation. To obtain \mathbf{P} , we introduce the Green-Lagrangian strain \mathbf{E} which characterizes the extent of deformation given by

$$\mathbf{E} = \frac{1}{2} (\mathbf{F}\mathbf{F}^T - \mathbf{I}). \quad (5)$$

In this work, the isotropic and linearly elastic material is used to describe the vortex generator and thus we can write the second Piola-Kirchhoff stress tensor \mathbf{S} which is symmetric, via the relation as

$$\mathbf{S} = \lambda \text{tr}(\mathbf{E}) \mathbf{I} + 2\mu \mathbf{E}, \quad (6)$$

with Lamé parameters λ and μ . Usually, the key material coefficients include the Young's modulus E , the Poisson ratio ν , the shear modulus G , and the bulk modulus K and each of them is dependent on the others as

$$E = 3K(1 - 2\nu), \quad (7)$$

$$G = \frac{E}{2(1 + \nu)}. \quad (8)$$

Finally, the first Piola-Kirchhoff stress tensor \mathbf{P} is calculated through

$$\mathbf{P} = \mathbf{F}\mathbf{S} = \mathbf{F}[\lambda \text{tr}(\mathbf{E}) \mathbf{I} + 2\mu \mathbf{E}]. \quad (9)$$

For the heat transfer process, the governing equation relates to the temperature rate following the Fourier law. For ease of simulating and to focus attention on the main points, no external heat source is considered. Thus the heat transfer equations can be expressed as

$$\frac{dT}{dt} = \nabla \cdot \left(\frac{k}{\rho c_p} \nabla T \right), \quad (10)$$

where T is the temperature, k the thermal conductivity coefficient and c_p the specific heat capacity.

3. Methodology

3.1 Theory and fundamental of SPH

In the SPH method, physical properties are approximated based on the integral representation over neighboring particles. The discrete form of a continuously defined function $f(\mathbf{r})$ at particle i is presented as

$$f(\mathbf{r}) = \sum_j V_j f_j W(\mathbf{r}_{ij}, h) = \sum_j \frac{m_j}{\rho_j} f_j W(\mathbf{r}_{ij}, h), \quad (11)$$

where i, j represent the particle indices and V_j is the particle volume. The smoothing function $W(\mathbf{r}_{ij}, h)$, with the smoothing length h deciding the support area, is radially symmetric concerning the particle position \mathbf{r}_i . The particle distance $\mathbf{r}_{ij} = \mathbf{r}_i - \mathbf{r}_j$. Also, m_j and ρ_j are the particle mass and density respectively. Correspondingly, the particle approximation for the derivative of the function $f(\mathbf{r})$ at particle i is expressed as

$$\begin{aligned} \nabla f(\mathbf{r}) &\approx \int_{\Omega} \nabla f(\mathbf{r}) W(\mathbf{r}_i - \mathbf{r}, h) dV \\ &= - \int_{\Omega} f(\mathbf{r}) \nabla W(\mathbf{r}_i - \mathbf{r}, h) dV \\ &\approx - \sum_j V_j f_j \nabla_i W_{ij}. \end{aligned} \quad (12)$$

Here, $\nabla_i W_{ij} = \nabla_i W(\mathbf{r}_{ij}, h) = \mathbf{e}_{ij} \frac{\partial W_{ij}}{\partial r_{ij}}$ stands for the gradient of the kernel function regarding the particle distance $\mathbf{r}_{ij} = \mathbf{r}_i - \mathbf{r}_j$ and unit vector $\mathbf{e}_{ij} = \frac{\mathbf{r}_{ij}}{r_{ij}}$. Following Ref. [36], when defining the local structure of a field, a strong form of Eq. (12) is usually applied as follows:

$$\nabla f_i = f_i \nabla 1 + \nabla f_i \approx \sum_j V_j \nabla_i W_{ij} f_{ij}, \quad (13)$$

where $f_{ij} = f_i - f_j$ is the difference within the particle pair (i, j) . Furthermore, to ensure the conservation of a variable at the surface, the weak form approximation of Eq. (12) is applied as

$$\nabla f_i = \nabla f_i - f_i \nabla 1 \approx -2 \sum_j V_j \tilde{f}_{ij} \nabla_i W_{ij}, \quad (14)$$

where $\tilde{f}_{ij} = \frac{f_i + f_j}{2}$ is the average value of particle pair (i, j) .

3.2 SPH discretization for fluid and solid

With Eqs. (13) and (14) in hand, the governing equation of the fluid can be discretized as [38]

$$\begin{cases} \frac{d\rho_i}{dt} = 2\rho_i \sum_j \frac{m_j}{\rho_j} (\mathbf{v}_i - \tilde{\mathbf{v}}_{ij}) \nabla_i W_{ij}, \\ \frac{d\mathbf{v}_i}{dt} = - \sum_j m_j \frac{p_i + p_j}{\rho_i \rho_j} \nabla_i W_{ij} + 2 \sum_j m_j \frac{\eta}{\rho_i \rho_j} \frac{\mathbf{v}_{ij}}{r_{ij}} \frac{\partial W_{ij}}{\partial r_{ij}} \\ \quad + \mathbf{F}_i^{S:p} + \mathbf{F}_i^{S:v}, \end{cases} \quad (15)$$

where $\tilde{\mathbf{v}}_{ij} = \frac{\mathbf{v}_i + \mathbf{v}_j}{2}$ is the average velocity. Direct implementation of Eq. (15) results in spurious pressure fluctuation as the pressure is calculated through the EoS of Eq. (2), leading to numerical instability. To remedy this issue, several algorithms, e.g., artificial viscosity [15], diffusive term in continuity equation [39] and Riemann-based scheme [40] have been proposed in literature. In this work, we apply the Riemann-based SPH [40], while only apply the Riemann-based diffusive term in the continuity equation other than both the mass and the momentum conservation. In this case, the artificial damping intrinsically introduced by the Riemann solver is decreased as viscous flows with a low Reynolds number is considered herein. It is worth noting that even Eq. (15) also works for hydrodynamic negative pressure field, but one needs a remedy to address the tensile instability issue. In this paper, the transport-velocity formulation is applied [41].

Subsequently, we use $\mathbf{v}^* = U^* \mathbf{e}_{ij} + (\tilde{\mathbf{v}}_{ij} - \tilde{U} \mathbf{e}_{ij})$ to replace $\tilde{\mathbf{v}}_{ij}$ in continuum equation

$$\frac{d\rho_i}{dt} = 2\rho_i \sum_j \frac{m_j}{\rho_j} (\mathbf{v}_i - \mathbf{v}^*) \nabla_i W_{ij}, \quad (16)$$

where U^* is the solution of inter-particle Riemann problem along the unit vector \mathbf{e}_{ij} . $\tilde{U} = \frac{U_L + U_R}{2}$ is inter-particle average where U_L and U_R are respectively left and right states. More details about the Riemann solution are available in Ref. [42].

To discretize the solid mechanics, we consider the initial undeformed configuration to be the reference state. First, aiming at restoring 1st order consistency, a correction matrix \mathbf{B}^0 [43,44] is adopted as

$$\mathbf{B}_a^0 = \left[\sum_b V_b (\mathbf{r}_b^0 - \mathbf{r}_a^0) \otimes \nabla_a^0 W_{ab} \right]^{-1}, \quad (17)$$

where indices a, b represent solid particles and $\nabla_a^0 W_{ab}$ is the gradient of the kernel function given by

$$\nabla_a^0 W_{ab} = \frac{\partial W(|\mathbf{r}_{ab}^0|, h)}{\partial |\mathbf{r}_{ab}^0|} \mathbf{e}_{ab}^0. \quad (18)$$

As mentioned before, with the superscript $(\cdot)^0$, \mathbf{B}_a^0 is computed only once under the initial reference configuration. Also the neighborhood of particle a is defined relating to the initial configuration and this set of neighboring particles remains fixed throughout the entire simulation. Then, the momentum conservation in Eq. (4) can be approximated in the strong form as

$$\frac{d\mathbf{v}_a}{dt} = \frac{2}{m_a} \sum_b V_a^0 V_b^0 \tilde{\mathbf{P}}_{ab} \nabla_a^0 W_{ab} + \mathbf{F}_a^{F:p} + \mathbf{F}_a^{F:v}, \quad (19)$$

where $\tilde{\mathbf{P}}_{ab}$ is the averaged first Piola-Kirchhoff stress of the particle pair (a, b) defined as

$$\tilde{\mathbf{P}}_{ab} = \frac{1}{2} (\mathbf{P}_a \mathbf{B}_a^0 + \mathbf{P}_b \mathbf{B}_b^0). \quad (20)$$

Note that the first Piola-Kirchhoff stress tensor is dependent on the deformation tensor \mathbf{F} which is computed from

$$\mathbf{F}_a = \left[\sum_b V_b (\mathbf{u}_b - \mathbf{u}_a) \otimes \nabla_a^0 W_{ab} \right] \mathbf{B}_a^0 + \mathbf{I}. \quad (21)$$

3.3 Treatment of fluid-structure and thermal coupling

In the fluid-structure coupling, the flexible structure is considered to be a moving boundary for the fluid by imposing a no-slip boundary condition. In this case, the fluid force exerted on the solid, and vice versa is resolved in a strong two-way coupling pattern. At the interface, the displacement, velocity and force of fluid-structure interface are supposed to be consistent. To ensure this compatibility, the density-weighted inter-particle averaged pressure

$$p_{ia} = \frac{p_i \rho_a^d + p_a^d \rho_i}{\rho_i + \rho_a^d} \quad (22)$$

is adopted when calculating the pressure force between the fluid-solid particle pair (i, a) . Following Zhang et al. [45], the pressure and viscous force exerting on a fluid particle i are calculated from

$$\mathbf{F}_i^{S:p} = -2 \sum_a V_i V_a p_{ia} \nabla_i W(\mathbf{r}_{ia}) \quad (23)$$

and

$$\mathbf{F}_i^{S:v} = 2 \sum_a \eta V_i V_a \frac{\mathbf{v}_i - \mathbf{v}_a^d}{\mathbf{r}_{ia}} \frac{\partial W(\mathbf{r}_{ia})}{\partial r_{ia}}, \quad (24)$$

respectively. With the normal vector of structure surface \mathbf{n}_a , we characterize the imaginary pressure p_a^d and velocity \mathbf{v}_a^d through

$$\begin{cases} p_a^d = p_i + \rho_i \max \left[0, \left(\mathbf{g} - \frac{d\mathbf{v}_a}{dt} \right) \cdot \mathbf{n}_a \right] (\mathbf{r}_{ia} \cdot \mathbf{n}_a), \\ \mathbf{v}_a^d = 2\mathbf{v}_i - \mathbf{v}_a. \end{cases} \quad (25)$$

The momentum conservation is fulfilled between fluid particles i and solid particle a along the center line of this interacting particle pair (i, a) due to the anti-symmetric property $\nabla_i W(\mathbf{r}_{ia}) = -\nabla_a W(\mathbf{r}_{ai})$ and the symmetric expression of inter-particle averaged pressure. Then, the condition of the continuity of normal stresses across the fluid-structure interface is enforced. Correspondingly, the pressure and viscous forces in Eq. (19) can be obtained accordingly through $\mathbf{F}_a^{F:p} = -\mathbf{F}_i^{S:p}$ and $\mathbf{F}_a^{F:v} = -\mathbf{F}_i^{S:v}$.

In the present work, heat transfer process occurs between the solid wall and fluid. Without exchanging any heat with fluid, flexible structure inside the flow only plays a role in generating vortices to mix the cold and hot stream. We consider the wall with constant temperature which is higher than that of the fluid, implying that the fluid always takes heat away from the contacting walls. Then the SPH discretized form of the heat diffusion of Eq. (10) can be represented as

$$\begin{aligned} \frac{dT_i}{dt} = \frac{1}{\rho c_p} & \left(\sum_j \frac{m_j}{\rho_j} \frac{4k_i k_j}{k_i + k_j} \frac{T_{ij}}{r_{ij}} \frac{\partial W_{ij}}{\partial r_{ij}} \right. \\ & \left. + \sum_a \frac{m_a}{\rho_a} \frac{4k_i k_a}{k_i + k_a} \frac{T_{ia}}{r_{ia}} \frac{\partial W_{ia}}{\partial r_{ia}} \right), \end{aligned} \quad (26)$$

where T_i only refers to fluid particles, implying that only the fluid experiences temperature evolution. The subscripts j and a respectively indicate contribution from neighboring fluid and solid particles within the compact support of particle i . Also $T_{ij} = T_i - T_j$ and $T_{ia} = T_i - T_a$ are the temperature difference. It is worth noting that the TFSI is straightforwardly coupled in Eq. (26) without introducing any other treatment, demonstrating the advantage of the present integrative method. According to Cleary and Monaghan [30], where heat conduction discretizations among different materials are analyzed, the present discretization of Laplacian of the temperature is spatially second order accurate and more details are referred to Ref. [30].

Compared with the original SPH form of heat conduction, an improved conduction term is applied in Eq. (26). The modified average value of thermal conductivity enables the above formulation to model more general heat transfer problems. With an explicit conductivity, the heat flux is consistent across the material interfaces naturally. Therefore, various materials with largely different conductivity can be coupled and specific heats are ensured to be accurately predicted.

Temperature dependent conductivity can also be easily implemented. For the sake of verification and simplicity, the fluid and solid conductivity is the same value $k_i = k_a$, as we can pay more attention to the relationship between the fluid vortex and heat mixing scheme rather than the material difference.

3.4 Time integration scheme

Following Ref. [46], a multi-time stepping scheme for integrating the FSI coupling is adopted herein. The computations of solid, fluid and heat dynamics may be executed several times within one time step to obtain the synchronized solutions between these physics, achieving a strong coupling. First of all, the dual-criteria time step is applied for the time integration of fluid to increase the computational efficiency. Specifically, fluid particle advection and acoustic speeds determine two time-step criteria named as Δt_{ad} and Δt_{ac} respectively given by

$$\begin{cases} \Delta t_{ad} = 0.25 \min \left(\frac{h}{U_{\max}}, \frac{h^2}{\nu} \right), \\ \Delta t_{ac} = 0.6 \frac{h}{c + U_{\max}}. \end{cases} \quad (27)$$

For the explicit integration of thermal diffusion equation, the maximum time step is given by

$$\Delta t_d = 0.5 \frac{\rho c_p h^2}{k}. \quad (28)$$

The particle interaction configuration is updated once within an advection time step and the smaller value between the acoustic and thermal diffusion criteria controls the frequency of fluid state updating. In our simulation cases, Δt_d is larger than Δt_{ac} . Consequently, during each advection time step Δt_{ad} , several pressure, density and heat transfer relaxation processes are performed with the acoustic time-step size of Δt_{ac} . In the physical relaxation process, the position-based Verlet scheme is applied [45]. At the beginning of the advection step, the viscous force is computed. During each advection time step, several acoustic time steps are integrated. Specifically, intermediate density and position are first computed as

$$\begin{cases} \rho_i^{n+\frac{1}{2}} = \rho_i^n + \frac{1}{2} \Delta t_{ac} \frac{d\rho_i}{dt}, \\ \mathbf{r}_i^{n+\frac{1}{2}} = \mathbf{r}_i^n + \frac{1}{2} \Delta t_{ac} \mathbf{v}_i^n. \end{cases} \quad (29)$$

Then, the acceleration induced by the pressure term is calculated and the fluid particle velocity at the next time step can be obtained by

$$\mathbf{v}_i^{n+1} = \mathbf{v}_i^n + \Delta t_{ac} \frac{d\mathbf{v}_i}{dt}. \quad (30)$$

Finally, the new velocity is employed to update the position of fluid particles at the new time step. Also, the density of fluid particles is updated as

$$\begin{cases} \mathbf{r}_i^{n+1} = \mathbf{r}_i^{n+\frac{1}{2}} + \frac{1}{2}\Delta t_{ac}\mathbf{v}_i, \\ \rho_i^{n+1} = \rho_i^{n+\frac{1}{2}} + \frac{1}{2}\Delta t_{ac}\frac{d\rho_i}{dt}. \end{cases} \quad (31)$$

In an acoustic time step, heat transfer equation is also solved to update the temperature field. An explicit, two-stage second-order Runge-Kutta integrator scheme is applied as [47]

$$\begin{cases} T' = T^n + \Delta t_{ac}R(T^n, t^n), \\ T'' = T' + \Delta t_{ac}R(T', t^{n+1}), \\ T^{n+1} = \frac{T^n + T''}{2}, \end{cases} \quad (32)$$

where T' and T'' are the intermediate temperature values between T^n and T^{n+1} , $R(T, t) = \frac{dT}{dt}$ the temperature change rate. This two-stage Runge-Kutta scheme has the advantage of being able to start the computation without any special devices, while retaining its accuracy and being easy to implement, especially when compared with implicit time-stepping methods. Within one Δt_{ac} , solid kinematics is calculated as $\kappa = \frac{\Delta t_{ac}^F}{\Delta t^S} + 1$ times with the solid time-step criterion Δt^S given by

$$\Delta t^S = 0.6 \min \left(\sqrt{\frac{h}{\left| \frac{d\mathbf{v}}{dt} \right|_{\max}}}, \frac{h}{|\mathbf{v}|_{\max} + c^S} \right), \quad (33)$$

where $c^S = \sqrt{\frac{K}{\rho}}$ is the artificial speed of sound for solid. Since different time steps are employed in the coupling, force-calculation mismatch in the FSI may be encountered. To solve this issue, referring to Ref. [45], we introduce a modified acceleration $\frac{d\tilde{\mathbf{v}}_a}{dt}$ and a single averaged velocity $\tilde{\mathbf{v}}_a$ for solid particles. Thus the imaginary pressure p_a^d and velocity \mathbf{v}_a^d in Eqs. (22) and (24) are modified to

$$\begin{cases} p_a^d = p_i + \rho_i \max \left[0, \left(\mathbf{g} - \frac{d\tilde{\mathbf{v}}_a}{dt} \right) \cdot \mathbf{n}_a \right] (\mathbf{r}_{ia} \cdot \mathbf{n}_a), \\ \mathbf{v}_a^d = 2\mathbf{v}_i - \tilde{\mathbf{v}}_a. \end{cases} \quad (34)$$

In structure integration, index κ indicates the individual time step, which processes from 0 to $\kappa - 1$. First, note that the change rate of deformation gradient $\frac{d\mathbf{F}_a}{dt}$ can be calculated based on the initial configuration through

$$\frac{d\mathbf{F}_a}{dt} = \left[\sum_b V_b^0 (\mathbf{v}_b - \mathbf{v}_a) \otimes \nabla_a^0 W_{ab} \right] \mathbf{B}_a^0. \quad (35)$$

The intermediate deformation tensor, density and particle position are updated as

$$\begin{cases} \mathbf{F}_a^{\kappa+\frac{1}{2}} = \mathbf{F}_a^\kappa + \frac{1}{2}\Delta t^S \frac{d\mathbf{F}_a}{dt}, \\ \rho_a^{\kappa+\frac{1}{2}} = \rho_a^0 \frac{1}{J}, \\ \mathbf{r}_a^{\kappa+\frac{1}{2}} = \mathbf{r}_a^\kappa + \frac{1}{2}\Delta t^S \mathbf{v}_a. \end{cases} \quad (36)$$

Subsequently, the pressure force generated from fluid working on structure, together with the viscous force from ambient fluid previously obtained, are applied to update the velocity of solid as

$$\mathbf{v}_a^{\kappa+1} = \mathbf{v}_a^\kappa + \Delta t^S \frac{d\mathbf{v}_a}{dt}. \quad (37)$$

At last, the deformation tensor and position of solid particles of next time step are updated with

$$\begin{cases} \mathbf{F}_a^{\kappa+1} = \mathbf{F}_a^{\kappa+\frac{1}{2}} + \frac{1}{2}\Delta t^S \frac{d\mathbf{F}_a}{dt}, \\ \rho_a^{\kappa+1} = \rho_a^0 \frac{1}{J}, \\ \mathbf{r}_a^{\kappa+1} = \mathbf{r}_a^{\kappa+\frac{1}{2}} + \frac{1}{2}\Delta t^S \mathbf{v}_a^{\kappa+1}. \end{cases} \quad (38)$$

4. Numerical tests

In this section, two benchmark tests, i.e., heat transfer in a micro-channel and flow passes a flexible beam clamped to a fixed cylinder, are first studied to validate the present method. Then, the integrated method is applied to study the heat transfer enhancement with introducing different vortex generators. In the simulation, the thermal properties of the working fluid are assumed to be constant and independent of the temperature variation. For all cases, we applied the Wendland kernel with $h = 1.3dp$, where dp is the initial particle spacing.

4.1 Channel heat transfer

We consider heat transfer in a Poiseuille flow, which is widely used as a benchmark where analytical data and numerical solutions are available for quantitative comparison. Following Ref. [8], a two-dimensional (2D)-horizontal infinitely long channel with a width of 2 mm is considered as shown in Fig. 1. The infinite length allows the thermal and velocity profile to fully develop. A temperature reset zone has been placed at the upstream region of the channel flow inlet with a constant initial temperature setup of 20°C. The top and bottom wall temperature are constantly set to be 20°C and 40°C, respectively. The constant thermal fluid properties are listed in Table 1. Following Zhang et al. [45], a periodic

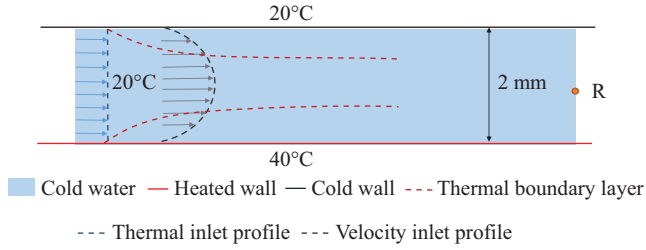


Figure 1 Schematic diagram of a heat transfer channel with a probe R in the middle of the channel located downstream.

Table 1 Working fluid information

Properties	Values
Density (kg/m^3)	1000
Kinematic viscosity (m^2/s)	1.0×10^{-6}
Thermal conductivity ($\text{W}/(\text{m K})$)	0.6
Heat capacity ($\text{J}/(\text{kg K})$)	4182

boundary condition is implemented for the channel and a 20 dp length inflow buffer region is adopted for velocity relaxation. We exert no-slip conditions on the both side walls. To achieve a laminar channel flow state, the Reynolds number $Re = U_0 H / \nu = 10$ and a parabolic velocity profile is imposed in the buffer region as

$$U(y) = \frac{1.5U(t,y)(H-y)y}{H^2}, \quad (39)$$

with a start-up smoothing procedure

$$U(t,y) = \begin{cases} 0.5U_0[1.0 - \cos(0.5\pi t)], & \text{if } t \leq 2.0 \text{ s,} \\ U_0, & \text{otherwise.} \end{cases} \quad (40)$$

In this case $U_0 = 0.01 \text{ m/s}$. The bottom wall corresponds to $y = 0$ and H is the channel width.

Figure 2 describes the vorticity and temperature contours at different time instants obtained by the present SPH solver. Only slight vortices occur in this bare channel since there are no disturbances present. As a consequence, the thermal layer thickness increases steadily in the downstream direction. Figure 3a shows the fully developed velocity profile and its comparison with the analytical solution, behaving good agreement. The temperature development at probe R over time is portrayed in Fig. 3b. Compared with the reference solution obtained by the FVM thermal solver of Hosain et al. [8], there is hardly any difference noted in the temperature profile. Generally, the efficiency and accuracy of the present SPH thermal solver are demonstrated.

For rigorous validation, we conduct a convergence study by applying different particle resolutions. Figure 4 portrays the mean square error (MSE) analysis between the SPH simulation and analytical solution by varying particle spacing. Clearly, the MSE decreases rapidly with the particle refinement. Also, the temperature profiles along the channel width at different time instances are observed and shown in Fig. 5. Note that when particle resolution is not enough refined as $\text{dp} = 10 \times 10^{-5}$ of the red line, the fluid temperature near the wall cannot be depicted accurately. As the resolution increases, the fluid temperature approaches the wall temperature as the blue line $\text{dp} = 2.5 \times 10^{-5}$ shows where the upper point is 40°C and lower 20°C , respectively. Obviously, the results obtained by the present SPH thermal solver are in good congruence with that by the FVM solver. The temperature development indicates that the SPH thermal solver

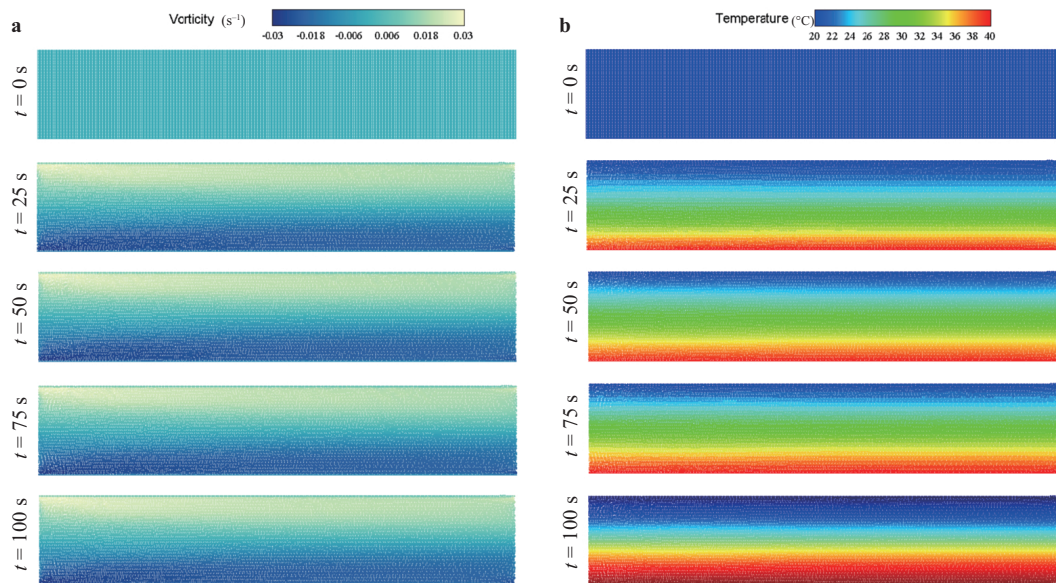


Figure 2 Heat transfer channel: **a** vorticity and **b** temperature contours at different times.

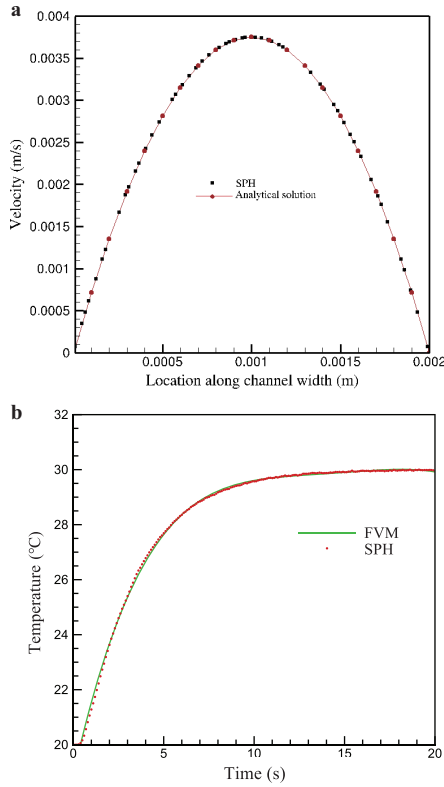


Figure 3 Heat transfer channel with particle spacing $dp = 5.0 \times 10^{-5}$: **a** velocity profile and its comparison with analytical solution and **b** temperature evolution and its comparison with FVM solution [8].

reaches satisfactory accuracy when the particle spacing value is $dp = 5 \times 10^{-5}$.

4.2 Fluid-structure interaction

Following Refs. [46,48], a well-documented 2D benchmark where a flexible beam clamped with the back surface of a rigid cylinder is tested herein. The physical configuration and computational setup of this problem are depicted in Fig. 6. With the cylinder diameter D being the characterized parameter, we set a $L = 11D$ length and $W = 4.1D$ width fluid domain. The cylinder is placed slightly off-center at $2.0D$ away from the bottom wall and $1.3D$ the inlet to induce a motion in the flexible beam in the early stage of simulation. Given the definition of the thickness $bh = 0.2D$ and length of $bl = 3.5D$, the elastic beam is attached to the rear surface of the cylinder. Comparatively soft beam is obtained with the Poisson ratio $\nu = 0.4$ and Young's modulus $E = 1.4 \times 10^3$ under the isotropic linear elastic material assumption. Other governing quantities are the solid to fluid density ratio $DR = \frac{\rho_s}{\rho_f} = 10$ and the Reynolds number $Re = \frac{DU_0\rho_f}{\mu} = 100$. For this case, an obvious oscillation would be observed under the wave of the flowing fluid. The uniform particle distribution has the same initial particle spacing $dp = 0.05D$ for both fluid and solid. Similar with that in Sect. 4.1, a parabolic in-

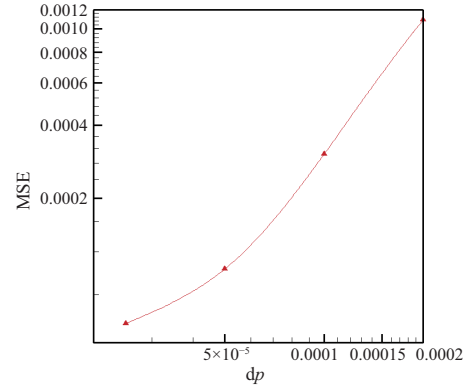


Figure 4 Velocity MSE between simulation and analytical solution with different particle spacing.

let velocity profile is adopted, while the dimensionless velocity $U_0 = 1.5$ and $t_s = 2.0$ herein and the artificial speed of sound $c_0 = 20U_0$. No-slip condition is prescribed on the both side walls and the fluid solid interface.

In the early stage of the simulation, the elastic beam experiences a minor vibration and the extent of deformation becomes larger due to the force from the ambient fluid. As the simulation progresses, the beam shows a regular oscillation, meaning that the self-sustaining state is achieved. Figure 7 depicts four snapshots of color contours considering von Mises stress for solid and vorticity for fluid during this equilibrium state. The formed vortices and wavelike beam deformation show a similar pattern to the observations in Refs. [45,48,49] and the results are within the data range of the literature. Figure 8 displays the evolution in time of the horizontal and vertical displacement and the motion curve of the beam tip point P labeled in Fig. 6. We can conclude that the beam deforms slightly in the firstly dimensionless time period of 20, but then the elastic beam enters into a equilibrium regime rapidly with a constant oscillation frequency when the simulation time approaches 40. In terms of the motion history of point P , similar with Ref. [45], a eight-shaped curve is formed and the frequency ratio concerning the y-axis and x-axis displacement is approximately 1:2. In addition, as reported in Table 2, we have quantitatively compared the displacement and frequency values from present solution to those given in other studies. With relatively small discrepancy, the values respectively converge to 0.92 and 0.178, showing good correspondence with those from previous simulations [45,48,49], validating the ability an accuracy of this solver to model FSI problems.

4.3 Thermal-fluid-structure interaction

Finally, this newly-integrated method is applied to study the thermal augmentation owing to the existence of vortices induced by different immersed structure configurations. We

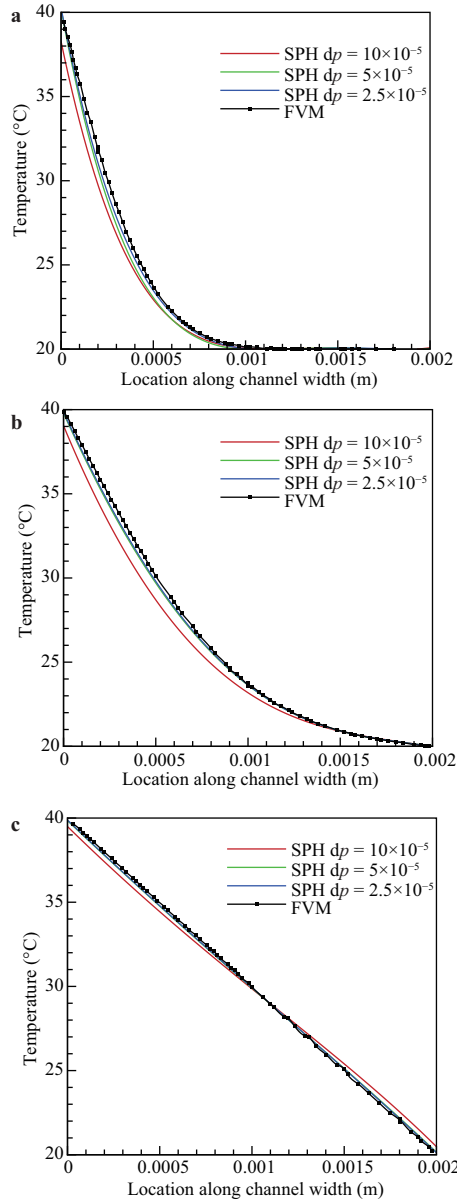


Figure 5 Heat transfer channel: the temperature profile along the channel width at different times with different particle spacing. The SPH results are compared with those obtained by the FVM in Ref. [8]. **a** $t = 0.5$ s; **b** $t = 2.0$ s; **c** $t = 5.0$ s.

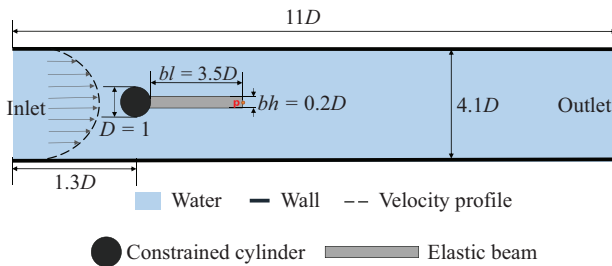


Figure 6 Geometric parameters of the 2D case involving a free beam clamped to a fixed cylinder.

consider the heat transfer problem, where different vortex generators as illustrated in Table 3 are involved in a channel

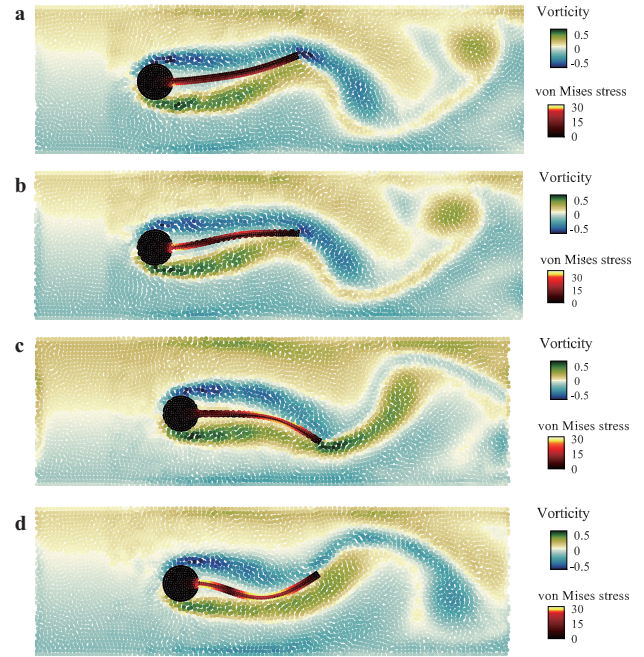


Figure 7 Fluid-structure interaction: four snapshots of color contours considering von Mises stress for solid and vorticity for fluid during this equilibrium state.

flow. The channel has a length of $31D$ and width of $4.0D$ with D denoting the cylinder diameter. Also the attached beam length is $3.5D$. Other parameters are the same with that in the FSI case. The heat diffusion constant is set to be $K = \frac{k}{\rho c_p} = 0.001$. The same velocity and thermal inflow profile as what mentioned in the heat transfer case are imposed herein. In order to examine the accompanying effect of vorticity dynamics on thermal augmentation efficiency, channel visualizations presenting stable temperature and vortex contours in four different cases are shown in Figs. 9 and 10. Obviously, in the bare heat transfer case, with a stable flowing regime, hardly any vortex alongside the boundary wall arises. Consequently, as the flowing fluid progresses downstream, the thermal boundary layer becomes thicker and hinders the removing of thermal energy of the fluid besides the walls. In the other cases, vortices periodically shed behind the rigid cylinder or the elastic beam or the both, preventing the growth of the thermal boundary layer and leading to a better heat transfer performance. To be specific, in case II, when flowing fluid encounters the obstacle cylinder, a class of symmetric vortices periodically occurs. These vortices interact with the channel walls, interrupting the accumulation of thermal energy and taking more heat from the walls than that in the bare one. While in case III, a similar pattern exists but the thermal augmentation undergoes minor changes compared with that of case II. This is attributed to the presence of the fixed beam attached to the cylinder, which prevents the formation of vortex groups. Thereby, existing vortices are

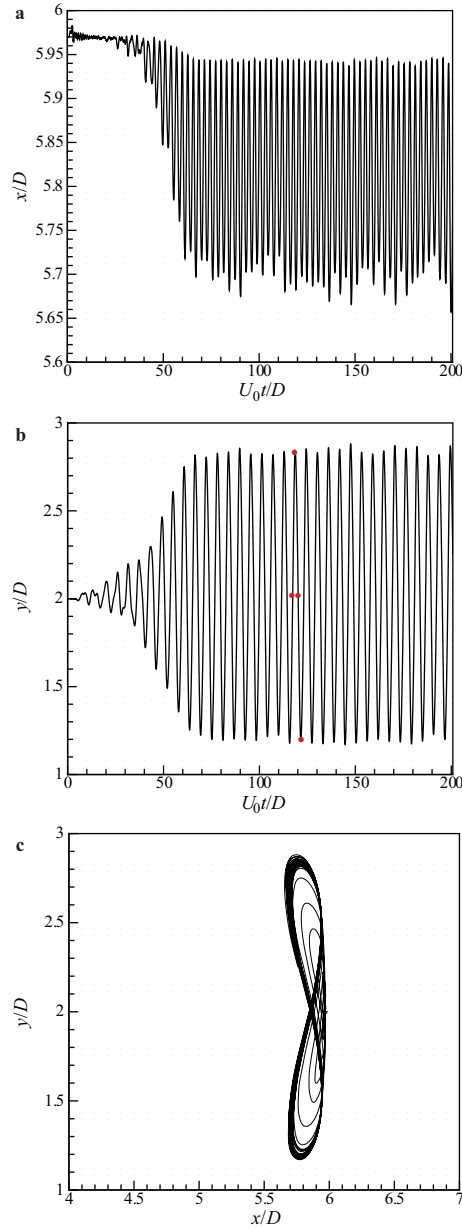


Figure 8 Fluid-structure interaction: a free beam clamped to a fixed cylinder. **a** Deflection of point S in x -direction, **b** deflection of point S in y -direction, and **c** the motion curve of point S .

Table 2 Fluid-structure interaction: the oscillation amplitude and frequency from the present solution compared with previous results

Methods	Frequency	Amplitude in y -axis
Turek and Hron [48]	0.19	0.83
Bhardwaj and Mittal [49]	0.19	0.92
Zhang et al. [45]	0.189	0.86
Present	0.178	0.92

stretched to become long but weak and have a relatively deficient interruption on the thermal energy accumulating. Also, a strong interaction between the vortices and wall shear lay-

Table 3 Four channels configuration

Channel configurations	Channel I	Channel II	Channel III	Channel IV
Cylinder	No	Yes	Yes	Yes
Beam	No	No	Yes-Solid	Yes-Flexible

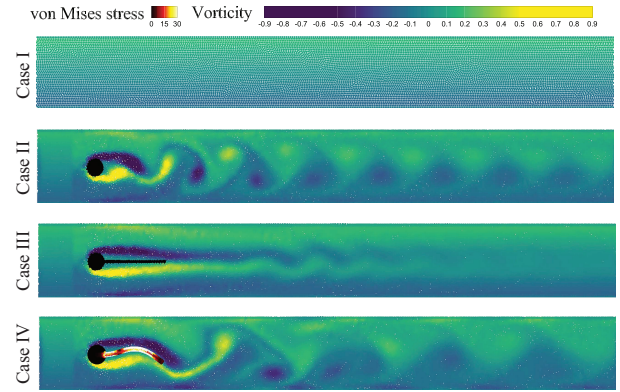


Figure 9 Stable vorticity contours in four different cases.

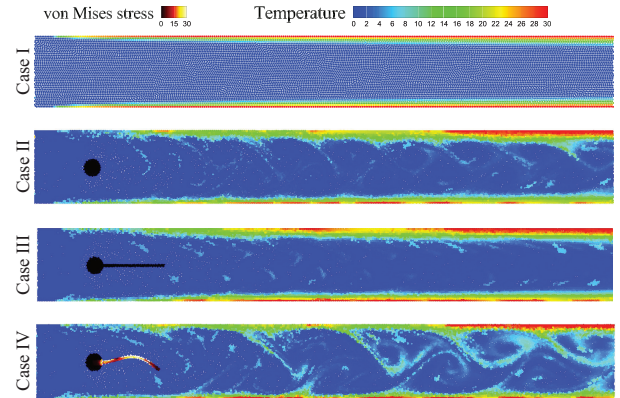


Figure 10 Stable temperature contours in four different cases.

ers happens in the case IV. The oscillating beam disrupts the localization of shedding vortices and delivers these segments to interact with the boundary layers, leading to a remarkable mixing of the central cold fluid with the hot fluid.

For a better illustration of TFSI regime, the instantaneous snapshots of the vorticity and temperature fields of case IV are depicted in Figs. 11 and 12, respectively. Without external force, the flowing fluid exerts periodic force on the beam, leading to the oscillation of the flexible beam and generating a train of vortices behind it. From the vorticity contour, it is observed that these relatively large and strong vortices are capable of penetrating into the central currents in the channel. In the downstream direction, these vortices coalesce together and dissipate slightly, imposing a continuous effect on the mixing. This finding can also be deduced in Fig. 12. With

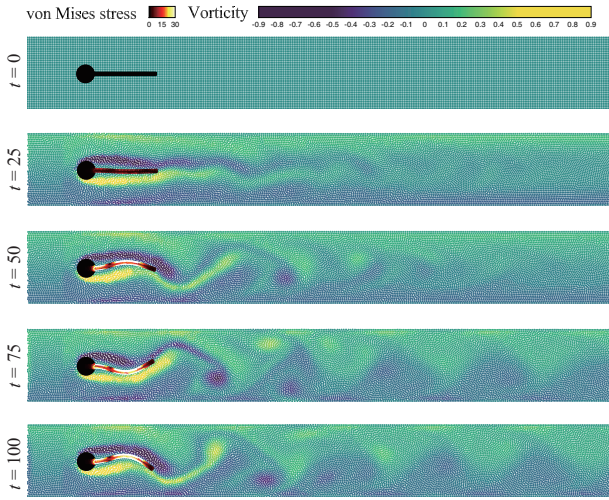


Figure 11 Vorticity contours at different time instants of case IV where an elastic beam is attached to a rigid cylinder.

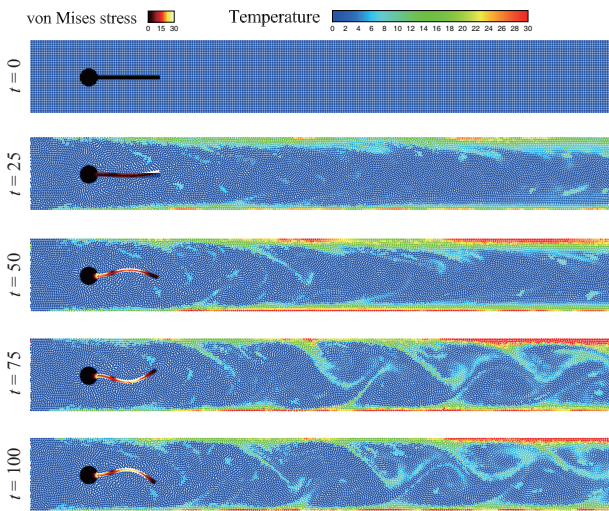


Figure 12 Temperature contours at different time instants of case IV where an elastic beam is attached to a rigid cylinder.

large-scale vertical velocity, these vigorous vortex structures of opposite rotation break the cold fluid into smaller elements. These small elements cause disorder within the boundary layer, taking the hot fluid along the walls into the central cold stream. Furthermore, the oscillatory nature of these vortices continuously interrupt the formation of the thermal boundary layer. Consequently, the greatest heat transfer enhancement is achieved.

To have a more clear comparison, vorticity profiles calculated on different vertical lines of a fully developed flow at the final state of $t = 100$ in four cases are plotted in Figs. 13 and 14. Generally, the largest vortex scale is observed in case IV, resulting in obvious temperature variation along the channel width and the most efficient heat mixing. Obvi-

ously, hardly any vortex occurs in case I, and cold fluid remains in the channel center without any disruption. In other three cases, vortices shed behind vortex generators and even though being damped as they travel downstream as shown over different vertical lines in Fig. 13, a better mixing of hot and cold fluid and a more uniform temperature distribution are observed in Fig. 14. Focusing on the upper and lower fluid zone near the hot walls in cases II, III, IV, the presence of small vortex elements close to the hot walls plays an important role in removing heat, causing the decrease of fluid temperature compared with that in case I as shown in Fig. 14. In the zone immediately behind the vortex generator corresponding to the vertical line $x = 5$, large vortex scales are observed in cases II, III, IV and great heat transfer rate is achieved since there is a noticeable increase in fluid temperature near the walls, denoting that the fluid near the wall absorbs the heat energy and transports it to the downstream. When vortices travel downstream, large vortices break into small but evenly distributed elements, leading to a more uniform mixing. This conclusion is especially vivid in case IV as a more corrugated temperature distribution regime presents in the middle of the channel.

To quantitatively assess the heat transfer enhancement, an instantaneous local Nusselt number is defined by

$$Nu = -\nabla T \frac{W}{T_w - T_m}, \quad (41)$$

where ∇T denotes the local temperature gradient at the channel wall boundary, T_w the wall temperature, T_m the average temperature of the fluid, and W the non-dimensional channel width. Figure 15 compares the Nusselt numbers along the wall when the flow is fully developed. Overall, local Nu decreases along the channel length, indicating the enhancement is weakened downstream. In case I, Nu decreases monotonically due to the presence of an increasing thermal boundary layer, while in the other three cases, corrugated variations of Nu are observed. This regime is attributed to the oscillation interaction between vortices and walls. Nu increases where vortices are present, illustrating an augmentation of heat transfer. Downstream from the vortex generator, damped vortices lead to an abatement of the interaction between walls and vortices. Consequently, Nu decreases in the other three cases. In case III, the fixed beam suppresses and limits the effect of the vortex dynamics by interrupting the shedding frequency in view of the previous discussion. Case IV performs the best in all of the cases. The oscillating beam strengthens the mixing process, having a great influence on Nu even at the outlet of the channel.

To determine the mixing rate of hot and cold fluids, a mixing coefficient D in the whole channel is defined in Eq. (42). It is the ratio of local-globally average temperature difference

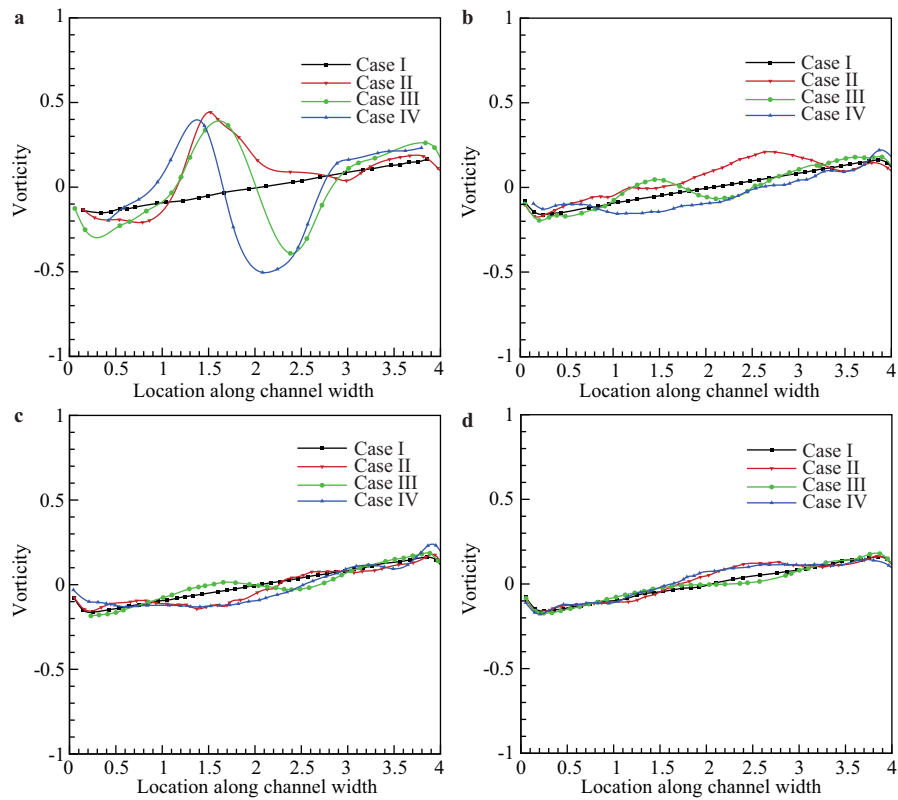


Figure 13 Vorticity distributions along the channel width at different vertical lines. **a** Line $x = 5$; **b** line $x = 15$; **c** line $x = 20$; **d** line $x = 30$.

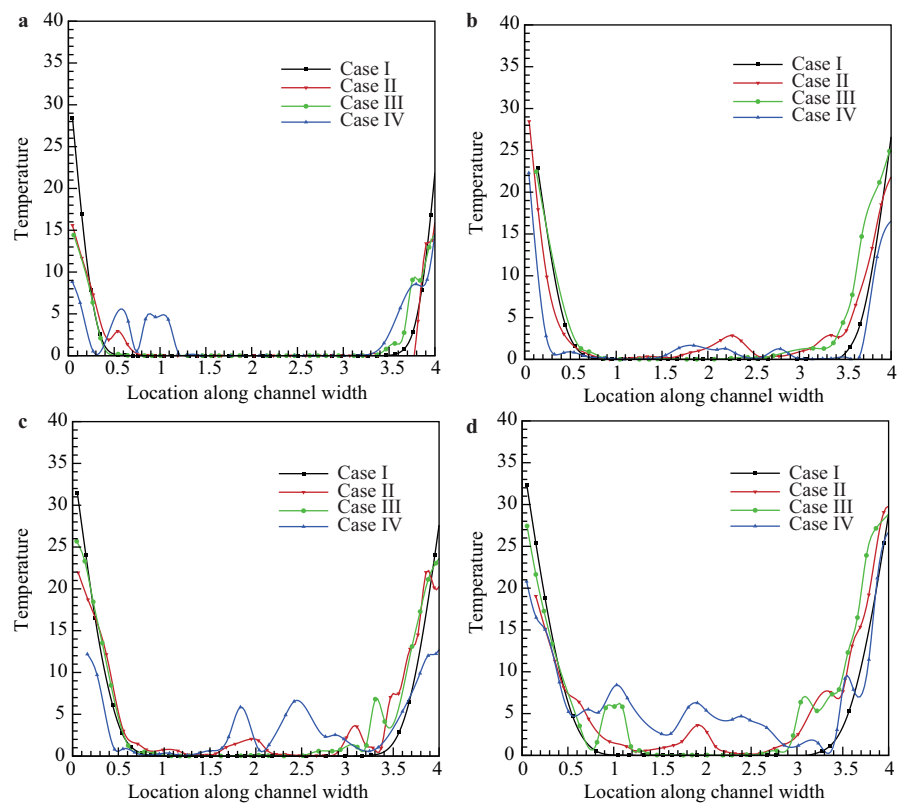


Figure 14 Temperature distributions along the channel width at different vertical lines. **a** Line $x = 5$; **b** line $x = 15$; **c** line $x = 20$; **d** line $x = 30$.

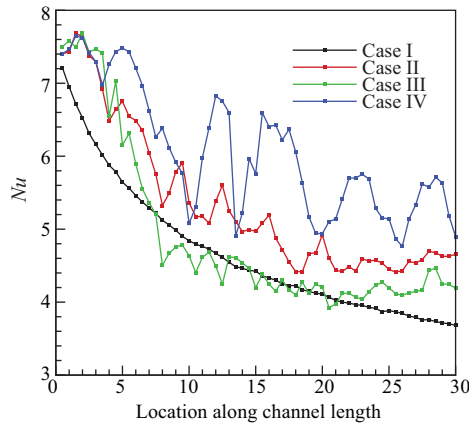


Figure 15 Local Nusselt number along the channel length in four cases.

and globally average temperature, representing the standard deviation of fluid temperature.

$$D = \sqrt{\frac{1}{N} \sum_{j=1}^N \left(\frac{T_j - T_{\text{avg}}}{T_{\text{avg}}} \right)^2}, \quad (42)$$

where N is the total particle number in the channel. Figure 16 exhibits the development of mixing rate D over time in four cases. A more uniform distribution of temperature is obtained as time goes, which can be concluded from the distinct decrease of standard mixing deviation in all cases. Cases II, III, and IV reach the bottom point within a time period of 20, showing a maximum mixing efficiency as the disordered vortices dominate the combing process, then approach the fully developed value. It is reasonable that mixing index D in case IV stabilizes at the lowest value, suggesting the most efficient mixing. The basis of such classification has been explained before.

5. Conclusion

In this paper, an integrative SPH solver is developed to study the TFSI problem. The solver is first validated by two benchmarks of heat transfer in a micro-channel and a FSI case. Having the validation in hand, heat transfer enhancement of vortices generated by different immersed structures is studied. With the unique advantage of capturing the moving interface in TFSI, the present solver clearly reveals the relationship between the vortex regime and the thermal dynamics, concluding that heat transfer augmentation is strongly dependent on vortex-thermal boundary layer interaction. The vortices penetrate into the central currents and break the cold fluid into smaller elements, which disrupt the thermal boundary layers continuously and take hot fluids into the central cold streams. A local Nusselt number and mixing index in

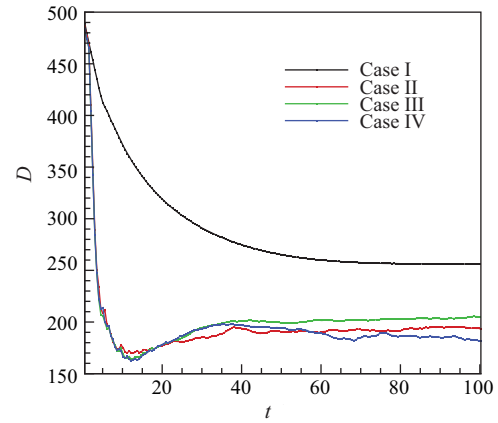


Figure 16 Variations of mixing index D as a function of time in four cases.

the channels are used to quantify the localized heat transfer performance and the fluid mixing rate respectively. Results show that each configuration with vortex generators in channel enhances heat transfer efficiency, with the flexible beam clamped to a fixed cylinder giving the best results over the other three cases. The study demonstrates that this integrative SPH method shows a good capability of capturing the thermal dynamics behavior in complex industrial cases, where traditional mesh-based methods reach their limits of applicability. The present SPH TFSI method can be extended for more realistic engineering problems, which is our continuing work.

Author contributions Xiaojing Tang developed the methodology, conducted the research and wrote the first draft of the manuscript. Chi Zhang designed the research, conducted the formal analysis and revised the manuscript. Oskar Haidn and Xiangyu Hu administered the project.

Acknowledgements Xiaojing Tang was partially supported by the China Scholarship Council (Grant No. 201906120034). Chi Zhang and Xiangyu Hu would like to express their gratitude to Deutsche Forschungsgemeinschaft (DFG) for their sponsorship of this research (Grant No. DFG HU1527/12-4).

- 1 H. Babar, and H. M. Ali, Towards hybrid nanofluids: Preparation, thermophysical properties, applications, and challenges, *J. Mol. Liquids* **281**, 598 (2019).
- 2 Z. Khattak, and H. M. Ali, Air cooled heat sink geometries subjected to forced flow: A critical review, *Int. J. Heat Mass Transfer* **130**, 141 (2019).
- 3 R. L. Webb, and N. Kim, Enhanced Heat Transfer (Taylor and Francis, New York, 2005).
- 4 Y. Chen, J. Yang, Y. Liu, and H. J. Sung, Heat transfer enhancement in a poiseuille channel flow by using multiple wall-mounted flexible flags, *Int. J. Heat Mass Transfer* **163**, 120447 (2020).
- 5 J. Armstrong, and D. Winstanley, A review of staggered array pin fin heat transfer for turbine cooling applications, *J. TurboMach.* **110**, 94 (1988).
- 6 G. Biswas, H. Chattopadhyay, and A. Sinha, Augmentation of heat

- transfer by creation of streamwise longitudinal vortices using vortex generators, *Heat Transfer Eng.* **33**, 406 (2012).
- 7 T. Long, P. Yang, and M. Liu, A novel coupling approach of smoothed finite element method with SPH for thermal fluid structure interaction problems, *Int. J. Mech. Sci.* **174**, 105558 (2020).
 - 8 M. L. Hosain, J. M. Domínguez, R. Bel Fdhila, and K. Kyprianidis, Smoothed particle hydrodynamics modeling of industrial processes involving heat transfer, *Appl. Energy* **252**, 113441 (2019).
 - 9 A. Al-Amiri, and K. Khanafer, Fluid-structure interaction analysis of mixed convection heat transfer in a lid-driven cavity with a flexible bottom wall, *Int. J. Heat Mass Transfer* **54**, 3826 (2011).
 - 10 M. Ghalambaz, E. Jamesahar, M. A. Ismael, and A. J. Chamkha, Fluid-structure interaction study of natural convection heat transfer over a flexible oscillating fin in a square cavity, *Int. J. Thermal Sci.* **111**, 256 (2017).
 - 11 A. Raisi, and I. Arvin, A numerical study of the effect of fluid-structure interaction on transient natural convection in an air-filled square cavity, *Int. J. Thermal Sci.* **128**, 1 (2018).
 - 12 M. Liu, and Z. Zhang, Smoothed particle hydrodynamics (SPH) for modeling fluid-structure interactions, *Sci. China-Phys. Mech. Astron.* **62**, 984701 (2019).
 - 13 A. K. Soti, R. Bhardwaj, and J. Sheridan, Flow-induced deformation of a flexible thin structure as manifestation of heat transfer enhancement, *Int. J. Heat Mass Transfer* **84**, 1070 (2015).
 - 14 L. B. Lucy, A numerical approach to the testing of the fission hypothesis, *Astron. J.* **82**, 1013 (1977).
 - 15 R. A. Gingold, and J. J. Monaghan, Smoothed particle hydrodynamics: Theory and application to non-spherical stars, *Mon. Not. R. Astron. Soc.* **181**, 375 (1977).
 - 16 J. J. Monaghan, Simulating free surface flows with SPH, *J. Comput. Phys.* **110**, 399 (1994).
 - 17 C. Zhang, G. M. Xiang, B. Wang, X. Y. Hu, and N. A. Adams, A weakly compressible SPH method with WENO reconstruction, *J. Comput. Phys.* **392**, 1 (2019).
 - 18 M. Rezavand, C. Zhang, and X. Hu, A weakly compressible SPH method for violent multi-phase flows with high density ratio, *J. Comput. Phys.* **402**, 109092 (2020), arXiv: 1903.09216.
 - 19 J. J. Monaghan, SPH without a tensile instability, *J. Comput. Phys.* **159**, 290 (2000).
 - 20 M. McLoone, and N. J. Quinlan, Coupling of the meshless finite volume particle method and the finite element method for fluid-structure interaction with thin elastic structures, *Eur. J. Mech.-B Fluids* **92**, 117 (2022).
 - 21 C. Zhang, Y. Zhu, Y. Yu, D. Wu, M. Rezavand, S. Shao, and X. Hu, An artificial damping method for total Lagrangian SPH method with application in biomechanics, *Eng. Anal. Bound. Elem.* **143**, 1 (2022).
 - 22 H. G. Lyu, P. N. Sun, X. T. Huang, S. H. Chen, and A. M. Zhang, On removing the numerical instability induced by negative pressures in SPH simulations of typical fluid-structure interaction problems in ocean engineering, *Appl. Ocean Res.* **117**, 102938 (2021).
 - 23 H. Gotoh, A. Khayyer, and Y. Shimizu, Entirely Lagrangian meshfree computational methods for hydroelastic fluid-structure interactions in ocean engineering—Reliability, adaptivity and generality, *Appl. Ocean Res.* **115**, 102822 (2021).
 - 24 A. Khayyer, H. Gotoh, and Y. Shimizu, On systematic development of FSI solvers in the context of particle methods, *J. Hydrodyn.* **34**, 395 (2022).
 - 25 A. Khayyer, Y. Shimizu, H. Gotoh, and K. Nagashima, A coupled incompressible SPH-Hamiltonian SPH solver for hydroelastic FSI corresponding to composite structures, *Appl. Math. Model.* **94**, 242 (2021).
 - 26 M. B. Liu, and G. R. Liu, Smoothed particle hydrodynamics (SPH): An overview and recent developments, *Arch. Computat. Methods Eng.* **17**, 25 (2010).
 - 27 M. Luo, A. Khayyer, and P. Lin, Particle methods in ocean and coastal engineering, *Appl. Ocean Res.* **114**, 102734 (2021).
 - 28 C. Zhang, Y. Zhu, D. Wu, and X. Hu, Review on smoothed particle hydrodynamics: Methodology development and recent achievement, arXiv preprint, arXiv: 2205.03074.
 - 29 H. Gotoh, and A. Khayyer, On the state-of-the-art of particle methods for coastal and ocean engineering, *Coast. Eng. J.* **60**, 79 (2018).
 - 30 P. W. Cleary, and J. J. Monaghan, Conduction modelling using smoothed particle hydrodynamics, *J. Comput. Phys.* **148**, 227 (1999).
 - 31 R. Rook, M. Yildiz, and S. Dost, Modeling transient heat transfer using SPH and implicit time integration, *Numer. Heat Transfer Part B-Fundam.* **51**, 1 (2007).
 - 32 X. Yang, and S. C. Kong, Numerical study of natural convection in a horizontal concentric annulus using smoothed particle hydrodynamics, *Eng. Anal. Bound. Elem.* **102**, 11 (2019).
 - 33 K. C. Ng, Y. L. Ng, T. W. H. Sheu, and A. Mukhtar, Fluid-solid conjugate heat transfer modelling using weakly compressible smoothed particle hydrodynamics, *Int. J. Mech. Sci.* **151**, 772 (2019).
 - 34 A. Farokhpanah, M. Bussmann, and J. Mostaghimi, New smoothed particle hydrodynamics (SPH) formulation for modeling heat conduction with solidification and melting, *Numer. Heat Transfer Part B-Fundamentals* **71**, 299 (2017), arXiv: 1608.04400.
 - 35 V. Vishwakarma, A. K. Das, and P. K. Das, Steady state conduction through 2D irregular bodies by smoothed particle hydrodynamics, *Int. J. Heat Mass Transfer* **54**, 314 (2011).
 - 36 C. Zhang, M. Rezavand, Y. Zhu, Y. Yu, D. Wu, W. Zhang, J. Wang, and X. Hu, SPHinXsys: An open-source multi-physics and multi-resolution library based on smoothed particle hydrodynamics, *Comput. Phys. Commun.* **267**, 108066 (2021), arXiv: 2010.12375.
 - 37 J. P. Morris, P. J. Fox, and Y. Zhu, Modeling low Reynolds number incompressible flows using SPH, *J. Comput. Phys.* **136**, 214 (1997).
 - 38 X. Y. Hu, and N. A. Adams, A multi-phase SPH method for macroscopic and mesoscopic flows, *J. Comput. Phys.* **213**, 844 (2006).
 - 39 A. Ferrari, M. Dumbser, E. F. Toro, and A. Armanini, A new 3D parallel SPH scheme for free surface flows, *Comput. Fluids* **38**, 1203 (2009).
 - 40 C. Zhang, X. Y. Hu, and N. A. Adams, A weakly compressible SPH method based on a low-dissipation Riemann solver, *J. Comput. Phys.* **335**, 605 (2017).
 - 41 S. Adami, X. Y. Hu, and N. A. Adams, A transport-velocity formulation for smoothed particle hydrodynamics, *J. Comput. Phys.* **241**, 292 (2013).
 - 42 C. Zhang, Y. Zhu, X. Lyu, and X. Hu, An efficient and generalized solid boundary condition for SPH: Applications to multi-phase flow and fluid-structure interaction, *Eur. J. Mech.-B Fluids* **94**, 276 (2022).
 - 43 R. Vignjevic, J. R. Reveles, and J. Campbell, SPH in a total Lagrangian formalism, *Comput. Model. Eng. Sci.* **14**, 181 (2006).
 - 44 P. W. Randles, and L. D. Libersky, Smoothed particle hydrodynamics:

- Some recent improvements and applications, *Comput. Methods Appl. Mech. Eng.* **139**, 375 (1996).
- 45 C. Zhang, M. Rezavand, and X. Hu, A multi-resolution SPH method for fluid-structure interactions, *J. Comput. Phys.* **429**, 110028 (2021).
- 46 C. Zhang, M. Rezavand, and X. Hu, Dual-criteria time stepping for weakly compressible smoothed particle hydrodynamics, *J. Comput. Phys.* **404**, 109135 (2020), arXiv: [1905.12302](#).
- 47 C. W. Shu, and S. Osher, Efficient implementation of essentially non-oscillatory shock-capturing schemes, *J. Comput. Phys.* **77**, 439 (1988).
- 48 S. Turek, and J. Hron, Proposal for numerical benchmarking of fluid-structure interaction between an elastic object and laminar incompressible flow, in: *Fluid-structure Interaction* (Springer, Berlin, 2006), pp. 371-385.
- 49 R. Bhardwaj, and R. Mittal, Benchmarking a coupled immersed-boundary-finite-element solver for large-scale flow-induced deformation, *AIAA J.* **50**, 1638 (2012).

A.2 Paper II

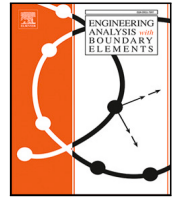
Xiaojing Tang, Dong Wu, Zhentong Wang, Oskar Haidn, Xiangyu Hu

Simulating plate and shell structures with anisotropic resolution using adaptive smoothed particle hydrodynamics

In *Engineering Analysis with Boundary Elements*, Volume 167, Pages 105886, 2024,

DOI:<https://doi.org/10.1016/j.enganabound.2024.105886>

Copyright ©2024 Elsevier. Reprinted with permission



Simulating plate and shell structures with anisotropic resolution using adaptive smoothed particle hydrodynamics

Xiaojing Tang, Dong Wu, Zhentong Wang, Oskar Haidn, Xiangyu Hu *

Technical University of Munich, School of Engineering and Design, Boltzmannstraße 15, Garching, 85748, Germany

ARTICLE INFO

Keywords:

Adaptive smoothed particle hydrodynamics
Plate and shell structures
Full-dimensional models
Reduced-dimensional models
Anisotropic resolution
Anisotropic kernel

ABSTRACT

When simulating plate and shell structures characterized by large aspect ratios, reduced-dimensional models are frequently employed due to their notable reduction in computational overhead in contrast to traditional isotropic full-dimensional models. However, in scenarios involving variations in the thickness direction, where adequate resolution in this dimension is required, reduced-dimensional models exhibit limitations. To capture variations in the thickness direction while simultaneously mitigating computational costs, an anisotropic full-dimensional model, integrated with an adaptive smoothed particle hydrodynamics method (ASPH), is developed for simulating behaviors of plate and shell structures in this study. The correction matrix, which is applied to ensure the first-order consistency, is modified accordingly by incorporating the nonisotropic kernel into it within the total Lagrangian framework of ASPH. A series of numerical examples, along with a specific application concerning the deformation of a porous film due to nonuniform internal fluid pressure in the thickness direction, are conducted to assess the computational accuracy and efficiency of the proposed ASPH method. Comparative analyses of our results against reference data and traditional isotropic SPH solutions demonstrate close agreements, affirming the suitability of the present ASPH method across various scenarios.

1. Introduction

The smoothed particle hydrodynamics (SPH) method has gained increasing interest as an alternative to mesh-based methods [1–4]. Based on the principle of using particles to discretize the computation domain, SPH has been widely applied to simulate fluid-flows [4–7], fluid–solid interaction [8–10], and solid mechanics [11–15] including the mechanical behavior of plate and shell structures [16–19] in recent years. Plate and shell structures, characterized by one dimension significantly smaller than the other two, have been explored in the literature using meshless methods like the element-free Galerkin formulation [20–22], and the reproducing kernel particle method [23–27]. Within the SPH framework, the reduced-dimensional models are commonly used in simulating the thin structures [28–31]. Specifically, these thin structures are discretized by a single layer of particles in SPH to reduce computation time. However, the reduced-dimensional models are not applicable in some specific situations involving parameter variations in the reduced thickness direction. For instance, in scenarios where a thin, porous membrane is partially filled with fluid, which is extensively observed in the fuel cell of battery [32,33], the presence of nonuniform fluid concentration necessitates fine resolution in the thickness direction to accurately represent deviations of fluid pressure.

While the traditional full-dimensional or volume-particle SPH method with isotropic resolutions can address this issue, as far as the authors knowledge, the application of thin structure involving the parameter variation in the thickness direction is still limited, since it often entails high computational costs, which promotes the adoption of anisotropic resolutions.

In the context of anisotropic particle resolution within SPH, the particle spacing along the large aspect of thin structures is much larger than that along the thickness direction. With such anisotropic discretization, adopting an isotropic smoothing kernel which defines a spherical influence domain in SPH becomes unsuitable. To maintain consistency, the adaptive smoothed particle hydrodynamics (ASPH) method, a variant of SPH incorporating anisotropic smoothing kernels, is considered. The strategy of anisotropic smoothing kernels in SPH was initially introduced by Bicknell and Gingold [34] to study the cosmological dynamics. Then, Owen et al. [35] refined the ASPH formulation in a mathematical formalism, replacing a scalar smoothing length, which defines a spherical interpolation kernel, with a smoothing tensor to identify ellipsoidal kernels through the use of a locally linear transformation of coordinates. Liu and Liu [36] employed the ASPH method to simulate micro-channel flows with high length width ratio

* Corresponding author.

E-mail addresses: xiaojing.tang@tum.de (X. Tang), dong.wu@tum.de (D. Wu), zhentong.wang@tum.de (Z. Wang), oskar.haidn@tum.de (O. Haidn), xiangyu.hu@tum.de (X. Hu).

<https://doi.org/10.1016/j.enganabound.2024.105886>

Received 6 March 2024; Received in revised form 23 July 2024; Accepted 24 July 2024

Available online 31 July 2024

0955-7997/© 2024 The Author(s). Published by Elsevier Ltd. This is an open access article under the CC BY license (<http://creativecommons.org/licenses/by/4.0/>).

where the adaptive kernel conforms to the geometry, thereby saving computational time. With a more generalized elliptical influence domain, ASPH has been used to simulate high-strain Lagrangian solid dynamics, where anisotropic volume changes occur [37]. By introducing the concept of ASPH with ellipsoidal kernels, Fu et al. [38] facilitated a relaxation of particle distribution towards an anisotropic target functions. However, to the best of the authors knowledge, the utilization of ASPH in the modeling of thin structures has not yet been documented.

In this paper, the concept of ASPH is extended to simulate thin structure problems in the combination with anisotropic resolutions. The smoothing kernel is defined coupled with a linear transformation tensor, and thus the support domain of one particle turns out to be an ellipsoid area, rather than a spherical domain. Furthermore, the correction matrix applied to the kernel gradient for first-order consistency is modified accordingly by integrating the nonisotropic kernel within the total Lagrangian framework in ASPH. The reminder of this paper is organized as follows. Section 2 summaries the theory and governing equations for elastic solid mechanics, along with a fluid-structure interaction model for porous media deforming. Additionally, this section covers previous knowledge of ASPH and the description of anisotropic discretization. In Section 3, the correction matrix evolving the nonisotropic kernel and the discretized governing equations within the total Lagrangian integration are presented. Section 4 outlines six numerical examples, including both two-dimensional and three-dimensional cases to comprehensively examine the ASPH method. The results obtained using the proposed method are compared with those from SPH method. Finally, Section 5 presents concluding remarks. The source code and data necessary for replicating this numerical simulations presented in this work can be accessed through SPHinxsys, an open-source multi-physics SPH library, available at <https://www.sphinxsys.org>.

2. Governing equations and ASPH theory

2.1. Continuum kinematics

2.1.1. Motion and deformation

In this section, we concisely introduce the fundamental physical concepts of solid deformation, along with the relevant notations and symbols within the total Lagrange framework that we use in the subsequent models. Our analysis considers a solid body B that occupies two regions: \mathcal{R}_0 and \mathcal{R} , representing the body configurations at time t_0 (where $t = 0$) and t , respectively. In the initial configuration \mathcal{R}_0 , the position vector of a material point is denoted by $\mathbf{X} \in \mathcal{R}_0$, while in the current configuration $\mathbf{x} \in \mathcal{R}$. The motion of the solid body, represented by the invertible mapping ϕ , transforms a material point \mathbf{X} to its corresponding vector $\mathbf{x} = \phi(\mathbf{X}, t)$, as shown in Fig. 1. Accordingly, the Lagrangian velocity of a material point is given by $\mathbf{v}(\mathbf{X}, t) = \frac{d\phi(\mathbf{X}, t)}{dt}$. The deformation gradient \mathbf{F} , which characterizes the deviation of a material point from its initially undeformed position to its deformed position, can be calculated from the displacement vector $\mathbf{u} = \mathbf{x} - \mathbf{X}$ by the following equation:

$$\mathbf{F} = \frac{d\mathbf{x}}{d\mathbf{X}} = \nabla^0 \mathbf{u} + \mathbf{I}, \quad (1)$$

where ∇^0 denotes the gradient operator defined in the initial reference configuration, \mathbf{I} the unit matrix.

2.1.2. Solid dynamics equations

The relevant governing equations are derived from the conservation laws of mass and momentum, while accounting for the characteristics of elastic materials. With the Lagrangian framework assumption, the governing equations of elastic structure read

$$\begin{cases} \rho = \rho_0 J \\ \rho_0 \frac{d\mathbf{v}}{dt} = \nabla^0 \cdot \mathbf{P}^T \end{cases} \quad (2)$$

where ρ and ρ_0 are the densities in the current configuration \mathcal{R} and the initial configuration \mathcal{R}_0 , respectively. The corresponding Jacobian determinant term $J = \det(\mathbf{F})$ indicates the local volume gain $J > 1$ or loss $J < 1$. \mathbf{v} denotes the velocity, and T the matrix transposition operator. Here, the first Piola–Kirchhoff stress tensor \mathbf{P} , relating to the stress within the initial configuration, can be obtained by

$$\mathbf{P} = \mathbf{F}\mathbf{S}, \quad (3)$$

where \mathbf{S} is the symmetric second Piola–Kirchhoff stress tensor. In the case of isotropic and linear elastic material behavior, \mathbf{S} can be determined through the following

$$\mathbf{S} = \lambda \text{tr}(\mathbf{E})\mathbf{I} + 2\mu\mathbf{E}, \quad (4)$$

where \mathbf{E} is the Green–Lagrangian strain, given by

$$\mathbf{E} = \frac{1}{2} (\mathbf{F}\mathbf{F}^T - \mathbf{I}). \quad (5)$$

Here, λ and μ denoting the Lamé parameters. Usually, the key material properties include the Young's modulus E , Poisson ratio ν , shear modulus $G = \mu$, bulk modulus $K = \lambda + 2\mu/3$, and each of them is dependent on the others as

$$E = 2G(1 + \nu) = 3K(1 - 2\nu), \quad (6)$$

2.1.3. Fluid–structure interaction equations

Considering a porous media partially filled with a fluid, following Refs. Gawin et al. [39], Korsawe et al. [40], Atkin and Craine [41], and Zhao and Papadopoulos [42], the presence of fluid induces pressure, leading to a deformation of the structural solid in the media. The total first Piola–Kirchhoff stress tensor \mathbf{P} acting on the solid is the sum of \mathbf{P}^s and the fluid pressure stress \mathbf{P}^f , written as:

$$\mathbf{P} = \mathbf{P}^s + \mathbf{P}^f = \mathbf{F}\mathbf{S} - J\sigma^f\mathbf{F}^{-T} = \mathbf{F}\mathbf{S} - Jp^f\mathbf{F}^{-T}, \quad (7)$$

where σ^f is the Cauchy stress arising from the fluid, and $p^f = Cc$ represents the fluid pressure, with C being a material constant, c the fluid saturation in the porous media. With the fluid dynamics adhering to the principles of diffusion, the evolution of the fluid saturation in the porous media can be expressed as

$$\frac{dc}{dt} = \nabla \cdot (D\nabla c), \quad (8)$$

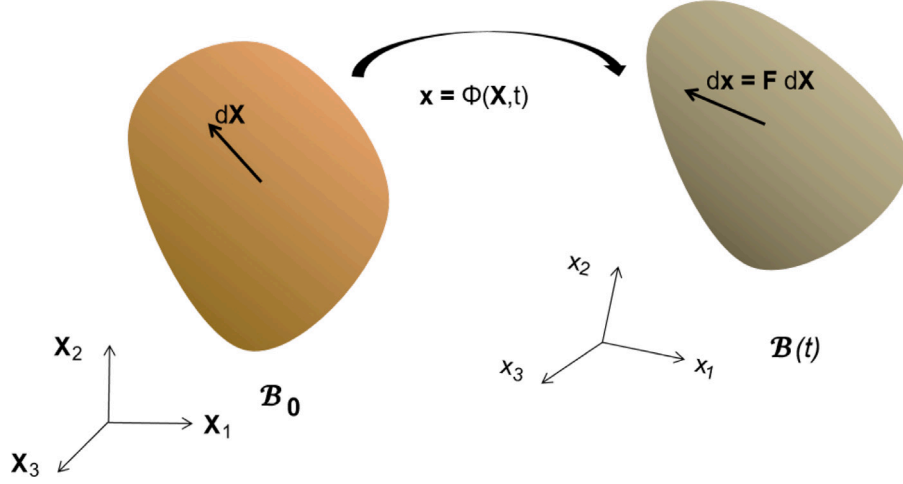
indicating that the fluid saturation variation is proportional to the diffusivity D .

2.2. ASPH method

Derived from smoothed particle hydrodynamics (SPH) method, the adaptive smoothed particle hydrodynamics (ASPH) method is predicated on an integral formulation, wherein pertinent physical quantities are approximated via the integration of neighboring particles, but the kernel function being evolved is adaptive. Compared with the SPH method established in general coordinates, an ellipsoidal kernel is used in ASPH to simulate problems with anisotropic particle volume changes, which can be portrayed as a localized, linear shift of coordinates. This shift transforms the coordinates to a system where the anisotropic volume changes appear uniform in all directions. This transformation is described by a tensor \mathbf{G} , which involves tensor smoothing lengths and angles of rotation between the kernel and real frames. Consequently, ASPH can be used to simulate scenarios, which isotropic SPH smoothing algorithm is seriously mismatched to.

2.2.1. Fundamental and theory of ASPH

Following Ref. Owen et al. [35], the position vector \mathbf{r} in the traditional isotropic SPH, is generalized to a normalized form $\boldsymbol{\eta}$ in ASPH through a linear coordinate transformation tensor \mathbf{G} . This transformation is expressed as $\boldsymbol{\eta} = \mathbf{G}\mathbf{r}$, resulting in the representation of the kernel function $W(\boldsymbol{\eta}) = W(\mathbf{G}\mathbf{r})$. In contrast to the isotropic kernel, the

Fig. 1. Finite deformation process on a body B .

normalization undergoes a change: SPH: $\eta = \mathbf{r}/h \rightarrow$ ASPH: $\eta = \mathbf{G}\mathbf{r}$. It is evident that SPH can be regarded as a degenerate case of ASPH, where the tensor \mathbf{G} becomes diagonal with a constant component of $1/h$.

Under such notations, the ASPH kernel value is obtained by $W'(\mathbf{G}\mathbf{r})$ and the kernel has the normalization property of

$$1 = \int W(\eta) d\eta = \int W'(\mathbf{G}\mathbf{r}) d\mathbf{r} = \int \|\mathbf{G}\| W(\eta) d\mathbf{r}. \quad (9)$$

Here, $\|\mathbf{G}\| d\mathbf{r} = d\eta$, where $\|\mathbf{G}\|$ is the determinant term $\|\mathbf{G}\| = \det(\mathbf{G})$. The discrete form of one continuously defined function f at a particle i is stated as

$$f_i = \int f W(\eta_i - \eta) d\eta = \int f \|\mathbf{G}\| W(\eta_i - \eta) d\mathbf{r}, \quad (10)$$

where i is the particle index and η_i the normalized particle position. By introducing the particle summation, Eq. (10) can be modified to

$$f_i = \sum_j \|\mathbf{G}\| V_j f_j W(\eta_i - \eta_j) = \sum_j \|\mathbf{G}\| \frac{m_j}{\rho_j} f_j W(\eta_i - \eta_j), \quad (11)$$

where V_j is the volume of the j th neighboring particle, m_j and ρ_j the particle mass and density, respectively, $\eta_{ij} = \eta_i - \eta_j$ the normalized particle distance vector pointing from particle j to i .

In addition, with the gradient of the kernel function $\nabla W(\eta)$ being expressed as [35]

$$\nabla W(\eta) = \nabla W'(\mathbf{G}\mathbf{r}) = \frac{\partial W(\mathbf{G}\mathbf{r})}{\partial \mathbf{r}} = \frac{\partial \eta}{\partial \mathbf{r}} \frac{\partial W}{\partial \eta} = \mathbf{G} \frac{\eta}{\eta} \frac{\partial W}{\partial \eta}, \quad (12)$$

one has the approximation of derivative of a variable field f at particle i by

$$\begin{aligned} \nabla f_i &\approx \int_{\Omega} \nabla f(\mathbf{r}) W(\mathbf{r}_i - \mathbf{r}, h) dV \\ &= - \int_{\Omega} f(\mathbf{r}) \nabla W'(\mathbf{G}(\mathbf{r}_i - \mathbf{r})) dV \\ &= -\|\mathbf{G}\| \int_{\Omega} f(\mathbf{r}) \nabla W(\eta) dV, \end{aligned} \quad (13)$$

Incorporating the particle summation, Eq. (13) can be modified into a weak form as

$$\nabla f_i = \nabla f_i - f_i \nabla 1 \approx -2 \sum_j \|\mathbf{G}\| V_j \tilde{f}_{ij} \nabla_i W_{ij}, \quad (14)$$

where $\tilde{f}_{ij} = (f_i + f_j)/2$ is the inter-particle average value. The weak-form approximation of the derivative is applied when computing surface integration with respect to a variable for solving its conservation law. In contrast with the weak form, Eq. (13) can be rewritten in the strong form as

$$\nabla f_i = f_i \nabla 1 + \nabla f_i \approx \sum_j \|\mathbf{G}\| V_j f_{ij} \nabla_i W_{ij}, \quad (15)$$

where $f_{ij} = f_i - f_j$ is the inter-particle difference value. The strong form approximation of the derivative is used to determine the local structure of a field.

Considering a spatially varying smoothing tensor, which is linked to the rotation angle of the semimajor axis of the support domain, the kernel function is individually defined for each particle. Thus, the kernel function needs to be symmetrized to ensure the conservation of quantities such as linear momentum. The symmetrization of kernel function W_{ij} and the gradient of which between two particles i and j can be implemented as the averaged formalism as

$$W_{ij} = \frac{1}{2}(W(\eta_{i,ij}) + W(\eta_{j,ij})), \quad \nabla W_{ij} = \frac{1}{2}(\nabla W(\eta_{i,ij}) + \nabla W(\eta_{j,ij})), \quad (16)$$

where

$$\eta_{i,ij} = \mathbf{G}_i \mathbf{r}_{ij}, \quad \eta_{j,ij} = \mathbf{G}_j \mathbf{r}_{ij}. \quad (17)$$

Since the quantities are expressed by the integration of a series of neighboring particles (each with the individual information including positions \mathbf{r}_j , volume V_j) in both ASPH and SPH, the solid dynamic equations could be derived in ASPH using the same approach as that in SPH. The point is to express quantities in terms of the normalized position vector η and replace the kernel gradient by a new one consisting of tensor \mathbf{G} as in Eq. (12).

2.2.2. Transformation tensor \mathbf{G}

Defined as a linear transformation that maps from real position space (\mathbf{r}) to normalized position space (η), \mathbf{G} is determined by the coupling of the geometrically scaling transformation and the rotational transformation, involving the smoothing lengths in different directions and the rotation angle of the axes deviated from the real frame. Detailed information can be found in the reference paper [35]. For a two-dimensional case, with h_1 denoting the length in semimajor axis direction and h_2 in the semiminor axis in an ellipse, θ being the rotation angle of the semimajor axis compared to the real frame, \mathbf{G} is given by,

$$\mathbf{G} = \begin{bmatrix} h_1^{-1} \cos^2 \theta + h_2^{-1} \sin^2 \theta & (h_1^{-1} - h_2^{-1}) \cos \theta \sin \theta \\ (h_1^{-1} - h_2^{-1}) \cos \theta \sin \theta & h_1^{-1} \sin^2 \theta + h_2^{-1} \cos^2 \theta \end{bmatrix}. \quad (18)$$

If a kernel frame is consistent with the real frame, in other words, rotation angle $\theta = 0$, \mathbf{G} can be simplified into

$$\mathbf{G} = \begin{pmatrix} h_1^{-1} & 0 \\ 0 & h_2^{-1} \end{pmatrix}. \quad (19)$$

While for a more complex three-dimensional case, with a vector (h_1, h_2, h_3) representing the smoothing lengths along different axes in

the kernel frame, and the rotation angle (ω, ψ, χ) between the kernel frame and the real (x, y, z) frames, \mathbf{G} can be expressed as

$$\mathbf{G} = \begin{pmatrix} G_{11} & G_{21} & G_{31} \\ G_{21} & G_{22} & G_{32} \\ G_{31} & G_{32} & G_{33} \end{pmatrix}, \quad (20)$$

where the six elements are defined as

$$\begin{aligned} G_{11} &= h_1^{-1} \omega_1^2 \psi_1^2 + h_2^{-1} (\omega_1 \psi_2 \chi_2 - \omega_2 \chi_1)^2 + h_3^{-1} (\omega_1 \psi_2 \chi_1 + \omega_2 \chi_2)^2, \\ G_{21} &= h_1^{-1} \omega_1 \omega_2 \psi_1^2 + h_2^{-1} (\omega_1 \psi_2 \chi_2 - \omega_2 \chi_1) (\omega_2 \psi_2 \chi_2 + \omega_1 \chi_1) \\ &\quad + h_3^{-1} (\omega_2 \psi_2 \chi_1 - \omega_1 \chi_2) (\omega_1 \psi_2 \chi_1 + \omega_2 \chi_2), \\ G_{31} &= -h_1^{-1} \omega_1 \psi_1 \psi_2 + h_2^{-1} \psi_1 \chi_2 (\omega_1 \psi_2 \chi_2 - \omega_2 \chi_1) \\ &\quad + h_3^{-1} \psi_1 \chi_1 (\omega_1 \psi_2 \chi_1 + \omega_2 \chi_2), \\ G_{22} &= h_1^{-1} \omega_2^2 \psi_1^2 + h_2^{-1} (\omega_2 \psi_2 \chi_2 + \omega_1 \chi_1)^2 + h_3^{-1} (\omega_2 \psi_2 \chi_1 - \omega_1 \chi_2)^2, \\ G_{32} &= -h_1^{-1} \omega_2 \psi_1 \psi_2 + h_2^{-1} \psi_1 \chi_2 (\omega_2 \psi_2 \chi_2 + \omega_1 \chi_1) \\ &\quad + h_3^{-1} \psi_1 \chi_1 (\omega_2 \psi_2 \chi_1 - \omega_1 \chi_2), \\ G_{33} &= h_1^{-1} \psi_2^2 + h_2^{-1} \psi_1^2 \chi_2^2 + h_3^{-1} \psi_1^2 \chi_1^2. \end{aligned} \quad (21)$$

Here, for a angle a ($a = \omega, \psi$ or χ), $a_1 = \cos a$ and $a_2 = \sin a$. When $\omega = \psi = \chi = 0$,

$$\mathbf{G} = \begin{pmatrix} h_1^{-1} & 0 & 0 \\ 0 & h_2^{-1} & 0 \\ 0 & 0 & h_3^{-1} \end{pmatrix}. \quad (22)$$

Clearly, SPH can be considered as a special case of ASPH with $h_1 = h_2 = h_3 = h$ and $\omega = \psi = \chi = 0$. Tensor \mathbf{G} is only needed to be calculated once. After \mathbf{G} is initialized, the kernel expressions are accordingly determined.

2.3. Kernel function with anisotropic smoothing

In the following cases, we use the Wendland kernel function and its first derivative which can be further written to match the anisotropic ellipsoidal smoothing kernel as

$$W^{v-D}(\eta) = A^{v-D} \begin{cases} (1 - \frac{\eta}{2})^4 (1 + 2\eta), & 0 \leq \eta \leq 2 \\ 0, & \eta > 2 \end{cases} \quad (23)$$

$$\nabla W^{v-D}(\eta) = A^{v-D} \mathbf{G} \frac{\eta}{\eta} \begin{cases} -5\eta(1 - \frac{\eta}{2})^3, & 0 \leq \eta \leq 2 \\ 0, & \eta > 2 \end{cases} \quad (24)$$

$$\frac{\partial W^{v-D}(\eta)}{\partial \eta} = A^{v-D} \left\| \frac{\mathbf{G}\eta}{\eta} \right\| \begin{cases} -5\eta(1 - \frac{\eta}{2})^3, & 0 \leq \eta \leq 2 \\ 0, & \eta > 2 \end{cases} \quad (25)$$

where v means the dimension and

$$A^{1-D} = \frac{3}{4} \|\mathbf{G}\|, \quad A^{2-D} = \frac{7}{4\pi} \|\mathbf{G}\|, \quad A^{3-D} = \frac{21}{16\pi} \|\mathbf{G}\|. \quad (26)$$

Benefiting from the tensor \mathbf{G} , the displacement between two particles is mapped to the generalized position vector η , the norm of which is compared with the cutoff radius to calculate the kernel function and kernel gradient value. Using normalized position vector η rather than \mathbf{r}/h in the discretization of quantities, the expression of dynamic equations in SPH and ASPH are identical.

2.4. Anisotropic resolution and support domain

Considering a thin structure with a high aspect ratio of length and thickness $R = l/d$, showing in Fig. 2(b), with an isotropic SPH discretization drafted in Fig. 2(a) (a cross section is used for an example), there is a minimal neighboring particle number in each direction to guarantee the numerical accuracy, and thus a large R would lead to a large amount of particles, increasing the computation efforts. Therefore, an anisotropic arrangement $dp_x \neq dp_y \neq dp_z$ is required to reduce the total particle number, as depicted in Fig. 2(c).

As for the definition of neighboring particles, in standard SPH with a scalar smoothing length h , the influence area of any given particle is typically represented by a sphere with a radius r , where usually $2h \leq r \leq 3h$. However, in a simulation adopting the anisotropic resolution, a sphere influence domain sampling isotropic interpolation

may result in either an excessive or insufficient coverage of neighboring particles, depending on the magnitude of the smoothing length h . This issue is illustrated in Fig. 3, focusing on a two-dimensional scenario. In the ASPH method, the conventional spherical support domain is substituted with an ellipsoidal shape in three-dimensional simulations or an ellipse in two-dimensional contexts. These shapes allow for different smoothing lengths to be applied along each axis, as depicted in Fig. 4. Furthermore, to match curved structures accurately, the support domain has to be rotated in ASPH simulations, as revealed in Fig. 4(b), which means the transform tensor \mathbf{G} varies on each particle, resulting in individually defined kernel functions.

3. ASPH discretization

3.1. Correction of the derivatives

To discretize the solid mechanics, we employ the initial undeformed configuration as the reference. First, aiming to restore 1st-order consistency, the configuration of particle i is corrected with a tensor \mathbf{B} in the total Lagrangian formalism, expressed as [43,44]

$$\mathbf{F}_i^0 = \left(\sum_j V_j (\mathbf{r}_j^0 - \mathbf{r}_i^0) \otimes \nabla_i^0 W_{ij} \right) \mathbf{B}_i^0 = \mathbf{I}, \quad (27)$$

where \mathbf{r}_i^0 and \mathbf{r}_j^0 denote the positions of particles i and j in the reference configuration. Equivalently,

$$\mathbf{I} = \sum_j V_j (\mathbf{r}_j^0 - \mathbf{r}_i^0) \otimes (\nabla_i^{0T} W_{ij} \mathbf{B}_i^0) = \sum_j V_j (\mathbf{r}_j^0 - \mathbf{r}_i^0) \otimes (\mathbf{B}_i^{0T} \nabla_i^0 W_{ij})^T. \quad (28)$$

The gradient correction \mathbf{B} is operated over ∇^0 to correct the kernel. We define

$$\tilde{\nabla}^0 = \mathbf{B}_i^{0T} \nabla^0, \quad (29)$$

where the symbol $\tilde{\nabla}_i^0$ represents the corrected approximation of the differential operator with respect to the initial material coordinates. From Eq. (27), involving the tensor \mathbf{G} , the correction matrix \mathbf{B}^0 of particle i in ASPH can be consequently calculated as:

$$\begin{aligned} \mathbf{B}_i^0 &= \left(\sum_j V_j (\mathbf{r}_j^0 - \mathbf{r}_i^0) \otimes \nabla_i^0 W_{ij} \right)^{-1} \\ &= \left(\sum_j V_j (\mathbf{r}_j^0 - \mathbf{r}_i^0) \otimes (\mathbf{G}_i \frac{\eta_{ij}}{\eta_{ij}} \frac{\partial W}{\partial \eta_{ij}}) \right)^{-1}. \end{aligned} \quad (30)$$

In total Lagrangian formulation, the neighborhood of particle i is defined in the initial configuration, and this set of neighboring particles remains fixed throughout the entire simulation. Therefore, \mathbf{B}_i^0 is computed only once under the initial reference configuration.

3.2. Corrected governing equations discretization

Considering the kernel correction, the momentum conservation in Eq. (2) can be approximated in the weak form as

$$\frac{d\mathbf{v}_i}{dt} = \frac{2}{\rho_i} \sum_j V_j \tilde{\mathbf{P}}_{ij} \nabla_i^0 W_{ij}, \quad (31)$$

where ρ_i represents the density of particle i , $\tilde{\mathbf{P}}_{ij}$ is the averaged first Piola–Kirchhoff stress of the particle pair (i, j) , and to keep the conservative of particles, the correction matrix \mathbf{B}^{0T} is performed on each particle, thus $\tilde{\mathbf{P}}_{ij}$ is stated as

$$\tilde{\mathbf{P}}_{ij} = \frac{1}{2} (\mathbf{P}_i \mathbf{B}_i^{0T} + \mathbf{P}_j \mathbf{B}_j^{0T}). \quad (32)$$

Note that in the anisotropic algorithm, considering the unsymmetrical smoothing kernel in different directions, \mathbf{B}^{0T} instead of \mathbf{B}^0 is conducted on the kernel gradient operation.

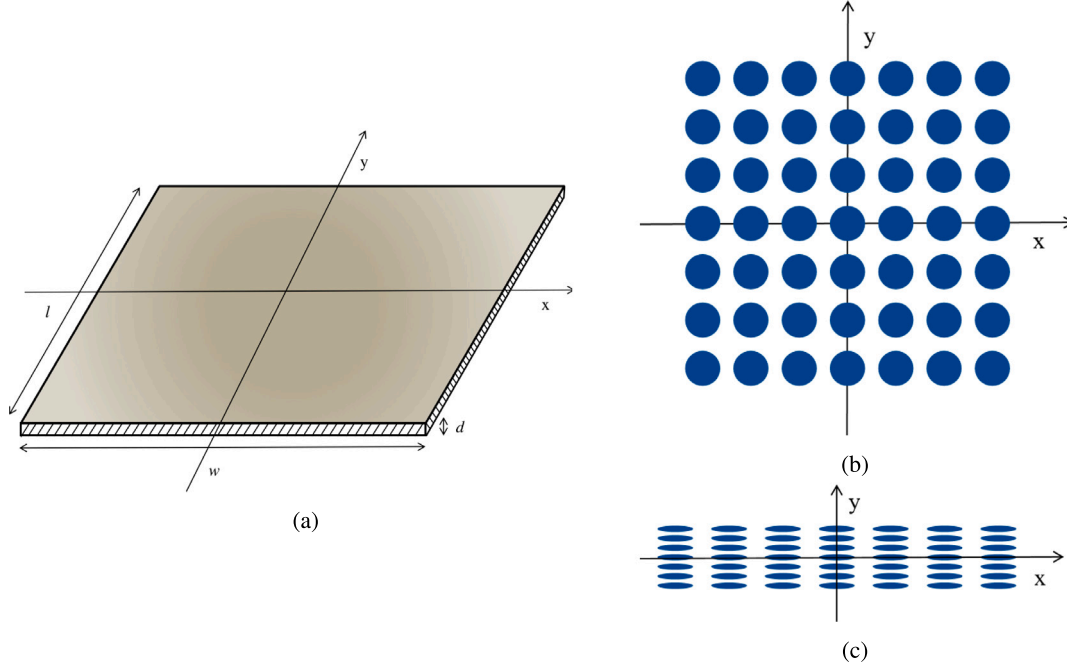


Fig. 2. Schematic view of a thin structure (a), isotropic resolution (b), anisotropic resolution (c).

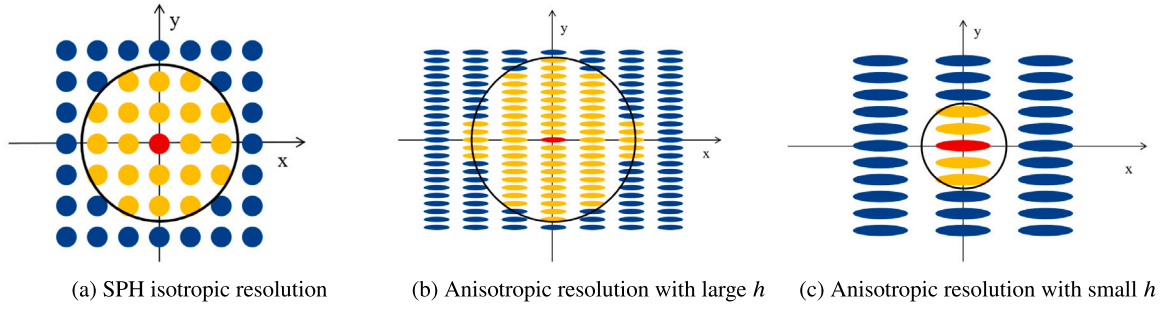


Fig. 3. Isotropic and anisotropic resolutions with large and small kernel smoothing length \$h\$ in SPH.

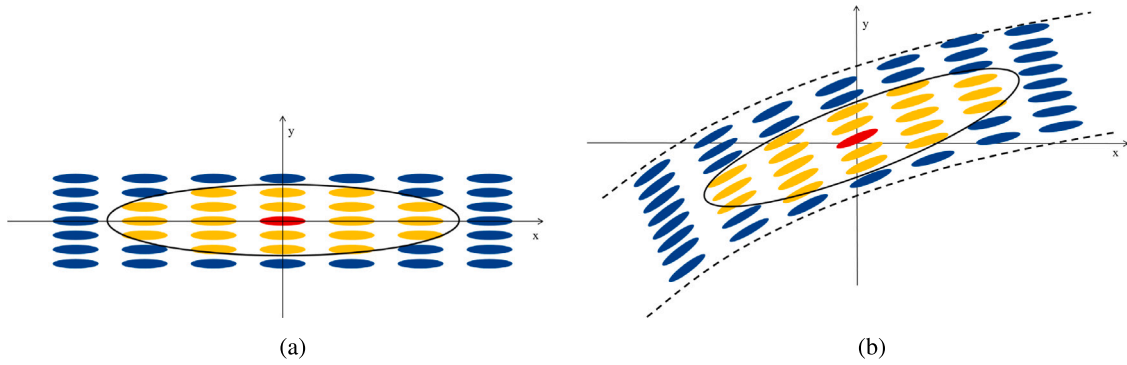


Fig. 4. Elliptical smoothing kernel (a) and rotated elliptical smoothing kernel (b) with an anisotropic discretization.

The first Piola–Kirchhoff stress tensor is dependent on the deformation tensor \mathbf{F} , referring to Eq. (27), the time derivative of which is computed from

$$\frac{d\mathbf{F}_i}{dt} = \left(\sum_j V_j (\mathbf{v}_j - \mathbf{v}_i) \otimes \nabla_i^0 W_{ij} \right) \mathbf{B}_i^0. \quad (33)$$

Referring to the work of Español and Revenga [45], the discretized form of the fluid diffusion equation Eq. (8), within the \mathbf{r} coordinate system

can be expressed as follows:

$$(\nabla^2 c)_r = 2D \int \frac{[c(\mathbf{r}) - c(\mathbf{r}')]}{r} \frac{\partial W(\mathbf{r})}{\partial r} d\mathbf{r} + \mathcal{O}(h^2). \quad (34)$$

Following the methodology of Tran-Duc et al. [46], upon implementing the coordinate transformation $\mathbf{r} = \mathbf{G}^{-1}\boldsymbol{\eta}$, the relationship between the weight functions $W(\boldsymbol{\eta})$ and $W(\mathbf{r})$ is given by

$$W(\mathbf{r}) = \frac{1}{\|\mathbf{G}^{-1}\|} W(\boldsymbol{\eta}), \quad (35)$$

and

$$r = \eta \| \mathbf{G}^{-1} \mathbf{e}_\eta \|, \quad (36)$$

with $\mathbf{e}_\eta = \boldsymbol{\eta}/\eta$ being the unit vector. Utilizing Eqs. (35) and (36), we obtain

$$\begin{aligned} \frac{\partial W(\mathbf{r})}{\partial r} &= \frac{1}{\| \mathbf{G}^{-1} \|} \frac{\partial W(\boldsymbol{\eta})}{\partial \boldsymbol{\eta}} \frac{\partial \boldsymbol{\eta}}{\partial r} \\ &= \frac{1}{\| \mathbf{G}^{-1} \|} \frac{1}{\| \mathbf{G}^{-1} \mathbf{e}_\eta \|} \frac{\partial W(\boldsymbol{\eta})}{\partial \boldsymbol{\eta}}. \end{aligned} \quad (37)$$

Consequently, considering $d\mathbf{r} = \| \mathbf{G}^{-1} \| d\boldsymbol{\eta}$, Eq. (34) can be reformulated in the transformed $\boldsymbol{\eta}$ coordinates systems as

$$\nabla^2 c = 2 \int \frac{[c(\boldsymbol{\eta}) - c(\boldsymbol{\eta}')] }{\eta \| \mathbf{G}^{-1} \mathbf{e}_\eta \|^2} \frac{\partial W}{\partial \boldsymbol{\eta}} d\boldsymbol{\eta} + \mathcal{O}(h^2). \quad (38)$$

Eq. (38) can be discretized using a particle approximation, yielding

$$(\nabla^2 c)_i = 2 \sum_j V_j \frac{c_{ij}}{\eta_{ij} \| \mathbf{G}^{-1} \mathbf{e}_{ij} \|^2} \frac{\partial W}{\partial \eta_{ij}}, \quad (39)$$

where $c_i - c_j$ denotes the saturation difference of particles i and j , $\mathbf{e}_{ij} = \boldsymbol{\eta}_{ij}/\eta_{ij}$, with $\eta_{ij} = \| \boldsymbol{\eta}_i - \boldsymbol{\eta}_j \|$ being the normalized distance.

4. Numerical examples

In this section, we apply this anisotropic kernel algorithm into different cases to test the accuracy and efficiency. Firstly, we use the two dimensional oscillating beam with different anisotropic resolutions and corresponding kernel feature to test the accuracy and validate the convergence. Secondly, we simulate the deformation of two and three dimensional flat thin plate to test the efficiency and compare the results with those from SPH method. Then, we apply the anisotropic kernel with rotation tensor to simulate the deformation of two dimensional curved shell and three dimensional curved thin roof. Finally, the fluid–structure interaction membrane is simulated to show the specific application of ASPH method. In all cases, simulation using SPH method are carried out for result comparisons. We apply $h_2 = 1.15d_p$ and $h_1 = rh_2$ with d_p being the particle spacing in the thickness direction.


4.1. Oscillating beam

For the first example, we consider a thin oscillating plate, which has been previously analyzed both theoretically [47] and numerically [48, 49] in the literature. A planar beam is modeled with one edge fixed by layers of particles, allowing the body to bend freely. This beam has a length of $L = 0.2$ m, perpendicular to the fixed edge, and thickness $H = 0.02$ m. With the length edge of plate aligned parallel to the x -axis, the end of this beam is subjected to a initial velocity profile defined as $v_y(x) = V_f \frac{F(x)}{F(L)} c_0$, where the constant $V_f = 0.05$ m/s, and

$$\begin{aligned} F(x) &= (\cos kL + \cosh kL)(\cosh kx - \cos kx) \\ &\quad + (\sin kL - \sinh kL)(\sinh kx - \sin kx), \end{aligned} \quad (40)$$

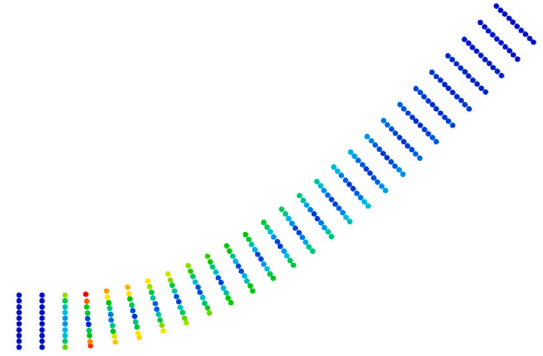
where k is the wave number, related with L as $kL = 1.875$. The plate properties are taken as Young's modulus $E = 2.0$ MPa, density $\rho = 1000.0$ kg/m³, Poisson ratio $\nu = 0.3975$. In this simulation, the particle spacing along the x -axis (dp_x) and y -axis (dp_y) is uniformly set at $dp_x = dp_y = 0.002$ m in SPH method. In ASPH approach, we define an anisotropic ratio $r = dp_x/dp_y$ to characterize the anisotropic resolution and the particle volume is expressed by $dp_x dp_y$. The simulation of the oscillating beam is conducted by using both the standard SPH algorithm and ASPH with varying anisotropic kernel function ratios corresponding to different r values to ensure the neighboring particle number remains consistent across different scenarios.

Using the ASPH method with anisotropic ratio $r = 4.0$, particle number in y direction (the vertical direction) $N_y = 10$, Fig. 5 illustrates snapshots of the beam deformation colored by von Mises strain at

von Mises strain 
0.02 0.04 0.06 0.08



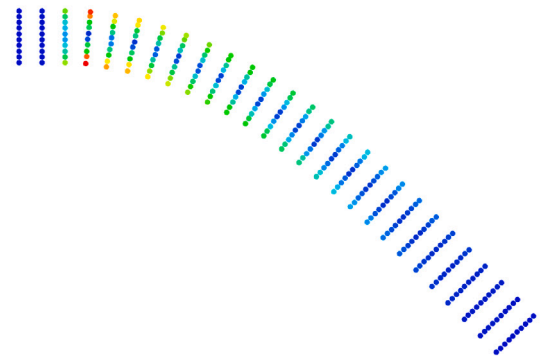
(a) ASPH method, $N_y = 10$, $r = 4.0$, time = 0 s



(b) ASPH method, $N_y = 10$, $r = 4.0$, time = 0.06 s



(c) ASPH method, $N_y = 10$, $r = 4.0$, time = 0.12 s



(d) ASPH method, $N_y = 10$, $r = 4.0$, time = 0.2 s

Fig. 5. 2D oscillating beam: the deformation colored by von Mises strain at different time instants within the first oscillation period using ASPH with anisotropic ratio $r = 4.0$, $N_y = 10$.

different time instances within the first oscillation period. Fig. 6 shows the deformed configuration colored by von Mises strain when time = 1.0 s using SPH and ASPH methods with different anisotropic ratios $r = 2.0, 4.0, 8.0$. Clearly, the contours exhibit consistent deformation

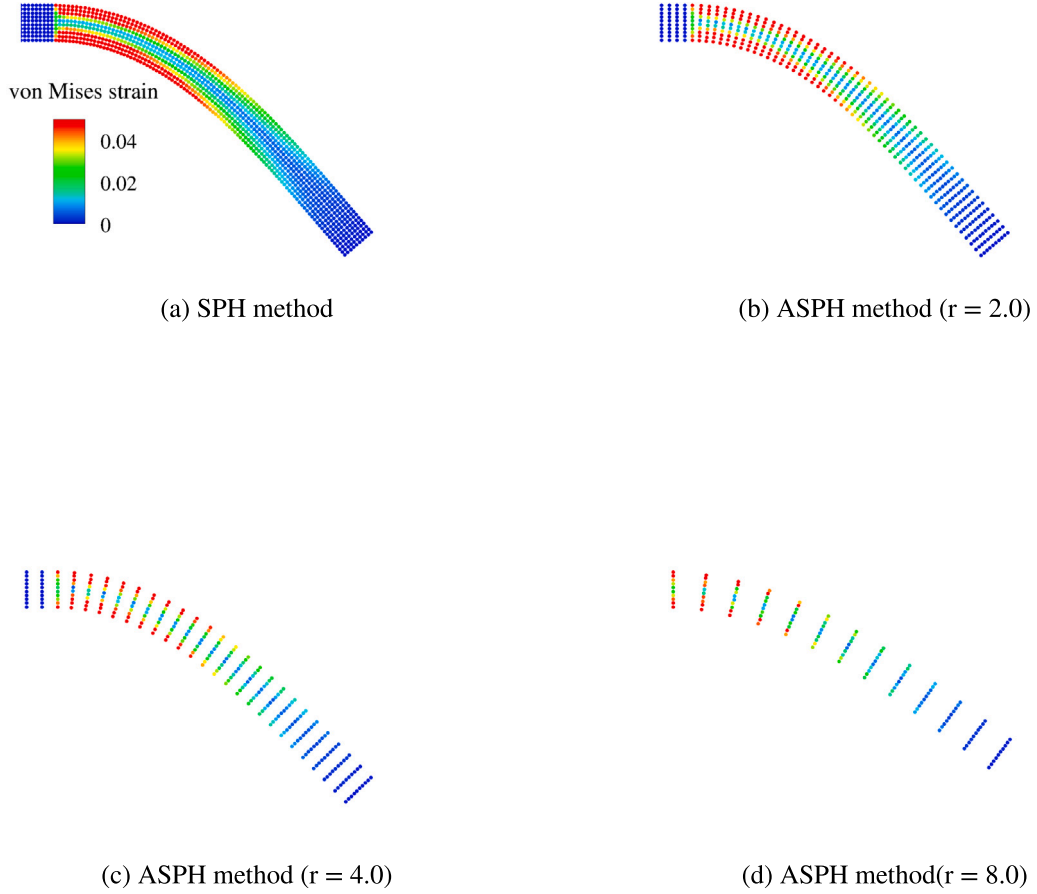


Fig. 6. 2D oscillating beam: the deformation colored by von Mises strain at $t = 1.0$ s from SPH and ASPH with different anisotropic ratios.

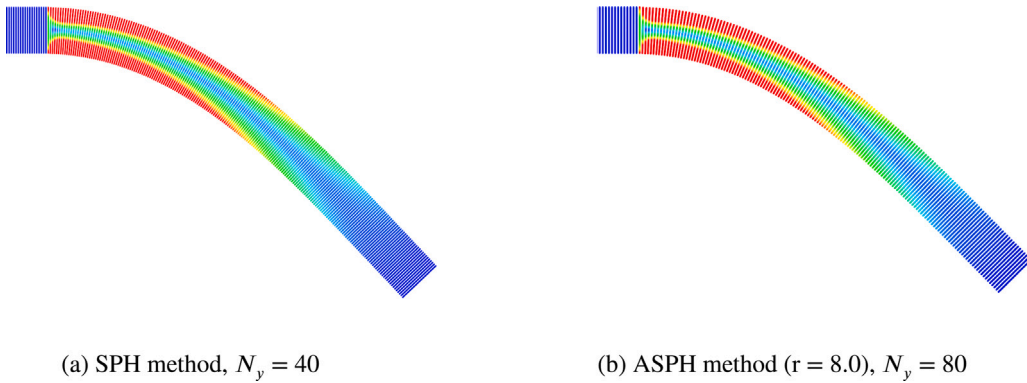


Fig. 7. 2D oscillating beam: the von Mises strain contours at $t = 1.0$ s from SPH and ASPH ($r = 8.0$) with high resolutions.

patterns and stress distributions across both methods, regardless of the anisotropic ratios. To test the accuracy, the convergence tests are performed. We increase the resolution to $N_y = 40$ when using SPH and $N_y = 80$ for ASPH with anisotropic ratio $r = 8.0$. The resultant results revealing the von Mises strain contours at time $t = 1.0$ s is represented in Fig. 7, illustrating a closely matched deformation pattern. Taking the anisotropic ratio $r = 4.0$ and $r = 8.0$ as examples, we maintain r constant while varying the total particle with four different particle distribution densities $N_y = H/dp_y = 10$, $N_y = H/dp_y = 20$, $N_y = H/dp_y = 40$, and $N_y = H/dp_y = 60$ with $dp_x = 4dp_y$ and another four different resolutions with $r = 8.0$, $dp_x = 8dp_y$. Fig. 8 plots the vertical displacement of the midpoint at the end of this beam as a function of time. With increasing particle density, the disparity in the amplitude and frequency of the oscillations between different

resolutions diminishes rapidly, indicating a convergence pattern with both two ratios. The converged results obtained from SPH and ASPH with r being 4.0 and 8.0 respectively are presented in Fig. 9. Three sets of results are visually indistinguishable in both the horizontal and vertical displacement of the midpoint at the beam end, validating the reliability of the ASPH method. To assess the accuracy and efficiency of this ASPH method quantitatively, cases with $N_y = 20$ applying various anisotropic ratios are investigated. A comparison of the particle number N , the first oscillation period T , computation time t as well as the difference of T between two methods is presented in Table 1. Evidently, pronounced computation time is saved while maintaining convergence. For instance, with an anisotropic ratio $r = 4$, the particle number is reduced to a quarter of that in SPH algorithm, but the difference is merely 0.022%, nearly negligible.

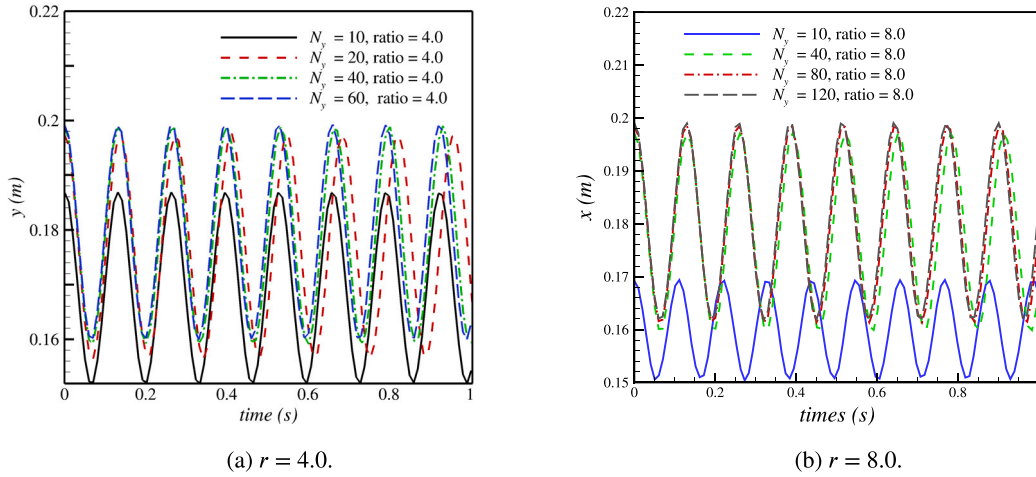


Fig. 8. 2D oscillating beam: convergence test of different particle spacing with different anisotropic ratios.

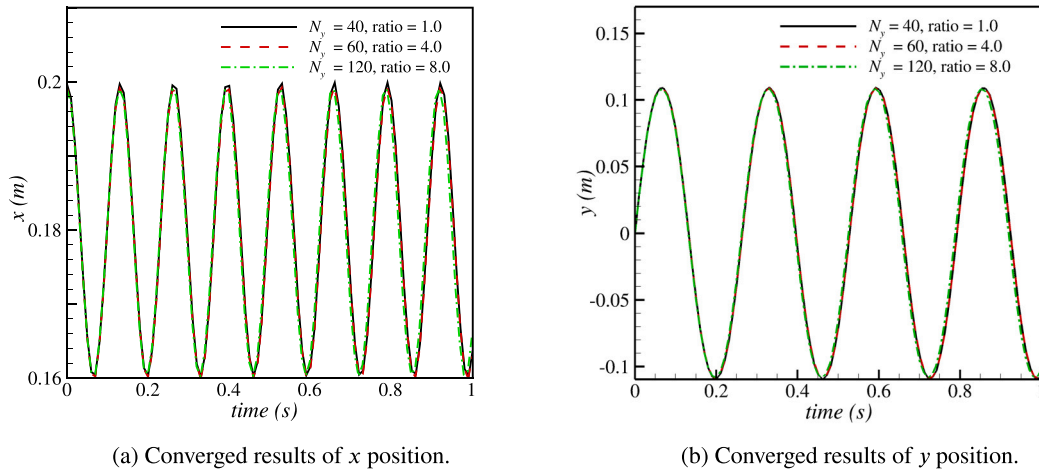


Fig. 9. 2D oscillating beam: comparisons of the converged result obtained from SPH and the present ASPH method with different anisotropic ratios.

Table 1

2D oscillating beam: quantitative comparison of the accuracy and efficiency of this present ASPH algorithm with different anisotropic ratios.

Method	N	t (s)	Time saved	T	Difference
SPH	4400	111.59	—	0.2718	—
ASPH ratio = 2.0	2200	56.21	49.63%	0.2718	0.0%
ASPH ratio = 4.0	1100	30.65	72.53%	0.2726	0.022%
ASPH ratio = 8.0	540	18.21	83.68%	0.2522	0.053%

4.2. 2D thin flat plate

In this section, a thin flat plate with length being $L = 508$ mm, width $W = 25.4$ mm is considered. A neo-Hookean material with Young's modulus $E = 53779.1$ MPa, density $\rho = 1600.0$ kg/m³, Poisson ratio $\nu = 0.3$ is employed for this structure. This plate is subjected to a uniform upward pressure $p = 0.01E$ with both sides constrained, implying zero displacement ($u_x = u_y = 0$) along all edges. To show the time evolution of the deformation, this plate is modeled using the proposed ASPH method with anisotropic ratio = 4.0, $N_y = 10$, i.e., $dp_x = 4 dp_y = 4 W/N_y$. The physical simulation time is 0.8s. The simulated deformation evolution is illustrated in Fig. 10, illustrating the upward bending of the plate under the applied load. A consistent trend is observed across different configurations. Furthermore, we implemented other three computations using the isotropic SPH method and the present ASPH with different ratios corresponding to varying

particle anisotropy. The stable configurations at the final time instants are shown in Fig. 11. It is observed all simulations exhibit similar behavior in terms of strain distribution and deformation pattern.

The nondimensionalized deflection variation of the central point of the plate against time for all simulation condition is depicted in Fig. 12. It is observed that the position of the center point remains consistent across all anisotropic ratios. Notably, compared to the SPH solution, the present ASPH method yields results of good quality, demonstrating both accuracy and high efficiency.

4.3. 3D thin flat plate

Similarly, a 3D thin flat plate with equal length and width dimensions of $L = W = 508$ mm, and a thickness of $H = 25.4$ mm, is simulated to assess the performance of the ASPH method. The same material model as the one used in the 2D plate simulation is employed, with identical parameter values. with all edges constrained by layers of particles $u_x = u_y = u_z = 0$, an upward pressure load is applied to this flat plate uniformly. Clearly, a large ratio of the length versus thickness necessitates a substantial number of particles if an isotropic particle spacing is applied. Under the upward pressure load, the final deformation configurations colored by von Mises strain, simulated using both SPH method and ASPH with anisotropic resolutions, are illustrated in Fig. 13. The particle number in the z direction is set as $N_z = 10$, with $dp_x = dp_y = r dp_z = r H/N_z$, and anisotropic ratio r is varied

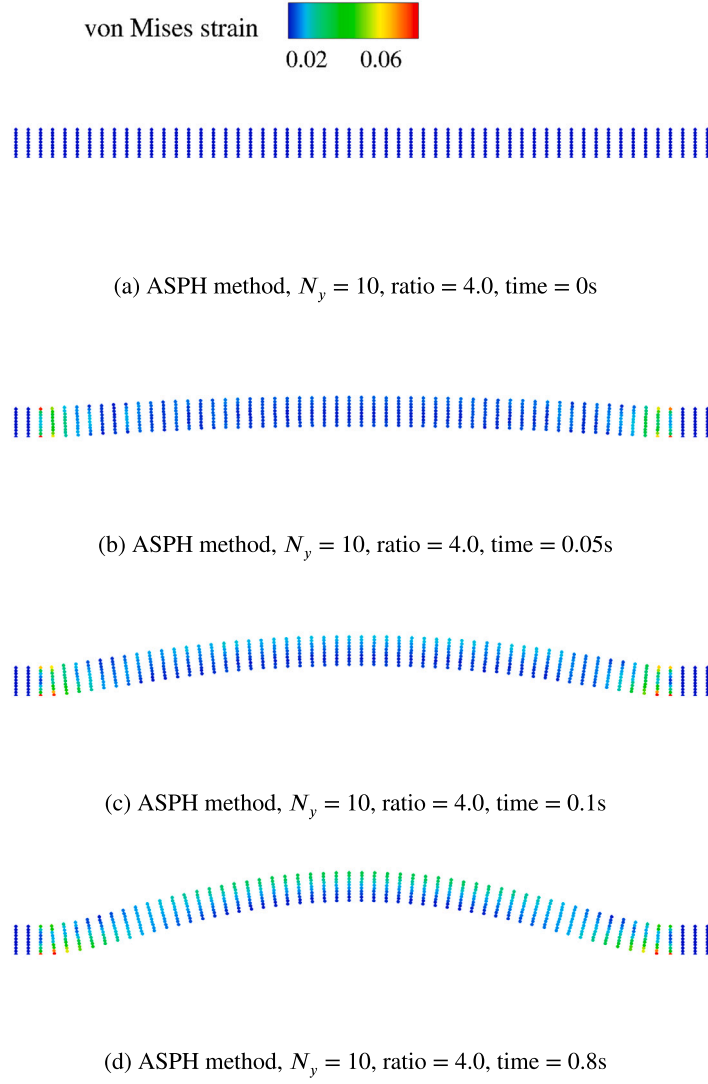


Fig. 10. 2D plate: the deformation colored by von Mises strain at different time instants under the pull force using ASPH with anisotropic ratio = 4.0, $N_y = 10$.

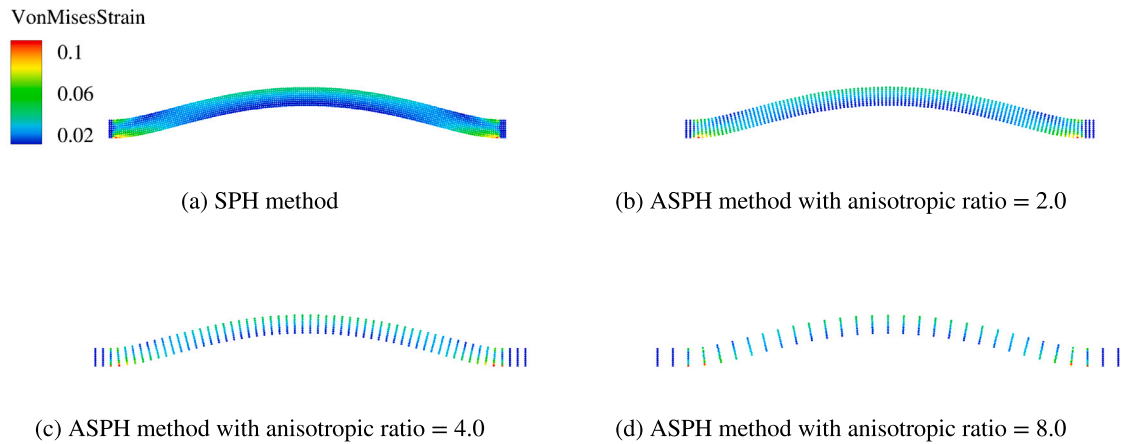


Fig. 11. 2D thin plate: the deformation at the final time instant colored by von Mises strain from SPH and ASPH with different anisotropic ratios.

as $r = 2.0$, $r = 4.0$ and $r = 8.0$, respectively. Similarly strain distribution and deformation patterns are observed across all four cases.

To facilitate a more clear observation, the time histories of the nondimensionalized displacement in the z direction at the center of the plate for various ASPH anisotropic ratios are depicted in Fig. 14.

With consistent load values and boundary conditions, the lines representing SPH and ASPH results coincide at the latter stage of simulation, i.e., the final stable results converge to the same value after slight fluctuations. Table 2 concludes the specific results values from these four cases including the particle number N , computation time t as well

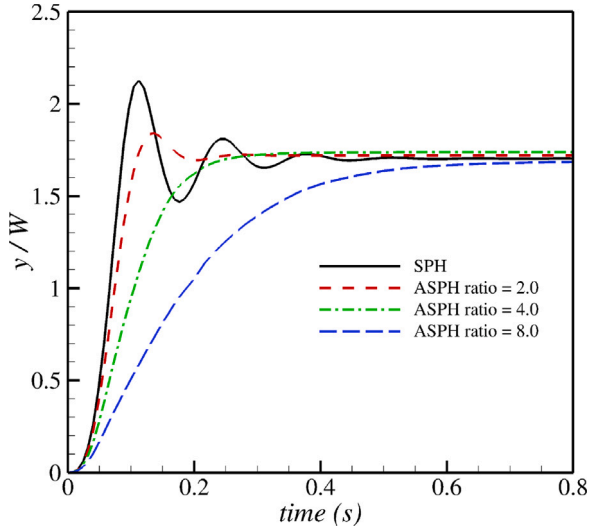


Fig. 12. 2D thin plate: the nondimensionalized y position of the very center point of the beam, from SPH and ASPH with different anisotropic ratios.

Table 2

3D thin flat plate: quantitative comparison of the accuracy and efficiency of this present ASPH algorithm with different anisotropic ratios.

Method	N	t (s)	Time saved	z/H	Difference
SPH	428 490	2366.97	–	3.314	–
ASPH ratio = 2.0	114 490	630.13	73.38%	3.338	0.75%
ASPH ratio = 4.0	32 490	230.61	90.26%	3.343	0.85%
ASPH ratio = 8.0	10 240	94.69	96.0%	3.320	0.18%

as the difference of the nondimensionalized deflection in the z direction compared with the SPH method. From this table, it can be inferred that the anisotropic kernel algorithm reduces both the number of particles and the computational time. Despite small deviations existing among different ASPH ratios, the results from ASPH are all very close to those from SPH method, with the difference no exceeding 2%, while achieving notable time savings.

4.4. 2D shell

Aiming to demonstrate the applicability of this ASPH method to curing structures, another test involving a 2D section of a cylindrical shell which is degenerated from a 3D roof, is simulated. The shell has a radius of $R = 100$ m and the angle from the left edge to the right edge of $\alpha = 20^\circ$, resulting in an arc length of $L = \alpha R = 34.88$ m, while the thickness $H = 1$ m, meaning the aspect ratio of length versus thickness is 34.88. Employing an elastic material model with Young's modulus $E = 432$ MPa, density $\rho = 36.0$ kg/m³, Poisson ratio $\nu = 0.3$, the shell is subjected to uniform gravity as $p = 144$ KPa, while the side edges are clamped with layers of particles. The particle number in the y direction is set to $N_y = 6$, resulting in a particle spacing of $dp_x = dp_y = H/6$ in SPH and $dp_x = r dp_y$ in ASPH, where $r = 2.0, 4.0$ and 8.0 are considered respectively in this case.

With a simulation time of $t = 0.8$ s, Fig. 15 portrays the initial and finally stable configurations of this shell modeled using both SPH method and ASPH method with anisotropic ratios of $r = 2.0, 4.0$, and 8.0 . Evidently, the deformation pattern obtained from SPH and ASPH exhibit good agreement. With increased resolution, a comparison of von Mises strain contours at the final time step is undertaken, utilizing SPH with $N_y = 12$ and ASPH (with anisotropic ratio $r = 8$) with $N_y = 48$, as depicted in Fig. 16. This comparison reveals a closely matched deformation pattern. Furthermore, considering the temporal evolution of von Mises strain at the end of the shell, derived from SPH and

Table 3

3D roof: quantitative comparison of the accuracy and efficiency of this present ASPH algorithm with different anisotropic ratios.

Method	N	t (s)	Time saved	z/H	Difference
SPH	183 119	7686.64	–	4.137	–
ASPH ratio = 2.0	47 459	2158.19	71.92%	4.236	2.42%
ASPH ratio = 4.0	12 599	551.77	92.82%	4.345	5.03%
ASPH ratio = 8.0	3569	146.82	98.09%	4.396	6.26%

ASPH with the same number of particles in the x -direction, is plotted in Fig. 17, illustrating identical stable solutions. For a quantitative assessment, we present the nondimensionalized vertical displacements of the shell midpoint against time, obtained from two methods with differing r , as shown in Fig. 18(a). Additionally, to validate the accuracy, the converged outcomes from both SPH and ASPH methods with $r = 8$ are illustrated in Fig. 18(b). The outcomes derived from these two methodologies exhibit good agreement, affirming the reliability and robustness of the ASPH approach.

4.5. 3D thin roof

We consider a thin roof having the same physical configuration as the two dimensional shell, consisting of a radius of $R = 100$ m, $\alpha = 20^\circ$ and thickness of $H = 1$ m but in three-dimensional with a width of $W = 20$ m. The same elastic material model as that used in the two-dimensional shell is applied, with Young's modulus $E = 432$ MPa, density $\rho = 36.0$ kg/m³, and Poisson ratio $\nu = 0.3$. In this model, the roof motion is induced by a uniform gravity pressure applied on the whole roof, represented by $p = 144$ kPa, while hinged boundary conditions are applied at the straight edges perpendicular to the y direction. The initial spacing between particles in the z direction is set to $dp_z = H/6 = 0.1667$ m, resulting in a particle spacing of $dp_x = dp_y = dp_z = 0.1667$ m in SPH method. and $dp_x = dp_y = r dp_z$ in ASPH. Similarly, simulations are carried out in four different cases $r = 2.0, 4.0$, and 8.0 .

The initial and finally stable states of the roof under SPH and ASPH with different anisotropic ratios are displayed in Fig. 19. Although quite similar results are observed in both methods, it should be noted that the particle number is significantly reduced by using ASPH method. The accuracy of this ASPH method numerical simulation is typically measured by the nondimensionalized z -displacement of the central point of the roof, plotted in Fig. 20(a). Despite showing different oscillating pattern, the static solutions from four cases are closely converged. With increasing resolution in ASPH ($r = 8$), the difference between results significantly diminishes, as presented in Fig. 20(b). The converged ASPH result ($N_z = 24$) closely aligns with the converged SPH result ($N_z = 9$), affirming the reliability of the ASPH method. Table 3 lists the comparison of different parameters in numerical format. Generally, the results obtained by ASPH method differ from those obtained with the SPH code by between 5% and 10%. The largest discrepancy, yielded by ASPH with anisotropic ratio $r = 8.0$ is typically around 6.26%, which is acceptable considering 98.09% reduction in computation time. With an anisotropic ratio of $r = 2.0$, using ASPH method saves 71.92% of computation time with only a 2.42% difference compared with SPH method. Absolutely, a smaller anisotropic ratio results in a closer solution. Furthermore, the accuracy is expected to improve with an increased resolution.

4.6. 3D thin membrane with internal pressure

In this section, we consider a biological case consisting a thin, porous membrane partially filled with fluid, causing deformation under internal pressure. The membrane is square-shaped with a length and width of $L = W = 2.5$ mm and a thickness of $H = 0.125$ mm, with the boundary sides being constrained to fix it in place. The central part of the membrane is in contact with a fluid droplet occupying

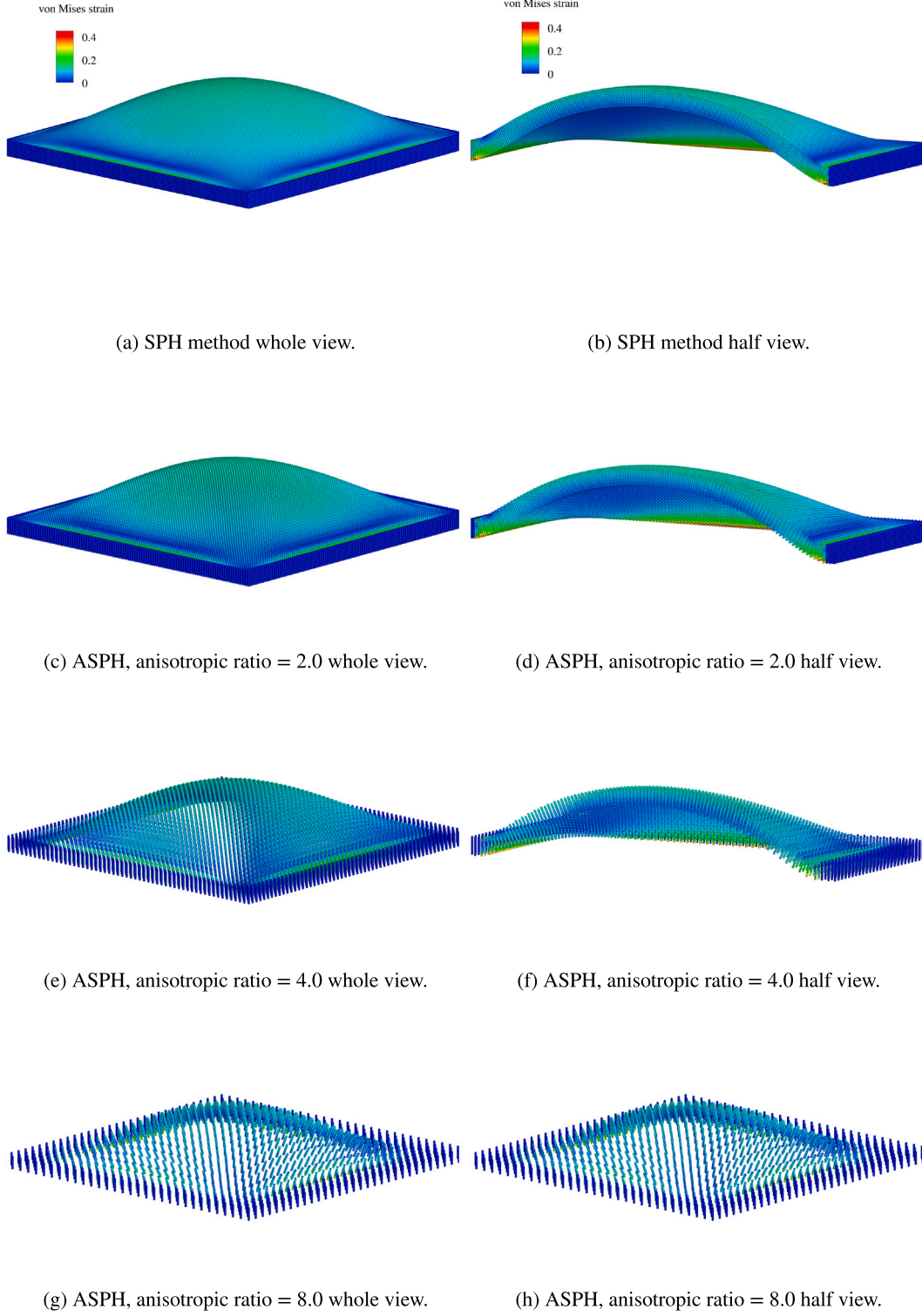


Fig. 13. 3D thin plate: the deformation colored by von Mises strain from SPH and ASPH with different anisotropic ratios.

a circular region with a radius of $R = 0.15L$. To ensure a smooth transition, the fluid saturation c follows a function of $c = c_0 (1 - R^2/R_0^2)$, where $c_0 = 0.4$, and R denotes the distance of particles from the center point of the membrane in $x - y$ plane, yielding to $R < R_0$. Given the thin nature but real thickness of the membrane, we assume the upper half part is filled with fluid. This nonuniform concentration of fluid necessitates fine enough resolution in the thickness direction to

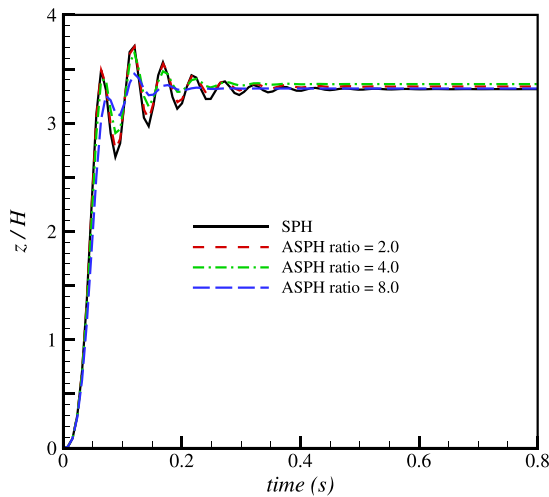
represent this deviation. A shell model with only one layer particle fails to indicate this difference, hence promoting the application of the present ASPH method. The solid material is considered as an elastic Nafion membrane, with water serving as the fluid. The physical properties and material parameters of this membrane are listed in Table 4, obtained from previous research papers [32,33]. In the simulation,

Table 4

Fluid–structure interaction: physical material parameters value of Nafion film.

Source: Data estimated from [32,33].

Parameters	ρ (kg/m ³)	Pressure coefficient C (MPa)	Young modulus (MPa)	Poisson ratio
Value	2000	3.0	8.242	0.2631

**Fig. 14.** 3D thin plate: the nondimensionalized z position of the very center point of the beam, from SPH, ASPH with different anisotropic ratios.

without specific explanation, eight particles are placed in the vertical direction in all cases.

The fluid distribution contour of the membrane using ASPH with an anisotropic ratio of 2.0 is depicted in Fig. 21, outlining the effect area of internal pressure. The finally stable snapshots of this membrane, colored by von Mises strain, obtained using SPH and ASPH with different anisotropic ratios are displayed in Fig. 22. The presence of the fluid droplet in the upper central region generates fluid pressure, as explained in Eq. (7), leading to a localized bending in the central region. The simulations produce quite similar results in all four cases but note that the particle number is remarkably reduced by using ASPH method. The nondimensionalized swelling degree versus time of the very center point of the membrane is plotted in Fig. 23(a). With small ratios, the displacements are closely converged, except for a relatively large deviation when the anisotropic ratio $r = 8.0$. This discrepancy arises because, as r increases, the resolution in the $x-y$ plane decreases when the particle number in the z direction is fixed, resulting in an initially lower fluid saturation, and consequently decreasing internal pressure. When we increase the resolution to 16 particles in the z direction and subsequently increase particle number in $x-y$ plane, it becomes evident that the swelling degree simulated from ASPH with $r = 8.0$ immediately approaches that from $r = 4.0$. Additionally, the converged result obtained from ASPH with anisotropic ratio being 8.0 ($N_z = 24$) corresponds well with the converged result of SPH ($N_z = 16$), as presented in Fig. 23(b), validating the reliability of the ASPH method.

The efficiency of the proposed ASPH is demonstrated through Table 5, which presents a quantitative comparison of the ASPH against the SPH approach in terms of total particle number N , computation time t , nondimensional displacement of the center point in the z direction. The results reveal that employing anisotropic resolution gains a great reduction in computation time, demonstrating a notable improvement in

efficiency with the ASPH approach. Specifically, when the anisotropic $r = 2.0$, the computational time is reduced by 72.14%, with only a 0.49% difference in comparison with the SPH method. The analysis of deflection in the z direction reveals that the maximum discrepancy of the present ASPH model compared to the reference SPH solution is about 34.42% when anisotropic $r = 8.0$, while decreasing 4.05% when $r = 4.0$. This difference is primarily attributed to the inferior resolutions in $x-y$ plane in cases with high r , which fail to adequately represent fluid saturation difference, rather than the error generated by the ASPH method itself.

Considering the diffusion process of the fluid inside this film, obtained from previous research paper [32,33], the diffusion coefficient is set as $1.0 \times 10^{-10} (\text{m}^2/\text{s})$. In this simulation, adopting ASPH method with anisotropic ratio $r = 4.0$, the particle spacing is set as $dp_z = H/6 = 2.083 \times 10^{-2} \text{ mm}$ and $dp_x = dp_y = 4 dp_z$. The fluid saturation and von Mises strain contours at different time instants are depicted in Fig. 24 respectively, showing the variations of the physical parameters in the thickness direction. To be more specific, the variation of fluid saturation and the von Mises strain along the central-vertical line at different time instants are plotted in Fig. 25.

5. Conclusion

By adopting an ASPH method with anisotropic ellipsoidal smoothing kernel coupled with the anisotropic resolution scheme, we have obtained a solution for simulating thin structures with large aspect ratios, particularly for those requiring sufficient resolution in the thickness direction to present quantities deviation, which the reduced-dimensional models fail to capture. By using fewer particles while maintaining 1st-order consistency, the proposed ASPH method demonstrates efficiency and equivalent accuracy compared to traditional full-dimensional SPH methods in both static and dynamic scenarios. Further investigation of this ASPH method for more applications is the subject of future work.

CRediT authorship contribution statement

Xiaojing Tang: Writing – original draft, Resources, Methodology, Investigation, Data curation, Conceptualization. **Dong Wu:** Writing – review & editing, Investigation, Formal analysis. **Zhentong Wang:** Writing – review & editing, Conceptualization. **Oskar Haidn:** Supervision, Resources. **Xiangyu Hu:** Writing – review & editing, Methodology, Conceptualization.

Declaration of competing interest

The authors declare that they have no known competing financial interests or personal relationships that could have appeared to influence the work reported in this paper.

Data availability

No data was used for the research described in the article.

Acknowledgments

Xiaojing Tang was partially supported by the China Scholarship Council (Grant No. 201906120034). Dong Wu was partially supported by the China Scholarship Council (Grant No. 20190613018). Dong Wu and Xiangyu Hu would like to express his gratitude to Deutsche Forschungsgemeinschaft (DFG) for their sponsorship of this research (Grant No. DFG HU1527/12-4).

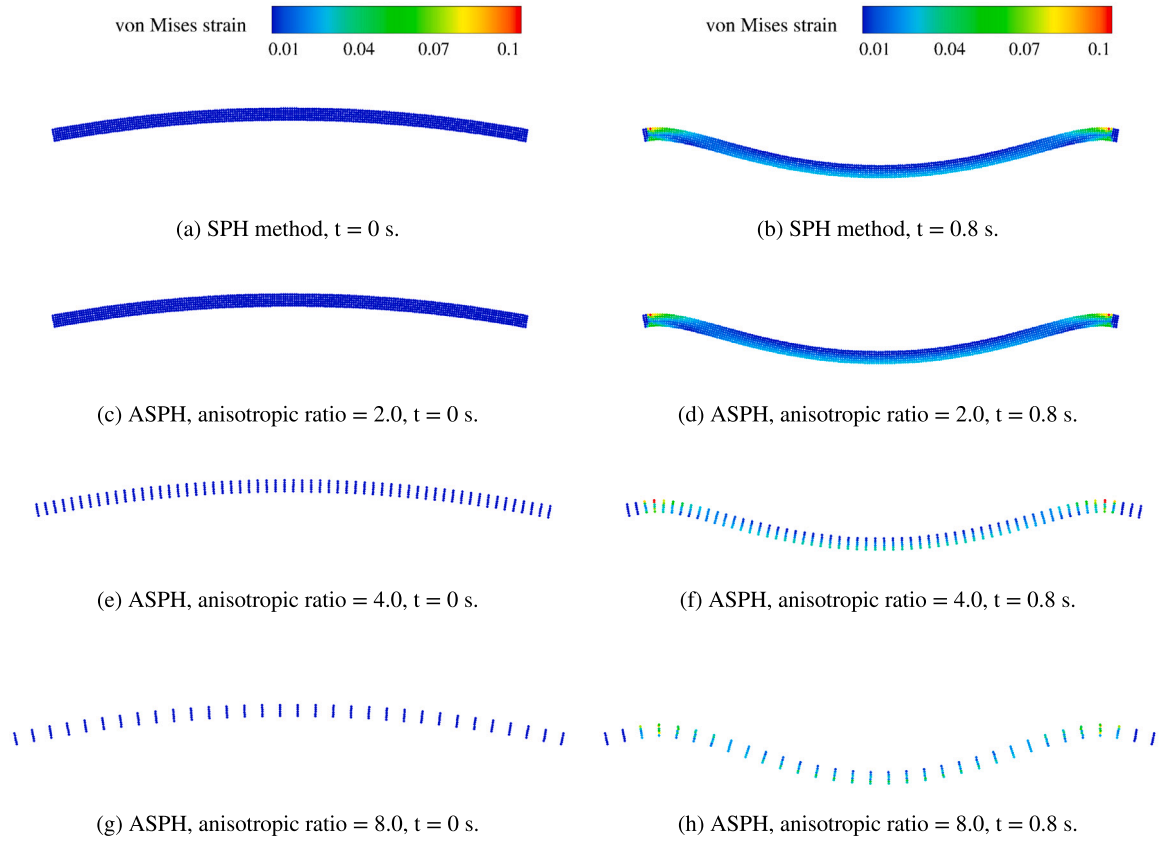


Fig. 15. 2D shell: the deformation colored by von Mises strain from SPH and ASPH with different anisotropic ratios at time = 0 s and time = 0.8 s.

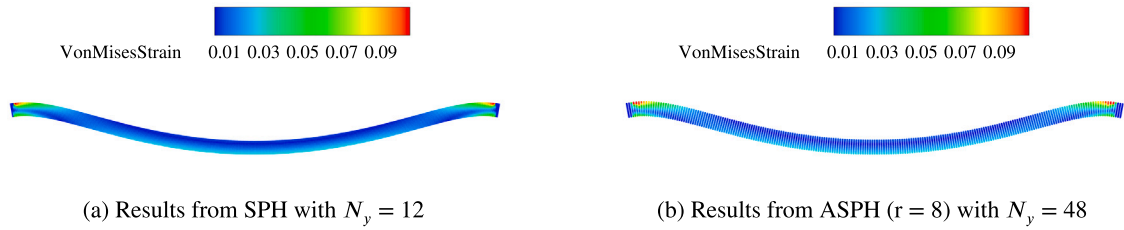


Fig. 16. 2D shell: the comparison of the von Mises strain contours at the final time step yielded by SPH and ASPH.

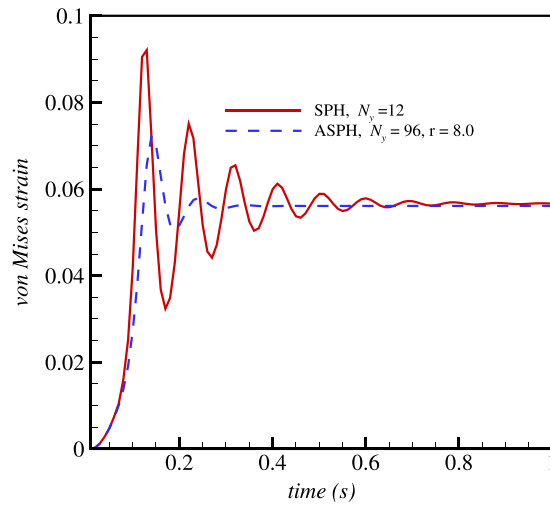


Fig. 17. 2D shell: the time history of von Mises strain at the end of the shell yielded by SPH and ASPH.

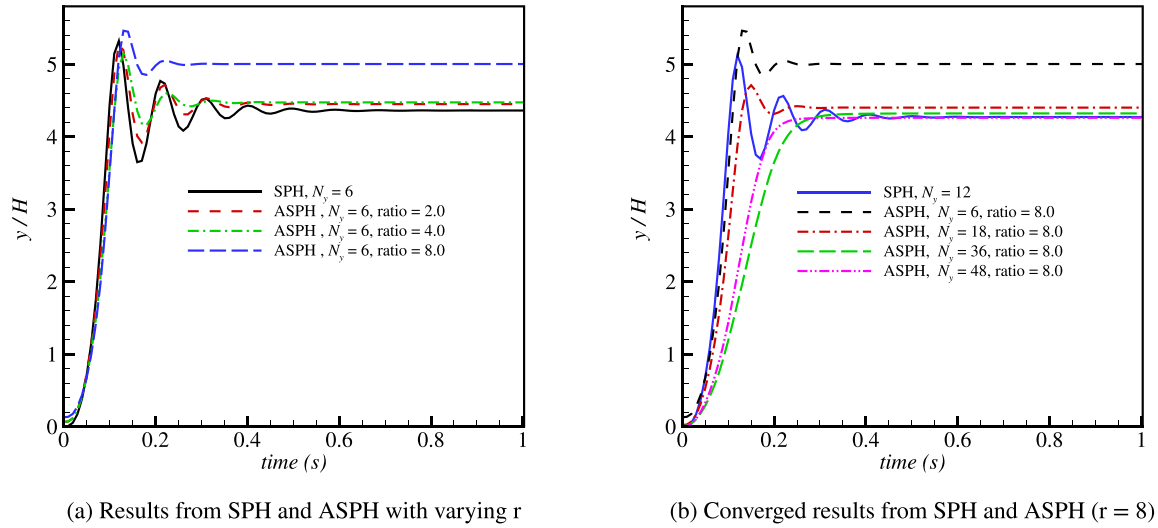


Fig. 18. 2D shell: the comparison of the nondimensionalized y displacement of the very center point of the curved shell.

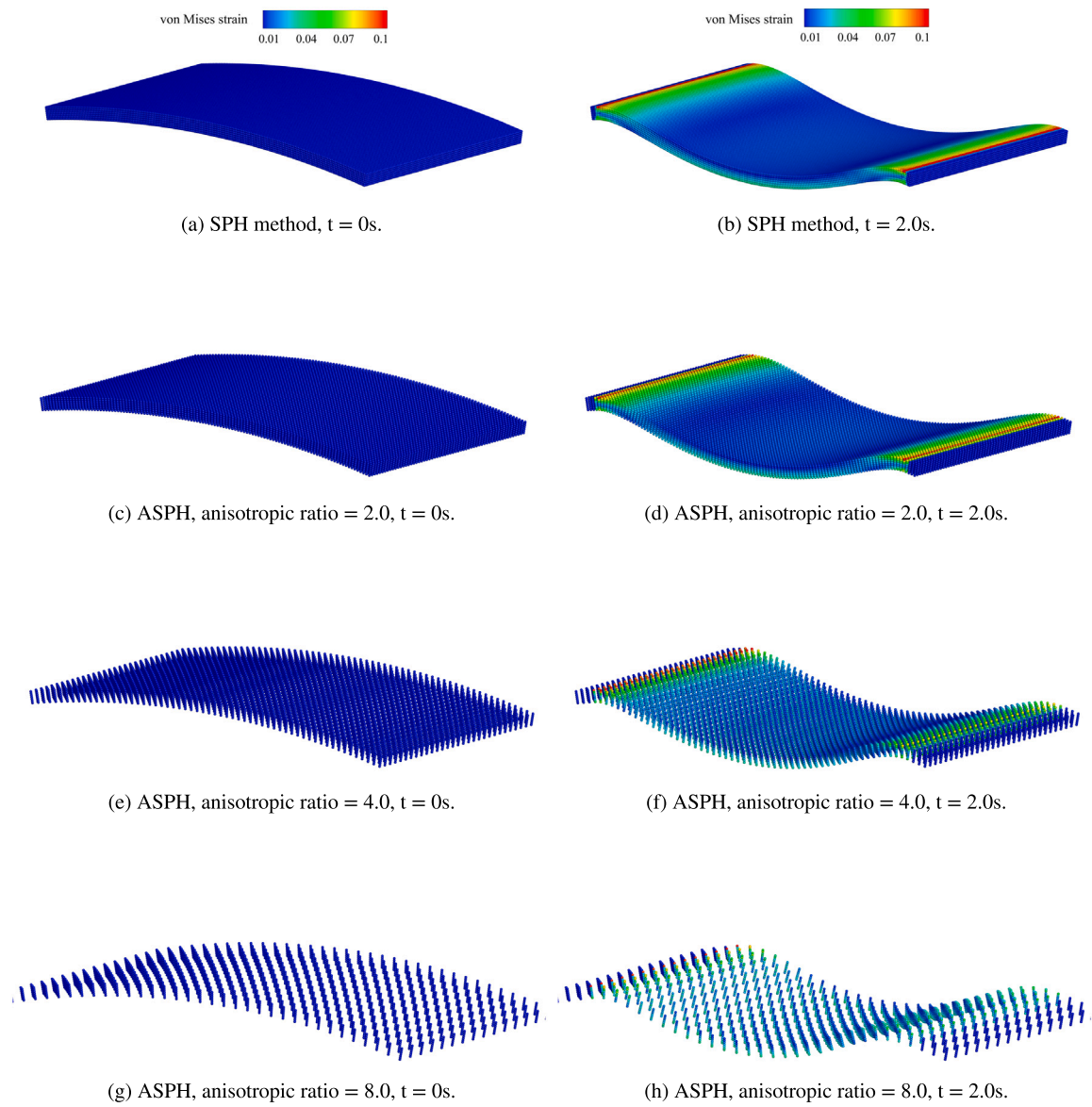
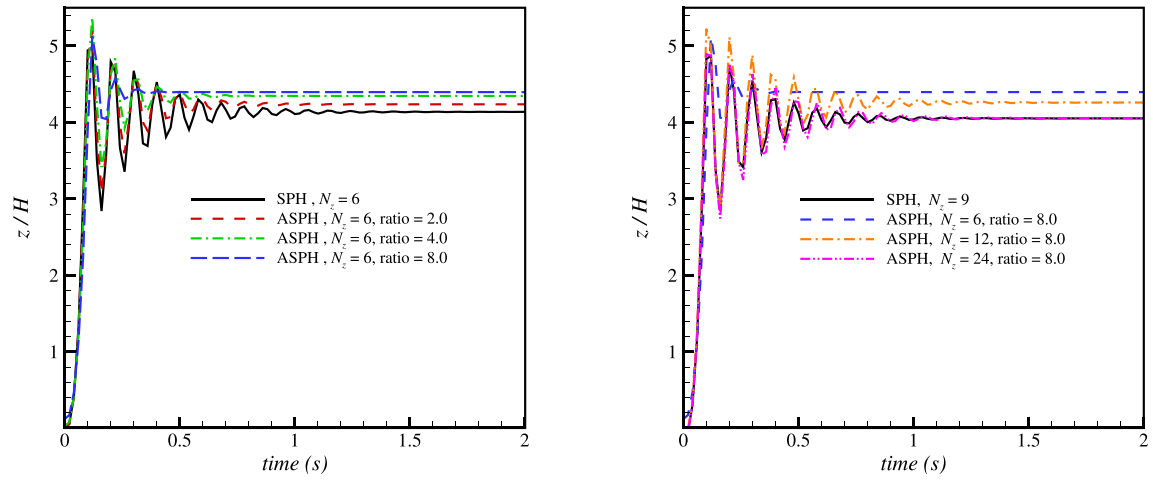
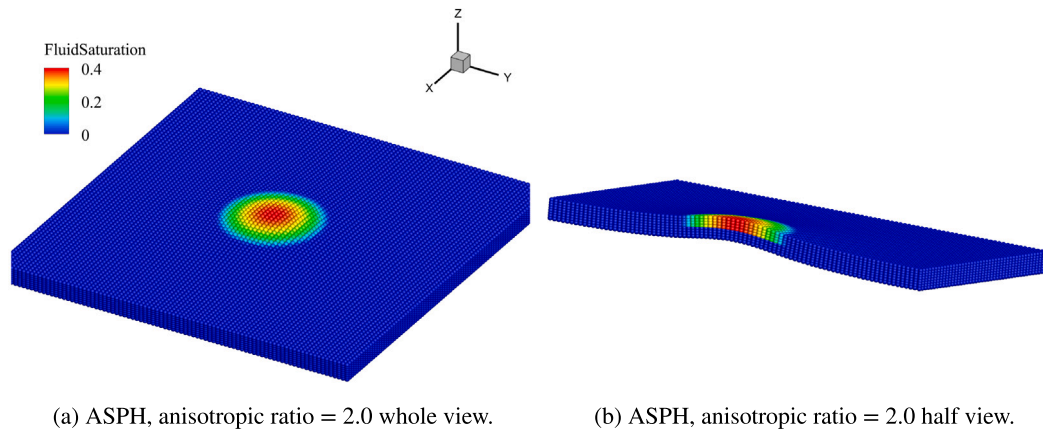


Fig. 19. 3D roof: the deformation colored by von Mises strain from SPH and ASPH with different anisotropic ratios at time = 0 s and time = 2.0 s.

(a) Results from SPH and ASPH with varying r .(b) Converged result from SPH and ASPH ($r = 8$).Fig. 20. 3D roof: the nondimensionalized z displacement comparison of the very center point of the curved roof.

(a) ASPH, anisotropic ratio = 2.0 whole view.

(b) ASPH, anisotropic ratio = 2.0 half view.

Fig. 21. 3D thin membrane with internal pressure: the sketch of fluid distribution in the membrane using ASPH with anisotropic ratio = 2.0.

Table 5

3D thin membrane with internal pressure: quantitative comparison of the accuracy and efficiency of this present ASPH algorithm with different anisotropic ratios.

Method	N	t (s)	Time saved	z/H	Difference
SPH, $N_z = 8$	223 111	1958.85	–	1.432	–
ASPH ratio = 2.0, $N_z = 8$	60 551	545.68	72.14%	1.439	0.49%
ASPH ratio = 4.0, $N_z = 8$	17 671	161.66	91.74%	1.374	4.05%
ASPH ratio = 8.0, $N_z = 8$	5837	52.63	97.31%	0.939	34.42%
ASPH ratio = 8.0, $N_z = 16$	35 344	650.32	66.80%	1.373	4.06%

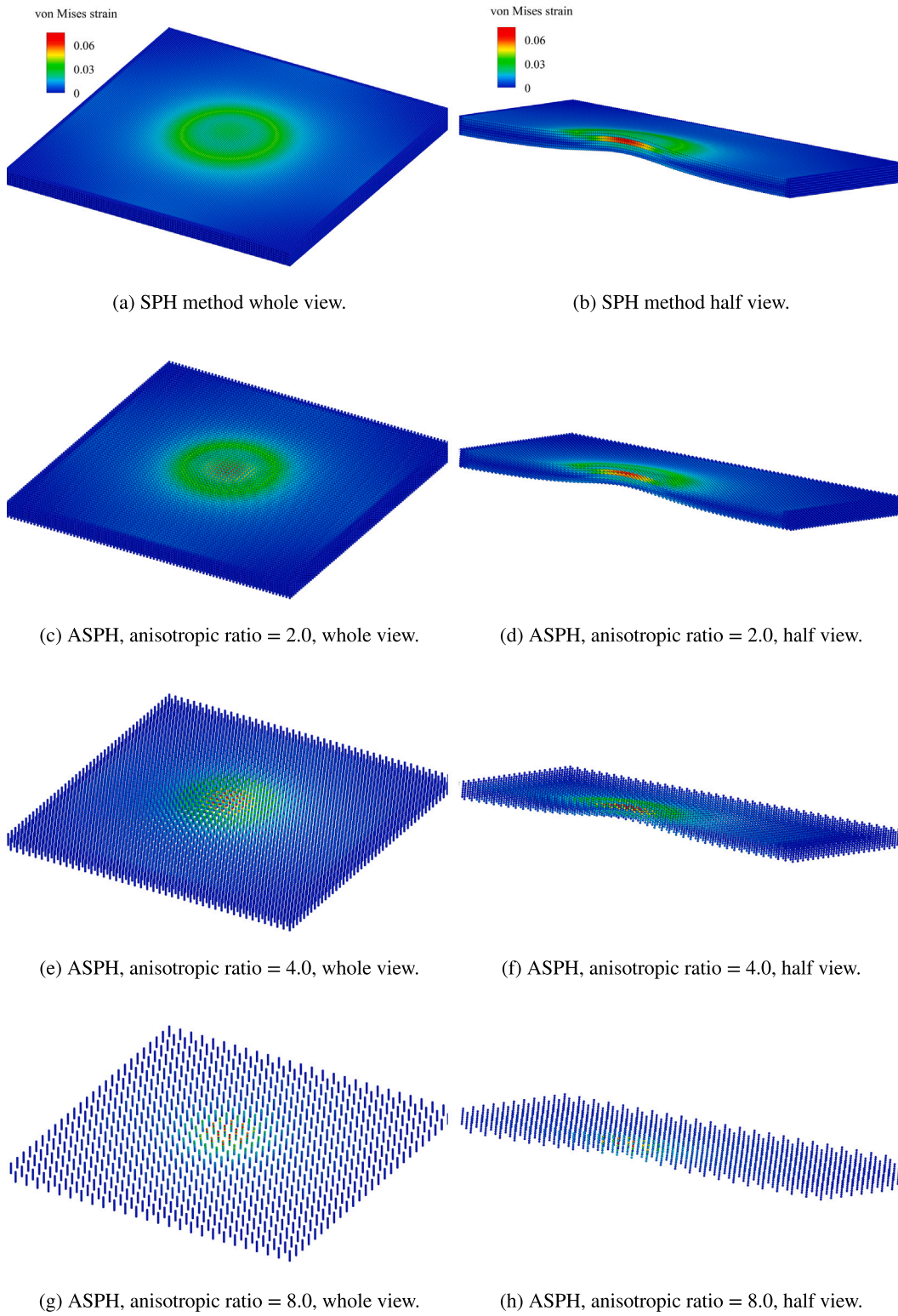


Fig. 22. 3D thin membrane with internal pressure: the deformation colored by von Mises strain from SPH and ASPH with different anisotropic ratios.

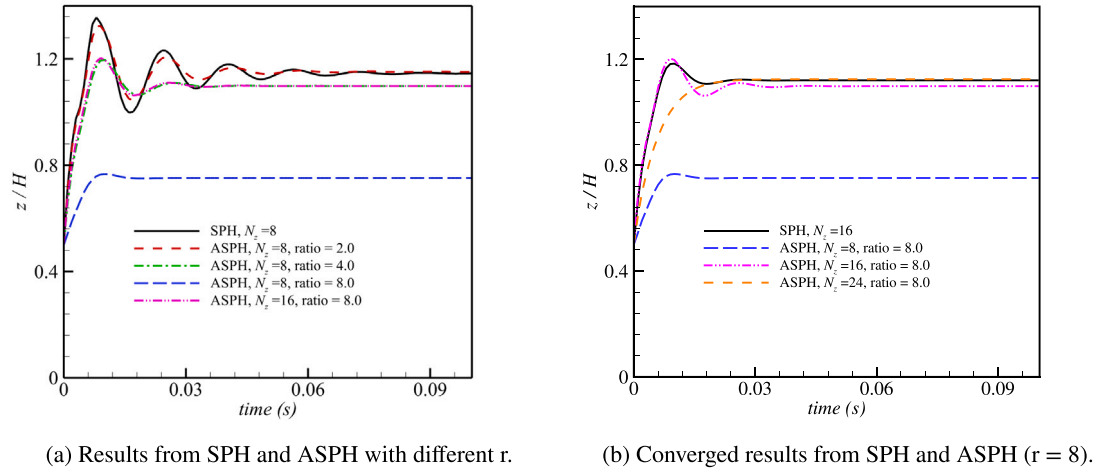


Fig. 23. 3D thin membrane with internal pressure: the comparison of nondimensionalized z-displacement of the very center point of the membrane.

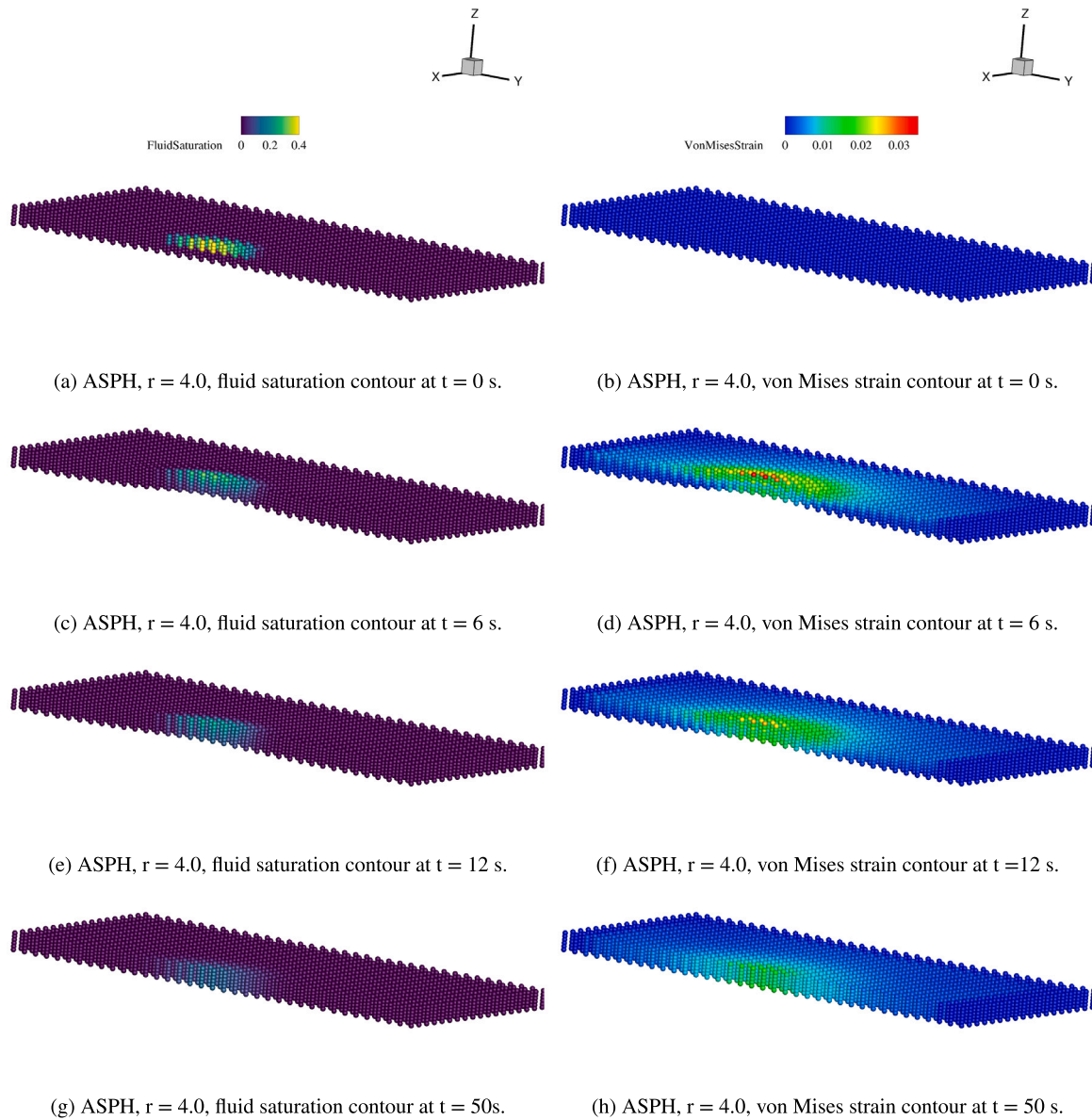
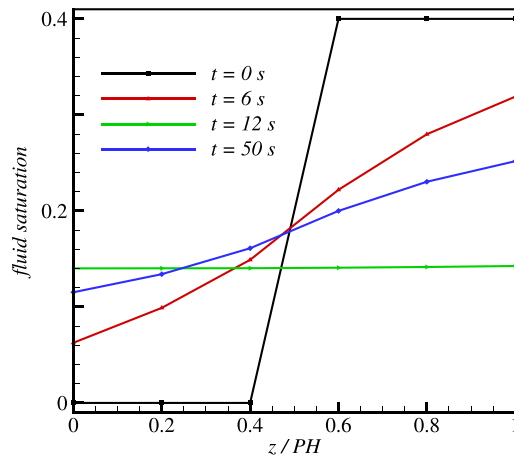
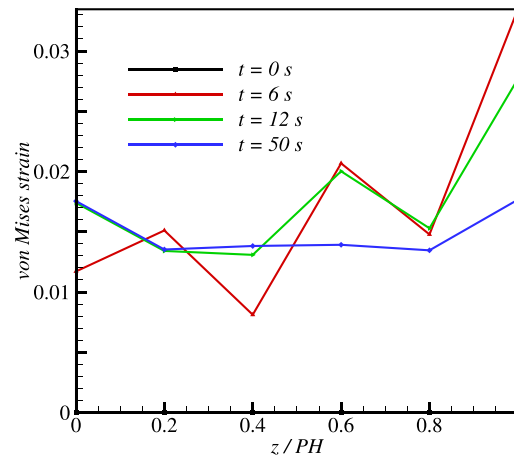


Fig. 24. 3D thin membrane with diffusion: fluid saturation and von Mises strain contours of the membrane at different time instants using ASPH with anisotropic ratio $r = 4.0$.



(a) The fluid saturation along the thickness direction.



(b) The von Mises strain along the thickness direction.

Fig. 25. 3D thin membrane with diffusion: the fluid saturation and von Mises strain along the thickness direction at the central-vertical line of the membrane at different time instants using ASPH with anisotropic ratio $r = 4.0$.

References

- [1] Liu M, Liu G. Smoothed particle hydrodynamics (SPH): an overview and recent developments. *Arch Comput Methods Eng* 2010;17(1):25–76.
- [2] Monaghan JJ. Smoothed particle hydrodynamics and its diverse applications. *Annu Rev Fluid Mech* 2012;44:323–46.
- [3] Luo M, Khayyer A, Lin P. Particle methods in ocean and coastal engineering. *Appl Ocean Res* 2021;114:102734. <http://dx.doi.org/10.1016/j.apor.2021.102734>.
- [4] Gotoh H, Khayyer A. On the state-of-the-art of particle methods for coastal and ocean engineering. *Coast Eng J* 2018;60(1):79–103. <http://dx.doi.org/10.1080/21664250.2018.1436243>.
- [5] Monaghan JJ. Simulating free surface flows with SPH. *J Comput Phys* 1994;110(2):399–406.
- [6] Shao S, Ji C, Graham DJ, Reeve DE, James PW, Chadwick AJ. Simulation of wave overtopping by an incompressible SPH model. *Coast Eng* 2006;53(9):723–35.
- [7] Huang C, Long T, Li S, Liu M. A kernel gradient-free SPH method with iterative particle shifting technology for modeling low-Reynolds flows around airfoils. *Eng Anal Bound Elem* 2019;106:571–87.
- [8] Antoci C, Gallati M, Sibilla S. Numerical simulation of fluid–structure interaction by SPH. *Comput Struct* 2007;85(11–14):879–90.
- [9] Han L, Hu X. SPH modeling of fluid–structure interaction. *J Hydrodyn* 2018;30(1):62–9.
- [10] Sun P, Le Touzé D, Zhang A-M. Study of a complex fluid–structure dam-breaking benchmark problem using a multi-phase SPH method with APR. *Eng Anal Bound Elem* 2019;104:240–58.
- [11] Libersky LD, Petschek AG. Smooth particle hydrodynamics with strength of materials. In: *Advances in the free-Lagrange method including contributions on adaptive gridding and the smooth particle hydrodynamics method*. Springer; 1991, p. 248–57.
- [12] Libersky LD, Petschek AG, Carney TC, Hipp JR, Allahdadi FA. High strain Lagrangian hydrodynamics: a three-dimensional SPH code for dynamic material response. *J Comput Phys* 1993;109(1):67–75.
- [13] Monaghan JJ. SPH without a tensile instability. *J Comput Phys* 2000;159(2):290–311.
- [14] Wang L, Xu F, Yang Y. An improved total Lagrangian SPH method for modeling solid deformation and damage. *Eng Anal Bound Elem* 2021;133:286–302.
- [15] Zhang C, Zhu Y, Yu Y, Wu D, Rezavand M, Shao S, Hu X. An artificial damping method for total Lagrangian SPH method with application in biomechanics. *Eng Anal Bound Elem* 2022;143:1–13.
- [16] Maurel B, Combescure A. An SPH shell formulation for plasticity and fracture analysis in explicit dynamics. *Int J Numer Methods Eng* 2008;76(7):949–71.
- [17] Ming F-R, Zhang A-M, Cao X-Y. A robust shell element in meshfree SPH method. *Acta Mech Sin* 2013;29(2):241–55.
- [18] Lin J, Naceur H, Coutellier D, Laksmi A. Efficient meshless SPH method for the numerical modeling of thick shell structures undergoing large deformations. *Int J Non-Linear Mech* 2014;65:1–13.
- [19] Wu D, Zhang C, Hu X. An SPH formulation for general plate and shell structures with finite deformation and large rotation. 2023, arXiv preprint arXiv:2309.02838.
- [20] Krysl P, Belytschko T. Analysis of thin plates by the element-free Galerkin method. *Comput Mech* 1995;17(1–2):26–35.
- [21] Krysl P, Belytschko T. Analysis of thin shells by the element-free Galerkin method. *Int J Solids Struct* 1996;33(20–22):3057–80.
- [22] Kanok-Nukulchai W, Barry W, Saran-Yasoonorn K, Bouillard P. On elimination of shear locking in the element-free Galerkin method. *Int J Numer Methods Eng* 2001;52(7):705–25.
- [23] Chen J-S, Wang D. A constrained reproducing kernel particle formulation for shear deformable shell in Cartesian coordinates. *Internat J Numer Methods Eng* 2006;68(2):151–72.
- [24] Li S, Hao W, Liu WK. Numerical simulations of large deformation of thin shell structures using meshfree methods. *Comput Mech* 2000;25:102–16.
- [25] Ren B, Li S. Modeling and simulation of large-scale ductile fracture in plates and shells. *Int J Solids Struct* 2012;49(18):2373–93.
- [26] Peng Y, Zhang A, Ming F. A thick shell model based on reproducing kernel particle method and its application in geometrically nonlinear analysis. *Comput Mech* 2018;62:309–21.
- [27] Ozdemir M, Tanaka S, Sadamoto S, Yu T, Bui T. Numerical buckling analysis for flat and cylindrical shells including through crack employing effective reproducing kernel meshfree modeling. *Eng Anal Bound Elem* 2018;97:55–66.
- [28] Love AEH. XVI. The small free vibrations and deformation of a thin elastic shell. *Philos Trans R Soc Lond A* 1888;(179):491–546.
- [29] Mindlin R. Influence of rotatory inertia and shear on flexural motions of isotropic, elastic plates. 1951.
- [30] Ghugal Y, Shimpi R. A review of refined shear deformation theories of isotropic and anisotropic laminated plates. *J Reinf Plast Compos* 2002;21(9):775–813.
- [31] Zhang L, Ademiloye A, Liew K. Meshfree and particle methods in biomechanics: Prospects and challenges. *Arch Comput Methods Eng* 2019;26(5):1547–76.
- [32] Motupally S, Becker AJ, Weidner JW. Diffusion of water in Nafion 115 membranes. *J Electrochem Soc* 2000;147(9):3171.
- [33] Goswami S, Klaus S, Benziger J. Wetting and absorption of water drops on nafion films. *Langmuir* 2008;24(16):8627–33.
- [34] Bicknell G, Gingold R. On tidal detonation of stars by massive black holes. *Astrophys J* 1983;273:749–60.
- [35] Owen JM, Villumsen JV, Shapiro PR, Martel H. Adaptive smoothed particle hydrodynamics: Methodology. II. *Astrophys J Suppl Ser* 1998;116(2):155.
- [36] Liu M, Liu G. Meshfree particle simulation of micro channel flows with surface tension. *Comput Mech* 2005;35:332–41.
- [37] Liu M, Liu G, Lam K. Adaptive smoothed particle hydrodynamics for high strain hydrodynamics with material strength. *Shock Waves* 2006;15:21–9.
- [38] Fu L, Hu XY, Adams NA. Adaptive anisotropic unstructured mesh generation method based on fluid relaxation analogy. *Commun Comput Phys* 2020;10.
- [39] Gawin D, Baggio P, Schrefler BA. Coupled heat, water and gas flow in deformable porous media. *Int J Numer Methods Fluids* 1995;20(8–9):969–87.
- [40] Korsawe J, Starke G, Wang W, Kolditz O. Finite element analysis of poro-elastic consolidation in porous media: Standard and mixed approaches. *Comput Methods Appl Mech Engrg* 2006;195(9–12):1096–115.
- [41] Atkin RJ, Craine R. Continuum theories of mixtures: basic theory and historical development. *Quart J Mech Appl Math* 1976;29(2):209–44.
- [42] Zhao Q, Papadopoulos P. Modeling and simulation of liquid diffusion through a porous finitely elastic solid. *Comput Mech* 2013;52(3):553–62.
- [43] Vignjevic R, Reveses JR, Campbell J. SPH in a total Lagrangian formalism. *CMC-Tech Sci Press* 2006;4(3):181.
- [44] Randles P, Libersky LD. Smoothed particle hydrodynamics: Some recent improvements and applications. *Comput Methods Appl Mech Engrg* 1996;139(1–4):375–408.
- [45] Espanol P, Revenga M. Smoothed dissipative particle dynamics. *Phys Rev E* 2003;67(2):026705.

- [46] Tran-Duc T, Bertevas E, Phan-Thien N, Khoo BC. Simulation of anisotropic diffusion processes in fluids with smoothed particle hydrodynamics. *Internat J Numer Methods Fluids* 2016;82(11):730–47.
- [47] Landau L, Lifchits E. *Course of theoretical physics: theory of elasticity* (p. 4). Kosevitch AM, Pitaevski LP. 1986.
- [48] Gray JP, Monaghan JJ, Swift R. SPH elastic dynamics. *Comput Methods Appl Mech Engrg* 2001;190(49–50).
- [49] Zhang C, Hu XY, Adams NA. A generalized transport-velocity formulation for smoothed particle hydrodynamics. *J Comput Phys* 2017;337:216–32.

A.3 Paper III

Xiaojing Tang, Dong Wu, Zhentong Wang, Oskar Haidn, Xiangyu Hu

An explicit multi-time stepping algorithm for multi-time scale coupling problems in SPH

In Communications in Computational Physics, Accepted

An explicit multi-time stepping algorithm for multi-time scale coupling problems in SPH

Xiaojing Tang, Dong Wu, Zhentong Wang, Oskar Haidn, Xiangyu Hu*

TUM School of Engineering and Design, Technical University of Munich, 85748 Garching, Germany

Abstract

Simulating physical problems with multi-time scale coupling presents a considerable challenge due to the concurrent solution of processes with different time scales. This complexity arises from the necessity to evolve large time scale processes over long physical time, while simultaneously small time step sizes are required to unveil the underlying physics in shorter time scale processes. To address this inherent conflict in the multi-time scale coupling problems, we propose an explicit multi-time step algorithm within the framework of smoothed particle hydrodynamics (SPH), coupled with a solid dynamic relaxation scheme, to quickly achieve equilibrium state in the comparatively fast solid response process. To assess the accuracy and efficiency of the proposed algorithm, a manuscript torsional example, two distinct scenarios, i.e., a nonlinear hardening bar stretching and a fluid diffusion coupled with Nafion membrane flexure, are simulated. The obtained results exhibit good agreement with analytical solution, outcomes from other numerical methods and experimental data. With this explicitly multi-time step algorithm, the simulation time is reduced firstly by independently addressing different processes being solved under distinct time step sizes, which stands in contrast to the implicit counterpart, and secondly decreasing the simulation time required to achieve a steady state for the solid by incorporating the dynamic relaxation scheme.

Keywords: SPH, Multi-time scale coupling, Multi-time step algorithm, Dynamic relaxation, Multi-physics problem

1. introduction

Smoothed Particle Hydrodynamics (SPH), a typically mesh-free method, which is originally introduced by Lucy [1], Gigold and Monaghan [2] for studying astrophysical problems, has been widely applied to simulate fluid-flows [3–6], solid mechanics [7–11], fluid-structure interaction (FSI) [12–15], etc., in recent years. Comprehensive reviews can be found in Refs. [16–20]. Despite its broad applicability, SPH exhibits limitations when addressing multi-scale coupling problems prevalent in diverse engineering domains, particularly in scenarios involving the rapid dynamic response of solids [21].

*Corresponding author.

Email addresses: xiaojing.tang@tum.de (Xiaojing Tang), dong.wu@tum.de (Dong Wu), zhentong.wang@tum.de (Zhentong Wang), oskar.haidn@tum.de (Oskar Haidn), xiangyu.hu@tum.de (Xiangyu Hu)

The large disparity in the time scales between fast and slow processes posts a continuing challenge to numerical simulations [22].

To solve multi-time scale problems, the implicit, explicit or two schemes coupling can be applied [23, 24]. The implicit scheme offers the advantage of using a larger time step in the time integration process [23, 25, 26], enabling the monolithic scheme to simultaneously solve the equations for both fast and slow processes. For instance, Zhao [27] utilized an implicit Newmark scheme to simulate fluid flow through a porous elastic solid, where solid dynamics and fluid diffusion occur at different time scales. Similarly, Gaston [28] employed an implicit scheme to analyze the coupling behavior among fluid dynamics, chemistry, and structural mechanics in a reactor. However, since the implicit scheme necessitates the inversion of the stiffness matrix for solving equations at each time step [29, 30], this approach incurs substantial computational costs and demands significant memory resources [31].

For enhancing computational efficiency, techniques involving explicit scheme are more favorable for addressing multi-time scale coupling problems due to its direct time integration and straightforward numerical formulation [32–35]. By partitioning the mesh into subdomains and the governing equations into subsystems, explicit-implicit and explicit-explicit partitions have been used to solve coupled-field dynamic problems, allowing multi-time step integrating with staggered solution procedures [36–38]. However, in systems displaying widely different characteristic response times, this methodology demands a large amount of staggered steps and data transfers per time step, rendering the treatment of realistic three-dimensional problems economically unfeasible [39]. Some researchers have employed explicit scheme to simulate material stretching and necking, where the load is applied over a long time period while the material’s dynamic response is instant and fast [40–42]. Since the realistic load is applied in a long time scale, a correspondingly long physical simulation time is expected. However, with a quite small stable time step size allowed in explicit scheme for the fast process, a substantial number of time steps, often reaching millions, is typically necessary to simulate the entire process, presenting practical challenges. To reduce the overall simulation time, loading rate is usually increased artificially [41]. Nevertheless, the adoption of high non-realistic loading rate may lead to certain limitations and inaccuracies in the simulation results [43], underscoring the delicate balance required in managing loading rates for accurate simulations.

This paper presents a multi-time stepping algorithm in SPH, where distinct large and small time steps are tailored to the slow and fast processes within the simulation, respectively. Two loops, specifically an outer and an inner loop, are organized to accommodate these respective time steps for effective time integration. Specifically, the slow process is integrated with a large time step in the outer loop, while the fast solid dynamic process with a considerably smaller time step in the inner loop. However, the small time step for the fast process may result in numerous iterations of solid stress relaxation within a single outer loop, leading to diminished computational efficiency. To address this issue, a dynamic relaxation method based on an implicit operator splitting scheme [44] is incorporated to accelerate the convergence rate of the fast dynamic process towards an equilibrium state. To evaluate the performance and computational efficiency of the proposed algorithm, simulations of a manuscript torsional example and tensile tests, including two-dimensional and three-dimensional cases, are firstly carried out. Subsequently, the algorithm is applied to simulate the evolution of fluid diffu-

sion in porous media coupled with elastic deformation. This fluid-structure coupling process occurs in chemical reactors, such as the fuel cell of a battery, where a fluid mixture diffuses through a Nafion membrane, which is a slow process, impacting battery performance through variations in fluid concentration and membrane deformation. The obtained results demonstrate that the proposed algorithm outperforms previous numerical methods in terms of both accuracy and efficiency.

The reminder of this paper is structured as follows. Section 2 summaries the theories and governing equations for nonlinear hardening plastic solid mechanics and fluid-structure interaction in porous media. The corresponding SPH discretization is described in Section 3. Section 4 presents a detailed exposition of the proposed multi-time stepping algorithm, incorporating dynamic relaxation. In Section 5, the physical problems are outlined, and the results obtained using the proposed algorithm are compared with those derived from previous methods and experiments. Finally, Section 6 presents concluding remarks. The source code and data for this numerical simulation work are available in SPHinXsys, an open-source multi-physics SPH library, accessed at <https://www.sphinxsys.org>.

2. Governing equations

In this section, the fundamental principles and concepts of solid dynamics are initially presented to establish the principal mass and momentum equations for solids, as they are applicable to both scenarios of elastic-plastic solid stretching and fluid-structure interaction in porous media. Subsequently, the specific models for hardening elastic-plastic behavior and fluid-structure interaction are provided separately.

2.1. Total Lagrangian of solid dynamics

In this section, we provide a concise introduction to solid dynamics within the framework of total Lagrange formulation. The analysis focuses on a solid body \mathcal{B} , spanning two regions: \mathcal{R}_0 and \mathcal{R} , representing the body configurations at time t_0 ($t = 0$) and t , respectively. In the initial configuration \mathcal{R}_0 , the position vector of a material point is denoted as $\mathbf{X} \in \mathcal{R}_0$, while in the current configuration, it is represented as $\mathbf{x} \in \mathcal{R}$. The motion of the solid body is characterized by the invertible mapping ϕ , which transforms a material point \mathbf{X} to its corresponding vector $\mathbf{x} = \phi(\mathbf{X}, t)$, as illustrated in Figure. 2.1. Based on this definition, the Lagrangian velocity of a material point is defined as $\mathbf{v}(\mathbf{X}, t) = \frac{\partial \phi(\mathbf{X}, t)}{\partial t}$. The deformation gradient \mathbf{F} , which characterizes the deviation of a material point from its initially undeformed position to its deformed position, can be computed from the displacement vector $\mathbf{u} = \mathbf{x} - \mathbf{X}$ as

$$\mathbf{F} = \frac{\partial \mathbf{x}}{\partial \mathbf{X}} = \nabla^0 \mathbf{u} + \mathbf{I}, \quad (1)$$

where \mathbf{I} is the unit matrix, and the superscript $(\bullet)^0$ accounts for quantities in the initial reference configuration. The corresponding Jacobian determinant term $J = \det(\mathbf{F})$ indicates the local volume gain $J > 1$ or loss $J < 1$. The governing equations of solid deformation within the total Lagrange framework are derived as

$$\begin{cases} \rho = \rho^0 \frac{1}{J} \\ \rho^0 \frac{d\mathbf{v}}{dt} = \nabla^0 \cdot \mathbf{P}^T \end{cases}, \quad (2)$$

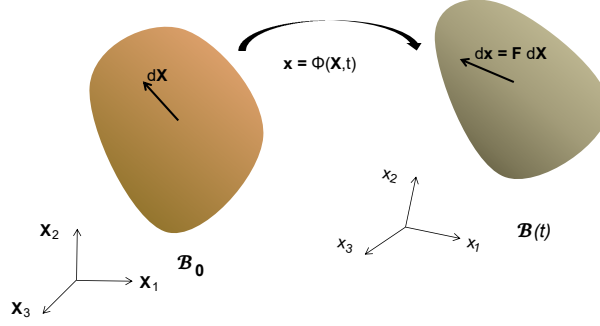


Figure 2.1: Finite deformation process on a body \mathcal{B} .

where ρ and ρ_0 are the densities in the current configuration \mathcal{R} and the initial configuration \mathcal{R}_0 , respectively, \mathbf{v} the velocity and \mathbf{P} the first Piola-Kirchhoff stress tensor. Different from the Cauchy stress $\boldsymbol{\sigma}$, which characterizes the force measured in the deformed configuration, \mathbf{P} relates to stress within the initial configuration, and the relationship between these two stresses is

$$\mathbf{P} = J\boldsymbol{\sigma}\mathbf{F}^{-T} = \boldsymbol{\tau}\mathbf{F}^{-T}, \quad (3)$$

where $\boldsymbol{\tau}$ is the Kirchhoff stress tensor, utilized in the hardening plastic model to calculate \mathbf{P} , obtained from the constitutive relation in Appendix A. The Cauchy stress $\boldsymbol{\sigma}$ is employed to represent the overall stress acting on the solid in the fluid-structure interaction model subsequently determine \mathbf{P} as elaborated in Appendix B, with a detailed explanation of their relationship provided in the subsequent section.

2.2. Fluid-structure interaction

For the coupled phenomena involving fluid diffusion in porous media concurrent with elastic deformation of the porous membrane, we introduce a fluid-structure interaction model. This model accounts for the simultaneous diffusion of fluid through the porous solid, resulting in heightened fluid pressure and deformation of the solid structure. In this model, the heterogeneous body is considered as a continuous solid medium

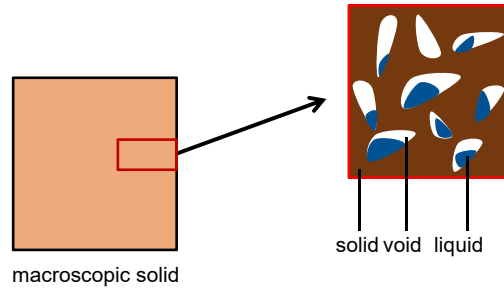


Figure 2.2: Partially saturated porous medium.

containing uniformly distributed small voids with a homogeneous porosity denoted by c . Upon interaction with a fluid, the fluid permeates into these small pores and diffuses

within the medium, driven by the fluid concentration gradient, resulting in the creation of a mixture consisting of solid and fluid components, as illustrated in Figure 2.2. To simplify this model, we adopt the methodology proposed by Zhao [27] to formulate a momentum equation for the mixture, with the fluid dynamics adhering to the principles of diffusion.

2.2.1. Mass and momentum equations

With a porosity c and fluid saturation level \tilde{c} (as defined in Appendix B.1), the locally effective fluid density ρ^l can be expressed as

$$\rho^l = \rho^L \tilde{c}, \quad (4)$$

where ρ^L is the fluid density. For a porous solid partially-saturated by fluid, the total linear momentum \mathbf{M} in the region \mathcal{R} is the sum of fluid momentum and solid momentum

$$\mathbf{M} = \rho \mathbf{v} = \rho^l \mathbf{v}^l + \rho^s \mathbf{v}^s, \quad (5)$$

where ρ and \mathbf{v} are the total density and velocity respectively, \mathbf{v}^l the velocity of fluid, ρ^s and \mathbf{v}^s the density and velocity of dry porous solid. Due to the difference between \mathbf{v}^l and \mathbf{v}^s , the fluid flux \mathbf{q} on the element boundary ∂V , considering a representative volume element dV , can then be expressed as

$$\mathbf{q} = \rho^l (\mathbf{v}^l - \mathbf{v}^s). \quad (6)$$

Obviously, if there is no fluid passing through the boundary, $\mathbf{q} = \mathbf{0}$, and the fluid mass in an element remains conserved. The transfer of fluid mass and momentum between micro-scale solid constituents happens when fluid flows from regions with higher fluid saturation to those with lower saturation. Therefore, within an element dV of the mixture, the balance of linear momentum implies that the time derivative of momentum \mathbf{M} is determined by two factors. One is the stress exerted on the element, and the other is the fluid flux of linear momentum $\mathbf{v}^l \otimes \mathbf{q}$ on the boundary ∂V , where the symbol \otimes means the outer product of two vectors or tensors. It follows that the conservation of total linear momentum of the mixture can be expressed as

$$\frac{d\mathbf{M}}{dt} = \nabla \cdot \boldsymbol{\sigma} - \nabla \cdot (\mathbf{v}^l \otimes \mathbf{q}), \quad (7)$$

where $\boldsymbol{\sigma}$ represents the Cauchy stress in the mixture acting on the solid. $\boldsymbol{\sigma}$ is determined by Cauchy stress $\boldsymbol{\sigma}^s$ due to deformation and the pressure stress $\boldsymbol{\sigma}^l$ resulting from the presence of the fluid phase, which is elaborated in Appendix B.2.

2.2.2. Fick's law

In a partially saturated solid, variations in fluid saturation drive fluid movement regions with higher fluid fraction to those with lower fractions, and the resulting flux follows the Fick's law as

$$\mathbf{q} = -D \rho^l \nabla \tilde{a}, \quad (8)$$

indicating that the fluid flux is proportional to the diffusivity D , the effective fluid density ρ^l , as well as the gradient of the fluid saturation \tilde{c} . Consequently, the time derivative of fluid mass within an element dV is attributed to the fluid flux \mathbf{q} across the element boundary ∂V , written as

$$\frac{d\rho^l}{dt} = -\nabla \cdot \mathbf{q}. \quad (9)$$

3. SPH implementation

In SPH, the continuum is discretized into a set of Lagrangian particles, each carrying various properties such as mass, position, velocity, and other attributes. The discretization of a variable field is achieved by employing SPH particles, and the mechanics are approximated by modeling the interactions among these particles using a kernel function. In this section, we transform the governing equations of two previously discussed models into SPH discretization.

3.1. SPH discretization for solid dynamics

To discretize the solid mechanics, we utilize the initial undeformed configuration as the reference. First, aiming to restore 1st order consistency, a correction matrix \mathbf{B}^0 [45, 46] of particle a is adopted as

$$\mathbf{B}_a^0 = \left(\sum_b V_b^0 (\mathbf{r}_b^0 - \mathbf{r}_a^0) \otimes \nabla_a^0 W_{ab} \right)^{-1}, \quad (10)$$

where V_b^0 represents the initial volume of the neighboring particle b , \mathbf{r}_a^0 and \mathbf{r}_b^0 denote the positions of particles a and b in the reference configuration, and $\nabla_a^0 W_{ab}$ is the gradient of the kernel function given by

$$\nabla_a^0 W_{ab} = \frac{\partial W(|\mathbf{r}_{ab}^0|, h)}{\partial |\mathbf{r}_{ab}^0|} \mathbf{e}_{ab}^0, \quad (11)$$

where \mathbf{e}_{ab}^0 is a unit vector pointing from particle a to b . In total Lagrangian formulation, the neighborhood of particle a is defined in the initial configuration, and this set of neighboring particles remains fixed throughout the entire simulation. Additionally, \mathbf{B}_a^0 is computed only once under the initial reference configuration. The momentum conservation in Eq. (2) can be approximated using the strong-form approximation of the spatial derivative [47, 48] as

$$\frac{d\mathbf{v}_a}{dt} = \frac{2}{\rho_a^0} \sum_b V_b^0 \tilde{\mathbf{P}}_{ab} \nabla_a^0 W_{ab}, \quad (12)$$

where ρ_a represents the density of particle a , $\tilde{\mathbf{P}}_{ab}$ is the averaged first Piola-Kirchhoff stress of the particle pair (a, b) , stated as

$$\tilde{\mathbf{P}}_{ab} = \frac{1}{2} \left(\mathbf{P}_a \mathbf{B}_a^{0T} + \mathbf{P}_b \mathbf{B}_b^{0T} \right). \quad (13)$$

With a symmetric smoothing kernel, \mathbf{B} is considered to be symmetric. Note that the first Piola-Kirchhoff stress tensor is dependent on the deformation tensor \mathbf{F} , approximated using the weak-form approximation of the spatial derivative [47, 48] as

$$\mathbf{F} = \left(\sum_b V_b^0 (\mathbf{u}_b - \mathbf{u}_a) \otimes \nabla_a^0 W_{ab} \right) \mathbf{B}_a^0 + \mathbf{I}, \quad (14)$$

and the time derivative of \mathbf{F} is computed from

$$\frac{d\mathbf{F}_a}{dt} = \left(\sum_b V_b^0 (\mathbf{v}_b - \mathbf{v}_a) \otimes \nabla_a^0 W_{ab} \right) \mathbf{B}_a^0, \quad (15)$$

where \mathbf{v}_a and \mathbf{v}_b denote the velocities of particles a and b .

3.2. SPH discretization for fluid-structure interaction

In the fluid-structure interaction model discretization, each particle carries the location $\mathbf{x}_n = \phi(\mathbf{X}, t_n)$ at time t_n , along with an initial representative volume V^0 that partitions the initial domain of the macroscopic solid. The deformation gradient \mathbf{F}_n of the solid phase is stored to update the solid current volume V_n and density ρ_n^s . Additionally, the fluid mass m_n^l , saturation \tilde{a}_n , and density-weighted velocity of the fluid relative to solid \mathbf{q}_n are stored. The fluid mass equation Eq. (9) of particle i is discretized as

$$\frac{dm_i^l}{dt} = 2V_i \sum_j \frac{m_j}{\rho_j} (\mathbf{q}_i - \mathbf{q}_j) \tilde{\nabla}_i W_{ij}. \quad (16)$$

Note that with the Eq (1), we have the relation of gradient kernel function in the total Lagrangian and updated Lagrangian $\tilde{\nabla}_i W_{ij} = \mathbf{B}_i^{0T} \mathbf{F}^{-1} \nabla_i^0 W_{ij}$. Once fluid mass is updated, the locally effective fluid density ρ^l is obtained subsequently. According to Eq. (42) and Eq. (8), we update the fluid saturation \tilde{a} and the fluid flux \mathbf{q} in the particle form

$$\mathbf{q}_i = -K\rho^l V_i \sum_j \frac{m_j}{\rho_j} (\tilde{c}_i - \tilde{c}_j) \tilde{\nabla}_i W_{ij}. \quad (17)$$

With the fluid flux and the stress in hand, we obtain discrete formulations for the momentum balance Eq. (7) as

$$\frac{d\mathbf{M}_i}{dt} = 2 \sum_j V_j (\boldsymbol{\sigma}_i + \boldsymbol{\sigma}_j) \tilde{\nabla}_i W_{ij} - 2 \sum_j V_j (\mathbf{v}_i^l \otimes \mathbf{q}_i + \mathbf{v}_j^l \otimes \mathbf{q}_j) \tilde{\nabla}_i W_{ij}, \quad (18)$$

where $\boldsymbol{\sigma}_i$ and $\boldsymbol{\sigma}_j$ are the stress tensors of particles i and j . We then compute the updated solid velocity \mathbf{v}^s using the total momentum definition Eq. (5), where the total density of the mixture is the sum of the solid and fluid densities $\rho = \rho^s + \rho^l$, written as

$$\mathbf{v}^s = \frac{\mathbf{M} - \mathbf{q}}{\rho} = \frac{\mathbf{M} - \mathbf{q}}{\rho^s + \rho^l}. \quad (19)$$

Subsequently, the fluid velocity \mathbf{v}^l is calculated using Eq. (6) as

$$\mathbf{v}^l = \mathbf{v}^s - \frac{\mathbf{q}}{\rho^l}. \quad (20)$$

4. Multi-time step algorithm

In multi-time scale coupling involving solid dynamic problems, different time scales coexist. A multi-time step algorithm using an explicit scheme to accommodate various time scale processes is introduced in this section. In this approach, the slow processes, e.g., stretch loading and fluid diffusion, are integrated with larger time step sizes, while the fast solid dynamics with smaller ones. With small time step size, the solid dynamics evolves to a quasi-equilibrium state. Further, to reduce the stress relaxation time of solid dynamics, a damping scheme is applied to accelerate the attainment of the equilibrium state.

4.1. Multi-time criteria

As the explicit integration operator is conditionally stable, a time step criterion Δt_s is required in solid simulation, given by

$$\Delta t_s = 0.6 \min \left(\frac{h}{c_s + |\mathbf{v}_s|_{max}}, \sqrt{\frac{h}{|\frac{d\mathbf{v}_s}{dt}|_{max}}} \right), \quad (21)$$

where the artificial sound speed of a solid structure is denoted as $c_s = \sqrt{K/\rho_s}$. In multi-time scale coupling problems, considering that the solid dynamic relaxation process is comparatively fast, Δt_s is usually limited to a small value. Conversely, the time step for internal diffusion evolution or stretch loading is allowed to be much larger. For the tensile test simulation, we divide the stretching process into N_S steps and the time step is

$$\Delta t_l = \frac{T_t}{N_S}, \quad (22)$$

where T_t is the entire process time of the tensile test, and Δt_l accordingly the time step for stretch loading. Similarly, for the fluid-structure interaction, according to the Fick's law, the maximum time step allowed for explicit time stepping of diffusion is characterized as [49]

$$\Delta t_d = 0.5 \frac{h^2}{D}, \quad (23)$$

stating that the time step is mainly limited by the diffusivity constant D and the kernel smoothing length h . To address the difference between these time step sizes for various time scale processes, we present a multi-time step algorithm to simulate these processes respectively with an iterative scheme.

4.2. Iterative scheme

Figure 4.1 summarizes the iterative scheme of the proposed multi-time step algorithm schematically. This algorithm consists of two loops, an outer loop governing the overall dynamic progression through incremental execution of prescribed displacements or diffusion relaxation denoted by g , and an inner loop describing the evolution of solid dynamics with k representing each stress relaxation step. The loading or diffusion criterion Δt_l or Δt_d regulates the external force exerting or the fluid diffusion process while Δt_s determines the frequency of solid stress relaxation. Within one external loading time step Δt_l or diffusion time step Δt_d , the time integration of structure should be computed as $k_0 = \lceil \frac{\Delta t_{l/d}}{\Delta t_s} \rceil + 1$ times. With a limited Δt_s and much larger Δt_l and Δt_d , k_0 is supposed to be considerably large and potentially resulting in a significant number of iteration steps in the computation of solid dynamics, increasing the computation time.

Upon achieving a static state in solid dynamics, the inner loop concludes, marking the commencement of another outer loop. Therefore, to optimize computation time, the inner loop is executed with a damping term to dissipate the kinetic energy and accelerate the relaxation of the solid transient response. Solid governing equations with additional damping are solved a small number of times k until the kinetic energy is reduced to a sufficiently small value E_k , marking the achievement of the equilibrium state of the system. Specific criteria values for the kinetic energy are established in different cases according to the reference energy which represents the system properties.

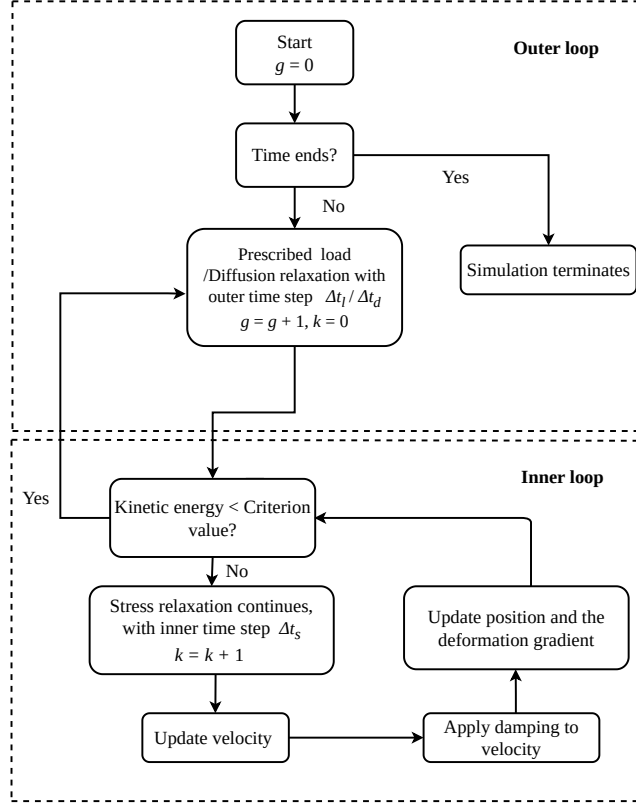


Figure 4.1: Flowchart of the iterative scheme in multi-time step algorithm.

In the simulations, we decrease the criteria values until the equilibrium state is achieved and the results converge. After the equilibrium state of the solid deformation is achieved in the inner steps, a new outer step initiates and this iterative process is repeated until the conclusion of the designated physical computation time.

4.3. Damping scheme

As mentioned previously, achieving equilibrium for a dynamic system can be excessively time-consuming in SPH method with explicit time-stepping. To mitigate this issue, we adopt the approach proposed by Zhu et al. [44] and introduce an artificial viscosity-based damping term into the stress relaxation to dissipate the extra kinetic energy. Without compromising the momentum conservation of the system, a viscous damping term \mathbf{f}^v is added to the solid momentum equation as

$$\frac{d\mathbf{v}}{dt} = \mathbf{f}^s + \mathbf{g} + \mathbf{f}^v, \quad (24)$$

where \mathbf{f}^s and \mathbf{g} represents the acceleration due to the surface and body forces, the added damping term \mathbf{f}^v can be discretized in the total Lagrangian form as

$$\mathbf{f}_a^v = \frac{\eta}{\rho_a} \nabla_a^2 \mathbf{v} = \frac{2\eta}{m_a} \sum_a V_a^0 V_b^0 (\mathbf{v}_a - \mathbf{v}_b) \nabla_a^0 W_{ab}, \quad (25)$$

where η is the dynamic viscosity, and for structures η is determined by the material properties and the physical shape of the solid body, defined as $\eta = \frac{\beta}{4} \sqrt{\rho E} L$, with L

denoting the characteristic length scale and β a parameter related to the body shape in specific problems. Note that, β may vary to change the speed of reaching the equilibrium with larger β accelerating the relaxation process to the final state. For further details, readers can refer to Zhu's work [44].

5. Numerical examples

In this section, firstly, a manufactured torsional deformation test case is conducted to validate the robustness of the present multi-time step algorithm in SPH for problems including large torsional deformations. Several tests, including the stretching-necking and the fluid diffusion coupling solid deformation in two and three dimensions, are simulated using the present method to demonstrate its accuracy and efficiency.

5.1. Manufactured torsional deformation

This section presents a generalized vortex example, featuring a ring centered at the origin ($x = y = 0$) with an inner radius of $R_i = 0.75$ m and an outer radius of $R_o = 1.25$ m. The ring is considered to be elastic and material parameters are taken as Young's modulus $E = 10^3$ Pa, initial density $\rho = 1000$ kg/m³, Poisson's ratio $\nu = 0.3$. As described in [50–52], given a prescribed deformation field initially, the loading force required to achieve this deformation can be analytically determined, according to the momentum governing equations. In this numerical simulation, using the present algorithm, the loading body force is imposed on the SPH particles with position constrained boundaries. Consequently, the present SPH algorithm can be verified by comparing the postulated deformation field with the numerical solution. The superimposed deformation is purely angular and the rotation angle α , which is dependent on the radial coordinate of the material point, is a function of radius R and time t , written as

$$\alpha(R, t) = g(t)h(R),$$

where $h(R)$ controls the radial deformation field and $g(t)$ the deformation magnitude $h(R) = 1 - 32(R - 1)^2 + 256(R - 1)^4$ and $g(t) = t \alpha_0/t_0$, where α_0 is the maximum imposed rotation angle, taken as 10° and t_0 is the total simulation time. Given this deformation field, the stresses \mathbf{P} can be obtained according to the constitution relation. For a quasi-static problem, the momentum equation involving the body force \mathbf{f}_b is in the form of

$$\frac{d\mathbf{P}}{dt} + \rho\mathbf{f}_b = 0.$$

Consequently, the mathematical expression of \mathbf{f}_b in the polar coordinate is written as

$$b_r = \frac{\mu A^2}{4\rho_o} R \left(\frac{t\alpha_0}{t_0}\right)^2 (-64(R - 1) + 1024(R - 1)^3)^2, \quad (26)$$

$$b_\theta = -\frac{32\mu A}{\rho_o} \frac{t\alpha_0}{t_0} (-45 + 188R - 240R^2 + 96R^3). \quad (27)$$

The derivation is detailed in the reference [51] and the Appendix A in [50]. The body force is applied on the ring over 10 equal load steps within a simulation time of $t_0 = 100$ s, coupling with the damping algorithm to obtain a smooth deformation field. Using the multi-time step coupling algorithm, the time step for the body force applying is defined as $D_t = 10$ s, while the stress relaxation time step is determined by the material properties. After each body force loading, stress relaxation coupled with damping is

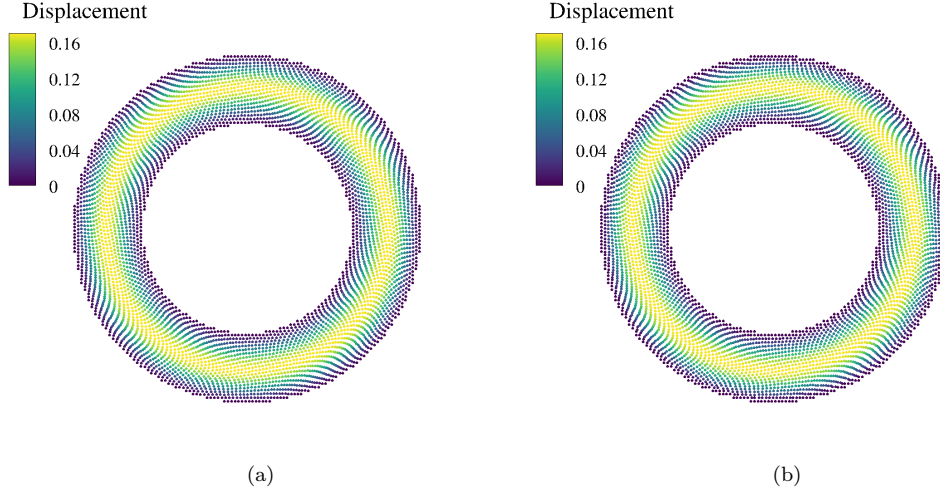


Figure 5.1: Manufactured torsional deformation: the analytical (a) and numerical (b) final deformed configuration colored by the magnitude of displacement.

performed. Following the work of Zhu [44], the damping ratio is $\eta = 150 \text{ kg}/(\text{m}\cdot\text{s})$ with $\beta = R_i/R_0$.

With a the particle spacing $d_p = (R_o - R_i)/20 = 0.05 \text{ m}$, the deformed state at peak rotation angle obtained using the multi-time step algorithm aligns well with the prescribed deformation field, as illustrated in Figure. 5.1. Figure 5.2 presents the displacement magnitude comparison of particles in the radial direction at $x = 0$ at the final time instant. Negligible difference is observed between the superimposed displacement and the numerical result. To quantitatively verify the accuracy, the relative error in terms of the displacement is computed as

$$\text{ERR} = \sqrt{\frac{\sum_{N_p} \|u_n^p - u_a^p\|^2}{\sum_{N_p} \|u_a^p\|^2}}, \quad (28)$$

where u_n^p and u_a^p represent the displacement vectors obtained by the simulation and analytical solution of particle p respectively, N_p the particle number. The relative error results at the peak rotation angle $\alpha = \alpha_0$ for a variety of particle spacing of $d_p = 0.1, 0.05, 0.025, 0.0125 \text{ m}$ is shown in Figure 5.3. It can be seen that the relative error decreases progressively as the particle domain resolution is refined.

To determine the point of equilibrium, we monitor the ratio of kinetic energy E_k to strain energy U . Equilibrium is deemed achieved when this ratio is damped below a defined threshold value. While the strain energy is defined as $U = \frac{1}{2}(\sigma_x \epsilon_x + \sigma_y \epsilon_y + \tau_{xy} \epsilon_{xy})$ and the maximum strain energy U_{max} occurs at the final state. We set a energy criterion $E_k = 1.0\%U_{max}$ initially and decrease this criterion step by step until the relative error is converged. Figure 5.4 shows the variation of displacement with different kinetic energy criteria. The results suggest that the convergence is obtained when $E_k = 0.02\%U_{max}$.

With a physical simulation time of $t_0 = 100 \text{ s}$, due to the time step size limitation in explicit scheme, the number of loading steps N_L and stress relaxation times N_s performed in the simulation are expected to be $N_S = N_s = t_0/\Delta t_s = 5.37 \times 10^5$. With this multi-time criteria algorithm, the loading steps is decreased to be $N_S = 10$ and benefiting from the damping, the relaxation times is reduced to $N_s = 7.32 \times 10^4$, increasing the commutation efficiency.

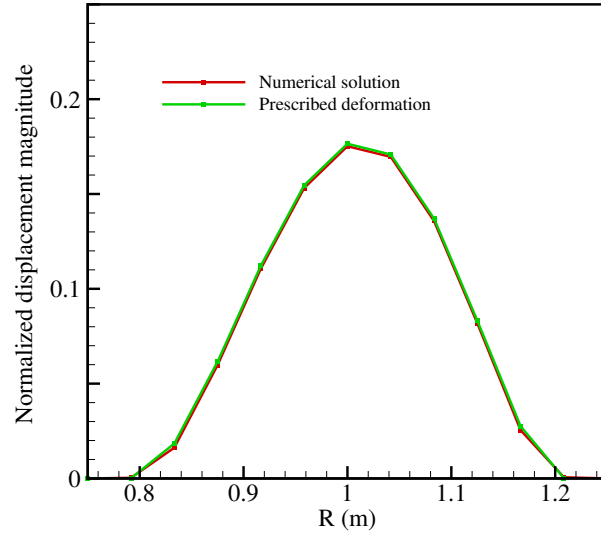


Figure 5.2: Manufactured torsional deformation: the comparison of normalized displacement magnitude in the radial direction at $t = 100$ s and $x = 0$.

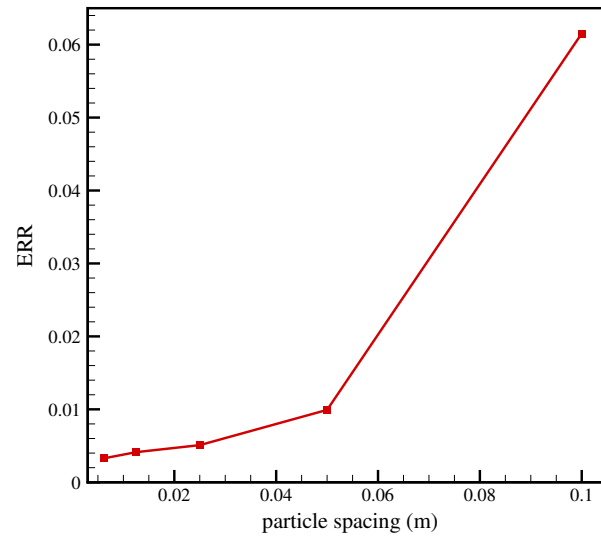


Figure 5.3: Manufactured torsional deformation: plot of the normalized displacement magnitude error as a function of the particle spacing obtained using the multi-time step algorithm.

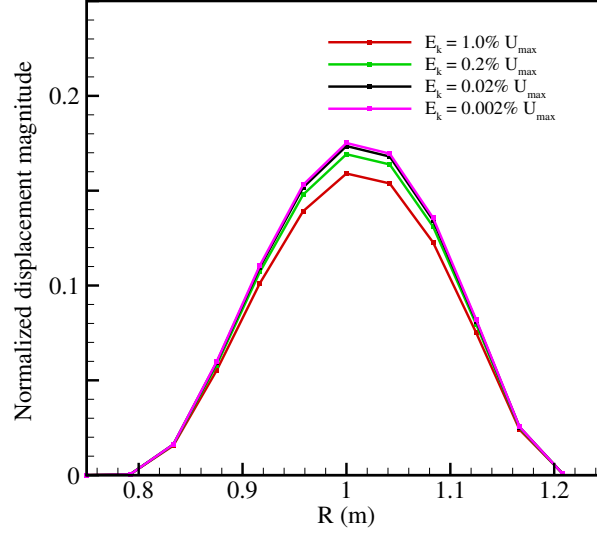


Figure 5.4: Manufactured torsional deformation: plot of the displacement magnitude variation with different energy criterion E_k .

5.2. Necking of a two-dimensional bar

The standard tensile necking test simulation has been previously studied in the existing literature [53–56], offering both experimental and numerical results for comparative analysis. The test sample, with dimensions $PL = 53.334$ mm in length and

Table 5.1: Necking test simulation: physical material parameters.

Parameters	Value
Density	7850 kg/m ³
Shear modulus	80.1938 Gpa
Bulk modulus	164.21 Gpa
Initial flow stress	450 MPa
Saturation flow stress	715 MPa
Saturation exponent	16.93
Linear hardening coefficient	129.24 MPa

$PH = 12.826$ mm in width, is subjected to stretching from its side edges under increasing uniaxial displacement. As the specimen undergoes elongation, a concurrent reduction in width is observed. A slight imperfection (1.8% reduction) is imposed initially at the center part of this sample as shown in Figure 5.5 to trigger the necking phenomenon. The specimen is composed of a elastic deformation depicted by the Neo-Hookean law and a plastic governed by the nonlinear isotropic hardening law. The material parameters are given in Table 5.1. A total stretching of 10 mm is achieved through a symmetric displacement boundary conditions. Three layers of particle are subjected to the specified boundary condition. Compared with experimental timescales of around 2 minutes, the simulation is conducted over a physical time of $t = 100$ s, with stretching steps $N_S = 10000$ and a corresponding velocity $v = 0.05$ mm/s. This differs from references where velocities are usually increased to approximately 1 m/s to reduce the physical time to 1.5×10^{-3} s. After each stretch loading step, stress relaxation

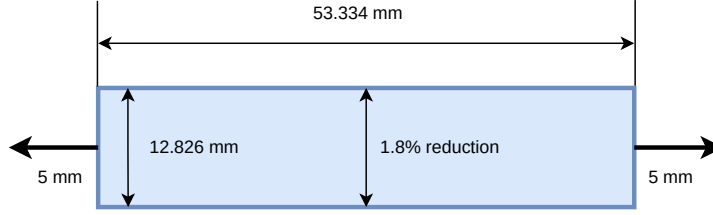


Figure 5.5: 2D tensile necking: geometry and initial and boundary condition setup.

coupled with damping is performed. The damping ratio is set to an experienced value of $\eta = 3.0 \times 10^4 \text{ kg}/(\text{m}\cdot\text{s})$ with $\beta = PH/PL$.

Figure 5.6 illustrates the deformation evolution colored by von Mises strain at various time instances under a spatial resolution $dp = PH/40 = 0.32065 \text{ mm}$. The corresponding von Mises strain at various time instances contour are depicted in Figure 5.7. A clear necking pattern is observed at the center of the specimen, aligning with that observed in both experimental studies and other numerical investigations [54–56]. The specimen undergoes three distinct stages: elastic strain, succeeded by uniform plastic strain, and ultimately necking strain. Figure 5.8 plots the radial evolution of the central region where necking occurs, as a function of the imposed stretching displacement. The result is compared with those from Ref. [56], where Q1, mixed Q1/P0, Q2 and Q3 (employing different mesh discretization and element types) are utilized to model this test. As time advances and the sample elongates, the radius displacement of the central part increases linearly, while after necking occurs, it experiences a rapid escalation. Figure 5.9 depicts the evolution of the reaction force over time. Following a short elastic response, characterized by the initial straight line, the specimen transitions into the stage of uniform plastic deformation, displaying a smooth increase in the reaction force. During this stage, plastic deformation slowly propagates and shows a homogeneous state throughout the specimen. Eventually, when the boundary displacement reaches a critical value, necking occurs in the central part, and the reaction force reaches its peak value. Subsequently, the deformation shifts to a mode where the plastic effect is concentrated in the central zone, resulting in a declining reaction force, which is more obvious in the subsequent three-dimensional case. A convergence study with progressively refined spatial resolution is conducted. Figure 5.10 presents the radial displacement and the reaction force versus the imposed displacement for three resolutions: $N_y = PH/dp = 20$, $N_y = PH/dp = 40$, $N_y = PH/dp = 60$. The results indicate that the differences between various solutions diminish as the spatial resolution increases, observed in terms of both reaction force and radial displacement.

Here, the elastic energy E_e is set as the refer energy, which is calculated using the formula $E_e = \frac{1}{2}F\Delta x$, with $F = 8000 \text{ N}$ and the stretching length $\Delta x = 10 \text{ mm}$ serving as reference values representing the maximum elastic energy attainable by the system, as the reaction force almost reaches 8000 N throughout the entire stretching process, as shown in Figure 5.9. To investigate the impact of the normalized kinetic energy threshold on simulation results, a series of stretching simulations with varying criteria were conducted. Figure 5.11 plots the variation in radial displacement and reaction force for different kinetic energy criteria when $dp = PH/40$, which suggests that $1\%_0 E_e$ is an

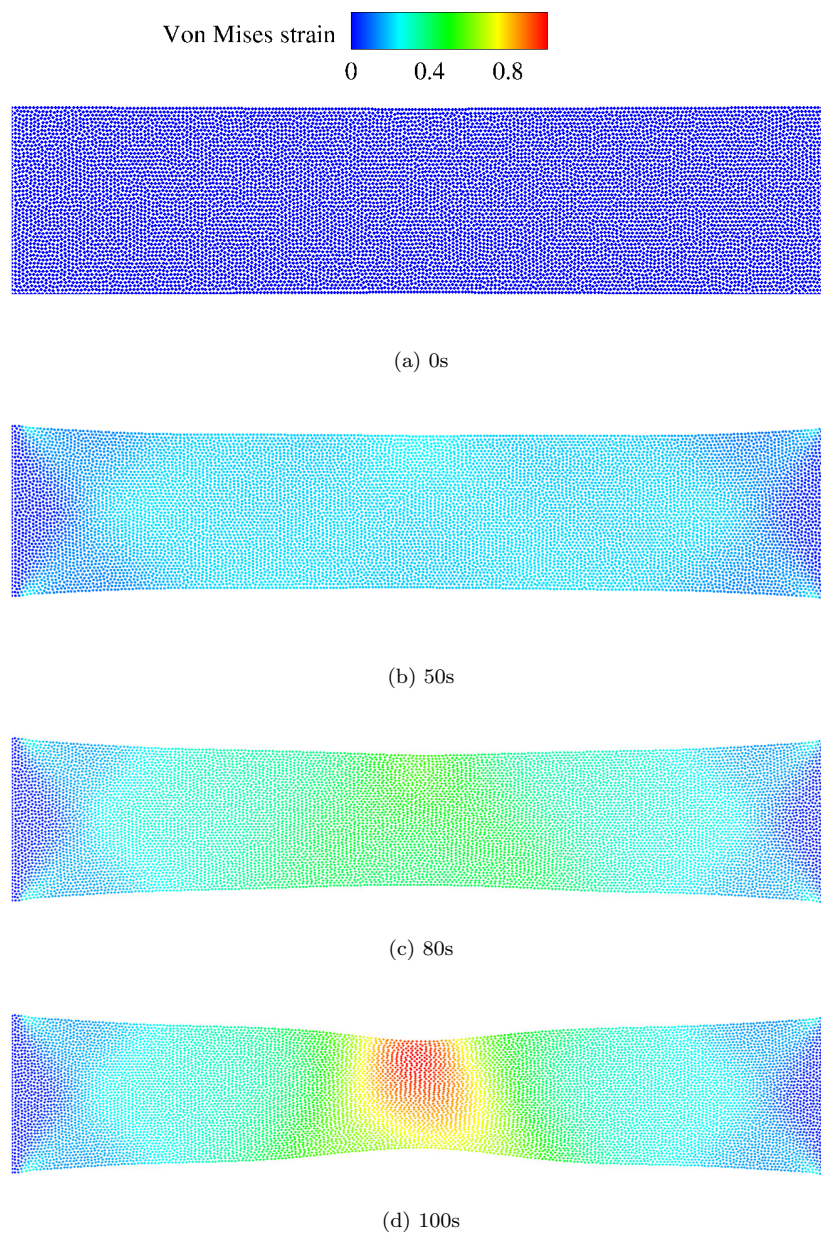


Figure 5.6: 2D tensile necking: the deformation colored by von Mises strain at different time instants.

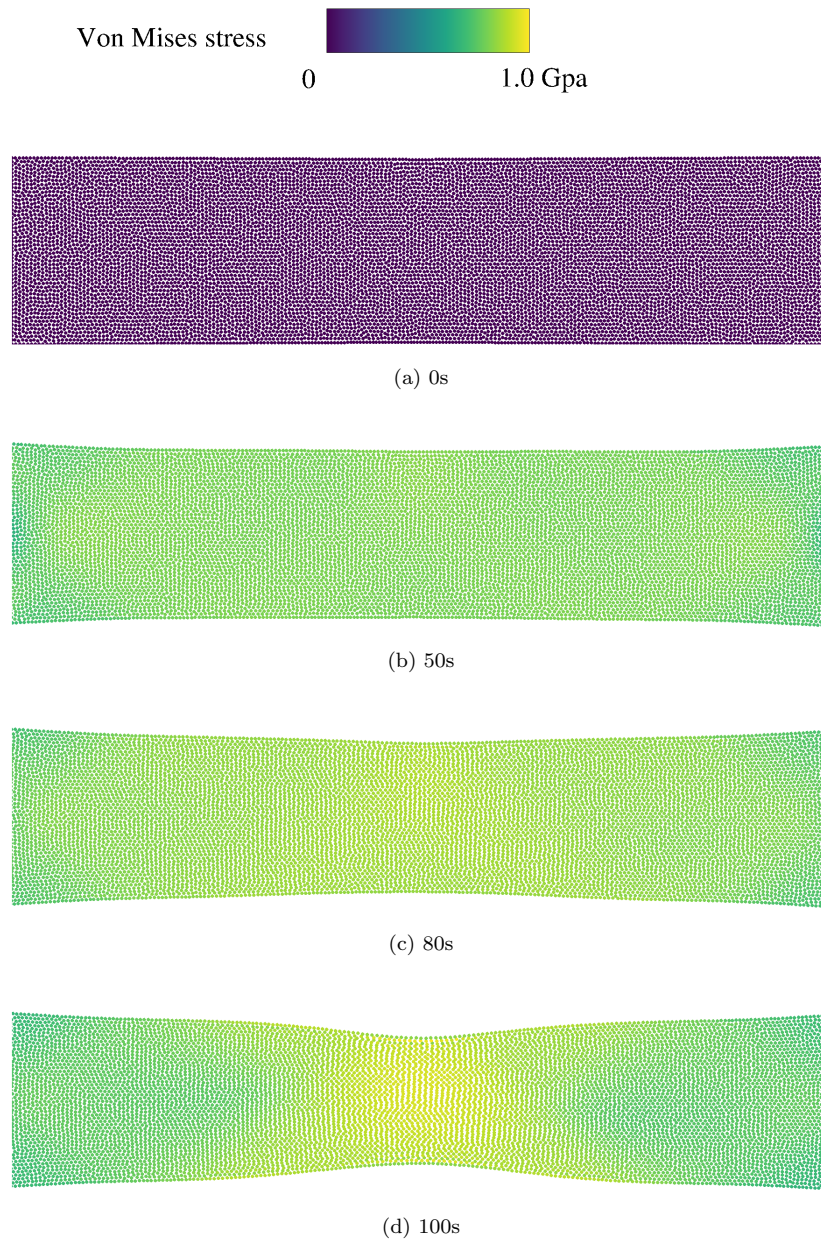


Figure 5.7: 2D tensile necking: the deformation colored by von Mises stress at different time instants.

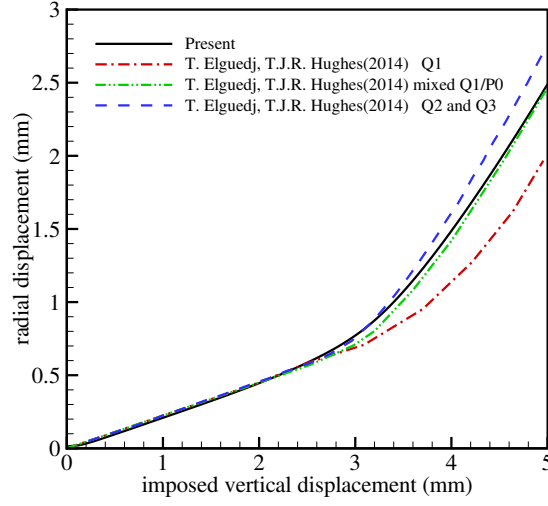


Figure 5.8: 2D tensile necking: the evolution of the radial displacement as a function of the imposed vertical displacement of the central part.

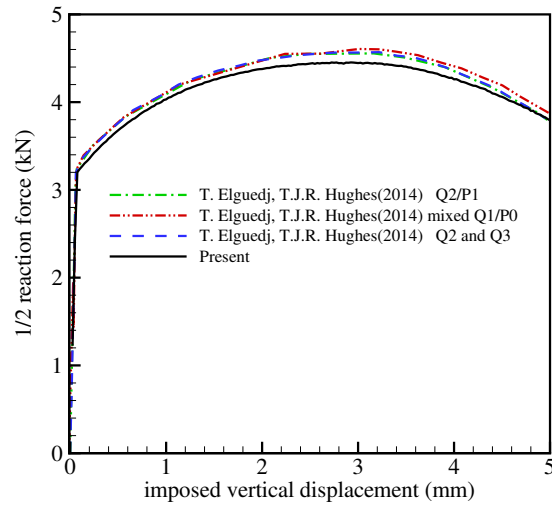


Figure 5.9: 2D tensile necking: the evolution of the reaction force versus the imposed vertical displacement.

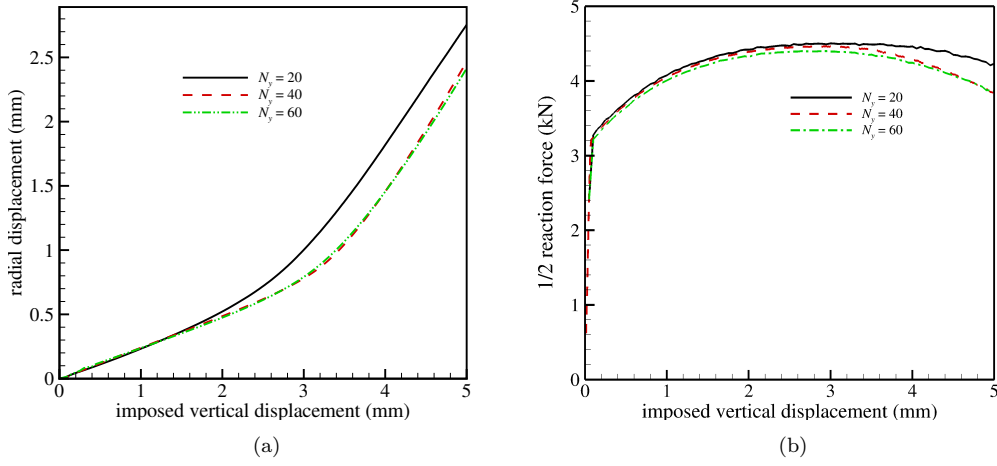


Figure 5.10: 2D tensile necking: radius displacement (a) and the loading force (b) convergence with different spatial resolutions.

appropriate kinetic energy criterion value for computational efficiency, as the difference between the criteria $1\%_0 E_e$ and $0.2\%_0 E_e$ is minimal. Note that both the comparison to reference results and convergence analyses are conducted under kinetic energy criterion of $1\%_0 E_e$.

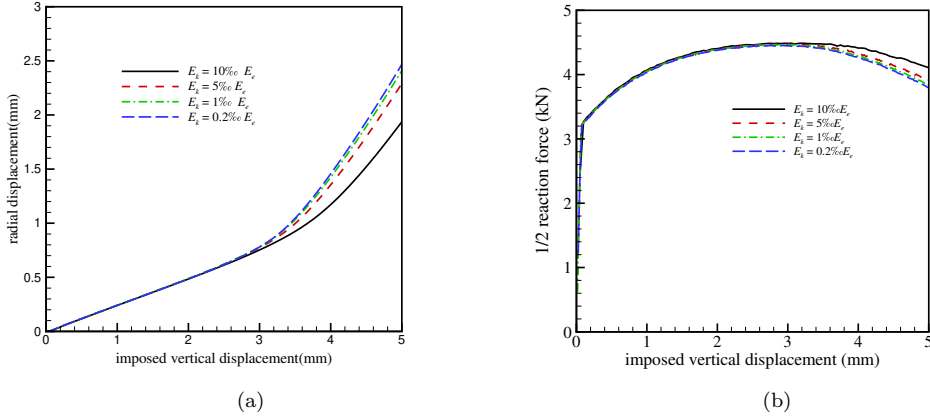


Figure 5.11: 2D tensile necking: radius displacement (a) and the loading force (b) convergence with different kinetic energy criteria.

The evolution of the kinetic energy after one stretching step at four different time instants, as evaluated by the elastic energy E_e , is depicted in Figure 5.12. As expected, here is a fluctuation in kinetic energy due to the stretching force. After each stretching event, the kinetic energy initially increases, followed by a decrease to a certain criterion value of $1\%_0 E_e$, attributable to the applied damping effects. The relative kinetic energy at the end of each stretching step approaches $1\%_0 E_e$, indicating that the system reaches equilibrium.

With a physical simulation time of $t = 100\text{s}$, due to the time step size limitation in explicit scheme, the number of stretching times N_S and stress relaxation times N_s performed in the simulation are expected to be $N_S = N_s = t/\Delta t_s = 4.43 \times 10^9$.

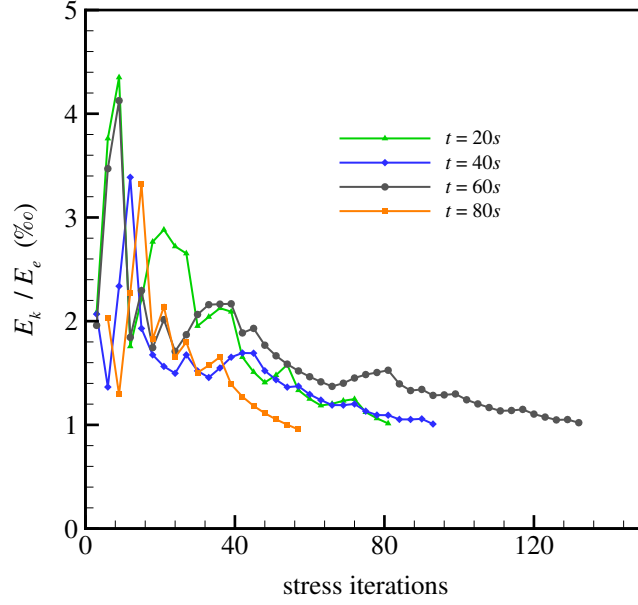


Figure 5.12: 2D tensile necking: evolution of kinetic energy evaluated by the elastic energy after one stretching at different time.

With this multi-time criteria algorithm, initially, the number of stretching time steps is reduced from 4.43×10^9 to $N_S = 1.0 \times 10^4$. Subsequently, the stress relaxation times are decreased from 4.43×10^9 to $N_s = 1.23 \times 10^6$ in this case by coupling the damping term to accelerate equilibrium attainment. Table 5.2 lists a comparison of the stress relaxation iterations performed in straightforward and multi-time step algorithms and quantifies the efficiency of the proposed algorithm compared to the straightforward one in terms of stretching N_S and stress relaxation iterations N_s , with the same total particle number N_p . It is obvious that the proposed algorithm yields a drastic reduction in computation time.

Table 5.2: 2D tensile necking: quantitative validation of the efficiency of this multi-time step algorithm.

algorithm	N_p	N_S	N_s	$N_{damping}$
straightforward algorithm	6948	4.43×10^9	4.43×10^9	-
multi-time step algorithm	6948	1.0×10^4	1.23×10^6	1.23×10^6

5.3. Necking of a three-dimensional bar

Further, a three-dimensional necking analysis of a cylindrical bar is conducted, a scenario previously investigated by Simo and Armero [53, 57], de Souza Neto et al. [54], Elguedj and Hughes [56]. The same geometry of radius 6.413 mm and length 53.334 mm with a slight reduction (1.8%) in the center of the bar as in the previous 2D case is considered. The loading is applied using displacement control, with a total stretching displacement of 6 mm applied on both side surfaces of the bar. The same material properties in Table 5.1 and elastic-plastic response as that applied in previous two-dimensional case are employed herein. In this case, initial particle spacing $dp =$

0.3 mm resulting in a total particle number of approximately $N_p = 2.5 \times 10^5$. With physical time of $t = 100$ s and stretching steps $N_S = 10000$, the corresponding stretching velocity is 0.06 mm/s, allowing the problem to be simulated in a real stretching rate. The damping ratio utilized is $\eta = 3.0 \times 10^4$ kg/(m·s).

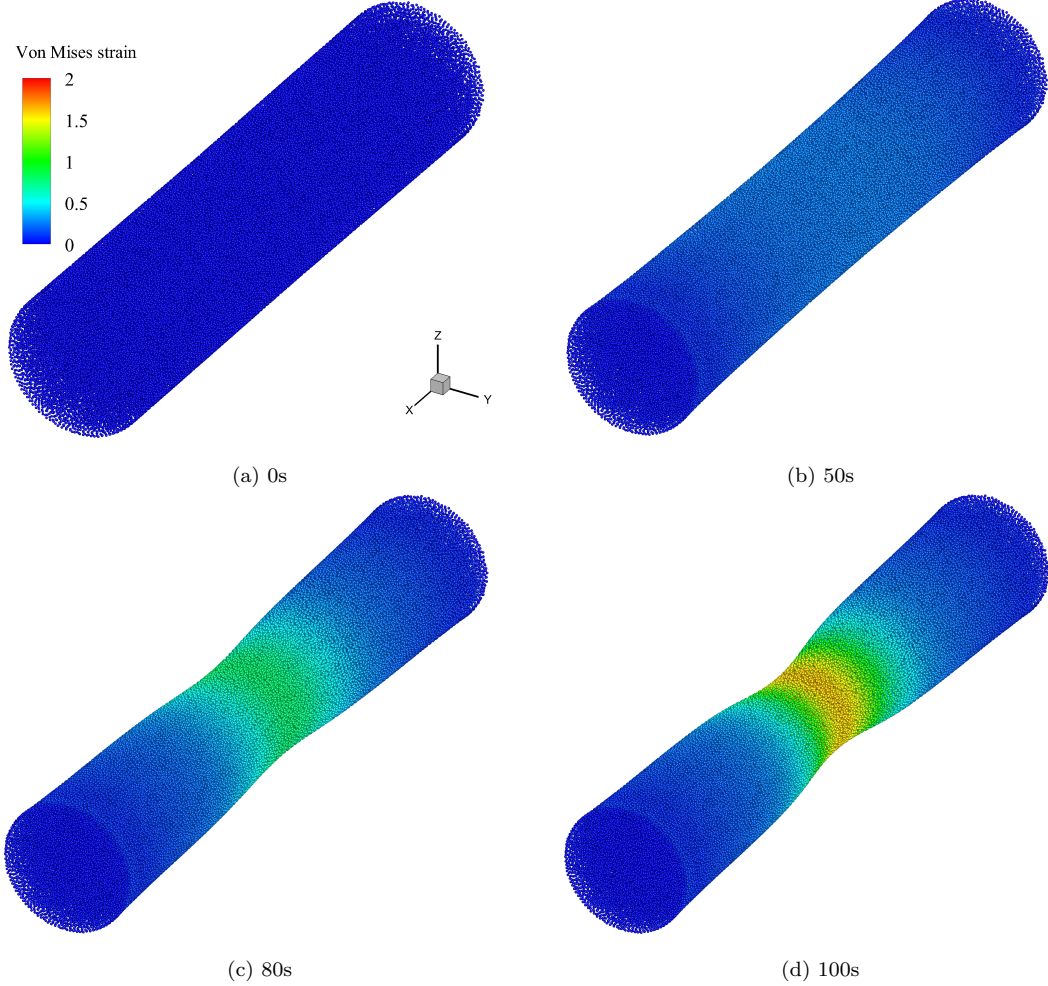


Figure 5.13: 3D tensile necking: the deformation colored by von Mises strain at different time instants.

Contour plots of the von Mises strain at different time instants from various perspectives are illustrated in Figure 5.13-5.14. Figure 5.15 illustrates the deformation evolution colored by von Mises stress and the plastic strain at various time instances, showing similar patterns with those in the reference [41]. The final plots display the deformed shape of the specimen at the final stage of the simulation, indicating the occurrence of necking in the center of the specimen. Based on these figures, we can infer the deformation evolution of this specimen: initially, the boundary conditions enabled the specimen to maintain a uniform elastic response in the short stage of the loading history; subsequently, in the post-peak regime, a diffuse necking mode emerged, ultimately leading to the formation of shear bands at high strain levels. These bands accumulated plastic deformations, ultimately resulting in the final necking even failure of the specimen. The evolution of this pattern is well-reproduced by the force and deformation data presented in Figures 5.16 and 5.17, which agrees well with experimental

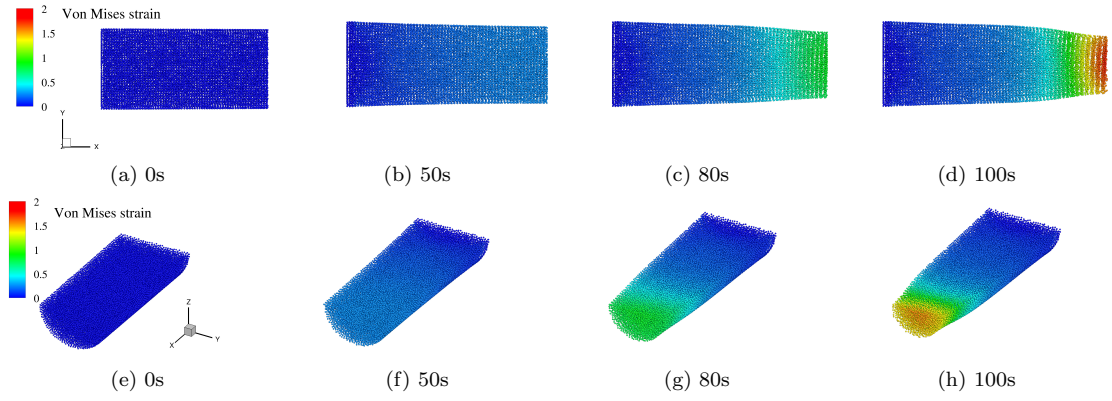


Figure 5.14: 3D tensile necking: the deformation colored by von Mises strain at different time instants, (a)-(d) top view of the quarter specimen, (e)-(h) top-side view of the half specimen.

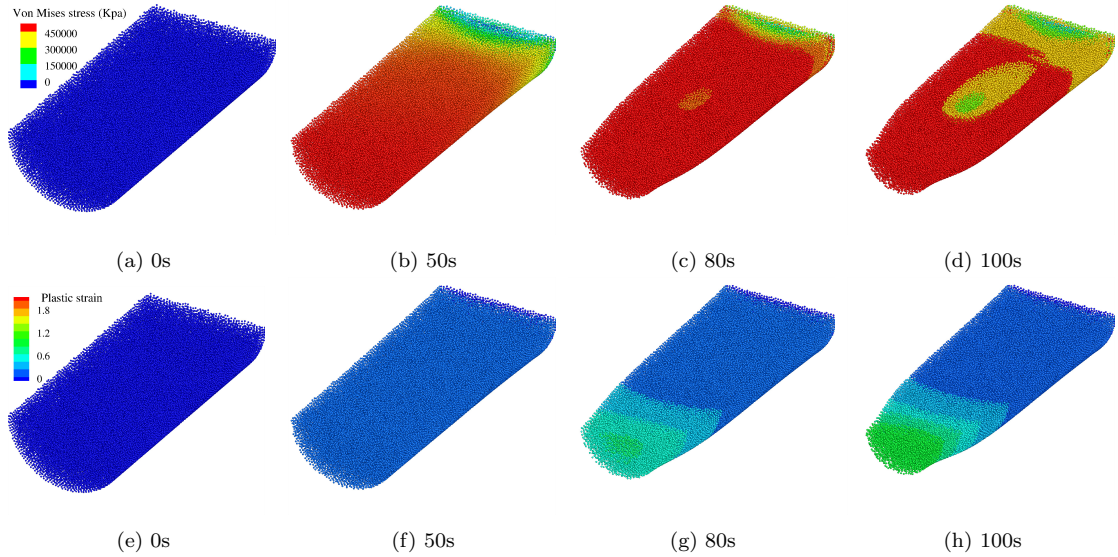


Figure 5.15: 3D tensile necking: the deformation colored by von Mises stress (a)-(d) and the corresponding plastic strain (e)-(h) at different time instants.

findings.

Specially, Figure 5.16 compiles the numerical data of the radius displacement, normalized by the initial radius, versus the length displacement, normalized by the initial bar length. The results are compared with experimental data and solutions reported in other works [41, 53, 58, 59]. The results obtained with the present method are in good agreement with the experimental and numerical data. The reaction force curve obtained from this simulation is presented in Figure 5.17 along with the results from other numerical works. While a slight difference is observed in the later stages, potentially attributed to the hourglass mode, the overall trend of the result curve aligns well with that of the references. Although this hourglass phenomenon cannot be fully removed in this study, which is also observed in prior research that utilized standard 3D elements in FEM [54], further improvements will be implemented in the future research.

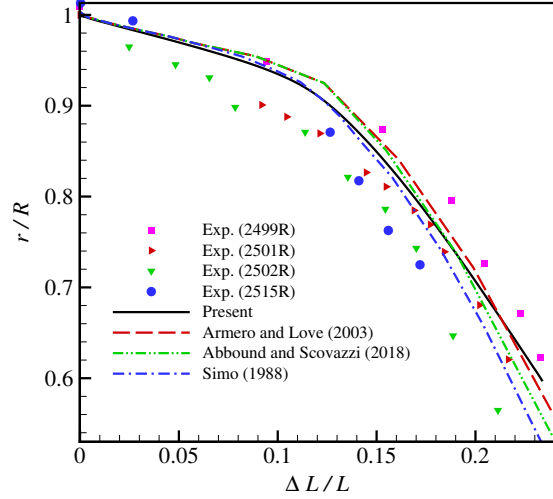


Figure 5.16: 3D tensile necking: the evolution of radial displacement of the central part compared with the reference [54, 56, 60].

As for determining the achievement of the static state, similar to the previous 2D case, the kinetic energy criterion is derived from the elastic energy $E_e = \frac{1}{2}F\Delta x$, where the load force is denoted as $F = 80000$ N, the rough reaction force value observed in Figure 5.17, and the stretching length $\Delta x = 0.014$ m. Employing the same method as in the 2D case, the results converge when the kinetic energy is reduced to $1\%E_e$. To assess the efficiency of the proposed algorithm, we computed the relaxation iterations and the results are summarized in Table 5.3. Evident reduction is obtained in stress relaxation times, saving the computation time significantly.

Table 5.3: 3D tensile necking: quantitative validation of the efficiency of this multi-time step algorithm.

algorithm	N_p	N_S	N_s	N_d
straightforward algorithm	250852	2.219	2.21×10^9	-
multi-time step algorithm	250852	1.0×10^4	3.21×10^5	3.21×10^5

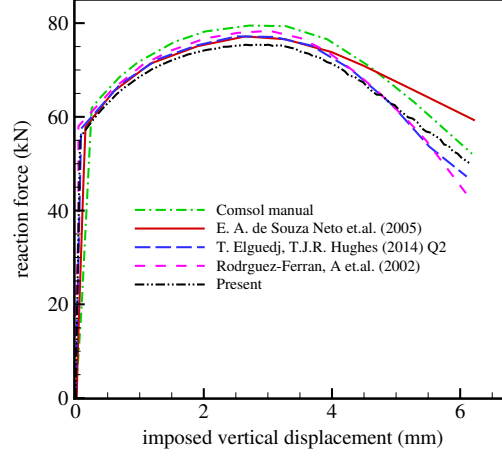


Figure 5.17: 3D tensile necking: the overall evolution of the reaction force versus the imposed vertical displacement compared with the reference [54, 56, 60].

5.4. Two-dimensional fluid-structure interaction

In this section, we perform a two-dimensional simulation of fluid diffusion coupling with porous solid deformation to validate the efficiency of the presented method. As illustrated in Figure 5.18, a thin porous beam with a length of $L = 10.0$ mm and width of $W = 0.125$ mm is considered. The left and right sides are constrained to prevent any curling or movement. The simulation starts with a fluid droplet contacting the center part of the beam, extending to a length of $0.3L$. This contact continues for 10 seconds while the total physical time is set to 100 seconds. Given the slender nature of the beam, we assume that initially, all pores in the upper half part are filled with fluid. As mentioned earlier, the relationship between fluid saturation \tilde{c} and solid porosity c is $0 \leq \tilde{c} \leq c < 1$. For this 2D and 3D cases discussed later, we assume a solid porosity of $c = 0.4$, implying that the fluid saturation \tilde{c} in the central part ($0.5W \times 0.3L$) is constrained to $\tilde{c} = c = 0.4$ for the initial 10 seconds, while in other regions $\tilde{c}_0 = 0.0$.

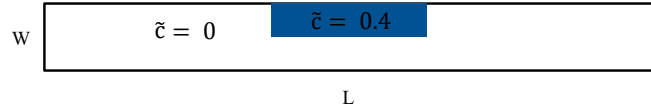


Figure 5.18: 2D fluid-structure interaction: physical configuration of the thin porous beam.

In alignment with the experimental setup, the solid material is modeled as a porous and elastic Nafion membrane, with water serving as the fluid. The physical properties and material parameters of this membrane are listed in Table 5.4. The pressure coefficient C has been calibrated to fit the experimentally measured flexure curves, while other parameters are obtained from previous research papers [61, 62]. In the simulation, eight particles are placed in the vertical direction, with a particle spacing of $dp = W/8 = 1.5625 \times 10^{-2}$ mm. In this simulation, an experienced damping ratio of $\eta = 10\eta_0 = 400$ kg/(m·s) in the damping term is utilized.

With the specified conditions, the simulation produces a deformed configuration colored by fluid saturation, illustrated in Figure 5.19. Initially, the presence of a water

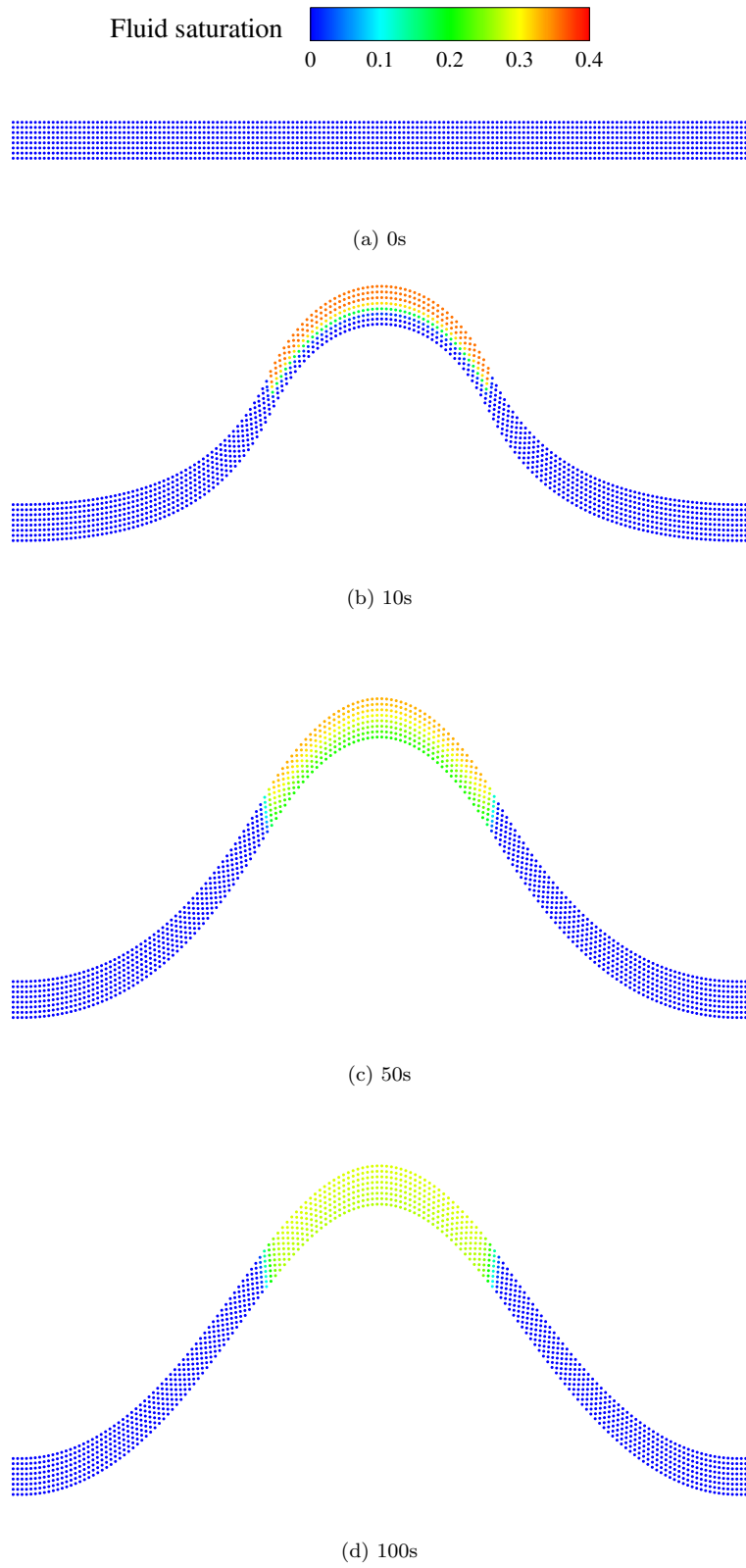


Figure 5.19: 2D fluid-structure interaction: the deformation colored by fluid saturation at different time instants.

Table 5.4: Fluid-structure interaction: physical material parameters value of Nafion film. Data estimated from Motupally and Goswami [61, 62].

Parameters	ρ (kg/m ³)	D (m ² /s)	Pressure coefficient C (MPa)	Young modulus (MPa)	Poisson ratio
Value	2000	1.0×10^{-10}	3.0	8.242	0.2631

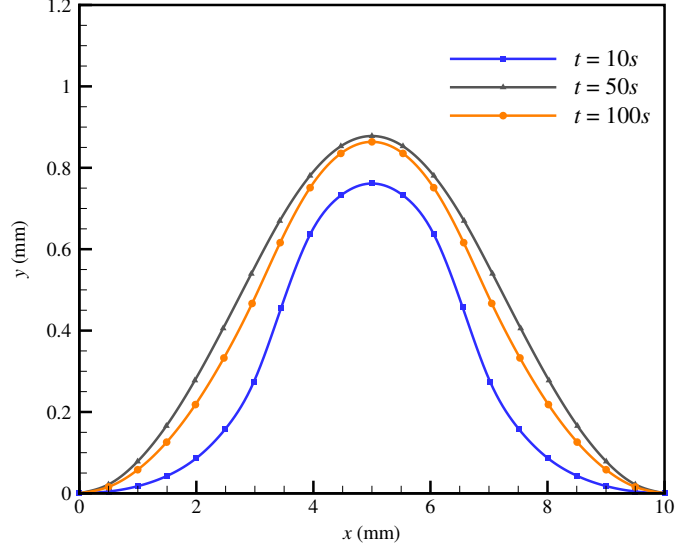


Figure 5.20: 2D fluid-structure interaction: bending amplitude of the beam at different time instants.

droplet in the upper central region induces fluid pressure, as explained in Eq. 46, leading to a localized bending in the central region. As time progresses, the saturation difference drives continuous water diffusion, causing an increase in the total water content within the porous solid and resulting in a rising flexure. This is also depicted in Figure 5.20, which records the vertical position y versus the horizontal x position of the beam at different time instants. After the contact concludes, no additional water is introduced into the beam, and the central water gradually flows into the side areas. The fluid saturation shows a smooth transition from the center to the surrounding area, as evident in Figure 5.19. Consequently, a more uniform pressure distribution develops, resulting in a smoother flexure of the beam as shown in Figure 5.20 in the later period. Given the the particle number in the y direction as $N_y = 4, 8, 12, 16$ respectively, the convergence test in terms of the resolution is carried out, as illustrated in Figure 5.21. The difference of beam bending amplitude at the final instant show a tendency to decrease as particle spacing becomes finer.

To establish the density kinetic energy criterion E_k , we utilize the pressure from water, p^l , stated in Eq. 46, as the reference since fluid pressure induces beam swelling. To evaluate the effect of the relative density kinetic energy threshold on the simulation results, a series of simulations are conducted with various criteria E_k . The final bending amplitude of the beam with different kinetic energy criteria is presented in Figure 5.22. Observations reveal that with a relatively large criterion value of $E_k = 5\%p^l$, the equilibrium state is not achieved and the energy is not fully eliminated with a relatively light deformation. Conversely, using a very small criterion value leads to unnecessary calculation steps, increasing computation time. Therefore, it is concluded that the

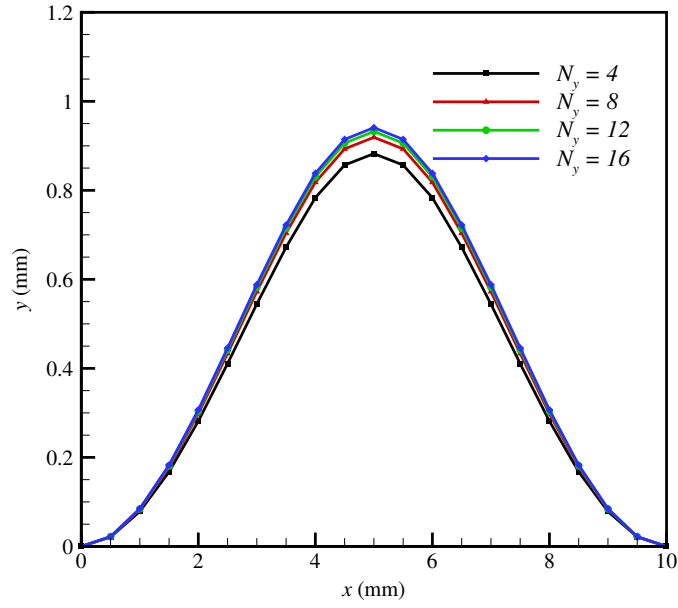


Figure 5.21: 2D fluid-structure interaction: the final bending amplitude convergence with different resolutions.

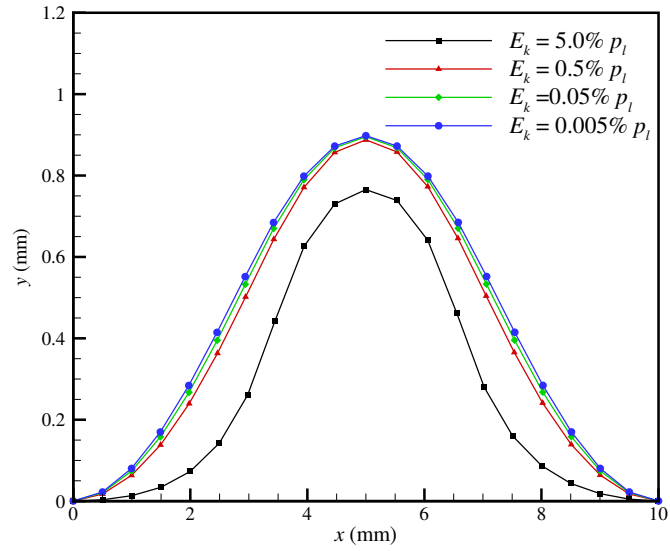


Figure 5.22: 2D fluid-structure interaction: bending amplitude convergence with different density kinetic energy criteria.

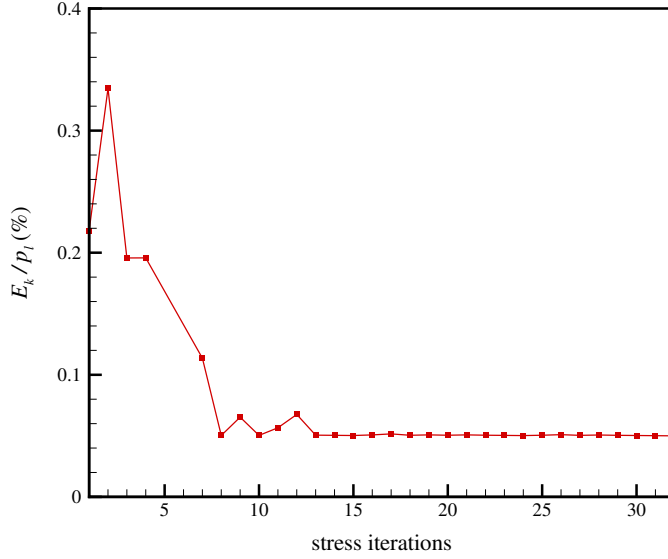


Figure 5.23: 2D fluid-structure interaction: the density kinetic energy variation within the diffusion period when $t = 20$ s valued by the water pressure p^l .

appropriate density kinetic energy criterion value for this 2D case is $0.05\%p^l$.

Referring to Figure 5.23, the evolution of the density kinetic energy during the diffusion period when $t = 20$ s, evaluated by the water pressure p^l , is presented. Due to water pressure, the density kinetic energy firstly experiences a peak after one diffusion performance, followed by a rapid decrease to a predetermined criterion value of $0.05\%p^l$, as set earlier, which is attributed to the damping effects. The relative density kinetic energy approaches $0.05\%p^l$ at the end of each diffusion step, indicating that the velocity almost vanishes, and equilibrium is achieved.

The efficiency of the proposed approach is demonstrated through Table 5.5, providing a quantitative comparison of the algorithm against the straightforward approach in terms of diffusion and stress relaxation iterations N_D , N_s with a total particle number N_p . The results reveal a great reduction in computation iterations, thus demonstrating the significant improvement in efficiency achieved by the proposed approach.

Table 5.5: 2D fluid-structure interaction: quantitative validation of the efficiency of this multi-time step algorithm.

algorithm	N_p	N_D	N_s	N_d
straightforward algorithm	1336	1.58×10^7	1.58×10^7	-
multi-time step algorithm	1336	125	3.25×10^5	3.25×10^5

5.5. Three-dimensional fluid-structure interaction

Next, we explore fluid diffusion coupling swelling in a three-dimensional film, specifically the diffusion of water within a porous Nafion membrane. This system has been previously investigated numerically by Zhao [27] and experimentally by Goswami [62]. This reference thin porous body takes the form of a polymer film with an x-y plane of dimensions $L_x = 10.0$ mm, $L_y = 10.0$ mm and a height of $L_z = 0.125$ mm. Four boundary

sides are constrained to prevent any curling or movement. The physical parameters are consistent with those listed in Table 5.4, and the initial conditions resemble those employed in the two-dimensional case. The central square part of the membrane in contact with water occupies a region of dimensions $0.3L_x \times 0.3L_y \times 0.5L_z$, and this contact lasts for 450 seconds, with the total physical time set to 2500 seconds. No fluid is allowed to diffuse out from the membrane. The fluid saturation \tilde{c} in the central square part is constrained to $\tilde{c} = c = 0.4$ for the initial 450 seconds, while in other regions $\tilde{c}_0 = 0$. With 4 particles set in z direction, the particle spacing $dp = W/4 = 3.125 \times 10^{-2}$ mm. In the stress relaxation process of the simulation, the experienced damping ratio is set to $\eta = 10\eta_0 = 400$ kg/(m·s). Regarding the convergence study of density kinetic energy criteria, following the same method as in the 2D case, the 3D case has a converged criterion value of $E_d = 0.1\% p^l$. In order to provide a more accurate representation of the experiment, the evaporation process is taken into consideration, acknowledging the gradual loss of water over time. During the initial period, deformation and flexure manifest, and subsequently, as the fluid mass diminishes from the membrane, a restoration of the original shape is observed.

Figure 5.24 illustrates membrane deformation colored by water saturation at different time instants. Over the first 450 seconds, the water amount continues to increase, leading to a rising flexure, as depicted in Figure 5.25, which records the time history of the height z of the central point. Once the contact period concludes, with no further water addition, central water gradually flows into the side areas. Concurrently, water evaporates from the membrane, resulting in a rapid decrease in water pressure and a corresponding reduction in flexure, as indicated by the blue line in Figure 5.25 beyond 450 seconds.

Figure 5.25 also presents corresponding data points from Goswami's experimental measurements [62] and results from other numerical models, showcasing the swelling degree of the central point versus different time instants. Evidently, the numerical simulation results exhibit good agreement with experimental results, capturing the deformation amplitude pattern, reproducing the increasing flexure during the water contact period and the subsequent decrease after the contact phase, consistent with saturation variations.

Drawing from the previous discussion, the optimal large outer time step is determined by the diffusion constant and the smoothing length, while the small inner time step is influenced by the material properties of the solid. Ideally, the outer time step allowed in principle is hundreds or thousands of times larger than the inner time step size allowed. However, in the standard explicit algorithm, the time step is limited to the smaller one, resulting in the execution of numerous stress relaxation steps and consuming a substantial amount of time. In the presented method, first, diffusion is performed with the larger time step, while stress relaxation is executed multiple times with damping effects until the kinetic energy threshold is reached. Our approach saves time in two ways. Firstly, the number of diffusion relaxation times is reduced since multi-time step algorithm allows diffusion to be performed with its own time step in the outer loop. Secondly, once the kinetic energy criterion is satisfied, equilibrium is considered achieved, and the inner loop is halted accordingly, avoiding unnecessary stress relaxation calculations. Figure 5.26 indicates the stress iterations N_s during this 3D simulation. There is a rapid increase in the initial 450 seconds when the fluid is in contact with the film, and then a slower increase in the later stages. Table 5.6 presents

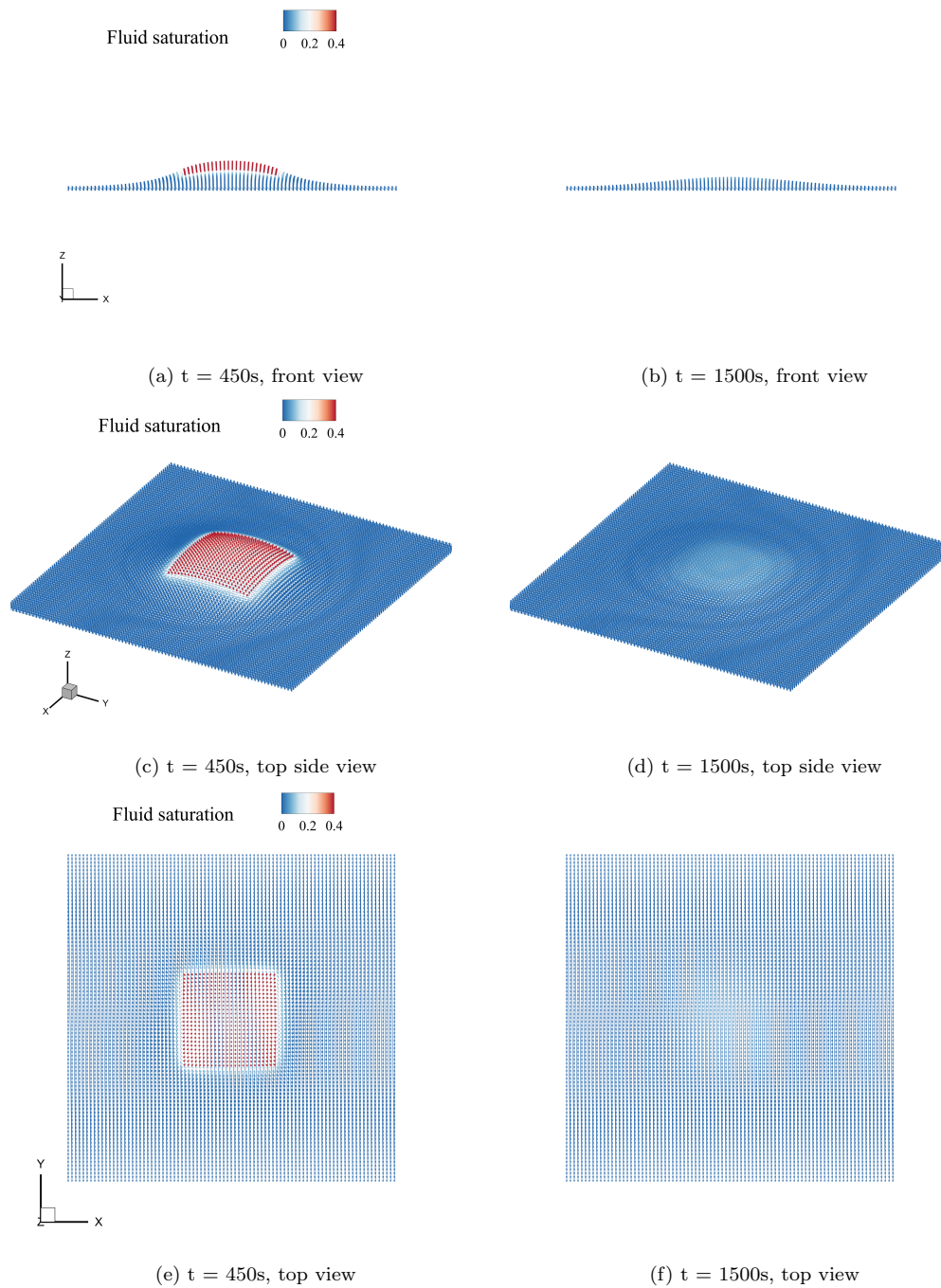


Figure 5.24: 3D fluid-structure interaction: the deformation colored by water saturation at different time instants.

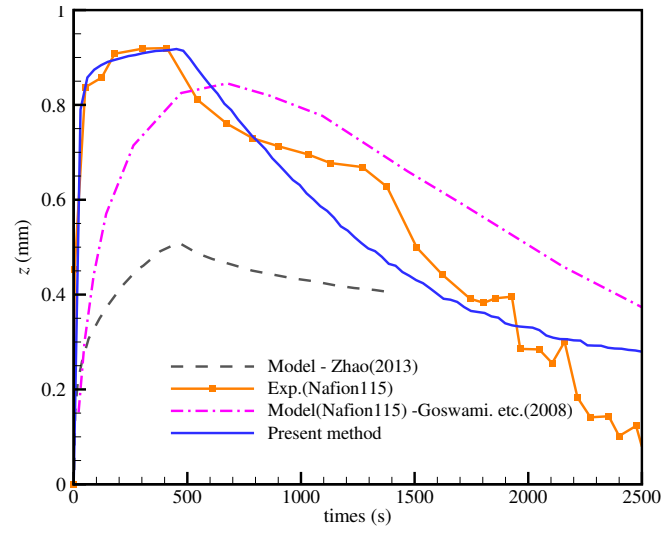


Figure 5.25: 3D fluid-structure interaction: bending amplitude of the center point compared with experimental data and results from other numerical models.

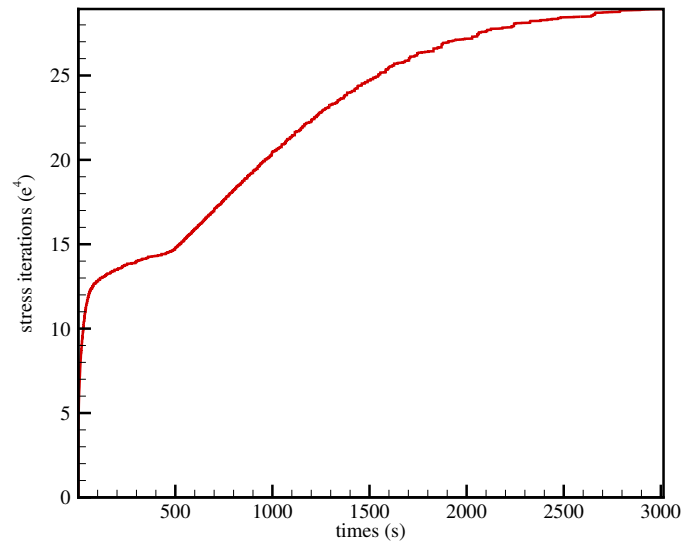


Figure 5.26: 3D fluid-structure interaction: the stress iterations history during the whole simulation.

the quantitative efficiency of our new algorithm compared to the straightforward one, by listing the diffusion iterations N_D and N_s separately. As shown in the table, both iterations are significantly reduced, representing a substantial improvement in saving computation time.

Table 5.6: 3D fluid-structure interaction: quantitative validation of the efficiency of this multi-time step algorithm.

algorithm	membrane	N_D	N_s	N_d
straightforward algorithm	60552	1.5×10^{10}	1.5×10^{10}	-
multi-time step algorithm	60552	1.25×10^5	2.89×10^6	2.89×10^6

6. Conclusion

This paper proposed an approach employing a multi-time step algorithm to address multi-time coupling problem involving solid dynamics. In this algorithm, the explicit scheme in time integration is utilized to simplify the solving of the equation system. Inner and outer loops with different time step sizes are conducted to accommodate various time scale process. A crucial aspect of this algorithm is the incorporation of a kinetic energy criterion to determine the equilibrium attainment of solid dynamics, along with a damping term to expedite this equilibrium process, This allows for the premature termination of the inner loop of solid stress relaxation, thereby avoiding redundant computations. Three types of multi-time coupling problem, including a manufactured torsional example, nonlinear hardening bar stretching and fluid diffusion in porous media coupling solid deformation are simulated to assess the performance of this algorithm. Results demonstrate both accuracy and a significant reduction in computation time. Furthermore, the application of this algorithm in practical fluid diffusion coupling hydrogel deformation paves the way for simulating complex multi-physics problems of multi-time scales in the field of complex chemistry reaction.

Authorship contribution statement

Xiaojing Tang made the methodology, designed the research, developed code and tested the present library components, performed the visualization and validation, and wrote the original draft of the manuscript. Dong Wu investigated the topic, made the methodology, developed code and tested the present library components, conducted the formal analysis, modified the draft. Zhentong Wang developed code and tested the present library components, and revised the manuscript. Oskar Haidn and Xiangyu Hu made the conceptualization, supervised and administered the project, and revised the manuscript.

Statements and Declarations

The authors have no known competing financial interests or personal relationships that could have appeared to influence the work reported in this paper.

Acknowledgments

Xiaojing Tang was partially supported by the China Scholarship Council (Grant No. 201906120034). Dong Wu was partially supported by the China Scholarship Council (Grant No. 20190613018). Dong Wu and Xiangyu Hu would like to express his gratitude to Deutsche Forschungsgemeinschaft (DFG) for their sponsorship of this research (Grant No. DFG HU1527/12-4).

References

- [1] L. B. Lucy, “A numerical approach to the testing of the fission hypothesis,” *The Astronomical Journal*, vol. 82, pp. 1013–1024, 1977.
- [2] R. A. Gingold and J. J. Monaghan, “Smoothed particle hydrodynamics: Theory and application to non-spherical stars,” *Monthly Notices of the Royal Astronomical Society*, vol. 181, no. 3, pp. 375–389, 1977.
- [3] J. J. Monaghan, “Simulating free surface flows with SPH,” *Journal of Computational Physics*, vol. 110, no. 2, pp. 399–406, 1994.
- [4] S. Shao, C. Ji, D. I. Graham, D. E. Reeve, P. W. James, and A. J. Chadwick, “Simulation of wave overtopping by an incompressible SPH model,” *Coastal engineering*, vol. 53, no. 9, pp. 723–735, 2006.
- [5] X. Zhang, H. Tian, L. Kuo, and W. Chen, “A contact sph method with high-order limiters for simulation of inviscid compressible flows,” *Communications in Computational Physics*, vol. 14, no. 2, pp. 425–442, 2013.
- [6] C. Zhang, G. Xiang, B. Wang, X. Hu, and N. Adams, “A weakly compressible SPH method with WENO reconstruction,” *Journal of Computational Physics*, vol. 392, pp. 1–18, 2019.
- [7] L. D. Libersky and A. G. Petschek, “Smooth particle hydrodynamics with strength of materials,” in *Advances in the Free-Lagrange Method Including Contributions on Adaptive Gridding and the Smooth Particle Hydrodynamics Method*. Springer, 1991, pp. 248–257.
- [8] J. J. Monaghan, “SPH without a tensile instability,” *Journal of Computational Physics*, vol. 159, no. 2, pp. 290–311, 2000.
- [9] C. Zhang, Y. Zhu, Y. Yu, D. Wu, M. Rezavand, S. Shao, and X. Hu, “An artificial damping method for total Lagrangian SPH method with application in biomechanics,” *Engineering Analysis with Boundary Elements*, vol. 143, pp. 1–13, 2022.
- [10] C. H. Lee, P. R. Refachinho de Campos, A. J. Gil, M. Giacomini, and J. Bonet, “An entropy-stable updated reference lagrangian smoothed particle hydrodynamics algorithm for thermo-elasticity and thermo-visco-plasticity,” *Computational Particle Mechanics*, vol. 10, no. 6, pp. 1493–1531, 2023.
- [11] A. Ghavamian, C. H. Lee, A. J. Gil, J. Bonet, T. Heuzé, and L. Stainier, “An entropy-stable smooth particle hydrodynamics algorithm for large strain thermo-elasticity,” *Computer Methods in Applied Mechanics and Engineering*, vol. 379, p. 113736, 2021.
- [12] C. Antoci, M. Gallati, and S. Sibilla, “Numerical simulation of fluid–structure interaction by SPH,” *Computers and Structures*, vol. 85, no. 11-14, pp. 879–890, 2007.

- [13] A. Khayyer, Y. Shimizu, H. Gotoh, and K. Nagashima, “A coupled incompressible sph-hamiltonian sph solver for hydroelastic fsi corresponding to composite structures,” *Applied Mathematical Modelling*, vol. 94, pp. 242–271, 2021.
- [14] A. Khayyer, H. Gotoh, and Y. Shimizu, “On systematic development of fsi solvers in the context of particle methods,” *Journal of Hydrodynamics*, vol. 34, no. 3, pp. 395–407, 2022.
- [15] A. Khayyer, Y. Shimizu, H. Gotoh, and S. Hattori, “A 3d sph-based entirely lagrangian meshfree hydroelastic fsi solver for anisotropic composite structures,” *Applied Mathematical Modelling*, vol. 112, pp. 560–613, 2022.
- [16] M. Liu and G. Liu, “Smoothed particle hydrodynamics (SPH): an overview and recent developments,” *Archives of computational methods in engineering*, vol. 17, no. 1, pp. 25–76, 2010.
- [17] J. J. Monaghan, “Smoothed particle hydrodynamics and its diverse applications,” *Annual Review of Fluid Mechanics*, vol. 44, pp. 323–346, 2012.
- [18] M. Luo, A. Khayyer, and P. Lin, “Particle methods in ocean and coastal engineering,” *Applied Ocean Research*, vol. 114, p. 102734, 2021.
- [19] C. Zhang, Y. Zhu, D. Wu, and X. Hu, “Review on smoothed particle hydrodynamics: Methodology development and recent achievement,” *arXiv preprint arXiv:2205.03074*, 2022.
- [20] H. Gotoh and A. Khayyer, “On the state-of-the-art of particle methods for coastal and ocean engineering,” *Coastal Engineering Journal*, vol. 60, no. 1, pp. 79–103, 2018.
- [21] J. U. Brackbill and B. I. Cohen, *Multiple time scales*. Academic Press, 2014, vol. 3.
- [22] D. Knoll, L. Chacon, L. Margolin, and V. Mousseau, “On balanced approximations for time integration of multiple time scale systems,” *Journal of Computational Physics*, vol. 185, no. 2, pp. 583–611, 2003.
- [23] T. Belytschko, H.-J. Yen, and R. Mullen, “Mixed methods for time integration,” *Computer Methods in Applied Mechanics and Engineering*, vol. 17, pp. 259–275, 1979.
- [24] W. K. Liu and T. Belytschko, “Mixed-time implicit-explicit finite elements for transient analysis,” *Computers & Structures*, vol. 15, no. 4, pp. 445–450, 1982.
- [25] A. Prior, “Applications of implicit and explicit finite element techniques to metal forming,” *Journal of Materials Processing Technology*, vol. 45, no. 1-4, pp. 649–656, 1994.
- [26] E. Gavalas, I. Pressas, and S. Papaefthymiou, “Mesh sensitivity analysis on implicit and explicit method for rolling simulation,” *International Journal of Structural Integrity*, 2018.

- [27] Q. Zhao and P. Papadopoulos, "Modeling and simulation of liquid diffusion through a porous finitely elastic solid," *Computational Mechanics*, vol. 52, no. 3, pp. 553–562, 2013.
- [28] D. Gaston, C. Newman, G. Hansen, and D. Lebrun-Grandie, "Moose: A parallel computational framework for coupled systems of nonlinear equations," *Nuclear Engineering and Design*, vol. 239, no. 10, pp. 1768–1778, 2009.
- [29] E. Gavalas and S. Papaefthymiou, "Brief overview on the application of finite element method on flat rolling processes," *Technology*, vol. 105, no. 1-2, pp. 110–118.
- [30] J. Sun, K. Lee, and H. Lee, "Comparison of implicit and explicit finite element methods for dynamic problems," *Journal of materials processing technology*, vol. 105, no. 1-2, pp. 110–118, 2000.
- [31] M. Rezaiee-Pajand and J. Alamatian, "The dynamic relaxation method using new formulation for fictitious mass and damping," *Structural engineering and mechanics*, vol. 34, no. 1, p. 109, 2010.
- [32] R. Yaghmaie and S. Ghosh, "Multi-time scale based modeling of piezoelectric materials coupling transient electrical and dynamic fields with finite deformation damage," *International Journal of Solids and Structures*, vol. 202, pp. 338–355, 2020.
- [33] J. C. Ragusa and V. S. Mahadevan, "Consistent and accurate schemes for coupled neutronics thermal-hydraulics reactor analysis," *Nuclear Engineering and Design*, vol. 239, no. 3, pp. 566–579, 2009.
- [34] L. Beuth, "Formulation and application of a quasi-static material point method," 2012.
- [35] F. Harewood and P. McHugh, "Comparison of the implicit and explicit finite element methods using crystal plasticity," *Computational Materials Science*, vol. 39, no. 2, pp. 481–494, 2007.
- [36] T. J. Hughes and W. Liu, "Implicit-explicit finite elements in transient analysis: Implementation and numerical examples," *Journal of Applied Mechanics, Transactions ASME*, vol. 45, no. 2, pp. 375–378, 1978.
- [37] T. Belytschko and R. Mullen, "Stability of explicit-implicit mesh partitions in time integration," *International Journal for Numerical Methods in Engineering*, vol. 12, no. 10, pp. 1575–1586, 1978.
- [38] T. Belytschko and Y. Lu, "Stability analysis of elemental explicit-implicit partitions by fourier methods," *Computer methods in applied mechanics and engineering*, vol. 95, no. 1, pp. 87–96, 1992.
- [39] C. A. Felippa and K.-C. Park, "Staggered transient analysis procedures for coupled mechanical systems: formulation," *Computer Methods in Applied Mechanics and Engineering*, vol. 24, no. 1, pp. 61–111, 1980.

- [40] S. Doll, K. Schweizerhof, R. Hauptmann, and C. Freischläger, “On volumetric locking of low-order solid and solid-shell elements for finite elastoviscoplastic deformations and selective reduced integration,” *Engineering Computations*, vol. 17, no. 7, pp. 874–902, 2000.
- [41] P. R. R. de Campos, A. J. Gil, C. H. Lee, M. Giacomini, and J. Bonet, “A new updated reference lagrangian smooth particle hydrodynamics algorithm for isothermal elasticity and elasto-plasticity,” *Computer Methods in Applied Mechanics and Engineering*, vol. 392, p. 114680, 2022.
- [42] Y. G. Rao, M. Nataraj, and P. Srinivas, “Explicit dynamic analysis of tensional & torsional propagations on composite material with dog bone shaped testing specimen,” *International Journal for Modern Trends in Science and Technology ISSN*, pp. 2455–3778, 2019.
- [43] M. Yılmaz, Ö. Anıl, B. Alyavuz, and E. Kantar, “Load displacement behavior of concrete beam under monotonic static and low velocity impact load,” *International Journal of Civil Engineering*, vol. 12, no. 4, pp. 488–503, 2014.
- [44] Y. Zhu, C. Zhang, and X. Hu, “A dynamic relaxation method with operator splitting and random-choice strategy for SPH,” *Journal of Computational Physics*, vol. 458, p. 111105, 2022.
- [45] R. Vignjevic, J. R. Reveles, and J. Campbell, “SPH in a total Lagrangian formalism,” *CMC-Tech Science Press-*, vol. 4, no. 3, p. 181, 2006.
- [46] P. Randles and L. D. Libersky, “Smoothed particle hydrodynamics: Some recent improvements and applications,” *Computer Methods in Applied Mechanics and Engineering*, vol. 139, no. 1-4, pp. 375–408, 1996.
- [47] J. J. Monaghan, “Smoothed particle hydrodynamics,” *Reports on Progress in Physics*, vol. 68, no. 8, p. 1703, 2005.
- [48] C. Zhang, Y.-j. Zhu, D. Wu, N. A. Adams, and X. Hu, “Smoothed particle hydrodynamics: Methodology development and recent achievement,” *Journal of Hydrodynamics*, vol. 34, no. 5, pp. 767–805, 2022.
- [49] P. W. Cleary and J. J. Monaghan, “Conduction modelling using smoothed particle hydrodynamics,” *Journal of Computational Physics*, vol. 148, no. 1, pp. 227–264, 1999.
- [50] L. Wang, W. M. Coombs, C. E. Augarde, M. Cortis, T. Charlton, M. Brown, J. Knappett, A. Brennan, C. Davidson, D. Richards *et al.*, “On the use of domain-based material point methods for problems involving large distortion,” *Computer Methods in Applied Mechanics and Engineering*, vol. 355, pp. 1003–1025, 2019.
- [51] K. P. Ruggirello and V. V. Nishawala, “Evaluating the material point method in cth using the method of manufactured solutions,” Sandia National Lab.(SNL-NM), Albuquerque, NM (United States), Tech. Rep., 2015.

- [52] K. Kamojjala, R. Brannon, A. Sadeghirad, and J. Guilkey, “Verification tests in solid mechanics,” *Engineering with Computers*, vol. 31, pp. 193–213, 2015.
- [53] J. C. Simo and T. J. Hughes, *Computational inelasticity*. Springer Science & Business Media, 2006, vol. 7.
- [54] E. D. S. Neto, F. A. Pires, and D. Owen, “F-bar-based linear triangles and tetrahedra for finite strain analysis of nearly incompressible solids. part I: Formulation and benchmarking,” *International Journal for Numerical Methods in Engineering*, vol. 62, no. 3, pp. 353–383, 2005.
- [55] C. A. de Saracibar, M. Chiumenti, Q. Valverde, and M. Cervera, “On the orthogonal subgrid scale pressure stabilization of finite deformation J2 plasticity,” *Computer Methods in Applied Mechanics and Engineering*, vol. 195, no. 9-12, pp. 1224–1251, 2006.
- [56] T. Elguedj and T. J. Hughes, “Isogeometric analysis of nearly incompressible large strain plasticity,” *Computer Methods in Applied Mechanics and Engineering*, vol. 268, pp. 388–416, 2014.
- [57] J.-C. Simo and F. Armero, “Geometrically non-linear enhanced strain mixed methods and the method of incompatible modes,” *International Journal for Numerical Methods in Engineering*, vol. 33, no. 7, pp. 1413–1449, 1992.
- [58] F. Armero and E. Love, “An arbitrary lagrangian–eulerian finite element method for finite strain plasticity,” *International Journal for Numerical Methods in Engineering*, vol. 57, no. 4, pp. 471–508, 2003.
- [59] J. C. Simo, “A framework for finite strain elastoplasticity based on maximum plastic dissipation and the multiplicative decomposition. part II: Computational aspects,” *Computer methods in applied mechanics and engineering*, vol. 68, no. 1, pp. 1–31, 1988.
- [60] A. Rodríguez-Ferran, A. Pérez-Foguet, and A. Huerta, “Arbitrary lagrangian–eulerian (ALE) formulation for hyperelastoplasticity,” *International Journal for Numerical Methods in Engineering*, vol. 53, no. 8, pp. 1831–1851, 2002.
- [61] S. Motupally, A. J. Becker, and J. W. Weidner, “Diffusion of water in Nafion 115 membranes,” *Journal of The Electrochemical Society*, vol. 147, no. 9, p. 3171, 2000.
- [62] S. Goswami, S. Klaus, and J. Benziger, “Wetting and absorption of water drops on Nafion films,” *Langmuir*, vol. 24, no. 16, pp. 8627–8633, 2008.
- [63] Y. Yue, B. Smith, C. Batty, C. Zheng, and E. Grinspun, “Continuum foam: A material point method for shear-dependent flows,” *ACM Transactions on Graphics (TOG)*, vol. 34, no. 5, pp. 1–20, 2015.
- [64] R. v. Mises, “Mechanik der festen körper im plastisch-deformablen zustand,” *Nachrichten von der Gesellschaft der Wissenschaften zu Göttingen, Mathematisch-Physikalische Klasse*, vol. 1913, pp. 582–592, 1913.

- [65] M. L. Wilkins, “Calculation of elastic-plastic flow,” California Univ Livermore Radiation Lab, Tech. Rep., 1963.
- [66] J.-P. Ponthot, “Unified stress update algorithms for the numerical simulation of large deformation elasto-plastic and elasto-viscoplastic processes,” *International Journal of Plasticity*, vol. 18, no. 1, pp. 91–126, 2002.
- [67] F. Dunne and N. Petrinic, *Introduction to computational plasticity*. OUP Oxford, 2005.
- [68] M.-H. Yu, *Generalized plasticity*. Springer Science & Business Media, 2006.
- [69] D. Gawin, P. Baggio, and B. A. Schrefler, “Coupled heat, water and gas flow in deformable porous media,” *International Journal for numerical methods in fluids*, vol. 20, no. 8-9, pp. 969–987, 1995.
- [70] J. Korsawe, G. Starke, W. Wang, and O. Kolditz, “Finite element analysis of poro-elastic consolidation in porous media: Standard and mixed approaches,” *Computer Methods in Applied Mechanics and Engineering*, vol. 195, no. 9-12, pp. 1096–1115, 2006.
- [71] J. Ghaboussi and E. L. Wilson, “Flow of compressible fluid in porous elastic media,” *International Journal for Numerical Methods in Engineering*, vol. 5, no. 3, pp. 419–442, 1973.
- [72] R. J. Atkin and R. Craine, “Continuum theories of mixtures: Basic theory and historical development,” *The Quarterly Journal of Mechanics and Applied Mathematics*, vol. 29, no. 2, pp. 209–244, 1976.

Appendix A Plasticity theory and nonlinear hardening plastic model

In this appendix, we present the J_2 plasticity theory coupling with a hardening elastic-plastic model to determine the plastic deformation. In A1, we describe the multiplicative decomposition technique for the material deformation. A2 presents the constitutive relation in this model. To describe the strain-stress evolution, the flow rule and a hardening plastic model is stated in A3. Then a return mapping algorithm is given in A4 to explain the time integration of strain and stress.

A.1 Multiplicative decomposition technique

To characterize the elastoplastic model, we adopt the flow plasticity theory, allowing for the multiplicative decomposition of total strain into elastic and plastic components [53, 63]. Using this technique, \mathbf{F} can be written as the product of its elastic volumetric part \mathbf{F}^e and plastic deviatoric part \mathbf{F}^p :

$$\mathbf{F} = \mathbf{F}^e \mathbf{F}^p. \quad (29)$$

And \mathbf{b}^e , the elastic part of the left Cauchy-Green tensor $\mathbf{b} = \mathbf{F}\mathbf{F}^T$, is defined as $\mathbf{b}^e = \mathbf{F}^e \mathbf{F}^{eT}$. When strains are within the elastic range, $\mathbf{F} = \mathbf{F}^e$ and $\mathbf{b} = \mathbf{b}^e$. For plasticity analysis, the plastic Lagrangian tensor \mathbf{C}^p is introduced as

$$\mathbf{C}^p = \mathbf{F}^{pT} \mathbf{F}^p. \quad (30)$$

The relationship between \mathbf{b}^e and \mathbf{C}^p can be described as

$$\mathbf{b}^e = \mathbf{F} \mathbf{C}^{p-1} \mathbf{F}^T. \quad (31)$$

Additionally, to adhere to the volume preserving assumption in plasticity, we assume that the determinant of the plastic deformation part $\det(\mathbf{F}^p) = 1$.

A.2 Constitutive relation

According to the theoretical framework proposed by Simo and Hughes [53], and adopting an isotropic stress response assumption, the elastoplastic constitutive model incorporates a nonlinear elastic strain energy function, decomposed into volumetric and deviatoric parts as

$$\mathfrak{W} = \mathfrak{W}_v(J) + \mathfrak{W}_s(\bar{\mathbf{b}}^e), \quad (32)$$

where $\bar{\mathbf{b}}^e$ is the elastic part of volume-preserving left-Cauchy Green tensor. The volumetric part, weighted by the bulk modulus K , is given by

$$\mathfrak{W}_v(J) = \frac{1}{2} K \left[\frac{1}{2} (J^2 - 1) - \ln J \right]. \quad (33)$$

The deviatoric part, related to the shear modulus μ , is obtained by

$$\mathfrak{W}_s(\bar{\mathbf{b}}^e) = \frac{1}{2} \mu [\text{Tr}(\bar{\mathbf{b}}^e) - D]. \quad (34)$$

Here, $D = \{1, 2, 3\}$ depends on the dimension of the problem. With E denoting Young's modulus and ν the Poisson ratio, the bulk and shear moduli are interconnected through the relationship:

$$E = 2\mu(1 + \nu) = 3K(1 - 2\nu). \quad (35)$$

With the energy function Eq. (32) in hand, the Kirchhoff stress tensor, representing the stress response, can be formulated as

$$\boldsymbol{\tau} = \frac{\partial W}{\partial \mathbf{F}^e} \mathbf{F}^{eT} = \frac{\kappa}{2} (J^2 - 1) \mathbf{I} + \mu \operatorname{dev}(\bar{\mathbf{b}}^e), \quad (36)$$

where the two terms on the right-hand side correspond to the volumetric and shear stresses, respectively. Note that in the equations above, the expression

$$\bar{\mathbf{T}} = [\det(\mathbf{T})]^{-1/3} \mathbf{T} \quad (37)$$

indicates the volume preserving treatment for a tensor \mathbf{T} . Additionally,

$$\operatorname{dev}(\mathbf{T}) = \mathbf{T} - \frac{\operatorname{Tr}(\mathbf{T})}{3} \mathbf{I} \quad (38)$$

represents the trace free part of the tensor \mathbf{T} , i.e., $\operatorname{Tr}[\operatorname{dev}(\mathbf{T})] = 0$.

A.3 Flow rule and hardening plasticity model

With the flow plasticity theory, a flow rule is needed to determine the orientation and magnitude of plastic deformation. In this paper, the classical J_2 flow theory, also known as the Mises–Huber yield condition proposed by Hube and von Mises [64], is used to model plastic stress-strain evolution. This theory states that the plastic behavior is governed by the deviatoric part of the Kirchhoff stress tensor $\boldsymbol{\tau}$, represented by the second term $\mu \operatorname{dev}(\bar{\mathbf{b}}^e)$ on the right side of Eq. (36). For simplicity, we define $\mathbf{s} = \operatorname{dev}(\boldsymbol{\tau}) = \mu \operatorname{dev}(\bar{\mathbf{b}}^e)$, and the normalized tensor of \mathbf{s} is given by $\hat{\mathbf{s}} = \mathbf{s}/s$, where the magnitude scalar $s = \|\mathbf{s}\|_F$ is computed using the Frobenius norm $\|\cdot\|_F$.

In mechanical engineering, isotropic work-hardening plastic behavior is frequently encountered. To incorporate this behavior, a scalar yield function $f(\boldsymbol{\tau}, \alpha)$ that depends on the hardening function $k(\alpha)$ is introduced, where α represents the equivalent plastic strain. The yield function is formulated as

$$f(\boldsymbol{\tau}, \alpha) = \|\operatorname{dev}(\boldsymbol{\tau})\|_F - \sqrt{\frac{2}{3}} k(\alpha) = s - \sqrt{\frac{2}{3}} k(\alpha), \quad (39)$$

where $k(\alpha)$ is defined by a nonlinear isotropic hardening law, as proposed by Simo et al. [53, 56]:

$$k(\alpha) = \sigma_0 + (\sigma_\infty - \sigma_0) [1 - \exp(-\delta\alpha)] + H\alpha, \quad (40)$$

Here, σ_0 represents the initial flow stress, also called yield stress, σ_∞ the saturation flow stress, δ the saturation exponent ($\delta > 0$), and H the linear hardening coefficient. The yield function f establishes the yield surface when $f = 0$, and classifies the purely elastic response when $f < 0$. When the yield condition is violated ($f > 0$), the stress response to deformation consists of both plastic and elastic components. Once the deformation enters the plastic regime, the material cannot revert to its original shape, undergoing a permanently plastic deformation.

A.4 Return mapping algorithm

To integrate the material deformation over time, the return mapping algorithm, which has been widely applied in literature [59, 65–68], is applied here. In this algorithm, the deviatoric part of the Kirchhoff stress tensor $\mathbf{s}^{pre} = \text{dev}(\boldsymbol{\tau}^{pre}) = \mu \text{dev}(\bar{\mathbf{b}}^{e,pre})$ is obtained using the predicted update of $\mathbf{b}^{e,pre}$, considering only the elastic strain. The yield condition is then checked using Eq. (39) to determine if plastic deformation occurs. If $f < 0$, the strain in the current step remains elastic, and the predicted update $\mathbf{b}^{e,pre}$ is considered acceptable. Otherwise, plastic correction (returning map) is introduced to obtain the final \mathbf{b}^e and \mathbf{s} for the next step. The framework of this algorithm is presented in Algorithm 1.

Appendix B Fluid-structure interaction model

In this appendix, we reference Zhao’s algorithm [27] to provide a concise overview of the porosity assumption for porous media model and its associated relations, including porosity and fluid saturation (B.1), as well as stress relations (B.2). In this mixture model, the definition of state variables including solid density ρ^s , locally fluid density ρ^l , solid velocity \mathbf{v}^s , and fluid saturation \tilde{c} enables the fluid velocity to be calculated with reference to the solid velocity. This simplified approach is practically significant, notably reducing the system complexity by eliminating the necessity for two separate sets of equations to describe the fluid and solid separately.

B.1 Porosity and fluid saturation

Considering a representative volume element dV , the macroscopic porosity c is defined as the ratio of the total volume of the pores dV^p to dV , yielding $c = \frac{dV^p}{dV}$. Note that $0 < c < 1$ holds for all cases. When the porous solid is partially saturated by fluid, the fluid saturation level \tilde{c} can be defined as

$$\tilde{c} = \frac{dV^l}{dV}, \quad (41)$$

where dV^l denotes the fluid volume in the representative element dV . Clearly, \tilde{c} is always less than or equal to the maximum possible saturation c , i.e., $\tilde{c} \leq c$. The locally effective fluid density ρ^l , defined as the mass of the fluid per unit volume, varies depending on the extent of fluid saturation and can be expressed as

$$\rho^l = \frac{dm^l}{dV} = \frac{dm^l}{dV^l} \frac{dV^l}{dV} = \rho^L \tilde{c}, \quad (42)$$

where dm^l represents the mass of the fluid within dV , ρ^L the fluid density which is assumed to be a constant for incompressible fluids.

B.2 Effective stress on solid

Following [69–72], the total stress acting on the solid is the sum of Cauchy stress $\boldsymbol{\sigma}^s$ due to deformation and the pressure stress $\boldsymbol{\sigma}^l$ due to the presence of the fluid phase, written as:

$$\boldsymbol{\sigma} = \boldsymbol{\sigma}^s + \boldsymbol{\sigma}^l = \boldsymbol{\sigma}^s - p^l \mathbf{I}. \quad (43)$$

where p^l is fluid pressure. For a hyper-elastic material, the constitutive equation for the solid component is given by

$$\boldsymbol{\sigma}^s = 2\mu\mathbf{e} + \lambda\text{tr}(\mathbf{e})\mathbf{I}, \quad (44)$$

where the Eulerian-Almansi finite strain tensor \mathbf{e} can be evaluated by

$$\mathbf{e} = \frac{1}{2}(\mathbf{I} - \mathbf{F}^T\mathbf{F}). \quad (45)$$

The Lamé parameter λ can be calculated via shear modulus μ and bulk modulus K as $\lambda = K - \frac{2\mu}{3}$.

The fluid pressure solely depends on the fluid saturation level within the porous solid element, represented by a function $p^l = p^l(\tilde{c})$. The relationship between fluid diffusion and the solid deformation satisfies a fundamental principle: The correlation between fluid diffusion and solid deformation adheres to a fundamental principle: as fluid flows out of a given zone, the saturation level decreases, resulting in a drop of pressure, and consequently, the material tends to contract inwardly. Conversely, when fluid penetrates a porous solid area, there exists a higher saturation level corresponding to a stronger pressure, leading to a material expansion. In the present model, this behavior is described mathematically by applying a linear relation, taking the form

$$p^l = C(\tilde{c} - \tilde{c}_0), \quad (46)$$

where C is a material constant, \tilde{c}_0 the initial saturation. Details can be referred to [72].

Algorithm 1: Return mapping algorithm for J_2 flow theory with nonlinear isotropic hardening.

1 Update deformation tensor

$$\mathbf{F}_{n+1} = \Delta t \frac{d\mathbf{F}}{dt}, \quad \bar{\mathbf{F}}_{n+1} = [\det(\mathbf{F}_{n+1})]^{-1/3} \mathbf{F}_{n+1}$$

2 Predict the elastic

$$\bar{\mathbf{b}}_{n+1}^{e,\text{pre}} = \bar{\mathbf{F}}_{n+1} \bar{\mathbf{C}}_p^{n-1} \bar{\mathbf{F}}_{n+1}^T, \quad \mathbf{s}_{n+1}^{\text{pre}} = \mu \operatorname{dev}(\bar{\mathbf{b}}_{n+1}^{e,\text{pre}})$$

3 Check the von Mises criterion

$$f_{n+1}^{\text{pre}} = s_{n+1}^{\text{pre}} - \sqrt{\frac{2}{3}} k(\alpha_n)$$

4 **if** $f_{n+1}^{\text{pre}} \leq 0$ **then**

5 Elastic state, Set $(\cdot)_{n+1} = (\cdot)_{n+1}^{\text{pre}}$, go to 10.

6 **else**

7 Perform 9 (the return mapping).

8 **end**

9 Compute the normlized shear modulus

$$\tilde{\mu} = \frac{1}{3} \operatorname{Tr}(\bar{\mathbf{b}}_{n+1}^{e,\text{pre}}) \mu$$

Initiate

$$\Delta\gamma = 0$$

Compute $\Delta\gamma$ so that

$$\hat{f}(\Delta\gamma) = \|\mathbf{s}_{n+1}^{\text{trial}}\| - \sqrt{\frac{2}{3}} k \left(\alpha_n + \sqrt{\frac{2}{3}} \Delta\gamma \right) - 2\tilde{\mu} \Delta\gamma = 0$$

$$\hat{\mathbf{s}} = \mathbf{s}_{n+1}^{\text{pre}} / s_{n+1}^{\text{pre}}$$

Return mapping

$$\mathbf{s}_{n+1} = \mathbf{s}_{n+1}^{\text{pre}} - 2\tilde{\mu} \Delta\gamma \hat{\mathbf{s}}, \quad \alpha_{n+1} = \alpha_n + \sqrt{\frac{2}{3}} \Delta\gamma$$

10 Update stress

$$J_{n+1} = \det(\mathbf{F}_{n+1}), \quad \boldsymbol{\tau}_{n+1} = \frac{\kappa}{2} (J_{n+1}^2 - 1) \mathbf{I} + \mathbf{s}_{n+1}, \quad \mathbf{P}_{n+1} = \boldsymbol{\tau}_{n+1} \mathbf{F}_{n+1}^{-T}$$

11 Update local configuration

$$\bar{\mathbf{b}}_{n+1}^e = \frac{1}{\mu} \mathbf{s}_{n+1} + \frac{1}{3} \operatorname{Tr}(\bar{\mathbf{b}}_{n+1}^{e,\text{pre}}) \mathbf{I}, \quad \bar{\mathbf{C}}_p^{n+1} = \bar{\mathbf{F}}_{n+1}^{-1} \bar{\mathbf{b}}_{n+1}^e \bar{\mathbf{F}}_{n+1}^{-T}$$

Bibliography

- [1] Al-Amiri, A. and Khanafer, K. “Fluid–structure interaction analysis of mixed convection heat transfer in a lid-driven cavity with a flexible bottom wall”. In: *International Journal of Heat and Mass Transfer* 54.17-18 (2011), pp. 3826–3836.
- [2] Atkin, R. J. and Craine, R. “Continuum theories of mixtures: Basic theory and historical development”. In: *The Quarterly Journal of Mechanics and Applied Mathematics* 29.2 (1976), pp. 209–244.
- [3] Belytschko, T. and Lu, Y. “Stability analysis of elemental explicit-implicit partitions by Fourier methods”. In: *Computer methods in applied mechanics and engineering* 95.1 (1992), pp. 87–96.
- [4] Belytschko, T. and Mullen, R. “Stability of explicit-implicit mesh partitions in time integration”. In: *International Journal for Numerical Methods in Engineering* 12.10 (1978), pp. 1575–1586.
- [5] Belytschko, T., Yen, H.-J., and Mullen, R. “Mixed methods for time integration”. In: *Computer Methods in Applied Mechanics and Engineering* 17 (1979), pp. 259–275.
- [6] Beuth, L. “Formulation and application of a quasi-static material point method”. In: (2012).
- [7] Bicknell, G. and Gingold, R. “On tidal detonation of stars by massive black holes”. In: *The Astrophysical Journal* 273 (1983), pp. 749–760.
- [8] Brackbill, J. U. and Cohen, B. I. *Multiple time scales*. Vol. 3. Academic Press, 2014.
- [9] Campos, P. R. R. de, Gil, A. J., Lee, C. H., Giacomini, M., and Bonet, J. “A New Updated Reference Lagrangian Smooth Particle Hydrodynamics algorithm for isothermal elasticity and elasto-plasticity”. In: *Computer Methods in Applied Mechanics and Engineering* 392 (2022), p. 114680.
- [10] Chen, J.-S. and Wang, D. “A constrained reproducing kernel particle formulation for shear deformable shell in Cartesian coordinates”. In: *International Journal for Numerical Methods in Engineering* 68.2 (2006), pp. 151–172.
- [11] Cleary, P. W. and Monaghan, J. J. “Conduction modelling using smoothed particle hydrodynamics”. In: *Journal of Computational Physics* 148.1 (1999), pp. 227–264.
- [12] Ding, M., Han, X., Wang, S., Gast, T. F., and Teran, J. M. In: *ACM Transactions on Graphics (TOG)* 38.6 (2019), pp. 1–14.
- [13] Doll, S., Schweizerhof, K., Hauptmann, R., and Freischläger, C. “On volumetric locking of low-order solid and solid-shell elements for finite elastoviscoplastic deformations and selective reduced integration”. In: *Engineering Computations* 17.7 (2000), pp. 874–902.
- [14] Farrokhpanah, A., Bussmann, M., and Mostaghimi, J. “New smoothed particle hydrodynamics (SPH) formulation for modeling heat conduction with solidification and melting”. In: *Numerical Heat Transfer, Part B: Fundamentals* 71.4 (2017), pp. 299–312.

- [15] Felippa, C. A. and Park, K.-C. “Staggered transient analysis procedures for coupled mechanical systems: formulation”. In: *Computer Methods in Applied Mechanics and Engineering* 24.1 (1980), pp. 61–111.
- [16] Fu, L., Hu, X. Y., and Adams, N. A. “Adaptive anisotropic unstructured mesh generation method based on fluid relaxation analogy”. In: *Communications in Computational Physics*, doi 10 (2020).
- [17] Gaston, D., Newman, C., Hansen, G., and Lebrun-Grandie, D. “MOOSE: A parallel computational framework for coupled systems of nonlinear equations”. In: *Nuclear Engineering and Design* 239.10 (2009), pp. 1768–1778.
- [18] Gavalas, E. and Papaefthymiou, S. “Brief Overview on the Application of Finite Element Method on Flat Rolling Processes”. In: *Technology* 105.1-2 (), pp. 110–118.
- [19] Gavalas, E., Pressas, I., and Papaefthymiou, S. “Mesh sensitivity analysis on implicit and explicit method for rolling simulation”. In: *International Journal of Structural Integrity* (2018).
- [20] Gawin, D., Baggio, P., and Schrefler, B. A. “Coupled heat, water and gas flow in deformable porous media”. In: *International Journal for numerical methods in fluids* 20.8-9 (1995), pp. 969–987.
- [21] Ghaboussi, J. and Wilson, E. L. “Flow of compressible fluid in porous elastic media”. In: *International Journal for Numerical Methods in Engineering* 5.3 (1973), pp. 419–442.
- [22] Ghalambaz, M., Jamesahar, E., Ismael, M. A., and Chamkha, A. J. “Fluid-structure interaction study of natural convection heat transfer over a flexible oscillating fin in a square cavity”. In: *International Journal of Thermal Sciences* 111 (2017), pp. 256–273.
- [23] Ghavamian, A., Lee, C. H., Gil, A. J., Bonet, J., Heuzé, T., and Stainier, L. “An entropy-stable Smooth Particle Hydrodynamics algorithm for large strain thermo-elasticity”. In: *Computer Methods in Applied Mechanics and Engineering* 379 (2021), p. 113736.
- [24] Ghugal, Y. and Shimpi, R. “A review of refined shear deformation theories of isotropic and anisotropic laminated plates”. In: *Journal of reinforced plastics and composites* 21.9 (2002), pp. 775–813.
- [25] Gingold, R. A. and Monaghan, J. J. “Smoothed particle hydrodynamics: Theory and application to non-spherical stars”. In: *Monthly Notices of the Royal Astronomical Society* 181.3 (1977), pp. 375–389.
- [26] Goswami, S., Klaus, S., and Benziger, J. “Wetting and absorption of water drops on Nafion films”. In: *Langmuir* 24.16 (2008), pp. 8627–8633.
- [27] Gotoh, H. and Khayyer, A. “On the state-of-the-art of particle methods for coastal and ocean engineering”. In: *Coastal Engineering Journal* 60.1 (2018), pp. 79–103. DOI: 10.1080/21664250.2018.1436243.
- [28] Gotoh, H., Khayyer, A., and Shimizu, Y. “Entirely Lagrangian meshfree computational methods for hydroelastic fluid-structure interactions in ocean engineering Reliability, adaptivity and generality”. In: *Applied Ocean Research* 115 (2021), p. 102822.
- [29] Harewood, F. and McHugh, P. “Comparison of the implicit and explicit finite element methods using crystal plasticity”. In: *Computational Materials Science* 39.2 (2007), pp. 481–494.
- [30] Hosain, M. L., Domínguez, J., Fdhila, R. B., and Kyprianidis, K. “Smoothed particle hydrodynamics modeling of industrial processes involving heat transfer”. In: *Applied Energy* 252 (2019), p. 113441.

- [31] Hu, X. Y. and Adams, N. A. "A multi-phase SPH method for macroscopic and mesoscopic flows". In: *Journal of Computational Physics* 213.2 (2006), pp. 844–861.
- [32] Hughes, T. J. and Liu, W. "Implicit-explicit finite elements in transient analysis: Implementation and numerical examples." In: *Journal of Applied Mechanics, Transactions ASME* 45.2 (1978), pp. 375–378.
- [33] Kanok-Nukulchai, W., Barry, W., Saran-Yasoonontorn, K., and Bouillard, P. "On elimination of shear locking in the element-free Galerkin method". In: *International journal for numerical methods in engineering* 52.7 (2001), pp. 705–725.
- [34] Keyes, D. E., McInnes, L. C., Woodward, C., Gropp, W., Myra, E., Pernice, M., Bell, J., Brown, J., Clo, A., Connors, J., et al. "Multiphysics simulations: Challenges and opportunities". In: *The International Journal of High Performance Computing Applications* 27.1 (2013), pp. 4–83.
- [35] Khayyer, A., Gotoh, H., and Shimizu, Y. "On systematic development of FSI solvers in the context of particle methods". In: *Journal of Hydrodynamics* 34.3 (2022), pp. 395–407.
- [36] Khayyer, A., Shimizu, Y., Gotoh, H., and Nagashima, K. "A coupled incompressible SPH-Hamiltonian SPH solver for hydroelastic FSI corresponding to composite structures". In: *Applied Mathematical Modelling* 94 (2021), pp. 242–271.
- [37] Knoll, D., Chacon, L., Margolin, L., and Mousseau, V. "On balanced approximations for time integration of multiple time scale systems". In: *Journal of Computational Physics* 185.2 (2003), pp. 583–611.
- [38] Korsawe, J., Starke, G., Wang, W., and Kolditz, O. "Finite element analysis of poroelastic consolidation in porous media: Standard and mixed approaches". In: *Computer Methods in Applied Mechanics and Engineering* 195.9-12 (2006), pp. 1096–1115.
- [39] Krysl, P. and Belytschko, T. "Analysis of thin plates by the element-free Galerkin method". In: *Computational Mechanics* 17.1-2 (1995), pp. 26–35.
- [40] Krysl, P. and Belytschko, T. "Analysis of thin shells by the element-free Galerkin method". In: *International Journal of Solids and Structures* 33.20-22 (1996), pp. 3057–3080.
- [41] Lee, C. H., Refachinho de Campos, P. R., Gil, A. J., Giacomini, M., and Bonet, J. "An entropy-stable updated reference Lagrangian smoothed particle hydrodynamics algorithm for thermo-elasticity and thermo-visco-plasticity". In: *Computational Particle Mechanics* 10.6 (2023), pp. 1493–1531.
- [42] Li, S., Hao, W., and Liu, W. K. "Numerical simulations of large deformation of thin shell structures using meshfree methods". In: *Computational Mechanics* 25 (2000), pp. 102–116.
- [43] Libersky, L. D. and Petschek, A. G. "Smooth particle hydrodynamics with strength of materials". In: *Advances in the Free-Lagrange Method Including Contributions on Adaptive Gridding and the Smooth Particle Hydrodynamics Method*. Springer, 1991, pp. 248–257.
- [44] Liu, M. and Liu, G. "Meshfree particle simulation of micro channel flows with surface tension". In: *Computational Mechanics* 35 (2005), pp. 332–341.
- [45] Liu, M. and Liu, G. "Smoothed particle hydrodynamics (SPH): an overview and recent developments". In: *Archives of computational methods in engineering* 17.1 (2010), pp. 25–76.
- [46] Liu, M., Liu, G., and Lam, K. "Adaptive smoothed particle hydrodynamics for high strain hydrodynamics with material strength". In: *Shock Waves* 15 (2006), pp. 21–29.

- [47] Liu, M. and Zhang, Z. “Smoothed particle hydrodynamics (SPH) for modeling fluid-structure interactions”. In: *Science China Physics, Mechanics and Astronomy* 62.8 (2019), pp. 1–38.
- [48] Liu, W. K. and Belytschko, T. “Mixed-time implicit-explicit finite elements for transient analysis”. In: *Computers & Structures* 15.4 (1982), pp. 445–450.
- [49] Long, T., Yang, P., and Liu, M. “A novel coupling approach of smoothed finite element method with SPH for thermal fluid structure interaction problems”. In: *International Journal of Mechanical Sciences* 174 (2020), p. 105558.
- [50] Love, A. E. H. “XVI. The small free vibrations and deformation of a thin elastic shell”. In: *Philosophical Transactions of the Royal Society of London. (A.)* 179 (1888), pp. 491–546.
- [51] Lucy, L. B. “A numerical approach to the testing of the fission hypothesis”. In: *The Astronomical Journal* 82 (1977), pp. 1013–1024.
- [52] Luo, M., Khayyer, A., and Lin, P. “Particle methods in ocean and coastal engineering”. In: *Applied Ocean Research* 114 (2021), p. 102734. DOI: 10.1016/j.apor.2021.102734.
- [53] Lyu, H.-G., Sun, P.-N., Huang, X.-T., Chen, S.-H., and Zhang, A.-M. “On removing the numerical instability induced by negative pressures in SPH simulations of typical fluid-structure interaction problems in ocean engineering”. In: *Applied Ocean Research* 117 (2021), p. 102938.
- [54] Mindlin, R. “Influence of rotatory inertia and shear on flexural motions of isotropic, elastic plates”. In: (1951).
- [55] Monaghan, J. J. “Simulating free surface flows with SPH”. In: *Journal of Computational Physics* 110.2 (1994), pp. 399–406.
- [56] Monaghan, J. J. “SPH without a tensile instability”. In: *Journal of Computational Physics* 159.2 (2000), pp. 290–311.
- [57] Morris, J. P., Fox, P. J., and Zhu, Y. “Modeling low Reynolds number incompressible flows using SPH”. In: *Journal of Computational Physics* 136.1 (1997), pp. 214–226.
- [58] Motupally, S., Becker, A. J., and Weidner, J. W. “Diffusion of water in Nafion 115 membranes”. In: *Journal of The Electrochemical Society* 147.9 (2000), p. 3171.
- [59] Ng, K. C., Ng, Y. L., Sheu, T., and Mukhtar, A. “Fluid-solid conjugate heat transfer modelling using weakly compressible smoothed particle hydrodynamics”. In: *International Journal of Mechanical Sciences* 151 (2019), pp. 772–784.
- [60] Owen, J. M., Villumsen, J. V., Shapiro, P. R., and Martel, H. “Adaptive smoothed particle hydrodynamics: Methodology. II.” In: *The Astrophysical Journal Supplement Series* 116.2 (1998), p. 155.
- [61] Ozdemir, M., Tanaka, S., Sadamoto, S., Yu, T., and Bui, T. “Numerical buckling analysis for flat and cylindrical shells including through crack employing effective reproducing kernel meshfree modeling”. In: *Engineering Analysis with Boundary Elements* 97 (2018), pp. 55–66.
- [62] Peng, Y., Zhang, A., and Ming, F. “A thick shell model based on reproducing kernel particle method and its application in geometrically nonlinear analysis”. In: *Computational Mechanics* 62 (2018), pp. 309–321.
- [63] Prior, A. “Applications of implicit and explicit finite element techniques to metal forming”. In: *Journal of Materials Processing Technology* 45.1-4 (1994), pp. 649–656.

- [64] Ragusa, J. C. and Mahadevan, V. S. "Consistent and accurate schemes for coupled neutronics thermal-hydraulics reactor analysis". In: *Nuclear Engineering and Design* 239.3 (2009), pp. 566–579.
- [65] Raisi, A. and Arvin, I. "A numerical study of the effect of fluid-structure interaction on transient natural convection in an air-filled square cavity". In: *International Journal of Thermal Sciences* 128 (2018), pp. 1–14.
- [66] Randles, P. and Libersky, L. D. "Smoothed particle hydrodynamics: Some recent improvements and applications". In: *Computer Methods in Applied Mechanics and Engineering* 139.1-4 (1996), pp. 375–408.
- [67] Rao, Y. G., Nataraj, M., and Srinivas, P. "Explicit Dynamic Analysis of Tensional & Torsional Propagations on Composite Material with Dog Bone Shaped Testing Specimen". In: *International Journal for Modern Trends in Science and Technology ISSN* (2019), pp. 2455–3778.
- [68] Ren, B. and Li, S. "Modeling and simulation of large-scale ductile fracture in plates and shells". In: *International Journal of solids and structures* 49.18 (2012), pp. 2373–2393.
- [69] Rezaiee-Pajand, M. and Alamatian, J. "The dynamic relaxation method using new formulation for fictitious mass and damping". In: *Structural engineering and mechanics* 34.1 (2010), p. 109.
- [70] Rezavand, M., Zhang, C., and Hu, X. "A weakly compressible SPH method for violent multi-phase flows with high density ratio". In: *Journal of Computational Physics* 402 (2020), p. 109092.
- [71] Rook, R., Yildiz, M., and Dost, S. "Modeling transient heat transfer using SPH and implicit time integration". In: *Numerical Heat Transfer, Part B: Fundamentals* 51.1 (2007), pp. 1–23.
- [72] Shao, S., Ji, C., Graham, D. I., Reeve, D. E., James, P. W., and Chadwick, A. J. "Simulation of wave overtopping by an incompressible SPH model". In: *Coastal engineering* 53.9 (2006), pp. 723–735.
- [73] Soti, A. K., Bhardwaj, R., and Sheridan, J. "Flow-induced deformation of a flexible thin structure as manifestation of heat transfer enhancement". In: *International Journal of Heat and Mass Transfer* 84 (2015), pp. 1070–1081.
- [74] Sun, J., Lee, K., and Lee, H. "Comparison of implicit and explicit finite element methods for dynamic problems". In: *Journal of materials processing technology* 105.1-2 (2000), pp. 110–118.
- [75] Vignjevic, R., Reveles, J. R., and Campbell, J. "SPH in a total Lagrangian formalism". In: *CMC-Tech Science Press*- 4.3 (2006), p. 181.
- [76] Vishwakarma, V., Das, A. K., and Das, P. "Steady state conduction through 2D irregular bodies by smoothed particle hydrodynamics". In: *International Journal of Heat and Mass Transfer* 54.1-3 (2011), pp. 314–325.
- [77] Wang, Z., Ma, J., and Zhang, L. "Finite element thermal model and simulation for a cylindrical Li-ion battery". In: *IEEE Access* 5 (2017), pp. 15372–15379.
- [78] Yaghmaie, R. and Ghosh, S. "Multi-time scale based modeling of piezoelectric materials coupling transient electrical and dynamic fields with finite deformation damage". In: *International Journal of Solids and Structures* 202 (2020), pp. 338–355.
- [79] Yang, X. and Kong, S.-C. "Numerical study of natural convection in a horizontal concentric annulus using smoothed particle hydrodynamics". In: *Engineering Analysis with Boundary Elements* 102 (2019), pp. 11–20.

- [80] Yesudasan, S. and Averett, R. D. “Recent advances in computational modeling of fibrin clot formation: A review”. In: *Computational biology and chemistry* 83 (2019), p. 107148.
- [81] Yilmaz, M., Anıl, Ö., Alyavuz, B., and Kantar, E. “Load displacement behavior of concrete beam under monotonic static and low velocity impact load”. In: *International Journal of Civil Engineering* 12.4 (2014), pp. 488–503.
- [82] Zhang, C., Xiang, G., Wang, B., Hu, X., and Adams, N. “A weakly compressible SPH method with WENO reconstruction”. In: *Journal of Computational Physics* 392 (2019), pp. 1–18.
- [83] Zhang, C., Rezavand, M., and Hu, X. “A multi-resolution SPH method for fluid-structure interactions”. In: *Journal of Computational Physics* 429 (2021), p. 110028.
- [84] Zhang, C., Rezavand, M., Zhu, Y., Yu, Y., Wu, D., Zhang, W., Wang, J., and Hu, X. “SPHinXsys: An open-source multi-physics and multi-resolution library based on smoothed particle hydrodynamics”. In: *Computer Physics Communications* 267 (2021), p. 108066.
- [85] Zhang, C., Zhu, Y., Wu, D., and Hu, X. “Review on smoothed particle hydrodynamics: Methodology development and recent achievement”. In: *arXiv preprint arXiv:2205.03074* (2022). DOI: 10.48550/arXiv.2205.03074.
- [86] Zhang, C., Zhu, Y., Yu, Y., Wu, D., Rezavand, M., Shao, S., and Hu, X. “An artificial damping method for total Lagrangian SPH method with application in biomechanics”. In: *Engineering Analysis with Boundary Elements* 143 (2022), pp. 1–13.
- [87] Zhang, L., Ademiloye, A., and Liew, K. “Meshfree and particle methods in biomechanics: Prospects and challenges”. In: *Archives of Computational Methods in Engineering* 26.5 (2019), pp. 1547–1576.
- [88] Zhao, Q. and Papadopoulos, P. “Modeling and simulation of liquid diffusion through a porous finitely elastic solid”. In: *Computational Mechanics* 52.3 (2013), pp. 553–562.
- [89] Zhu, Y., Zhang, C., and Hu, X. “A dynamic relaxation method with operator splitting and random-choice strategy for SPH”. In: *Journal of Computational Physics* 458 (2022), p. 111105.